Towards a heat transfer based distance sensor for measuring sub-micrometer separations

Bijster, R.J.F.

DOI
10.4233/uuid:39db65ee-6e96-4dc5-a654-22893e5c8a29

Publication date
2021

Document Version
Final published version

Citation (APA)
Bijster, R. J. F. (2021). *Towards a heat transfer based distance sensor for measuring sub-micrometer separations*. [Dissertation (TU Delft), Delft University of Technology]. https://doi.org/10.4233/uuid:39db65ee-6e96-4dc5-a654-22893e5c8a29

Important note
To cite this publication, please use the final published version (if applicable).
Please check the document version above.

Towards a heat transfer based distance sensor for measuring sub-micrometer separations

Proefschrift

ter verkrijging van de graad van doctor
aan de Technische Universiteit Delft,
op gezag van de Rector Magnificus prof.dr.ir. T.H.J.J. van der Hagen,
voorzitter van het College voor Promoties,
in het openbaar te verdedigen op
woensdag 29 september 2021 om 15:00 uur

door

Roy Jacobus Franciscus BIJSTER

Ingenieur in de Luchtvaart- en Ruimtevaart,
Technische Universiteit Delft, Nederland
geboren te Valkenswaard, Nederland.

Dit proefschrift is goedgekeurd door de promotoren.

Samenstelling promotiecommissie bestaat uit:

Rector Magnificus,	voorzitter
Prof. dr. ir. A. van Keulen,	Technische Universiteit Delft, promotor
Prof. dr. ir. G. Gerini,	Technische Universiteit Eindhoven, promotor
Onafhankelijke leden:	
Prof. dr. A. Stemmer,	ETH Zürich
Prof. dr. A. Kittel,	Carl v. Ossietzky Universität Oldenburg
Prof. dr. ir. M. Steinbuch,	Technische Universiteit Eindhoven
Prof. dr. U. Staufer,	Technische Universiteit Delft
Dr. S.M.B. Bäumer,	TNO Delft
Prof. dr. P.G. Steeneken,	Technische Universiteit Delft, reservelid

Keywords: heat transfer, near field, cantilever, microscopy, sensing, distance

Printed by: Gildeprint

Front & Back: Photo of the heart of the experimental setup with in the very center the probe and the prism that acts as the sample. Photo courtesy of TNO. Photo by Rogier Bos.

ISBN 978-94-6384-235-8

An electronic version of this dissertation is available at
`http://repository.tudelft.nl/`.

for Nina
for my parents, Johan and Francis

Table of Contents

Summary

Since the late 1500s, people have used optical microscopes to aid the eye in perceiving the small details of the world around us. The resolution of these microscopes is limited by the diffraction limit to half the wavelength of the used light. In practice, this boils down to a resolution of roughly 200 nm. New lens types have become available that can attain better resolution in optical microscopy by extracting information from the evanescent field: the electromagnetic fields that only exist near the surface of the sample. To make these lenses work, however, the lens needs to be positioned at a distance that is smaller than the wavelength of interest. For visible light, this translates to distances of mere tens of nanometers. This positioning of the lens requires a sensor that is capable of reliably measuring such small distances and can ideally be integrated close to the lens.

The aim of this thesis is to develop a proof-of-principle demonstration of using heat flux between two bodies for determining the distance between them. This thesis presents an instrument architecture in Chapter 2 towards realizing such a device and focuses on understanding and characterizing the elements that contribute to the heat flux measurement.

The sensing element (or probe) consists of a microsphere that is located at the end of multilayer cantilever beam. Changes in the temperature of the probe result in mechanical deformation that is measured using the Optical Beam Deflection (OBD) method. In this technique, laser light is reflected of the cantilever onto a position sensitive detector (PSD). The power of the incident laser light is modulated to compensate the change in temperature. In Chapter 2, a model is constructed that relates the heat flux at the tip of the probe to the system parameters. The model provides a relation for the output signal of the PSD to the heat flux absorbed at the tip of the probe.

In the instrument, the distance between the probe and the sample is measured independently using a total internal reflection microscope (TIRM). The use of a TIRM allows for a continuous measurement of the separation between the microsphere and the sample. TIRM is a well-known technique for measuring the distance between a flat interface and microspheres. However, the implementation of this technique in combination with an optical beam deflection system is not straightforward. As is shown in Chapter 3, the presence of a microcantilever and its clamp limit the accessible volume. This makes it impossible to capture the light scattered in the forwardscattering direction, in which the scattering intensity is highest. Moreover, the intensity of the

light that is scattered by the roughness of the prism easily exceeds that of the TIRM signal. Although detection in the backscattering direction suffers strongly from this effect, it remains the most viable configuration. This layout decouples the TIRM and OBD system and does not penalize the OBD performance.

The performance of the instrument is for a large part determined by the properties of the probe. In Chapter 4, a cantilever is designed that provides high sensitivity and low noise in heat flux measurements. The design of the cantilever considers the probe as an integral part of the instrument and takes into account the constraints that are imposed by the instrument architecture. In the design, it is assumed that the OBD system uses an infinitessimal spot at the free-end of the cantilever. In Chapter 5, the reduction of the cantilever sensitivity caused by a finite spot size and different spot location is studied. It is shown that under realistic conditions, the sensitivity is reduced to 50 % to 90 % of the ideal value.

The size, shape and roughness of the microsphere that is attached to the free-end of the cantilever influence the instrument performance. The size, for example, determines the total amount of heat that is transferred between the probe and the sample and influences the dynamic properties of the probe. The roughness limits the smallest separation that can be achieved between the probe and the sample, before microscopic contact is likely to occur. Chapter 6 shows the measured shapes, sizes and roughnesses of both the sample (the surface of a prism) and the microsphere that are obtained using interferometry and atomic force microscopy. Based on the measurements, it is concluded that the roughness of the sphere and the presence of local surface features limit the minimum separation to approximately 100 nm.

The cantilever deforms due to the heat flux at its free end. However, a thermal gradient exists between the part of the sphere that is closest to the sample and its connection to the cantilever. To quantify this gradient, a lumped-parameter model is developed for heat conduction across a solid sphere in Chapter 7. This model is used to show that the effective conductance of the microsphere changes by approximately a factor of two for spheres of radii between 10 µm and 100 µm and separations to the sample ranging from 1 nm to 100 nm. This adds an additional source of uncertainty to the measured heat flux that was previously not considered.

The sphere and cantilever are joined into one probe in Chapter 8. Due to the high temperatures that are reached at the cantilever tip, only soluble silicates are found to be suitable adhesives for joining the sphere to the probe. The spheres were successfully attached to the cantilevers, but the bonds failed during use. It is hypothesised that the bonds break due to (rapid) thermal expansion at the interface, but this could not be verified experimentally.

The breaking bonds between the sphere and the cantilever beam prohibited measurements of near-field radiative heat flow and the intended demonstration of using heat flow for distance measurements. This thesis, however, contributes a system architecture that allows the further development of such a sensor system. Moreover, this research contributes a detailed study of the

role of the microsphere and the cantilever beam in conjunction with the OBD system, and the other subsystems.

Samenvatting

Sinds het einde van de 16^{e} eeuw, gebruiken mensen optische microscopen om het oog te helpen in het waarnemen van de kleinste details van de wereld om ons heen. De resolutie van deze microscopen wordt beperkt door de diffractielimiet tot de helft van de golflengte van het gebruikte licht. In de praktijk komt dit neer op een resolutie van circa 200 nm. Nieuwe lenstypes zijn beschikbaar gekomen die een betere resolutie beschikbaar maken in optische microscopie door informatie uit het nabije veld te halen: de elektromagnetische velden die alleen bestaan nabij het oppervlakte van het monster. Om deze lenzen te laten werken, moet de lens echter worden gepositioneerd op een afstand die kleiner is dan de gebruikte golflengte. Voor zichtbaar licht vertaalt zich dit in afstanden van slechts enkele tientallen nanometers. Het positioneren van de lens vereist een sensor die in staat is om betrouwbaar zulke kleine afstanden te meten en die dicht bij de lens geïntegreerd kan worden.

Het doel van dit proefschrift is het ontwikkelen van een *proof-of-principle* demonstratie van het gebruik van warmtetransport tussen twee lichamen voor het bepalen van de onderlinge afstand. In Hoofdstuk 2 van dit proefschrift wordt de instrumentarchitectuur uiteengezet met als doel een dergelijk apparaat te realiseren. De focus ligt in dit proefschrift daarbij op het begrijpen en karakteriseren van de elementen die bijdragen aan de meting van de warmtestroom.

De sensor (of sonde) bestaat uit een microbol die zich aan het uiteinde van een vrijliggende balk bevindt. Veranderingen van de temperatuur van de sonde resulteren in mechanische vervorming. Deze vervorming wordt gemeten met de *Optical Beam Deflection* (OBD) methode. In deze techniek wordt laserlicht via de vrijhangende balk gereflecteerd richting een positiegevoelige detector (PSD). Het vermogen van het opvallende laserlicht wordt gemoduleerd om de temperatuursverandering te compenseren. In Hoofdstuk 2 wordt een model ontwikkeld dat de warmtestroom aan de punt van de sonde relateert aan de systeemparameters. Het model voorziet in een relatie tussen het uitgangssignaal van de PSD en de warmtestroom die wordt geabsorbeerd aan de punt van de balk.

In het instrument wordt de afstand tussen de sonde en het monster onafhankelijk van de actuator gemeten door middel van een totale interne reflectiemicroscoop (TIRM). Het gebruik van deze microscoop maakt het continu meten van de afstand tussen de microbol en het monster mogelijk. TIRM is

een bekende techniek voor het meten van afstanden tussen een vlak en microbollen. De implementatie van TIRM in combinatie met OBD is echter niet vanzelfsprekend. Zoals uiteengezet in Hoofdstuk 3 beperken de aanwezigheid van de vrijhangende balk en de bijhorende klem het volume dat toegankelijk is voor detectie. Dit zorgt ervoor dat het onmogelijk is om het licht in de voorwaardse richting, waarin de verstrooiing het sterkst is, te detecteren. Bovendien is de intensiteit van het door de ruwheid van het prisma verstrooide licht groter dan de intensiteit van het signaal van de TIRM. Detectie vanuit de terugwaardse richting blijft de meest geschikte optie, ondanks dat detectie vanuit deze richting sterk de nadelen van dit effect ondervindt. Dit ontwerp ontkoppelt de TIRM en het OBD-systeem en beperkt de prestaties van het OBD systeem niet.

De prestaties van het instrument worden voor een groot deel bepaald door de eigenschappen van de sonde. In Hoofdstuk 4 wordt een vrijhangende balk ontworpen die voorziet in een hoge gevoeligheid en een lage ruis in warmtestroommetingen. In het ontwerp wordt de balk als een integraal deel van het instrument beschouwd en worden de beperkingen die worden opgelegd door de architectuur van het instrument meegenomen. Er wordt in dit ontwerp aangenomen dat de OBD een oneindig kleine vlek aan het vrijliggende uiteinde van de balk belicht. In Hoofdstuk 5 wordt de reductie in gevoeligheid door het gebruik van een vlek van eindige grootte en andere locaties van de vlek op de balk bestudeerd. Onder realistische omstandigheden kan de gevoeligheid van de balk worden teruggebracht tot 50 % á 90 % van de ideale waarde.

De grootte, vorm en ruwheid van de microbol die aan het einde van de balk zit, beïnvloedt de prestaties van het instrument. De totale warmtestroom tussen het monster en de sonde en de dynamische eigenschappen van de sonde worden bijvoorbeeld (mede) bepaald door de grootte van microbol. De ruwheid beperkt de kleinste afstand tussen de sonde en het monster die kan worden gerealiseerd voordat microscopisch contact tussen beide reëel is. De gemeten vormen, groottes en ruwheden van zowel het monster (het oppervlakte van een prisma) en de microbollen zoals verkregen door middel van interferometrie en atoomkrachtmicroscopie (AFM) staan omschreven in Hoofdstuk 6. Op basis van deze metingen wordt geconcludeerd dat de ruwheid van de bol en de aanwezigheid van lokale details op het oppervlakte daarvan ervoor zorgen dat de minimale afstand beperkt wordt tot circa 100 nm.

De balk vervormt door de warmtestroom aan diens vrijhangende uiteinde. Er bestaat een thermische gradiënt tussen het deel van de bol dat het dichtst bij het monster is en de verbinding met de balk. Om deze gradiënt te kwantificeren, wordt een model voor de warmtegeleiding door een solide bol uitgewerkt in Hoofdstuk 7. Met behulp van dit model wordt aangetoond dat de effectieve geleiding door de microbol met circa een factor twee verandert voor bollen met een straal tussen de 10 µm en 100 µm en voor afstanden tot het monster tussen 1 nm en 100 nm. Dit geeft een extra bron van onzekerheid in de gemeten warmtestroom die niet eerder werd overwogen.

De bol en de balk worden in Hoofdstuk 8 samengebracht om samen één

sonde te vormen. Door de hoge temperaturen die bereikt worden aan het vrijliggende einde van de balk, zijn alleen oplosbare silicaten geschikt als lijm voor het verbinden van de bol en de balk. De bollen werden succesvol aan de balken bevestigd, maar de verbinding faalde tijdens gebruik. Er wordt verondersteld dat de verbinding breekt door de (snelle) thermische uitzetting ter hoogte van de verbinding, maar dit kon niet experimenteel worden bevestigd.

Door de falende verbindingen tussen de bol en de vrijhangende balk is het niet mogelijk om stralingswarmtetransport in het nabije veld te meten en het gebruik van warmtestroom voor afstandsmetingen te demonstreren. Dit proefschrift draagt echter een systeemarchitectuur bij waarmee een dergelijke sensorsysteem verder kan worden ontwikkeld. Bovendien voorziet dit onderzoek in een gedetailleerde studie in de bijdrage van de microbol, de bijdrage van de vrijhangende balk samen met het OBD-systeem en de bijdrages van de overige subsystemen.

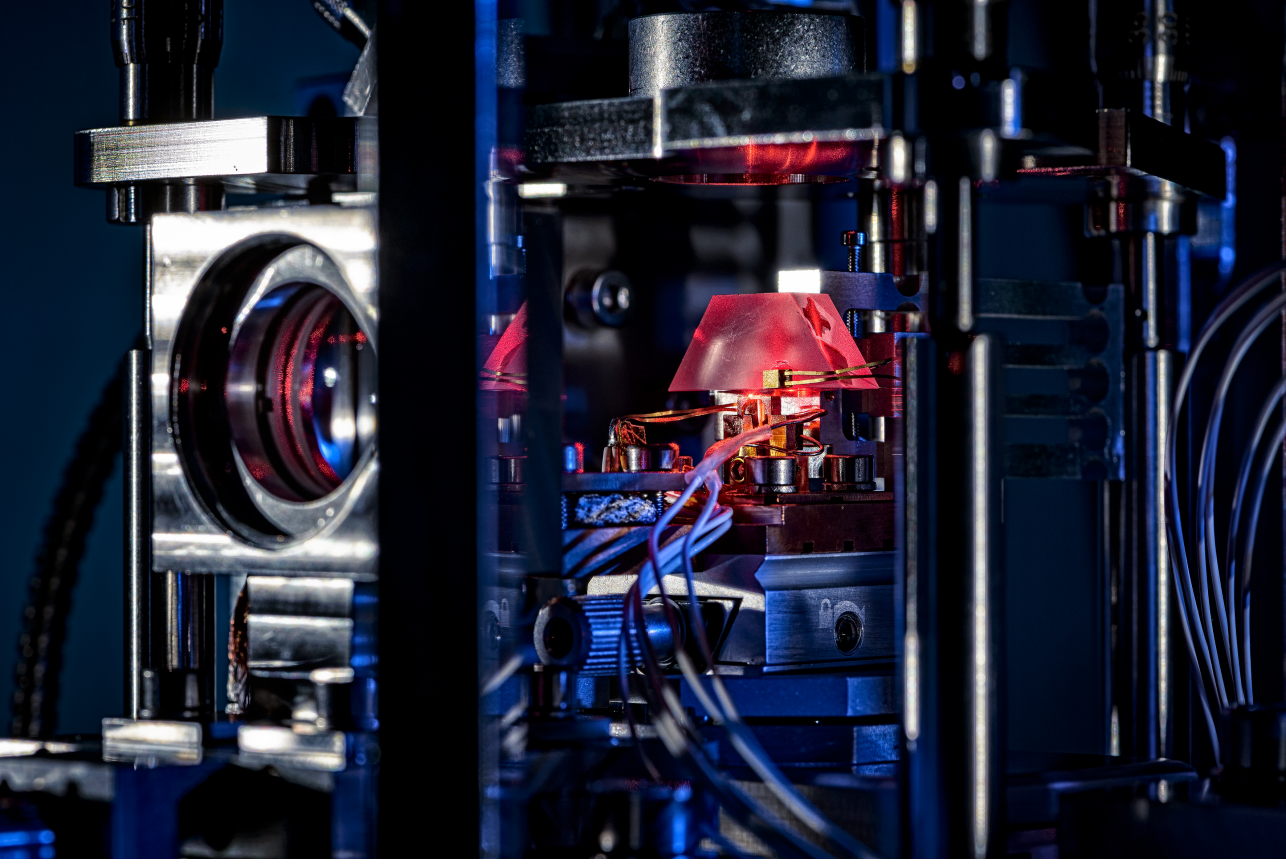

1. Introduction

The invention of the 'compound optical microscope', so called because it consists of multiple lenses to create a magnified image, heralded a long chain of scientific discovery and innovation. Merely a century after its invention in the late 1500s, Antoni van Leeuwenhoek resolved features mere micrometers in size [1]. Four hundred years later, the performance of conventional optical microscopes approaches the Abbe diffraction limit, which says that the resolution cannot exceed half the wavelength of the used light [2]. In practice, this equates to a resolution of roughly 200 nm, which is more than adequate for many applications in both science and engineering.

To illustrate how these microscopes were and still are instrumental in many discoveries we need not look far, because the examples are plentiful. In biology, for example, Louis Pasteur used a compound optical microscope to discover that micro-organisms can cause infections [3]. Metallurgists use the

Title photo: close-up of the internals of the instrument. The light source of the total internal reflection microscope is used close to the edge of the prism to make it light up. Photo by Rogier Bos, courtesy of TNO.

same instruments to study phase structures and dimensions in alloys [4], and manufacturers of integrated circuits use optical microscopes to realign their masks and wafers between production steps [5].

However, nanometer resolution is beyond the reach of the conventional optical microscope. It is, instead, a task for scanning microscopes. While imaging microscopes, such as the compound optical microscope described earlier, record the complete image at once, scanning devices construct the micrograph point-by-point by traversing a probe or beam across the sample. In doing so, they can achieve much higher resolution than conventional optical microscopes, and atomic resolution is not unheard of [6].

For example, in the case of the atomic force microscope (AFM), a small mechanical probe 'feels' the force between its tip and the surface to construct a detailed map of the surface topography [7, 8]. In other instances, a highly energetic beam of electrons is focused on the sample while the intensity of the backscattered or the transmitted electrons is measured [9]; these techniques are respectively known as scanning electron microscopy (SEM) and scanning transmission electron microscopy (STEM). Even scanning near-field optical microscopes (SNOM) can be used to record the local intensity of the electromagnetic field that exists close to the surface to the same effect [10].

Unfortunately, scanning is inherently slow in comparison to imaging, whereas the latter offers comparatively low resolution. Although substantial advances have been made to increase the speed of scanning techniques [11], the combination of high throughput and high resolution is hard to realize in a single device. It is currently only achieved by means of massive parallelization, where multiple microscopes are used to record the same sample at different locations or multiple samples at the same time [12].

Another solution may lie in ongoing developments in near-field optics, that promise high-resolution imaging microscopes. Using a layered arrangement of alternating metals and dielectrics, a flat lens known as a 'hyperlens' can be realized [13, 14]. It can be used to *image* the evanescent field that exists only close to the sample surface, but contains all details that are inaccessible to conventional lenses. By using this information much higher resolution can be achieved.

Once paired with a high-bandwidth positioning platform, the resulting instrument may be able to bridge the gap between the high-resolution, but slow-scanning probe microscopes on the one hand and the fast, but low-resolution imaging microscopes on the other. Elsewhere, we presented one such instrument architecture [15], that uses cascaded actuators to achieve a large stroke of several millimeters and sub-nanometer positioning resolution and a high positioning bandwidth of over 500 kHz. A photo of this positioning platform is shown in Figure 1.1.

To make such a microscope work in practice, however, the resulting instrument will need to position the 'lens' at a distance smaller than the wavelength of interest to be able to pick up the evanescent field. For visible light, this translates to distances of mere tens of nanometers. In addition to the aforementioned actuator, this requires a high-resolution position sensor to measure

Figure 1.1: Realized positioning and tracking platform for near-field imaging microscopes developed by TNO [15]. Shown is a three-stage positioning platform with a long stroke linear stepper motor, a pre-stressed piezo stage and a micro-electro-mechanical system. Photo by Rogier Bos, courtesy of TNO/NOMI.

the distance between the lens and the sample surface. Ideally, the position sensor is independent from material properties, provides high-resolution and accuracy, offers a high-measurement bandwidth and can be miniaturized easily to be integrated into the instrument and positioned close to the lens. However, existing techniques that are typically used for measuring such small distances, e.g., interferometry or capacitive sensors, are difficult to miniaturize, and more importantly rely on the sample surface being either reflective or electrically conductive. Both conditions cannot be guaranteed.

The heat transferred between two bodies increases rapidly with diminishing separation at micrometer length scales and can be made largely material-independent. To illustrate the potential for using it for measuring microscopic distances, the sensitivity of an ideal sensor is plotted in Figure 1.2. A sensor with a resolution of 1 nW for the flux measurement has a corresponding resolution of 1 pm or 1 nm for a distance measurement when using gas conduction or near-field radiation, respectively. This makes it a promising candidate for a distance sensor.

Such a sensor needs to be capable of measuring minute quantities of heat transfer with high precision and accuracy. This is not a trivial pursuit and has been an active field of research for over 50 years. The measurement systems devised so far can be categorized into three archetypes: (1) parallel plates, (2) miniature thermocouples, and (3) thermo-mechanical probes.

In 1969, Clifford Hargreaves published a seminal paper on the measurement of what was then called “anomalous radiative transfer between closely-spaced bodies” [18]. By using piezo-crystals for positioning two plates and three capacitive sensors to measure their local separation, he solved the issues his contemporaries faced in maintaining an extremely high degree of parallelism at small separations [19, 20]. The heat transferred between the plates is measured by setting one of the two plates at a constant temperature, while measuring the required heating power that is needed to keep the temperature of the second plate constant. This system architecture is one of

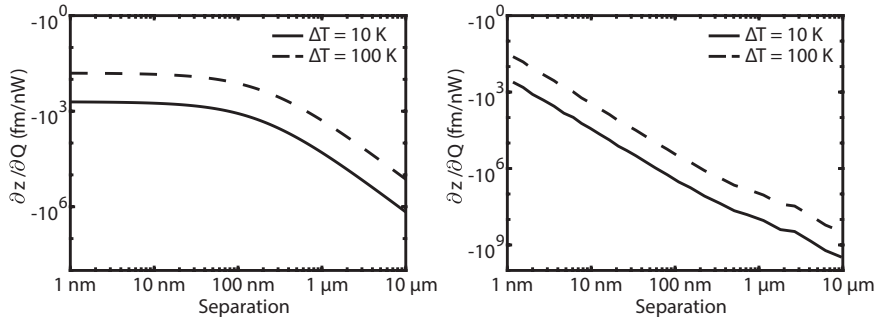

Figure 1.2: Ideal sensitivity of a distance sensor based on heat transfer using gas conduction (left) or near-field radiation (right). In these figures, the gap and the total heat flux are denominated z and Q, respectively. The sensitivity via gas conduction is derived from the analytical model by Masters *et al.* [16], while that for near-field radiation is based on measurements performed by Rousseau *et al.* [17]. Both are good approximations for parallel plates that are separated by microscopic gaps.

the three archetypes, and formed the foundation of several setups over the past 60 years with only minor changes [21–24]. To reduce system complexity, some have attempted to maintain parallelism by passive means. They have used spacers, e.g., to create a gap of a known, constant width [25–30]. Others have resorted to microfabrication techniques to create suspended plates [31–35] or beams [36, 37]. The parallel plate geometry is ideal for the validation of theory and for thermophotovoltaic applications, such as energy harvesting and contactless cooling. The long time constants associated with the macroscopic plates, and the difficulties in maintaining the plates parallel, makes them non-ideal for distance sensing applications.

The second archetype was proposed by Williams and Wickramasinghe in 1986 [38]. They replaced one of the plates by an AFM probe with a thermocouple embedded in its tip. The close-range thermal interactions induced a measurable temperature change, which was used to map the surface topography. Similar setups were realized by Xu *et al.* in 1994 [39] and later by Müller-Hirsch *et al.* in 1999 [40] using modified scanning tunneling microscope probes that also included a thermocouple. This improved design has been under further development by the same group [41–43], and formed the basis of a similar design by Cui *et al.* [44]. The probe-sample separation is determined from the calibration of the position actuator. A datum (zero distance) is established using the tunneling current measured by the STM. This method is sensitive to actuator drift, where the position changes without a change in actuator signal. This introduces additional uncertainty in measurements of heat flux as function of separation. Moreover, the temperature difference across the gap between the probe and sample is allowed to change. Because the thermal spectra are temperature-dependent this introduces a non-linear dependency that cannot be controlled. This geometry is best suited for applications in scanning probe microscopes.

The third and last archetype uses multilayer AFM probes that are positioned perpendicular to a planar sample. In this architecture, a (glass) microsphere, which acts as the replacement of the second surface, is attached to the free end of one of these probes. The heat transferred between the sphere and the sample causes the probe to deform. This deformation is used as a proxy for the heat flux. This concept was first proposed by Narayanaswamy *et al.* in 2008 [45] and has served as the foundation for many similar setups since [17, 46–49]. The spherical probe tip makes it insensitive to misalignment or rotation of the probe and approximates that of two parallel plates for small separations. Moreover, the probes are simple in comparison to those with embedded thermocouples, and can be calibrated to function as temperature sensors. Its weaknesses, however, are similar to the micro-thermocouple probes: the distance between the probe and the sample has to be inferred from the actuator calibration, and the temperature of the sphere is allowed to vary with gap size.

The aim of this thesis is to develop a proof-of-principle demonstration of using the heat flux between a probe and a sample as a proxy for their separation, thus constructing a distance sensor. The proposed instrument architecture is unique in solving three problems found in comparable setups. First, the distance between the probe and sample is measured independently using a total internal reflection microscope, whereas others have relied on indirect measurement of the separation or measured it far away from the point of interest. Second, the thermal balance of the probe is kept constant using closed-loop control, so that the conditions are constant throughout the duration of the measurement. This allows the flux to be measured directly, rather than via an otherwise needed temperature change. And lastly, the measurement does not require calibration of the probe, but only of the actuator that is used in the control loop. This can be done in a manner that makes the measurement traceable to the International System of Units (SI).

The first step towards realizing such a distance sensor is constructing an accurate calorimeter. The focus in this thesis is therefore on understanding and characterizing the elements that contribute to the heat flux measurement and significantly reduce the measurement uncertainty with respect to comparable systems.

Outline of the thesis

A system as described above consists of many parts. In this thesis, the description of the system is split into two main sections. The first section covers the measuring instrument, that consists of a sensing element, the detection system and all the supporting systems. The system architecture and these building blocks are discussed separately in Chapter 2. In this chapter, the designs of the detection system and the supporting systems are discussed. The separation between the probe and the sample is measured independently using a total internal reflection microscope, which is discussed in Chapter 3.

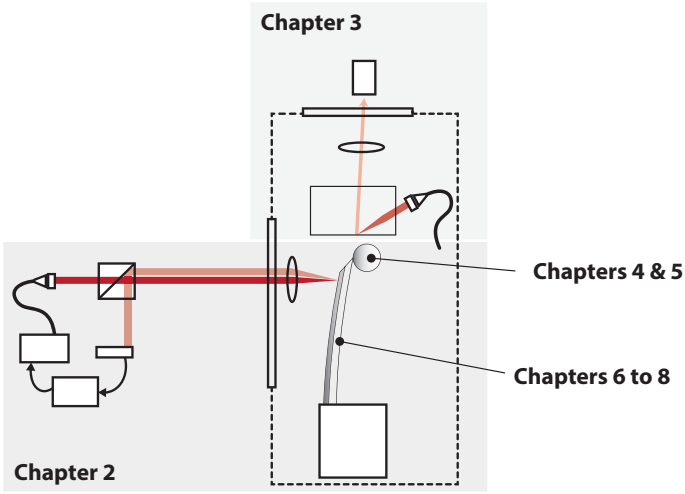

Figure 1.3: Visual outline of the thesis.

In the second section of the thesis, the focus is moved to the sensing element, also known as the probe. This element consists of a microsphere that is attached to a multilayer cantilever. The design of the latter is discussed in detail in Chapter 4 which includes a theoretical model that describes its behavior, a computational benchmark against a probe that is often used by others, and the experimental validation. Chapter 5 discusses how the cantilever sensitivity is negatively affected by finite spot sizes used in the detection system and how this manifests itself in practice.

The probe has a microsphere that is attached to the free end of the cantilever. In the measurements, the heat is transferred between the sample and the microsphere. The surface qualities of both provide limits to the minimum separation that can be achieved and provide limits to the agreement between the theoretical models of heat transfer and the experiments. In Chapter 6, the measurements of the shape and surface roughness of both the sample and the probe are discussed. Due to its shape, a sphere cannot be modeled accurately as a one-dimensional conductor using Fourier's law. The conduction through a sphere is considered numerically in Chapter 7 by calculating the conduction between two unequally sized circular caps on arbitrary locations on the surface of the sphere. This chapter also includes a discussion on the implications on the probe design.

The two main components of the probe - the cantilever and the sphere - are brought together in Chapter 8. This chapter discusses the choice for the adhesive and the gluing procedure and the problems that are encountered at elevated cantilever temperatures.

This thesis is concluded with a discussion concerning the current state-of-affairs and areas of possible improvement in Chapter 9 and the concluding remarks in Chapter 10.

Bibliography

[1] W. J. Croft. *Under the Microscope: A Brief History of Microscopy*. World Scientific Publishing Co. Pte. Ltd., 2006.

[2] E. Abbe. Beiträge zur Theorie des Mikroskops und der mikroskopischen Wahrnehmung. *Archiv für mikroskopische Anatomie*, 9(1):413–418, 1873.

[3] L. Pasteur. The Physiological Theory Of Fermentation. In *Scientific Papers*, p. 1909–1914. The Harvard Classics, 1897.

[4] G. F. V. Voort. *ASM Handbook Volume 9: Metallography and Microstructures*. ASM International, Materials Park, OH, USA, 2004.

[5] M. K. A. Kuni. Method and apparatus for reduction-projection type mask alignment, 1976.

[6] D. J. Smith. Progress and perspectives for atomic-resolution electron microscopy. *Materials Today*, 12:10–16, 2010.

[7] G. Binnig, C. F. Quate, and C. Gerber. Atomic Force Microscope. *Physical Review Letters*, 56(9):930–933, 1986.

[8] G. Binnig, C. Gerber, E. Stoll, T. R. Albrecht, and C. F. Quate. Atomic Resolution with Atomic Force Microscope. *Europhysics Letters (EPL)*, 3(12):1281–1286, 1987.

[9] D. McMullan. Scanning electron microscopy 1928-1965. *Scanning*, 17(3):175–185, 2006.

[10] E. A. Ash and G. Nicholls. Super-resolution Aperture Scanning Microscope. *Nature*, 237(5357):510–512, 1972.

[11] A. J. Katan and C. Dekker. High-Speed AFM Reveals the Dynamics of Single Biomolecules at the Nanometer Scale. *Cell*, 147(5):979–982, 2011.

[12] H. Sadeghian, R. Herfst, B. Dekker, J. Winters, T. Bijnagte, and R. Rijnbeek. High-throughput atomic force microscopes operating in parallel. *Review of Scientific Instruments*, 88(3):033703, 2017.

[13] W. Wang, H. Xing, L. Fang, Y. Liu, J. Ma, L. Lin, C. Wang, and X. Luo. Far-field imaging device: planar hyperlens with magnification using multi-layer metamaterial. *Optics Express*, 16(25):21142, 2008.

[14] Z. Jacob, L. V. Alekseyev, and E. Narimanov. Optical Hyperlens: Far-field imaging beyond the diffraction limit. *Optics Express*, 14(18):8247, 2006.

[15] R. J. F. Bijster, R. W. Herfst, J. P. F. Spierdijk, A. Dekker, W. A. Klop, G. F. I. Kramer, L. K. Cheng, R. A. J. Hagen, and H. Sadeghian. A high speed positioning and tracking platform for near-field imaging microscopes. p. (submitted), 2016.

[16] N. D. Masters, W. Ye, and W. P. King. The impact of subcontinuum gas conduction on topography measurement sensitivity using heated atomic force microscope cantilevers. *Physics of Fluids*, 17(10):100615, 2005.

[17] E. Rousseau, A. Siria, G. Jourdan, S. Volz, F. Comin, J. Chevrier, and J.-J. Greffet. Radiative heat transfer at the nanoscale. *Nature Photonics*, 3(9):514–517, 2009.

[18] C. Hargreaves. Anomalous radiative transfer between closely-spaced bodies. *Physics Letters A*, 30(9):491–492, 1969.

[19] E. G. Cravalho, C. L. Tien, and R. P. Caren. Effect of Small Spacings on Radiative Transfer Between Two Dielectrics. *Journal of Heat Transfer*, 89(4):351, 1967.

[20] E. Cravalho, G. Domoto, and C. Tien. Measurements of thermal radiation of solids at liquid-helium temperatures. In *3rd Thermophysics Conference*, p. 531–542, Reston, Virigina, 1968. American Institute of Aeronautics and Astronautics.

[21] R. S. Ottens, V. Quetschke, S. Wise, A. A. Alemi, R. Lundock, G. Mueller, D. H. Reitze, D. B. Tanner, and B. F. Whiting. Near-Field Radiative Heat Transfer between Macroscopic Planar Surfaces. *Physical Review Letters*, 107(1):014301, 2011.

[22] T. Kralik, P. Hanzelka, M. Zobac, V. Musilova, T. Fort, and M. Horak. Strong Near-Field Enhancement of Radiative Heat Transfer between Metallic Surfaces. *Physical Review Letters*, 109(22):224302, 2012.

[23] T. Ijiro and N. Yamada. Near-field radiative heat transfer between two parallel SiO 2 plates with and without microcavities. *Applied Physics Letters*, 106(2):023103, 2015.

[24] H. Salihoglu, W. Nam, L. Traverso, M. Segovia, P. K. Venuthurumilli, W. Liu, Y. Wei, W. Li, and X. Xu. Near-Field Thermal Radiation between Two Plates with Sub-10 nm Vacuum Separation. *Nano Letters*, 20(8):6091–6096, 2020.

[25] R. S. DiMatteo, P. Greiff, S. L. Finberg, K. A. Young-Waithe, H. K. H. Choy, M. M. Masaki, and C. G. Fonstad. Enhanced photogeneration of carriers in a semiconductor via coupling across a nonisothermal nanoscale vacuum gap. *Applied Physics Letters*, 79(12):1894–1896, 2001.

[26] X. J. Hu, A. Jain, and K. E. Goodson. Investigation of the natural convection boundary condition in microfabricated structures. *International Journal of Thermal Sciences*, 47(7):820–824, 2008.

[27] K. Ito, A. Miura, H. Iizuka, and H. Toshiyoshi. Parallel-plate submicron gap formed by micromachined low-density pillars for near-field radiative heat transfer. *Applied Physics Letters*, 106(8):083504, 2015.

[28] K. Ito, K. Nishikawa, A. Miura, H. Toshiyoshi, and H. Iizuka. Dynamic Modulation of Radiative Heat Transfer beyond the Blackbody Limit. *Nano Letters*, 17(7):4347–4353, 2017.

[29] J. DeSutter, L. Tang, and M. Francoeur. A near-field radiative heat transfer device. *Nature Nanotechnology*, 14(8):751–755, 2019.

[30] X. Ying, P. Sabbaghi, N. Sluder, and L. Wang. Super-Planckian Radiative Heat Transfer between Macroscale Surfaces with Vacuum Gaps Down to 190 nm Directly Created by SU-8 Posts and Characterized by Capacitance Method. *ACS Photonics*, 7(1):190–196, 2020.

[31] S. Sadat, E. Meyhofer, and P. Reddy. Resistance thermometry-based picowatt-resolution heat-flow calorimeter. *Applied Physics Letters*, 102(16):163110, 2013.

[32] B. Song, Y. Ganjeh, S. Sadat, D. Thompson, A. Fiorino, V. Fernández-Hurtado, J. Feist, F. J. Garcia-Vidal, J. C. Cuevas, P. Reddy, and E. Meyhofer. Enhancement of near-field radiative heat transfer using polar dielectric thin films. *Nature Nanotechnology*, 10(3):253–258, 2015.

[33] B. Song, D. Thompson, A. Fiorino, Y. Ganjeh, P. Reddy, and E. Meyhofer. Radiative heat conductances between dielectric and metallic parallel plates with nanoscale gaps. *Nature Nanotechnology*, 11(6):509–514, 2016.

[34] D. Thompson, L. Zhu, R. Mittapally, S. Sadat, Z. Xing, P. McArdle, M. M. Qazilbash, P. Reddy, and E. Meyhofer. Hundred-fold enhancement in far-field radiative heat transfer over the blackbody limit. *Nature*, 561(7722):216–221, 2018.

[35] A. Fiorino, D. Thompson, L. Zhu, B. Song, P. Reddy, and E. Meyhofer. Giant Enhancement in Radiative Heat Transfer in Sub-30 nm Gaps of Plane Parallel Surfaces. *Nano Letters*, 18(6):3711–3715, 2018.

[36] R. St-Gelais, B. Guha, L. Zhu, S. Fan, and M. Lipson. Demonstration of Strong Near-Field Radiative Heat Transfer between Integrated Nanostructures. *Nano letters*, 14(12):6971–6975, 2014.

[37] R. St-Gelais, L. Zhu, S. Fan, and M. Lipson. Near-field radiative heat transfer between parallel structures in the deep subwavelength regime. *Nature Nanotechnology*, 11(6):515–519, 2016.

[38] C. C. Williams and H. K. Wickramasinghe. Scanning thermal profiler. *Applied Physics Letters*, 49(23):1587, 1986.

[39] J.-B. Xu, K. Läuger, R. Möller, K. Dransfeld, and I. H. Wilson. Heat transfer between two metallic surfaces at small distances. *Journal of Applied Physics*, 76(11):7209, 1994.

[40] W. Müller-Hirsch, A. Kraft, M. T. Hirsch, J. Parisi, and A. Kittel. Heat transfer in ultrahigh vacuum scanning thermal microscopy. *Journal of Vacuum Science & Technology A: Vacuum, Surfaces, and Films*, 17(4):1205, 1999.

[41] A. Kittel, W. Müller-Hirsch, J. Parisi, S.-A. Biehs, D. Reddig, and M. Holthaus. Near-Field Heat Transfer in a Scanning Thermal Microscope. *Physical Review Letters*, 95(22):224301, 2005.

[42] U. F. Wischnath, J. Welker, M. Munzel, and A. Kittel. The near-field scanning thermal microscope. *Review of Scientific Instruments*, 79(7):073708, 2008.

[43] K. Kloppstech, N. Könne, S.-A. Biehs, A. W. Rodriguez, L. Worbes, D. Hellmann, and A. Kittel. Giant heat transfer in the crossover regime between conduction and radiation. *Nature Communications*, 8(1):14475, 2017.

[44] L. Cui, W. Jeong, V. Fernández-Hurtado, J. Feist, F. J. García-Vidal, J. C. Cuevas, E. Meyhofer, and P. Reddy. Study of radiative heat transfer in Ångström- and nanometre-sized gaps. *Nature Communications*, 8(1):14479, 2017.

[45] A. Narayanaswamy, S. Shen, and G. Chen. Near-field radiative heat transfer between a sphere and a substrate. *Physical Review B*, 78(11):115303, 2008.

[46] S. Shen, A. Narayanaswamy, and G. Chen. Surface phonon polaritons mediated energy transfer between nanoscale gaps. *Nano letters*, 9(8):2909–13, 2009.

[47] P. J. van Zwol, L. Ranno, and J. Chevrier. Tuning Near Field Radiative Heat Flux through Surface Excitations with a Metal Insulator Transition. *Physical Review Letters*, 108(23):234301, 2012.

[48] F. Menges, M. Dittberner, L. Novotny, D. Passarello, S. S. P. Parkin, M. Spieser, H. Riel, and B. Gotsmann. Thermal radiative near field transport between vanadium dioxide and silicon oxide across the metal insulator transition. *Applied Physics Letters*, 108(17):171904, 2016.

[49] P. L. Sambegoro. *Experimental Investigations on the Influence of Curvature and Materials on Near-field Thermal Radiation*. Doctoral dissertation, Massachusetts Institute of Technology, 2016.

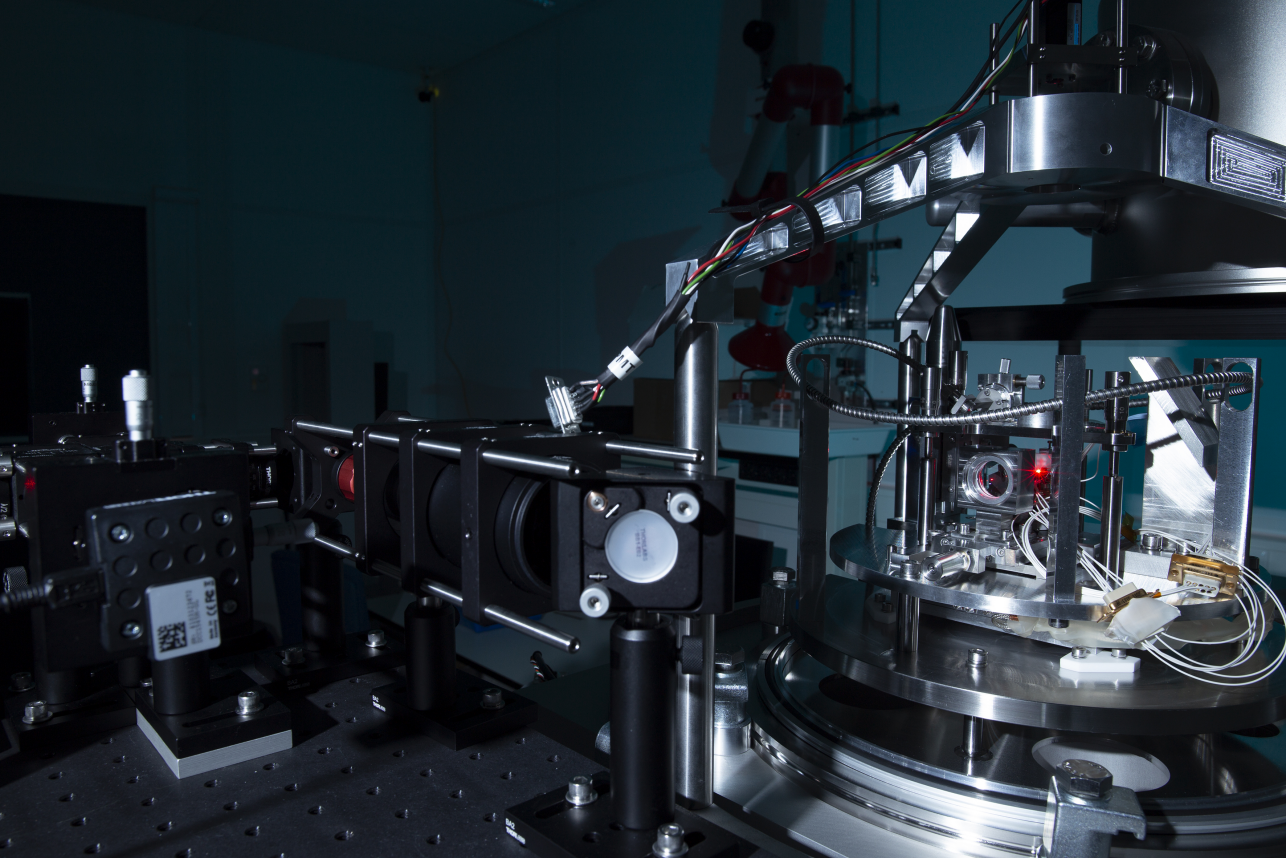

2. Designing the instrument

To support the development of a heat transfer-based distance sensor as described in Chapter 1, an instrument is developed that mimics the essential parts of such a sensor system and provides the testing environment. The instrument is designed with three goals in mind. First, it can be used to measure heat transfer as a function of the separation between the probe and the sample to replicate the results obtained by others. Secondly, it will be possible to scan the probe across the sample to study ways of dealing with variations in the separation and effectively construct a scanning probe microscope. Lastly, it will be used to measure the separation between the probe and the sample by means of the heat transferred between them, while the separation is measured by independent means for comparison.

In this chapter, the system is developed in increasing levels of detail. The system architecture and the governing equations are developed in Section 2.1 to Section 2.3. The sub-systems that are essential for the heat transfer mea-

Title photo: overview of the internals of the instrument. Photo by Roy Bijster. Parts of this chapter have been published in Review of Scientific Instruments **92**, 025008 (2021).

surement are worked out in more detail in Section 2.3 to Section 2.9. The details of the independent distance measurement are provided in Chapter 3. The underlying choices for specific pieces of equipment are not discussed, because these choices are driven by balancing functionality and performance against cost price and availability.

2.1 Developing the system architecture

The system architecture is constructed with the sensing element in mind. Using the third archetype as discussed in Chapter 1 as a basis, the sensing element consists of a multilayer probe with a microsphere attached to its free end. The probe is oriented perpendicular to the sample surface and brought into close proximity of the sample. As heat is transferred between the sample and the sphere, the probe deforms.

2.1.1 Measuring the probe rotation

The deflection and/or rotation of the probe can be measured by optical [1, 2], electrical [3], or capacitive [4] means. Of these methods, the Optical Beam Deflection (OBD) method [1] is a very popular choice for Scanning Probe Microscopy (SPM) systems. Light is reflected of the surface of the probe onto a Position Sensitive Detector (PSD). The spot on the detector moves as the probe deforms. This simple architecture separates the detection mechanism from the probe itself, allowing for relatively simple probe design. Because of this, the OBD method is chosen as the detection mechanism for the instrument.

2.1.2 Controlling the probe temperature

The conductance of the gap that separates the probe and the sample depends on the size of the gap. Unless the temperatures in the system are controlled, they change accordingly. In theoretical models that describe the distance dependency of radiative near-field heat transfer, the temperatures of the probe and the sample are assumed to be constant and independent of distance. If the experimental determination of heat flow is to agree with the theory, it is important that the temperature variation with distance is either measured or removed.

Previous designs that are based on this system archetype [2, 5–8] contain temperature sensors for the probe and sample and often use closed-loop temperature control for the sample and the probe clamp. However, the temperature of the free-end of the probe is left to vary with separation. To quantify the expected tip temperature variation in (quasi-)steady state conditions, it is modeled using a simple lumped parameter model as depicted in Figure 2.1.

The model uses four nodes: (1) the sample, (2) the point on the sphere that is closest to the sample, (3) the point on the sphere that is in contact

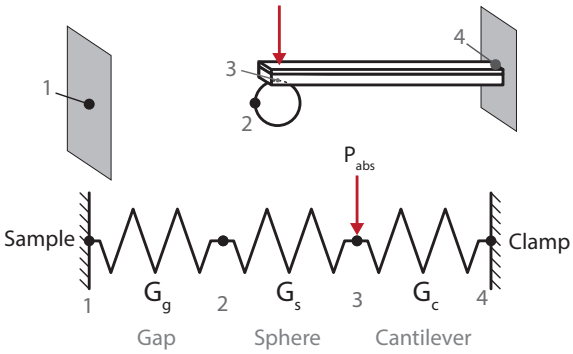

Figure 2.1: Thermal resistance network model of the probe and the sample.

with the probe, and (4) the clamp of the probe. The nodes are connected by three thermal conductors: G_g describing the heat transfer through the (vacuum) gap, G_s modeling the conduction through the microsphere and G_c representing the conduction through the cantilever. A heat source P_abs is included at Node 3 to model the heat input from the OBD illumination. For a typical incident power of 1 mW and a typical absorption of 10 %, this heat source is estimated at 100 µW.

For this order of magnitude approximation, the conductance of the gap G_g is assumed to range between $1 \times 10^{-8}\,\mathrm{W\,K^{-1}}$ for large distances and $1 \times 10^{-6}\,\mathrm{W\,K^{-1}}$ for nanometer separation. These numbers are based on the experimental work by Rousseau *et al.* [2], in which a silicon dioxide microsphere of 40 µm was used. The conductance of the sphere G_s and of the cantilever G_c are estimated to be approximately $1 \times 10^{-5}\,\mathrm{W\,K^{-1}}$ and $1 \times 10^{-6}\,\mathrm{W\,K^{-1}}$, respectively. The bases for these estimations are available in Chapter 4 and Chapter 7.

For the design of the system architecture, two cases are of immediate interest for the thermal balance of this system. In the first case, the power of the laser is kept constant and the temperature of Node 3 is allowed to vary. In the second case, measures are taken to stabilize the temperature of this node. In both cases, the sample (Node 1) and the clamp (Node 4) are considered thermal baths that are maintained at constant temperatures. In the first case (constant power), the temperatures of Nodes 2 and 3 are equal to

$$T_2 = \left(G_\mathrm{g} + G_\mathrm{s} - \frac{G_\mathrm{s}^2}{G_\mathrm{s} + G_\mathrm{c}}\right)^{-1} \left(G_g T_1 + \frac{G_\mathrm{s}}{G_\mathrm{s} + G_\mathrm{c}} P_\mathrm{abs} + \frac{G_\mathrm{s} G_\mathrm{c}}{G_\mathrm{s} + G_\mathrm{c}} T_4\right), \tag{2.1}$$

$$T_3 = \frac{1}{G_\mathrm{s} + G_\mathrm{c}} P_\mathrm{abs} + \frac{G_\mathrm{s}}{G_\mathrm{s} + G_\mathrm{c}} T_2 + \frac{G_\mathrm{c}}{G_\mathrm{s} + G_\mathrm{c}} T_4. \tag{2.2}$$

In the second case (temperature T_3 is kept constant), the temperature of

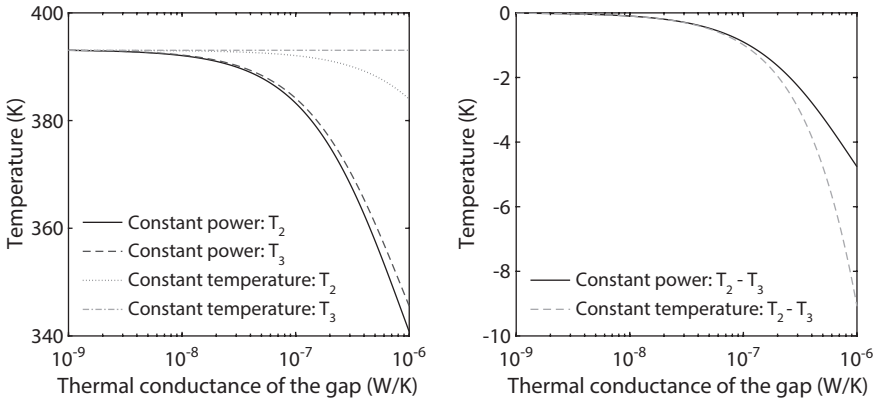

Figure 2.2: (left) The change of the probe temperatures as a function of the conductance of the gap. The conductance of the sphere and the cantilever are set at $G_\mathrm{s} = 1 \times 10^{-5}\,\mathrm{W\,K^{-1}}$ and $G_\mathrm{c} = 1 \times 10^{-6}\,\mathrm{W\,K^{-1}}$, respectively. The temperatures of the clamp and the sample are equal $T_1 = T_4 = 293.15\,\mathrm{K}$ and the absorbed power $P_\mathrm{abs} = 100\,\mu\mathrm{W}$. (right) The temperature gradient over the microsphere.

Node 2 is equal to

$$T_2 = \frac{G_\mathrm{g}}{G_\mathrm{g} + G_\mathrm{s}} T_1 + \frac{G_\mathrm{s}}{G_\mathrm{g} + G_\mathrm{s}} T_3. \tag{2.3}$$

For both cases, the temperatures for Nodes 2 and 3 are shown in Figure 2.2. The temperature of Node 2 changes by 52 K from the far-field to the extreme near-field, when the temperature of the free end of the probe is not stabilized. Stabilization reduces this to 9 K. However, it is important to note that in the temperature gradient across the sphere (i.e., $T_2 - T_3$) is larger in the second case. This can be alleviated by using a sphere with a higher conductance.

The stabilization of the temperature of the free end of the probe can be achieved in several ways. When the OBD method is used for read-out, tuning the incident laser power is the most straightforward option. Other options rely for example on heaters that are embedded in the probe and that are often combined with embedded thermocouples [9]. Although this can provide better performance, it complicates the layout of the probe and its manufacturing, requiring localized doping of materials and multiple lithographic masks. This is therefore not preferred in these stages of development.

2.1.3 Determining the separation

Measurement of the heat flux as function of separation, requires accurate knowledge of the smallest distance between the sphere and the sample. Depending on the materials used for the sample and for the probe, several methods can be used to measure it. In all cases found in literature, a datum

("zero distance") is established. The distances are then determined afterwards with respect to this datum by adding the actuator setpoint, but are not actively measured. Xu *et al.* [10] use a capacitive force sensor embedded in the sample to detect the small displacement of the sample at the moment of contact. Müller-Hirsch *et al.* [11] use a preset tunneling current between probe and sample to establish "zero distance". The latter requires that both the probe and the sample are sufficiently electrically conductive, and are therefore not suited for experiments with dielectrics. For that reason, Narayanaswamy *et al.* [12] use the fact that contact between the sphere and the sample manifests as a large change in the PSD signals. However, if the sphere can roll over the sample, the PSD signals only change gradually in which case the moment of contact is difficult to identify.

To establish a continuous measurement of the separation, a Total Internal Reflection Microscope (TIRM) is integrated in the instrument. The sample is illuminated from the back under total internal reflection. A non-propagating, evanescent field exists on the interface. The intensity of the scattering of this evanescent field by the microsphere has a direct relation to the separation. Moreover, the signal saturates at contact so that the datum can be identified more easily [13]. The design considerations for this subsystem are discussed in Chapter 3. It is important to note that in the presence of roughness, contact is ill-defined. The roughness of the sample and of the probe need to be significantly lower than the allowed uncertainty on the smallest separation. All of the methods described above suffer from this. To establish bounds on the minimum separation, the roughness of the microsphere and the sample are measured. The methods employed for this and the results are discussed in Chapter 6.

2.1.4 The main building blocks

The system architecture consists of three main building blocks as depicted in Figure 2.3: a probe consisting of a multilayer cantilever and an attached microsphere, the OBD system with closed-loop control on the laser power to stabilize the temperature of the free end of the cantilever and a TIRM for measuring the separation between the sphere and the sample.

In addition to these main building blocks, additional supporting systems are required. A vacuum system is used to lower the ambient pressure and effectively eliminate heat transfer through convection and gas conduction. In addition to this, two thermal control systems are used to stabilize the temperatures of the sample and the probe clamp. An optical microscope is embedded in the OBD system to aid in the alignment of the OBD light source on the probe and in the alignment of the probe to the sample. The sample is mounted to a three-axis translation stage, which is used to scan the probe relative to the sample and to control the separation.

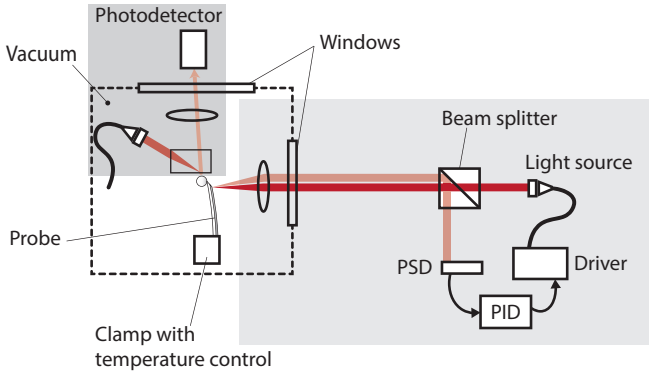

Figure 2.3: The system consists of three building blocks: a probe consisting of a multilayer cantilever and an attached microsphere, the OBD system with closed loop control on the laser power to stabilize the temperature of the free end of the cantilever and a TIRM for measuring the separation.

2.2 Modeling the temperature-induced deformation of a bilayer cantilever

A bilayer cantilever makes for an effective transducer of heat flux into mechanical motion. This simple, yet effective geometry uses the differential expansion of the two layers upon heating to create a measurable change in curvature. Moreover, if the temperature distribution can be modeled accurately, the simple geometry makes it possible to find analytical expressions that describe the behavior of the cantilever and that can be used for design purposes. In this section, the relations that describe these probes from a thermo-mechanical point of view are derived and expressions for the sensitivities of certain parameters to heat flux or spurious influences are developed. In the following derivations, algebraic manipulations are skipped, and only the main steps in the derivations are highlighted for the sake of brevity. In the following derivations, the cantilever has a rectangular cross-section and a rectangular plan form of width w and length L. It is composed of two perfectly connected layers with thicknesses t_1 and t_2. These dimensions are schematically indicated in Figure 2.4.

2.2.1 Modeling of the thermo-mechanical behavior

It is assumed that the clamped end (base) of the cantilever is kept at a constant temperature T_{base} and that a thermal flux P is present at its free end. Moreover, it is assumed that there is only a one-way coupling from the thermal response to the mechanical response, and conduction through the cantilever is considered to be the only agent of heat transfer. The cantilever is assumed to be thin ($(t_1 + t_2)/L \ll 1$) and slender, so that temperature gradients along the width and across the thickness are negligible. Under these assumptions, the resulting temperature distribution along the cantilever

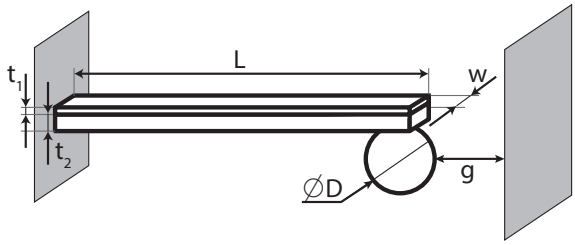

Figure 2.4: Schematic representation of the calorimeter that consists of a bilayer cantilever and a microsphere at its free end. The relevant dimensions of length, width and thicknesses are indicated. The subscripts 1 and 2 refer to the reflective coating and the substrate, respectively. The distance g is the separation between the probe and the sample.

length $T(x)$ is given by

$$T(x) = \frac{P}{GL}x + T_{\text{base}}, \tag{2.4}$$

where G is the effective thermal conductance. When the heat is added at the free end of the cantilever, the effective conductance of a bilayer beam is accurately approximated [14] by

$$G = \frac{w}{L}\left(t_1 k_1 + t_2 k_2\right), \tag{2.5}$$

where k_i and t_i are the thermal conductivity and thickness of each respective layer. These assumptions are valid under (ultra)high vacuum conditions, where heat loss to the surrounding gas is negligible, and at moderate temperatures, at which the nonlinear effects of heat loss to the environment through radiation is a higher-order effect [14, 15] (also see Section 4.5.2). In the remainder of this text, indices 1 and 2 refer to the reflective coating and the substrate, respectively.

A change of the temperature distribution causes the two layers to expand at different rates. If the layers are allowed to expand separately, a mismatch strain ϵ_m between the two will exist. This mismatch strain ϵ_{m} is resolved by a change in curvature κ of the cantilever

$$\kappa(x) = \frac{\partial^2 z}{\partial x^2} = \beta \epsilon_{\text{m}}(x), \tag{2.6}$$

where z is the local out-of-plane deflection. The curvature is related to the mismatch strain through a parameter β, which can be written as

$$\beta = \frac{6hm}{t_2}\left(\frac{1+h}{1+2hm\left(2+3h+2h^2\right)+h^4m^2}\right), \tag{2.7}$$

where $h = t_1/t_2$, $m = M_1/M_2$ and the biaxial modulus $M_i = E_i/(1-\nu_i)$ [16–18]. Here ν_i is the Poisson's ratio of the material used for layer i, and E_i is the corresponding elastic modulus. The mismatch strain is assumed to be only

a function of the local temperature $T(x)$, the stress-free temperature T_{SFT} (e.g., the temperature at which the top layer is added), and the difference between thermal expansion coefficients $\Delta\alpha = \alpha_1 - \alpha_2$, so that

$$\epsilon_{\mathrm{m}}(x) = \Delta\alpha\left(T(x) - T_{\mathrm{SFT}}\right). \tag{2.8}$$

The cantilever is further assumed to be slender ($L \geq 10w$) and thin ($L, w \gg t_i$), such that heat transfer is much quicker along these directions than along the length. This renders the temperature gradients along these directions negligible for the present discussion in comparison to the gradient along the length of the cantilever.

The OBD method [1] is used to measure the local out-of-plane rotation of the cantilever. The rotation as a result of the temperature distribution of Equation (2.4) is found from integration of the curvature κ from the clamped end to the point of measurement x (see Figure 2.4 for reference). The local rotation and deflection are found through repeated integration of Equation (2.6):

$$\theta(x) = \int_0^x \kappa(x)\,\mathrm{d}x = \beta\Delta\alpha\left[\frac{P}{GL}\frac{x^2}{2} + \left(T_{\mathrm{base}} - T_{\mathrm{SFT}}\right)x\right] + \theta(0), \tag{2.9}$$

$$z(x) = \int_0^x \theta(x)\,\mathrm{d}x = \beta\Delta\alpha\left[\frac{P}{GL}\frac{x^3}{6} + \left(T_{\mathrm{base}} - T_{SFT}\right)\frac{x^2}{2}\right] + \theta(0)\,x + z(0), \tag{2.10}$$

where the boundary conditions at the clamped end are $\theta(0) = 0$, $z(0) = 0$ and $T(0) = T_{\mathrm{base}}$.

2.2.2 Sensitivities and power equivalents

For design purposes and for propagation of uncertainties, the necessary sensitivities of several quantities are derived. All uncertainties are expressed in units of *equivalent* heat flux for easier comparison and interpretation. In other words, an uncertainty or sensitivity in one quantity translates to an equivalent uncertainty or sensitivity in the measured flux. For clarity, equivalent fluxes are denoted with a circumflex on top of the symbol.

Sensitivity to thermal load

The sensitivity of the cantilever deflection to changes in the flux at the tip can be written as

$$\frac{\partial z}{\partial P}(x) = \frac{\beta\Delta\alpha}{6GL}x^3. \tag{2.11}$$

By inverting this relation, the equivalent flux as a function of the measured tip deflection ($x = L$) reads

$$\frac{\partial \hat{P}}{\partial z}(x = L) = \frac{6G}{\beta \Delta \alpha L^2}. \tag{2.12}$$

This sensitivity can be used to propagate uncertainty in the tip deflection to an uncertainty in the measured heat flux (e.g., thermal random vibrations). Similarly, the sensitivity of the tip rotation to heat flux can be derived to be

$$\frac{\partial \theta}{\partial P}(x = L) = \frac{\beta \Delta \alpha L}{2G}, \tag{2.13}$$

or in terms of equivalent flux

$$\frac{\partial \hat{P}}{\partial \theta}(x = L) = \frac{2G}{\beta \Delta \alpha L}. \tag{2.14}$$

Drift of clamp temperature

The temperature gradient along the length of the cantilever is the result of the flux at its free end and the temperature at its clamped end. In practice, the latter may drift in time due to the flux in the cantilever and the spurious heat fluxes elsewhere in the system. The clamp temperature is, therefore, only known to a certain accuracy, ΔT_{base}. Because the OBD method provides a point measurement of the tip rotation, it is not possible to discriminate rotation induced by a change in flux from one induced by a change in temperature at the clamped end. From Equation (2.9), we find the sensitivity of tip rotation to a change in the clamp temperature as

$$\frac{\partial \theta}{\partial T_{\text{base}}}(x) = \beta \Delta \alpha x. \tag{2.15}$$

Combined with Equation (2.14) this relation gives the equivalent measured flux due to a temperature change at the base ($x = L$) as

$$\Delta \hat{P}_{\Delta T_{\text{base}}} = \frac{\partial \hat{P}}{\partial \theta} \frac{\partial \theta}{\partial T_{\text{base}}} \Delta T_{\text{base}} = 2G \Delta T_{\text{base}}. \tag{2.16}$$

To minimize the measurement uncertainty due to ΔT_{base}, the conductance of the cantilever and the temperature variation at the clamp have to be minimized. For the latter, a stability of 1 mK has been achieved as is demonstrated in Section 2.6.

Cantilever vibration due to thermal noise

Brownian motion causes the cantilever to vibrate constantly. The mean amplitude of this thermal noise as integrated over all frequencies can be found using the methodology developed by Butt and Jaschke [19] as

$$\sqrt{\langle z \rangle^2} = \sqrt{\frac{4}{3} \frac{k_{\text{B}} T_{\text{avg}}}{C}}, \tag{2.17}$$

where k_B is Boltzmann's constant, T_avg is the average temperature of the cantilever and C is the equivalent spring constant. When the rotation is measured at the very tip of the cantilever, the spring constant can be written as $C = 3EI/L^3$. The bending stiffness EI of a bilayer cantilever [16] is

$$EI = \frac{w t_2^3 t_1 E_2 E_1}{12\,(t_1 E_1 + t_2 E_2)} K_1, \tag{2.18}$$

where K_1 is

$$K_1 = 4 + 6h + 4h^2 + \frac{E_1}{E_2} h^3 + \frac{E_2}{E_1}\frac{1}{h}. \tag{2.19}$$

In this relation, w refers to the width of the cantilever, t_i to the thickness of layer i, and E_i is the Young's modulus of the corresponding layer.

The noise-equivalent flux can be found by multiplying this vibration amplitude by Equation (2.12):

$$\Delta\hat{P}_\mathrm{noise} = \frac{\partial \hat{P}}{\partial z}\sqrt{\langle z \rangle^2} = \frac{4G}{\beta\Delta\alpha}\sqrt{\frac{k_\mathrm{B} T_\mathrm{avg}}{EI}}\frac{1}{\sqrt{L}}. \tag{2.20}$$

Surprisingly, a longer cantilever results in a lower noise-equivalent flux. This counterintuitive result follows from the competing proportionalities to L: $\sqrt{\hat{z}^2} \propto L^{3/2}$ in case of the thermal noise amplitude and $\frac{\partial P}{\partial z} \propto L^{-2}$ in case of the sensitivity. Combined with Equation (2.5) this yields the proportionality of $\Delta\hat{P}_\mathrm{noise} \propto L^{-3/2}$.

2.3 Modeling the detection system

The motion of the cantilever probe is measured using the OBD method [1]. In this method, the incident beam is reflected (specularly) off the reflective coating of the cantilever onto a position sensitive detector (PSD). In the instrument, a confocal layout [20] is employed for this system. A compact setup can be realized by using the same optics for the incident and the reflected light. Because the optics are collimated for the largest part of the optical path, the larger part of the optics can be kept at ambient conditions and the light can enter and exit the vacuum vessel via a viewport. The layout is outlined in Figure 2.5 on page 22.

The incident and reflected beams are separated by using two orthogonal linear polarization states. When the light from the light sources is linearly polarized, wave-plates can be used to rotate the polarization. Polarizing beam splitters are used to separate the incident and the reflected beams. Two half-wave plates are placed between the beam splitters to control the ratio of transmitted and reflected light at each beam splitter. Using a quarter waveplate, the polarization of the incident beam is rotated by 45°. The polarization of the reflected light is rotated by another 45° to realize the orthogonal polarization states for the incident and reflected beams.

The incident beam is created by combining the outputs from a stabilized 'high' power beam of several milliwatts, and a 'low' power beam of several

microwatts using a 50:50 beam splitter. This provides finer control over the optical power that is incident on the cantilever probe, than would be possible using a single diode laser and a single current controller.

To simplify the alignment of the incident beam onto the cantilever, two 45° mirrors are used in a Z-fold configuration [21]. Both laser diodes are fiber-coupled to collimators that are mounted on kinematic tip/tilt stages. Together with the Z-fold configuration, the beams are aligned so that the beams are parallel and coincident on the cantilever.

2.3.1 Position sensitive detector

The returning beam is incident onto a Maypa-OPS40 position-sensitive detector, which internally utilizes a beam splitter arrangement to split the beam onto four separate photo detectors [22]. This avoids the dead gap between the cells that is common in conventional quad cell detectors and allows for a high measurement bandwidth. The working principle is schematically depicted in Figure 2.6. Because the incident optical power is divided over the four separate cells A to D, the PSD outputs two potentials X_p and Y_p that relate to the spot position along the two perpendicular directions x and y

$$X_{\mathrm{p}} = X^{+} - X^{-} = (B + D) - (A + C)\,, \tag{2.21}$$

$$Y_{\mathrm{p}} = Y^{+} - Y^{-} = (A + B) - (C + D)\,. \tag{2.22}$$

To adjust for drift in the optical power, X_p and Y_p are normalized by the total potential I

$$I = A + B + C + D. \tag{2.23}$$

Note that this does not correct for changes in the incident power due to shot noise or speckle noise, but does correct for overall drift and variations in the power that is incident on the PSD. Any drift in the output power will also cause the cantilever to deform. The signal drift that results from this cannot be canceled in this way.

2.3.2 Optical model of the OBD

The incident beam is assumed to have a Gaussian intensity profile. This is a valid first order approximation for laser diodes operating in the lowest transverse electromagnetic (TEM_{00}) mode. The intensity profile is in such case adequately described by $f\,(x, y)$ as

$$f\,(x, y) = P_{\mathrm{PSD}} \frac{1}{2\pi\sigma^2} \exp\left(-\frac{1}{2}\left(\frac{x - x_0}{\sigma}\right)^2\right) \exp\left(-\frac{1}{2}\left(\frac{y - y_0}{\sigma}\right)^2\right), \tag{2.24}$$

where x_0 and y_0 are the respective distances from the center of the PSD, and P_{PSD} is the optical power incident on the detector. This situation is schematically represented in Figure 2.7. The width of the spot is introduced

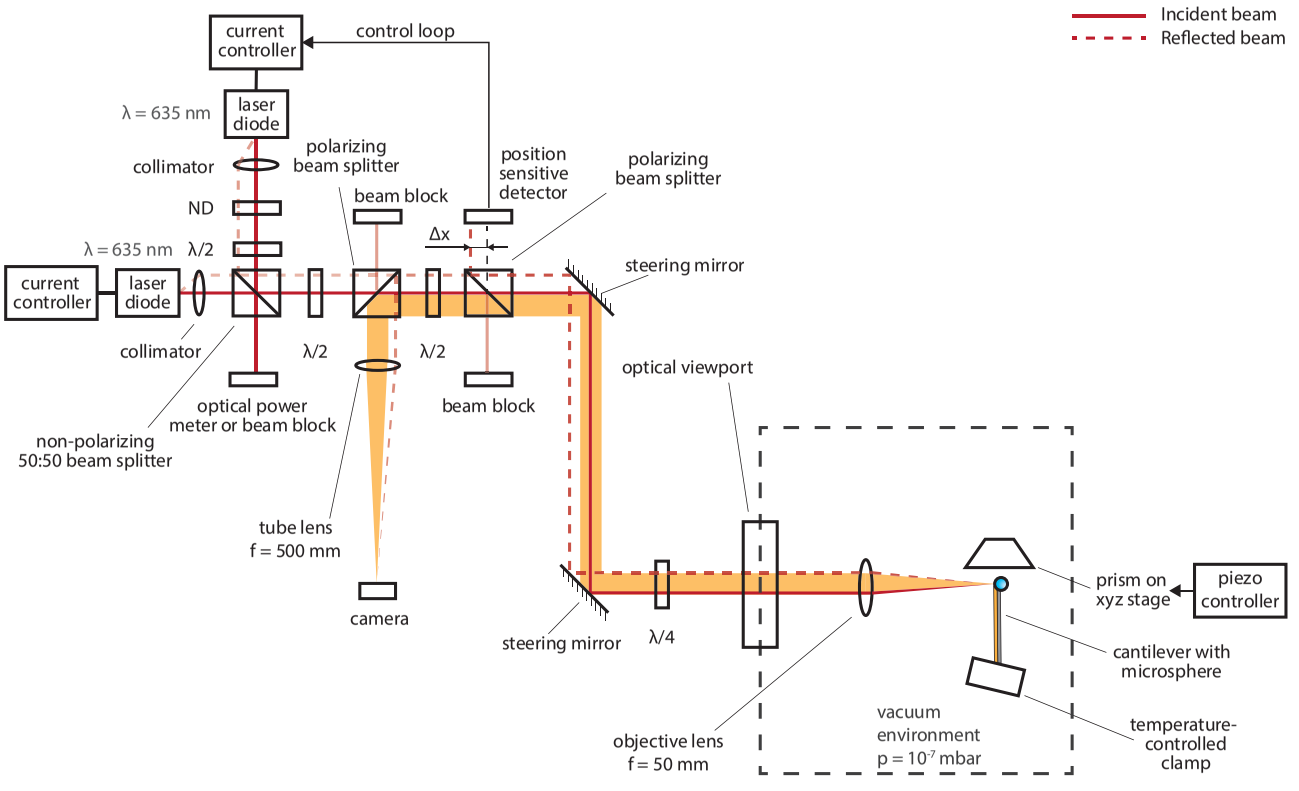

Figure 2.5: Schematic representation of the optical layout for the optical beam deflection system and the integrated optical alignment microscope.

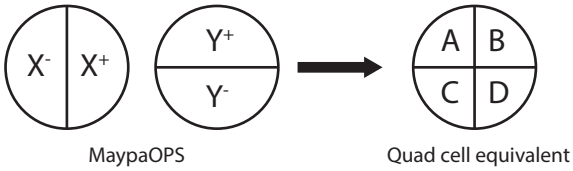

Figure 2.6: The equivalent between the MaypaOPS system and a conventional quad cell position sensitive photo detector.

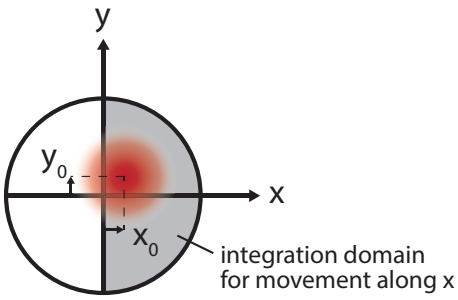

Figure 2.7: The spot incident on an equivalent quad cell photo detector. The integration interval for motion along the x-axis is indicated.

through the standard deviation σ, which is directly related to the full-width half maximum (FWHM) w_{FWHM} of the beam profile

$$w_{\mathrm{FWHM}} = 2\sqrt{2\ln 2}\sigma \approx 2.35\sigma, \tag{2.25}$$

and the $1/e^2$ waist diameter w_{1/e^2} as

$$w_{1/e^2} = 4\sigma. \tag{2.26}$$

The remainder of the analysis is constrained to movement solely along one axis as a representative case. As the spot shifts from the center of the PSD to the right, the power incident on the right half of the detector is found through integration,

$$P^+ = P_{\mathrm{PSD}} \int_{\infty}^{\infty}\int_{0}^{\infty} f(x,y)\,\mathrm{d}x\,\mathrm{d}y = \frac{P_{\mathrm{PSD}}}{2}\left(\operatorname{erf}\left(\frac{x_0}{\sigma\sqrt{2}}\right)+1\right). \tag{2.27}$$

From Equation (2.21) follows that the output signal of the detector is equal to

$$X_{\mathrm{p}} = S\left(2P^+ - P_{\mathrm{PSD}}\right) = SP_{\mathrm{PSD}}\operatorname{erf}\left(\frac{x_0}{\sigma\sqrt{2}}\right), \tag{2.28}$$

where S is the photon sensitivity $\left(\mathrm{V\,W^{-1}}\right)$. The sensitivity of this signal to a change in spot location reads

$$\frac{\partial X_{\mathrm{p}}}{\partial x_0} = SP_{\mathrm{PSD}}\sqrt{\frac{2}{\pi}}\frac{1}{\sigma}\exp\left(-\frac{x_0^2}{2\sigma^2}\right). \tag{2.29}$$

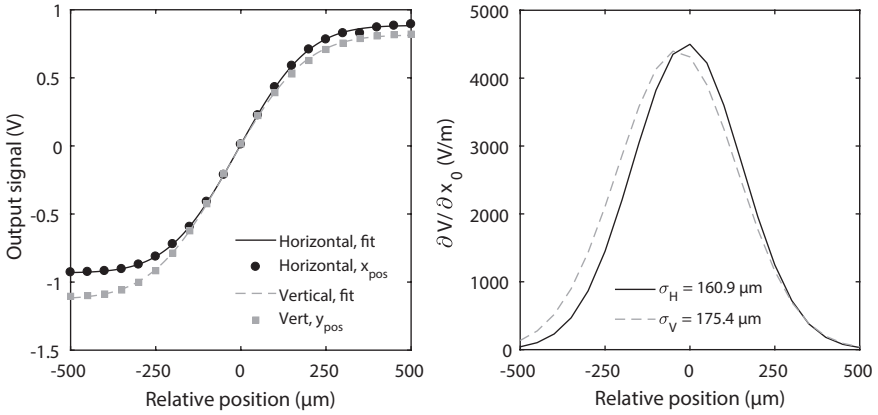

Figure 2.8: (left) Measured x-position and y-position signals for displacement of the incoming laser beam with respect to the entrance pupil of the PSD along the repective axes. (right) Numerical derivative of said signals show the Gaussian beam profiles.

These relations were verified experimentally by traversing the PSD entrance pupil relative to the incident beam along both the horizontal and vertical axes. The model of Equation (2.28) is fitted to the resulting output signals, which are plotted in Figure 2.8. Excellent agreement is achieved for both axes between the data and

$$X_{\mathrm{p}} = SP_{\mathrm{PSD}} \operatorname{erf}\left(\frac{x_0 - \delta x}{\sigma\sqrt{2}}\right) + X_{\mathrm{p},0}, \tag{2.30}$$

where δx is a shift with respect to the estimated position, and $X_{\mathrm{p},0}$ is the voltage at the starting position. At an incident power of 1.3 mW, the sensitivities S are $689.7\,\mathrm{V\,W^{-1}}$ and $745.7\,\mathrm{V\,W^{-1}}$ for displacements of the beam along the x- and y-axis, respectively. The corresponding beams have standard deviations of 160.9 µm and 175.4 µm. The extracted beam profile was checked using a knife-edge that was moved into the beam, while recording the transmitted optical power using an photodiode [23, 24]. The resulting beam profile and its numerical derivative are displayed in Figure 2.9. The standard deviations were found to be 189.7 µm along the horizontal direction and 201.8 µm along the vertical direction. Both methods show that the beam is slightly elliptical. These latter values were obtained 20 cm further down the optical path and the small difference between the two methods can be explained by non-perfect collimation. The values are in good agreement with what can be expected from the used combination of fiber and collimator (maximum output waist of $w_{1/e^2} = 0.86\,\mathrm{mm}$).

2.3.3 Propagation of sensitivities through the optical beam deflection system

In the confocal configuration of the OBD method (Figure 2.10), the reflected beam is displaced with respect to the incident beam by a distance Δx as a

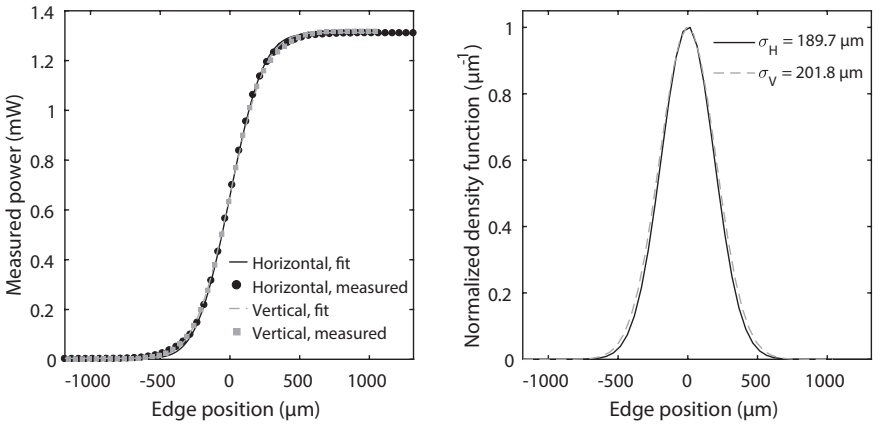

Figure 2.9: (left) Measured power as a function of the relative knife edge position fitted to an error function. (right) The numerical derivative of the power profile allows the beam profile to be recovered. The standard deviation of the distribution along the horizontal axis is 189.7 µm and for the vertical axis is 201.8 µm. The shown distribution is normalized with the peak value.

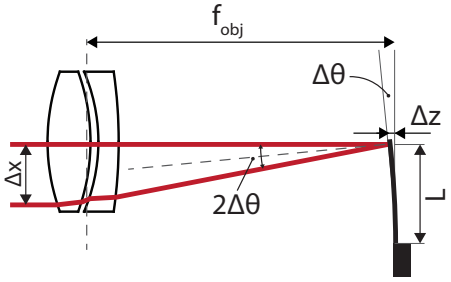

Figure 2.10: Schematic path of the OBD laser beam reflecting back from a cantilever undergoing an angular change $\Delta\theta$.

result of a change in the angle of incidence of $\Delta\theta$. From the geometry, the amplitude of this shift is found to be

$$\Delta x = f_{\mathrm{obj}} \tan(2\Delta\theta) \approx 2\Delta\theta f_{\mathrm{obj}}, \tag{2.31}$$

where f_{obj} is the effective focal length of the lens.

When the cantilever rotates, the reflected beam moves across the PSD. The output signal of the detector due to a change in absorbed flux at the cantilever tip follows from multiplication of the relevant sensitivities

$$\frac{\partial X_{\mathrm{p}}}{\partial P} = \frac{\partial X_{\mathrm{p}}}{\partial x}\frac{\partial x}{\partial \theta}\frac{\partial \theta}{\partial P}(L). \tag{2.32}$$

Using Equation (2.29), Equation (2.31) and Equation (2.13), the system sen-

sitivity can be written as

$$\frac{\partial X_{\mathrm{p}}}{\partial P} = \sqrt{\frac{2}{\pi}} S P_{\mathrm{OBD}} \frac{f_{\mathrm{obj}}}{\sigma} \frac{\beta \Delta \alpha L}{G}, \tag{2.33}$$

assuming that the spot is centered on the PSD. Equation (2.33) can be considered the system equation, as it relates the output signal directly to the input flux.

2.4 Sizing the optical beam deflection system

From Equation (2.33) it is clear that the system sensitivity scales with f_{obj}/σ. It is thus paramount to maximize this ratio within the constraints of the available hardware. Moreover, for a high signal-to-noise ratio on the PSD, the power reflected onto the PSD has to be maximized.

We settled on a focal length of 50 mm to provide sufficient working distance, while keeping $\Delta x/\Delta\theta$ sufficiently small to work within the constraints of 25.4 mm (1 inch) diameter optics. The selected objective lens is a Thorlabs ACA254-050-A air-spaced achromatic doublet, which has been customized for use in a high-vacuum environment. The mount is left uncoated/unpainted and holes are drilled in strategic places to allow air that is trapped in the mount to evacuate.

The minimum beam waist radius r_{w} of a Gaussian beam is related to the wavelength λ, the beam diameter d_{b} $(1/e^2)$, and the focal length of the objective lens as [25, 26]

$$2r_{\mathrm{w}} = \frac{4\lambda}{\pi} \frac{f_{\mathrm{obj}}}{d_{\mathrm{b}}}. \tag{2.34}$$

Figure 2.11 shows the beam waist diameter for $\lambda = 635\,\mathrm{nm}$ and $f_{\mathrm{obj}} = 50\,\mathrm{mm}$. It should be noted here that this is a mere theoretical limit for perfect Gaussian beam profiles and diffraction limited optics. In real systems, the achieved spot size will be larger due to optical aberrations.

Not all light contained in the Gaussian beam will hit the target. The power incident on a target of radius r_{a} can be written as

$$P\left(r_{\mathrm{a}}\right) = P_0 \left(1 - \exp\left(-2\frac{r_{\mathrm{a}}^2}{r_{\mathrm{w}}^2}\right)\right), \tag{2.35}$$

where P_0 is the total power in the beam. This relationship is depicted in Figure 2.12. Assuming a circular target area on the probe of 10 µm in diameter, these two relations combined result in a required beam diameter of 6.7 mm for 99 % of the power contained in the beam to be incident on the target. This is a realistic solution for the tuning laser, of which the beam reflected off the cantilever is of no concern to the OBD system. For this laser a Thorlabs F810FC-635 fixed focal length collimator is used to achieve this beam diameter. The performance of the OBD system is, however, negatively impacted when such a large diameter beam is used on the OBD laser. Therefore, a beam diameter of 2.1 mm is created by using a Thorlabs CFC-11X-A

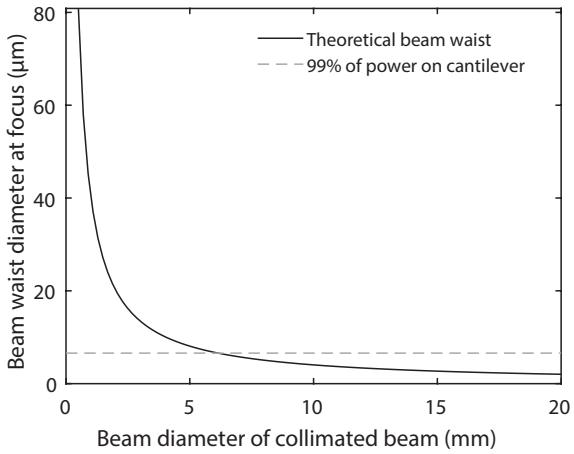

Figure 2.11: Waist diameter as a function of the beam diameter ($1/e^2$) for a focal length of 50 mm and a wavelength of 635 nm.

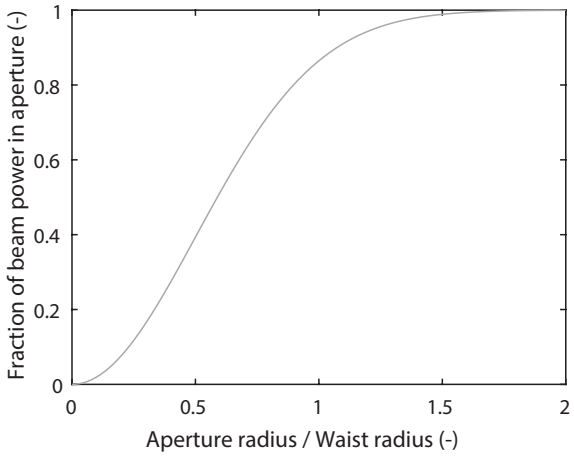

Figure 2.12: Fraction of the incident power of a Gaussian beam passing through a circular aperture. The target on the cantilever is assumed to be 10 µm in diameter.

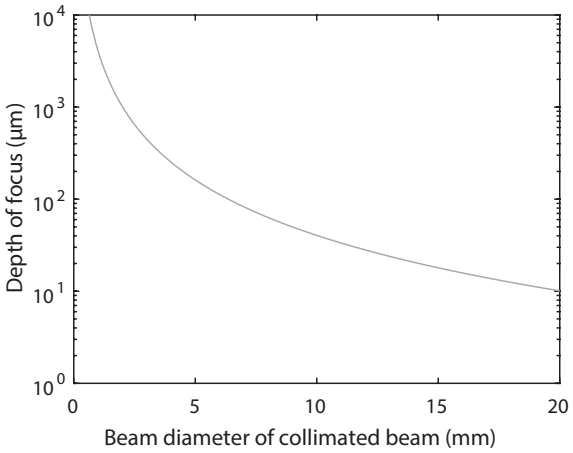

Figure 2.13: Depth of focus as a function of the beam diameter ($1/e^2$) for a focal length of 50 mm and a wavelength of 635 nm.

collimator. In combination with the chosen focal length for the objective lens, this results in $2r_\mathrm{w} = 19.3\,\mu\mathrm{m}$. With a target diameter of 10 µm, 41 % of the power contained in the beam will be incident on the target.

When allowing the beam diameter to vary within a factor $\pm\sqrt{2}$ of the minimum beam waist, the depth of focus can be defined as

$$d_\mathrm{dof} = \frac{8\lambda}{\pi}\left(\frac{f_\mathrm{obj}}{d_\mathrm{b}}\right)^2. \tag{2.36}$$

Figure 2.13 shows the depth of focus as a function of the beam diameter for a focal length of 50 mm and a wavelength of 635 nm.

The chosen configuration results in a depth-of-focus of approximately 917 µm for the OBD laser and 90 µm for the power tuning laser, which are both more than sufficient for the expected out-of-plane motion of the cantilever.

2.5 Designing the optical alignment microscope

An optical microscope is integrated in the optical layout in aid of manual alignment of the lasers and the prism with respect to the cantilever. It is constructed from commercial-off-the-shelf components around a simple two-lens design. Its limited utility renders optical performance of lesser importance than magnification and cost. Figure 2.5 shows how the alignment microscope is integrated in the OBD system.

A two-lens system can be described by the thin-lens equation,

$$\frac{1}{f_k} = \frac{1}{s_{i,k}} + \frac{1}{s_{o,k}}, \tag{2.37}$$

where f_k is the focal length, $s_{i,k}$ is the image distance and $s_{o,k}$ is the object distance of the k^{th} element. The elements are separated by a distance L, such that

$$s_{o,2} = L - s_{i,1}, \tag{2.38}$$

In an ideal, infinity-corrected system, the distance L can be disregarded, but in this case it needs to be taken into account in the relative placement of the elements. The magnification of each element can be expressed as

$$m_k = -\frac{s_{i,k}}{s_{o,k}} = -\frac{f_k}{s_{o,k} - f_k}, \tag{2.39}$$

where $k = \{1, 2\}$. The distance between the objective lens, element 1, and the cantilever is slightly larger than its focal length, such that the intermediate image is $\leq 12.7\,\text{mm}$ high. This way it fits within the available aperture of the optics and vignetting is avoided. The choice of the objective lens is described in Section 2.4.

The system magnication of a two-lens system is equal to

$$m_{\text{sys}} = m_1 m_2 = \frac{f_1 f_2}{(s_{o,1} - f_1)(L - f_2) - s_{o,1} f_1}. \tag{2.40}$$

When the object is placed at the focal plane of the first lens ($s_{o,1} = f_1$), this simplifies to

$$m_{\text{sys}} = -\frac{f_2}{f_1}. \tag{2.41}$$

A 500 mm lens was selected (Thorlabs AC254-500-A-ML, achromatic doublet) to achieve a total magnification of 10 times. The image is recorded on a Thorlabs DCC1545M CMOS camera, that has 1280x1024 pixels on a 6.66 mm x 5.32 mm sensors. With this combination both the cantilever probe, the laser spots and the prism edge can be seen as demonstrated in Figure 2.14.

The prism is mounted on a linear stage that allows it to move vertically. Live feedback from the camera is used to adjust the prism position such that it is barely in contact with the sphere at the end of the cantilever.

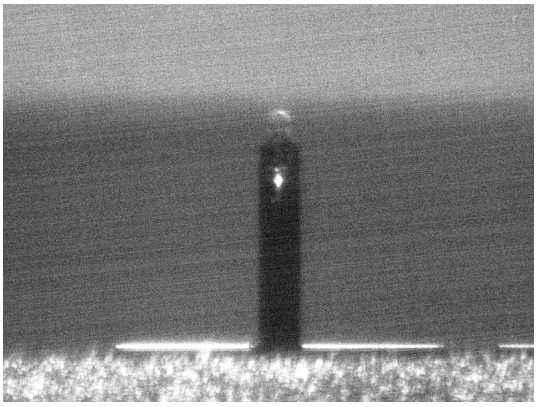

Figure 2.14: Micrograph from the confocal optical microscope showing the prism front surface at the top of the image with the the microsphere and the cantilever probe right underneath it. The image is cropped by approximately 50 % and rotated slightly to correct for camera tilt.

2.6 Controlling the temperature to milliKelvin stability

The temperatures of the prism and cantilever chip need to be stabilized to ± 1 mK to minimize the effects of temperature drift on the measurement. This level of stability is attained using two separate temperature control systems.

2.6.1 Design of the thermal control system

The temperature control systems consist of a passive and an active part. The air temperature of the laboratory is stabilized using an air conditioning unit to a stability of ± 1 K. As the measurement is conducted inside a vacuum chamber, the chamber walls isolate the experiment from the ambient air. With the chamber at ambient pressure, the added thermal mass of the chamber brings the natural temperature variation at the prism and cantilever down to approximately ± 100 mK, while at a working pressure of $\leq 1 \times 10^{-6}$ mbar this is further reduced to ± 50 mK.

To regulate the temperature of the prism, a miniature heater (343-HEATER-2x10, Allectra Ltd., United Kingdom) is glued to the backside of the prism. The prism mount acts as an adequate heat sink. For heating the cantilever chip a custom silicon nitride heating element (FLE100212, Bach Resistor Ceramics, GmbH, Germany) is clamped to the cantilever clamp assembly. For both assemblies the temperature is measured as close as possible to the point of interest using silicon diode sensors (DT670A-SD, Lake Shore Cryotronics, Inc., United States of America) that are glued in place using a 0.1 mm thick layer of Araldite AV138M. The sensors are monitored using a temperature monitor (SIM922, Stanford Research Systems, Inc., United States of America). This combination provides a measurement resolution of 0.6 mK r.m.s. and an accuracy better than 40 mK around room temperature.

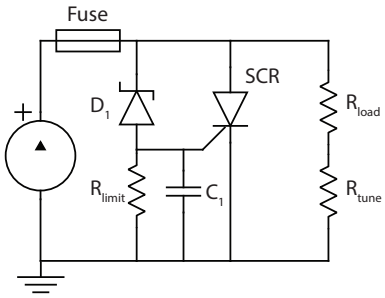

Figure 2.15: Schematic of the 'crow bar circuit' used to prevent overcurrent conditions.

Two bench power supplies (ES 030-5, Delta Elektronika B.V., The Netherlands) supply current to the heaters. The power supplies are controlled via analog programming using the 10 V analog output on the DACS. A 1:9 voltage divider scales the programming signal range from 10 V to 1 V to attain a higher programming resolution. This allows for a maximum output current of 1 A. The control software enforces a saturation limit of 300 mA to prevent the glue layers from overheating. An additional 'crow bar circuit' as shown in Figure 2.15 prevents against currents in excess of 350 mA. The heaters (R_{load}) are protected against overcurrent and consequently overheating by Joule heating by latching a silicon-controlled rectifier (SCR) that is in parallel to the heater. If the voltage drop across R_{load} and R_{tune} exceeds the breakdown voltage of the Zener-diode D_1, the silicon-controlled rectifier (SCR) effectively shorts the connection. If the overcurrent is sustained for long enough, the fuse will fail. The SCR only resets as soon as all power is removed from the circuit. The resistance R_{limit} limits the current through the Zener-diode and capacitor C_1 prevents inadvertent latching of the SCR due to noise.

2.6.2 Tuning of the control parameters

The control loops are tuned manually using a step response of a 0.1 A current to the heaters. The temperature response is fitted to a second order transfer function with delay:

$$G(s) = \left(\frac{k_1}{\tau_1 s + 1} + \frac{k_2}{\tau_2 s + 1} \right) \exp\left(-\tau_{\mathrm{d}} s\right), \tag{2.42}$$

where k_i are the gains ($\mathrm{K\,s\,A^{-2}}$), τ_i are the corresponding time constants (s) and τ_{d} is the delay (s). This model allows for two coupled masses with different response rates, and for a delay that is inherently present in systems where the actuator and the sensor are not co-located. Figure 2.16 shows these fitted responses and the fitting error. For both control loops, the error with respect to the model does not exceed 100 mK and is typically lower than 10 mK. The obtained fitting values are listed in Table 2.1. This accuracy is

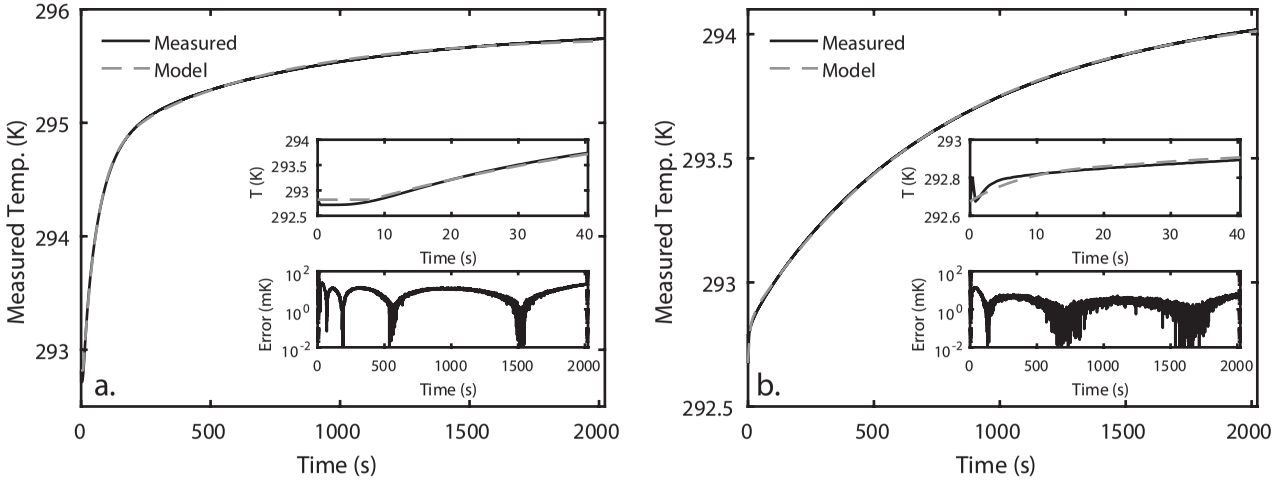

Figure 2.16: Temperature response of prism (left) and cantilever mount (right) after a current step of 100 mA. The insets show the temperature response in the first 40 s and the absolute error between the model and the measured response. The prism and cantilever mount have delays in the temperature response of 6 s and 0.8 s, respectively.

Table 2.1: Fitting parameters for open-loop temperature response to a 0.1 A step input at ambient pressure ($p \approx 1018$ mbar), and high vacuum conditions ($p = 5 \times 10^{-7}$ mbar).

Controller	k_1 (K s A^{-2})	k_2 (K s A^{-2})	τ_1 (s)	τ_2 (s)	τ_d (s)
Prism, amb.	102.8	190.1	658.1	56.2	7.7
Chip, amb.	124.1	16.8	795.1	7.2	0.4
Prism, vac.	286.9	388.7	2421.7	104.0	5.0
Chip, vac.	548.8	17.1	4984.4	624.9	1.2

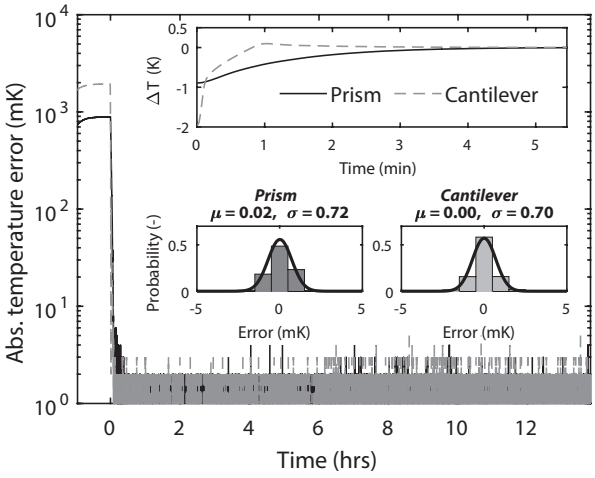

Figure 2.17: Absolute error observed by the temperature controllers after tuning for the prism assembly and the cantilever mount assembly. At $t = 0$ the controllers are engaged. The insets show the settling behaviour in the first few minutes, and the statistics of the absolute error measured after the ultimate stability of ± 1 mK has been achieved. The prism and cantilever temperatures reach this state after 22.4 min and 8.2 min, respectively. Results were obtained at ambient pressure.

sufficient for tuning the controllers. Because the heat dissipation is governed by Joule heating ($P \propto I^2$), the control output is in terms of I^2 instead of I.

The PID controllers were tuned manually using the fitted plant models. This resulting controller attained a stability of ± 1 mK, as demonstrated by a temperature measurement for 12 h time span. The results of this test are shown in Figure 2.17. The prism and cantilever mount temperatures achieve their set point temperatures of 293.7 K and 294.7 K (1 K and 2 K above room temperature) within 22.4 min and 8.2 min, respectively. The insets show the statistical distributions of the errors measured from that point forward. Both controllers exhibit an error with a standard deviation of 0.7 mK, which is in agreement with the noise of the temperature diodes and temperature monitor. The stability was replicated at high vacuum conditions using the same control parameters. Therefore, the same control parameters are used irrespective of the ambient pressure.

2.6.3 Online outlier detection and removal

Occassionally (once every 40 000 to 400 000 samples), the data transfer between the diode monitor and the PC is corrupted. In such an event, a 0 K reading is received, to which the control loop immediately responds by applying a high current to the heaters. This causes a large temperature increase that disrupts the measurement. To prevent this and similar disturbances, a simple but effective outlier detection and removal algorithm is implemented. The filter computes the difference between the most recent and the previous sample, $\Delta T = T_i - T_{i-1}$, and compares that to the maximum temperature change that can be physically achieved in the system between two measurements. The filter uses

$$T_i = \begin{cases} T_i & \text{if } |T_i - T_{i-1}| \leq s\Delta T_{\max} \\ T_{i-1} & \text{if } |T_i - T_{i-1}| > s\Delta T_{\max}, \end{cases} \tag{2.43}$$

where $s \geq 1$ is a safety factor, i is the current instance, and $\Delta T_{\max}$ is the maximum temperature difference that can be achieved physically between two measurements. Because the system is passively cooled, there exist two distinct maxima: the maximum rate of heating and the maximum rate of cooling. The former is found with the system temperature starting (close to) ambient temperature, while maximum power is applied to the heater. The latter is found with the system (close to) its maximum temperature and with no heater power applied. Logic can be added to the filter to distinguish between those two cases. However, to keep the implementation in Labview simple, the absolute maximum change is used:

$$\Delta T_{\max} = \max \begin{cases} \left|\frac{\mathrm{d}T}{\mathrm{d}t}\Delta t\right| \text{ for } T = T_{\min}, P = P_{\max} \\ \left|\frac{\mathrm{d}T}{\mathrm{d}t}\Delta t\right| \text{ for } T = T_{\max}, P = P_{\min}. \end{cases} \tag{2.44}$$

The safety factor s is included to account for uncertainty in the found maximum temperature changes, and only needs to be marginally larger than 1. The outlier filter can be manually enabled as soon as a stable temperature is reached.

2.7 Designing and characterizing the vacuum system

At ambient pressure and temperature, the contribution of radiative heat transfer is orders of magnitude smaller than those of conduction and convection. In order to measure the radiative heat transfer component, the others are strongly attenuated by lowering the pressure. In this section, the required operational pressure is estimated using an analytical model for gas conduction and limits imposed by vapor condensation. The realized vacuum system and its performance are discussed at the end of this section.

2.7.1 Modeling the heat transfer across the gap

The total amount of heat transferred across the gap between the microsphere and the prism is the combination of radiation, convection and conduction. The efficiency at which gas molecules can collide and transfer thermal energy from one surface to the other, is determined by the distance the molecules have to travel (the gap between microsphere and prism), and the gas pressure. This problem spans multiple length scales and requires intensive computations. However, an analytical multi-scale model describing the heat transferred through the gas layer was presented by Masters *et al.* [27].

According to Masters *et al.* , the effective heat transfer coefficient $\bar{k}$ of a continuum gas bounded by two parallel surfaces that are maintained at temperatures T_L and T_H, respectively, can be effectively estimated as:

$$\bar{k} = \frac{15\,(9\gamma - 5)\,k_\mathrm{B}}{126 d^2}\sqrt{\frac{k_\mathrm{B} T_\mathrm{eff,c}}{\pi m}}. \tag{2.45}$$

In this relation, the specific heat ratio $\gamma = c_p/c_v$ is the ratio of the specific heat at constant pressure to the specific heat at constant volume ($\gamma = 1.4$ for air), k_B is Boltzmann's constant, $T_\mathrm{eff,c} = (T_H + T_L)/2$ is the average temperature, d is the effective hard shell diameter of the molecule ($\approx 0.3\,\mathrm{nm}$ for air) and m is the effective molecular mass ($28.97\,\mathrm{g\,mol^{-1}}$ for air [28]). At the considered length scales of nanometer- and micrometer-sized gaps, this formulation can be adapted to take into account the molecular flow and transitional flow regimes and reads

$$k_\mathrm{eff} = \frac{\bar{k}}{\lambda}\left(\frac{1}{\lambda} + \frac{C}{\lambda}\right)^{-1}, \tag{2.46}$$

where λ is the mean free-path length of the gas and scaling parameter C is given by

$$C = \frac{15\pi\sqrt{2}\,(9\gamma - 5)\,(\gamma - 1)\,\sqrt{T_\mathrm{H} + T_\mathrm{L}}\left(\sqrt{T_\mathrm{H}} + \sqrt{T_\mathrm{L}}\right)}{128\alpha\,(\gamma + 1)\,\sqrt{T_\mathrm{H} T_\mathrm{L}}}. \tag{2.47}$$

The mean free-path length λ for a simple gas of hard-sphere molecules is given as

$$\lambda = \frac{1}{\sqrt{2}\pi d^2 n}, \tag{2.48}$$

with $n = P/(k_\mathrm{B}\mathrm{eff,c})$ the number density at pressure P. As this model needs to take into account molecular flow, the parameter α is introduced to describe the accommodation of the walls, in which $\alpha = 1$ represents a fully accommodated wall [29, 30]. Using this model, the total flux via gas conduction is expressed as

$$Q_\mathrm{c} = k_\mathrm{eff}\frac{T_\mathrm{H} - T_\mathrm{L}}{g}, \tag{2.49}$$

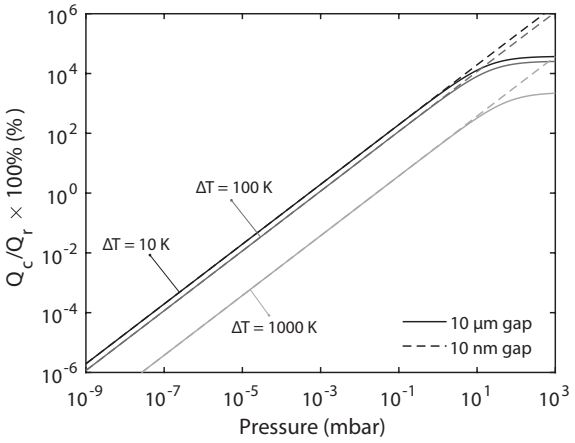

Figure 2.18: Ratio of heat transfer through gas conduction to radiative heat transfer. The model considers two parallel plates with the cold plate set at 293 K. The hot plate is set at 10 K, 100 K and 1000 K above that. The intermediate gas is assumed to be air that is represented using a hard-sphere model using an effective atom radius of 0.3 nm, effective molecular mass of $28.97\,\mathrm{g\,mol^{-1}}$ and a wall accommodation $\alpha = 1$. For radiation only far-field black-body components are taken into account.

where g is the width of the gap.

The total radiative component Q_r is estimated under the assumption that both surfaces behave as ideal black-body radiators as

$$Q_\mathrm{r} = \sigma_\mathrm{B} \left(T_\mathrm{H}^4 - T_\mathrm{L}^4 \right), \tag{2.50}$$

where σ_B is Stefan's constant. This does not take into account the near-field contributions that are expected to increase the heat flow, and can therefore be considered a realistic lower limit for the expected radiative component. Even though grey bodies would emit less radiation, realistic values of the emissivities for silica, would only reduce this by 15 %. This is sufficiently accurate to determine the required vacuum regime.

The ratio of flux via gas conduction to flux via radiation is plotted in Figure 2.18. Therein the cold plate is set at 293 K and the hot plate at respectively 10 K, 100 K and 1000 K above that. At an operational pressure of 1×10^{-6} mbar and a temperature difference of 10 K, gas conduction accounts for less than 20 ppm. At a pressure of 1×10^{-7} mbar, this drops to ≈ 2 ppm.

2.7.2 Vapor condensation in small gaps

Capillary condensation in small gaps puts a second limit on the operational pressure. When a small gap is created, water vapor can condensate and bridge the space by forming a meniscus. The formation of such a meniscus has to be avoided to prevent strong capillary forces from influencing the deflection of the probe and to prevent a thermally conductive path of liquid from forming between the probe and the sample. Atomic force microscopy

Figure 2.19: Vacuum system on top of its support structure, with ion getter pump (in red) and gate valve visible.

studies on condensation of water vapor in micrometer and nanometer sized gaps by Rozhok *et al.* [31] have shown that lowering the relative humidity to 0% is not sufficient to prevent a water meniscus from forming. Only at pressures of $\leq 2.8 \times 10^{-7}$ Pa no meniscus was formed. Taking this in consideration an operational pressure of 1×10^{-7} Pa (1×10^{-9} mbar) is required to achieve sub-10 nm gaps. However, the roughness of the microspheres limits the minimum achievable gap size to roughly 20 nm. Therefore, a pressure of 1×10^{-9} mbar is deemed unnecessarily low.

2.7.3 Vacuum system and performance

The vacuum chamber measures 318 mm in inner diameter and 264 mm in height. The top-hat design, as shown in Figure 2.19, features a window on the top for the total-internal reflection microscope and a window on the side for the optical beam deflection system. The pumps are suspended from the bottom flange, as are the electrical and optical feedthroughs. The bottom flange also serves as the support for the rest of the vacuum setup.

The vacuum system uses a Vacuubrand MD-4-NT diaphragm pump to reach a coarse vacuum pressure of 1 mbar. In conjunction with a Pfeiffer TMU-071-P turbomolecular pump, an operational pressure of 1×10^{-6} mbar is achieved. A SAES HV 200 ion getter pump is used as a final pump stage to reach an absolute pressure of 5×10^{-7} mbar, as shown in Figure 2.20. Both the turbomolecular pump and the ion getter pump can each be locked behind gate valves to seal the vacuum chamber. During the heat transfer measure-

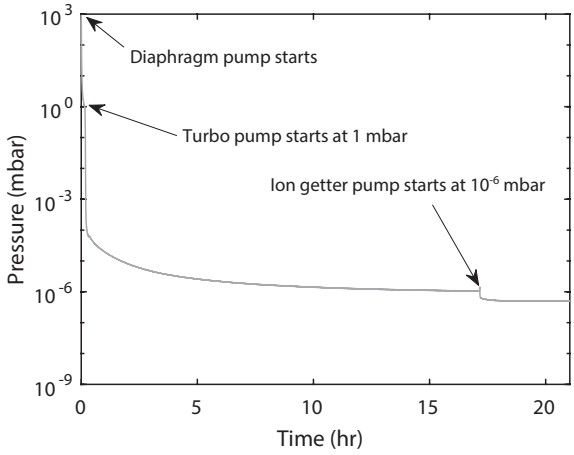

Figure 2.20: Pump down characteristics of the vacuum systems. A pressure of 1 mbar is achieved with the diaphragm pump after roughly 9 min. Once the turbopump starts, the pressure drops to 1×10^{-6} mbar after approximately 17 h. The ion getter pump allows to reach an operational pressure of 5×10^{-7} mbar.

ments, the turbomolecular pump is sealed off and shut down to minimize the mechanical vibrations that are induced by the pumping action. During the experiment, the ion getter pump is used to keep the operational pressure below 1×10^{-6} mbar. Figure 2.21 shows the pressure as a function of time for this scenario. Sealing off the turbomolecular pump is followed by a rapid increase in pressure to roughly 7.4×10^{-7} mbar, after which the pressure increases almost linearly at a rate of 0.36×10^{-7} mbar h^{-1}. At this rate, the turbomolecular pump can remain inactive for over 7 h by first order approximation, which is more than the 3 h needed to measure the heat transfer between the probe and the sample at a displacement rate of 0.5 nm s^{-1} and a full stroke of 5 µm.

Switching off the diaphragm pump and turbopump reduces the noise floor by more than a factor of 2 as shown in Figure 2.22. The noise floor was measured with the laser of the optical beam deflection system focused on the chip that holds the probes. In both cases, i.e. mechanical pumps on and off, the output signal of the position sensitive detector was measured at a rate of 200 kSamples/s for more than 100 s. The shown spectra are the average of 50 spectra obtained from 50 sections of the complete time series. Besides an overall lower noise level, switching off the mechanical pumps also removes resonance peaks between 10 Hz and 200 Hz.

2.7.4 Operational pressure

The operational pressure was selected as $\leq 1 \times 10^{-6}$ mbar, to minimize the contribution of heat transfer through the gas layer. Better vacuum conditions were considered unnecessary, because the surface roughness of the available

microspheres severely restricts reliable measurement of the heat transfer at probe-sample separations smaller than 20 nm.

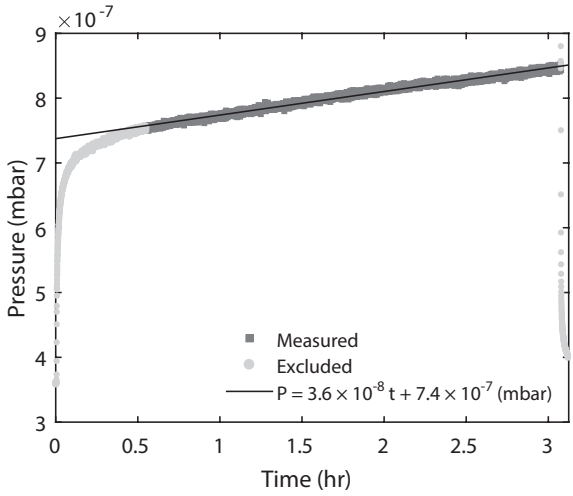

Figure 2.21: Evolution of pressure with time with the turbomolecular pump locked off and the ion getter pump working against the leaks. A pressure of $\leq 1 \times 10^{-6}$ mbar can be maintained for ≥ 3 h. After 3 h the pump is reactivated and the pressure drops again.

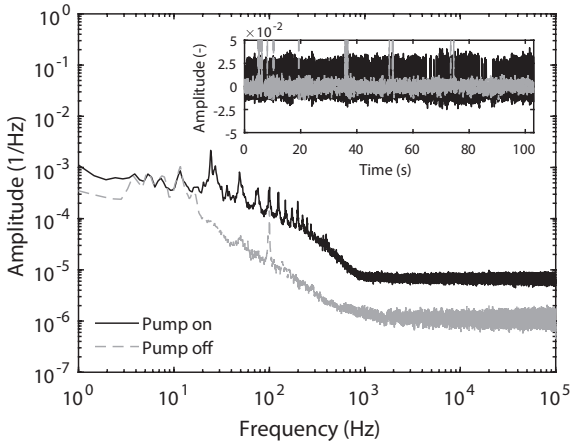

Figure 2.22: Noise spectra of the normalized signal of the position sensitive detector. The laser was focused on the base of the probe chip. The inset shows the measured time series of the signals (corrected for mean offset). The shown spectra are the average of 50 spectra obtained from 50 sections of the complete time series.

2.8 Optical noise and drift

The laser beams used to measure the rotation of the cantilever tip and to correct its temperature exhibit noise and drift in their intensities. In this section, the intensity noise and drift are analyzed and measured.

2.8.1 Performance bounds from current-driver

The laser controller introduces intensity noise through noise in the drive current it supplies to the laser diode. The manufacturer characterizes the noise of the drive current as a sum of its components: the noise without ripple (root mean square (r.m.s.) value over a band of 10 Hz to 10 MHz), ripple (r.m.s. at 50/60 Hz), current transients caused by the processor, current transients caused by other processes and short-term fluctuations [32]. The last group is neglected in the analysis, as the manufacturer has confirmed upon inquiry that these are not present during continuous operation [33] and only manifest during warm-up. The noise of the optical intensity that is eventually used for heating the cantilever is calculated using the slope efficiency of the laser diode and the absorptance of the cantilever. The contributions of the individual components is detailed in Table 2.2.

This calculation predicts a fluctuation of 180 nW r.m.s. in the power absorbed by the cantilever. As will be shown, we have measured considerably lower variations in the optical power.

2.8.2 Relative intensity noise

Light amplification by stimulated emission of radiation is an inherently stochastic process. When a laser diode is operated at an electric current below the lasing threshold, the larger part of the emitted radiation is from random emission. Above the threshold, stimulated emission quickly leads to a cascade of stimulated radiation. As most of the emitted photons are in phase and do not destructively interfere with each other, intensity fluctuations are suppressed. Although the process itself becomes less noisy,

Table 2.2: Calculation of the laser controller induced noise intensity fluctuations.

Component	Value	Unit
Ripple	8.0×10^{-7}	A, r.m.s.
Noise w/o ripple	1.0×10^{-6}	A, r.m.s.
Transients (processor)	1×10^{-5}	A, r.m.s.
Root square sum	1.0×10^{-5}	A
Slope efficiency	0.20	$\mathrm{W\,A^{-1}}$
Intensity noise	2.0×10^{-6}	W
Absorptance of cantilever	0.09[a]	-
Power absorbed by cantilever	1.8×10^{-7}	W

[a] For an aluminium-coated silicon nitride cantilever.

temporal variations of the cavity length and optical feedback are causes for an increased intensity noise.

The optical intensity noise in our system was measured using a method that is similar to the ones proposed by Shi *et al.* [34] and by the Agilent corporation [35]. The laser diode was coupled to a high speed photo diode (New Focus 1006) through a single mode fiber. The signal of the photo diode was probed by a performance spectrum analyzer (PSA, Agilent E4446A) after passing through a 26 dB broadband amplifier (Miteq JS-3-01001800-29-5A). For the reader's reference, a schematic representation of the described setup is given in Figure 2.23. The relative intensity noise (RIN) is then determined as the ratio of the noise power spectral density $n(\omega)$ to the average power dissipated in the spectrum analyzer input P_{DC}.

To obtain the noise power spectral density, the background signal $B(\omega)$ is subtracted from the measured noise power $S(\omega)$. The result is consecutively scaled by the amplifier gain G and normalized by the corresponding resolution bandwidth $\Delta\omega$ of the power spectral density,

$$n(\omega) = \frac{S(\omega) - B(\omega)}{G\Delta\omega}. \tag{2.51}$$

The background signal is obtained by measuring the noise power with all equipment switched on except for the laser diode and the signal generator. This allows for correction of the measurement data for systematic offsets and other sources of noise, that are introduced by the environment or the measurement equipment.

The average dissipated power cannot be measured using the PSA and is instead determined in a separate measurement of the voltage drop V_{out} over a 50 Ω resistor R. The resistor takes the place of the combination of the PSA and amplifier. By matching the impedance of these devices, it mimics the relevant electrical response and minimizes spurious reflections of the RF signal. The average power dissipated in the resistor is easily determined as $P_{\mathrm{DC}} = \left\langle V_{\mathrm{out}}^2 \right\rangle / R$.

This leaves the RIN to be expressed as

$$\frac{\Delta I(\omega)}{I} = \frac{n(\omega) R}{\langle V_{\mathrm{out}}^2 \rangle}. \tag{2.52}$$

To translate from relative fluctuations to absolute optical power fluctuations, the RIN is multiplied by the average optical power, which is known through calibration using an optical power meter. This means that the absolute optical power fluctuations can be expressed as

$$\Delta P_{\mathrm{opt}}(\omega) = \frac{\Delta I(\omega)}{I} P_{\mathrm{opt}}. \tag{2.53}$$

The root mean square intensity noise for a given bandwidth $\tilde{\omega}$ is obtained via

$$\Delta P_{\mathrm{opt,\ RMS}} = \int_0^{\tilde{\omega}} \Delta P_{\mathrm{opt}}(\omega)\, \mathrm{d}\omega. \tag{2.54}$$

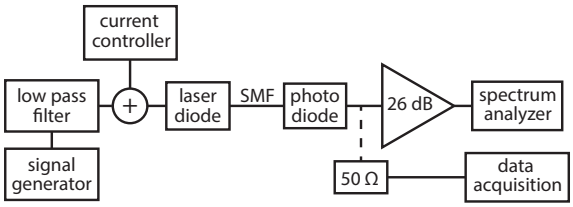

Figure 2.23: Schematic of the experimental setup that is used to measure the relative intensity noise. The light is coupled from the laser diode into a single-mode fiber (SMF) and directly into the photo diode. The electrical output signal of the photo diode is then passed into a radio frequency (RF) amplifier and into the spectrum analyzer (high frequency content). The average signal amplitude is measured by disconnecting the amplifier and spectrum analyzer, and terminating the output of the photo diode by a 50 Ω resistor. The resulting voltage drop over the resistor is measured using a data acquisition system.

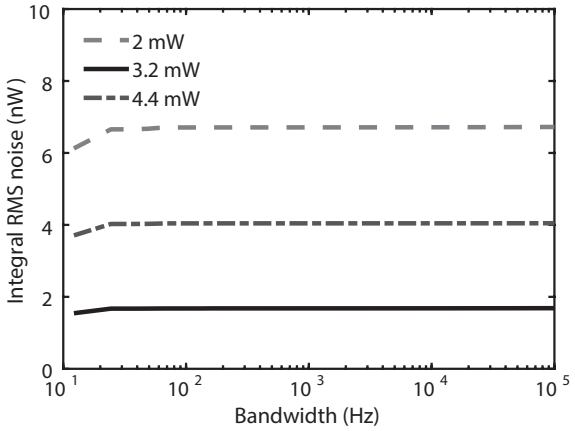

Figure 2.24: Measured root mean square optical noise as function of the bandwidth. At all tested power levels the noise remains below 10 nW r.m.s.

This results in a conservative root mean square (r.m.s.) intensity noise of ≤ 10 nW for a 100 kHz bandwidth, or approximately 0.9 nW in absorbed power. The results are shown in Figure 2.24. This number includes the noise introduced by the controller and is considerably more favorable than the estimated worst-case 180 nW. An attempt to further reduce the relative intensity noise using high frequency injection in the laser diode was abandoned. This method and its limited utility for existing systems are discussed in Appendix D.

Power fluctuations that occur at time scales much shorter than the thermal response time of the microsphere or of the cantilever probe are effectively filtered out. As discussed in more detail in Chapter 4, the thermal response time of the probe is typically below 10 kHz.

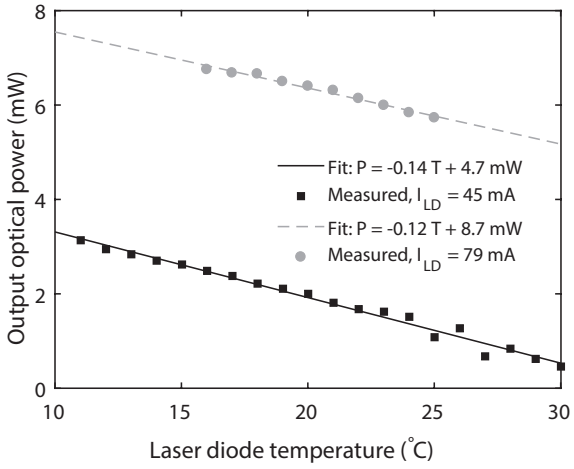

Figure 2.25: Optical output power of the laser diode as function of diode temperature with the diode driver operating in constant current mode. The driving current was kept constant at 45 mA and 79 mA, respectively. The corresponding temperature coefficients are $-0.14\,\mathrm{mW\,K^{-1}}$ and $-0.12\,\mathrm{mW\,K^{-1}}$.

2.8.3 Temperature coefficient

The optical power produced by the laser diode depends on the diode temperature as shown in Figure 2.25 for drive currents of 45 mA (slightly above the threshold current) and 79 mA (slightly under the maximum current). The temperature coefficient is only slightly dependent on the drive current, and was estimated to be $-0.12\,\mathrm{mW\,K^{-1}}$ to $-0.14\,\mathrm{mW\,K^{-1}}$. At the same time, the intensity noise also varies with the diode temperature as depicted in Figure 2.26. To minimize signal drift of the laser diode, its temperature is stabilized to within 1 mK from the reference temperature of 20 °C by a thermo-electric heater in the diode mount (Thorlabs LM9LP) and a temperature controller (Thorlabs TED8020). This puts a bound of 0.14 µW on the power variation of the laser, and approximately 13 nW in the absorbed power due to temperature variations of the laser diode.

2.8.4 Laser intensity drift

Besides the power variation due to noise, the power also slowly drifts in time. We measured the drift of both the read-out laser (high power, slope efficiency of $0.45\,\mathrm{W\,A^{-1}}$) and the tuning laser (low power, actuated, slope efficiency of $0.18\,\mathrm{W\,A^{-1}}$) using a Newport 1936-R power meter and the Newport 918D-UV-OD3 sensor with its optical attenuator in place. The results of these measurements are shown in Figure 2.27, in which each point is the average of 100 samples taken at a rate of 1 kHz. The standard deviation per point is at most 3 nW. The measurements were taken in the assembled system of Figure 2.5 at the location of the first beam stop (near the 50:50 beam

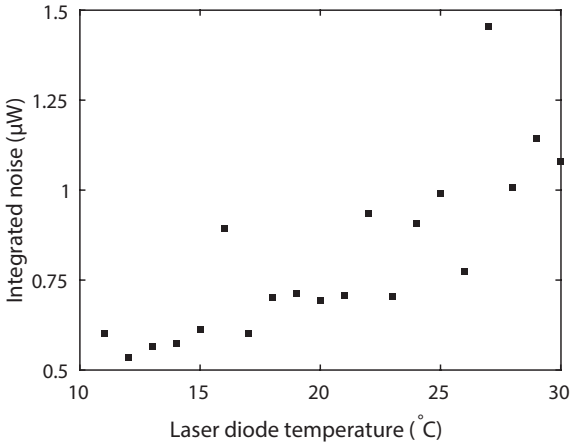

Figure 2.26: Intensity noise of laser diode as function of diode temperature measured over a 4 GHz bandwidth. The driving current was kept constant at 45 mA.

splitter). For the read-out laser, a mean power 3.2 mW was measured with a peak-to-peak variation of 3.7 µW in constant current mode, and 4.1 µW in constant power mode. Similarly, for the tuning laser we registered a mean power of 1.2 mW with a peak-to-peak variation of 2.0 µW in constant current mode, and 2.1 µW in constant power mode. Surprisingly, perhaps, there is little difference between running the diodes in constant current mode or in constant power mode. In constant power mode, an integrated photodiode is used to measure the output power of the laser diode so that it can be actively controlled–in this case to little effect. The control parameters are set by the manufacturer and cannot be tuned. Performance may be better with other laser diodes.

The amplitude of these drifts cannot be explained by a drift in the temperature of the laser diode (± 1 mK), a drift in the applied current (≤ 0.5 µW over 60 min), or by digitization effects in the current driver (1.5 µA). Their added effects do only account for 0.5 µW and 1.0 µW drift amplitudes for the tune laser and read-out laser, respectively. Figure 2.30 shows the inherent drift of the optical power meter, which depends on the set measurement range. At the set range of 6.941 mW, the drift amplitude of the power meter does not exceed 0.69 µW and can thus also not explain the measured drift amplitudes. The cause of the measured drift in laser intensity is, therefore, currently unknown.

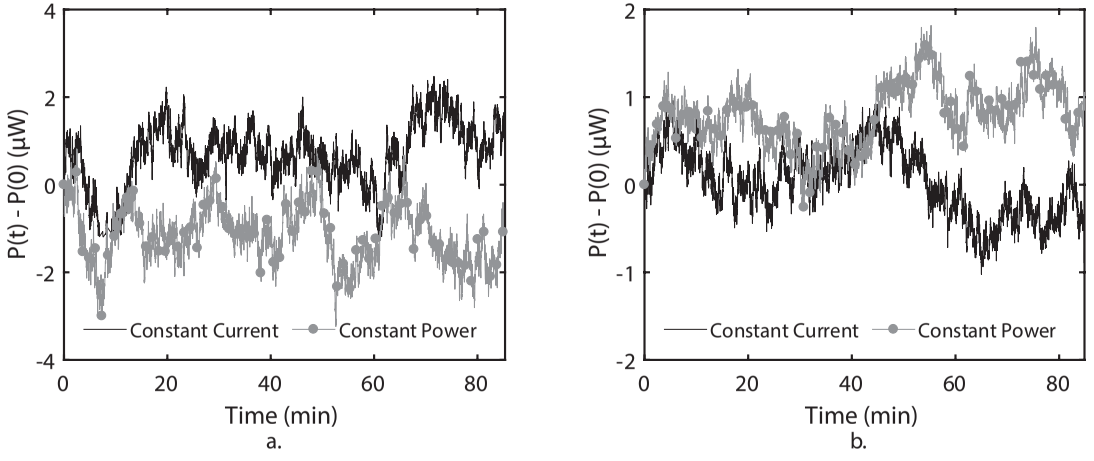

Figure 2.27: Absolute variations in laser output power measured after the first 50:50 beam splitter. (a) Read-out laser, mean power measured at 3.2 mW and a measured variation of 3.7 µW peak-to-peak in constant current mode, and 4.1 µW peak-to-peak in constant power mode. (b) Tuning laser, mean power measured at 1.2 mW and a measured variation of 2.0 µW peak-to-peak in constant current mode, and 2.1 µW peak-to-peak in constant power mode. For both figures the initial power was subtracted from the series.

2.9 Electronic noise and drift

In addition to optical noise introduced via the laser diodes, additional noise and drift are introduced into the measurement signal through the position sensitive detector and read-out electronics. In this section, these sources are further analyzed.

2.9.1 Detector noise and drift

For the optical beam deflection method, a Maypa OPS-40 is used as the position sensitive detector. The sensitivity of its output signal X_p to changes in the power absorbed P by the cantilever is expressed in Equation (2.33):

$$\frac{\partial X_\mathrm{p}}{\partial P} = \sqrt{\frac{2}{\pi}} S P_\mathrm{OBD} \frac{f_\mathrm{obj}}{\sigma} \frac{\beta \Delta \alpha L}{G}.$$

The output signal of the PSD can be written as the sum of the following contributions

$$X_\mathrm{p}(t) = X_{\mathrm{p}_0} + \frac{\partial X_\mathrm{p}}{\partial P} \left(\Delta P_\mathrm{HT}(t) + \alpha \Delta P_\mathrm{LD}(t)\right) + S\eta \Delta P_\mathrm{LD}(t) + \Delta X_{\mathrm{p}_1}(t), \tag{2.55}$$

where X_{p_0} is the offset of the signal, ΔP_HT is the amount of heat absorbed by the probe due to heat transfer with the sample, α is the absorption coefficient of the probe for the incident light, ΔP_LD is the change in the incident power, S is the sensitivity of the PSD for changes in incident power, η is the efficiency of the optical path from the laser diode to the PSD and ΔX_{p_1} is a catch-all term for non-optical contributions to the signal (e.g., thermal drift or drift due to movement of the PSD itself). The offset can be removed by measuring X_p when the probe is far removed from the sample. The absorption α and the efficiency of the optical path η can be determined using the method described in Appendix B. If an optical power meter is included in the system, the effects of the laser power drifting can be compensated for. The last remaining term, $\Delta X_{\mathrm{p}_1}(t)$ contains components of electronic drift and noise and thermo-mechanical effects that can cause the optical beam to move with respect to the PSD.

According to the specification, the used sensor exhibits an electronic noise of 200 µV r.m.s. for an incident power on the detector plane of 1 mW. The equivalent noise in the flux measurement due to electronic noise on the detector output $\Delta \hat{P}_\mathrm{PSD}$ reads

$$\Delta \hat{P}_\mathrm{PSD} = \frac{\partial P}{\partial X_\mathrm{p}} \Delta X_\mathrm{p}. \tag{2.56}$$

Using the design parameters this equates to 1.6×10^{-11} W.

To confirm this noise level experimentally, the beam of a 635 nm wavelength semiconductor laser is split using a 50:50 beam splitter. The power of one of the resulting beams is measured using an optical power meter, whilst

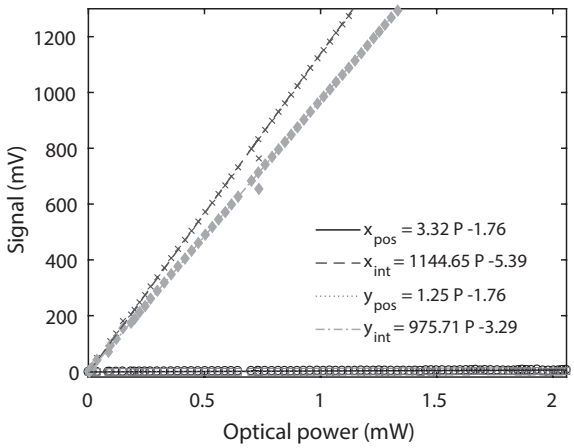

Figure 2.28: Calibration curves for this specific beam alignment on the OPS.

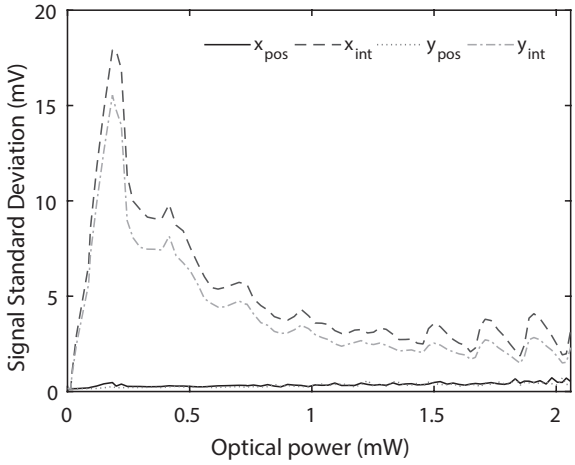

Figure 2.29: Standard deviation of the measured output signals of the OPS for 1000 samples at 200 kHz as function of the incident optical power.

the other one is incident on the PSD. The PSD signals resulting from this, x_{pos}, x_{int}, y_{pos} and y_{int}, are sampled at 200 kHz for a total of 1000 samples per channel. Figure 2.28 shows the calibration curves of the average output signals of the PSD as a function of the incident optical power. Similarly, the standard deviation of each trace is shown in Figure 2.29. The noise clearly drops with higher input power.

Interestingly, the noise of each channel varies with the incident power and cannot be explained with the intensity noise of the laser. As shown in Figure 2.24, the intensity noise does not exceed 6 nW at the used measurement bandwidth. Using the calibration of Figure 2.28, this translates into an output voltage fluctuation of at most 7 µV, which is close to three orders of magnitude

smaller than the measured values.

The drift of the OPS signals over time can be partially explained by drift of the optical power. Figure 2.33 shows that the intensity signals x_{int} and y_{int} correlate well with the measured drift in laser power with Pearson correlation coefficients of 0.76 in both cases and Spearman correlation coefficients of 0.72 and 0.73, respectively. The correlations of position signals x_{pos} and y_{pos} with the measured power drift is much weaker. For these signals, the Pearson correlation coefficients are 0.15 and 0.29, respectively, while the Spearman correlation coefficients are 0.16 and 0.29.

The poor correlation between the position signals (x_{pos} and y_{pos}) and the laser power indicates that other (currently unidentified) sources dominate the drift.

Power meter drift

To explore whether the measured differences can be explained by uncertainties in the measurement equipment, the drift of the power meter was investigated separately. The optical power meter (Newport 1936-R with 918D-UV-OD3 sensor) has an uncertainty of 0.2 % in the measured power and 2 % in the sensor current. The latter is dominated by temperature effects, which are compensated for in the power meter within the calibration limits. The manufacturer does not specify the drift characteristics or how the total uncertainty is built up. At 1 mW laser power, a 0.2 % uncertainty equates to 2 µW absolute uncertainty. To exclude the possibility of the measured drifts to be solely traced to drift of the power meter, the drift of the power meter was measured in a darkened room and for several measurement ranges. Figure 2.30 shows how the peak-to-peak amplitudes of the drift varies with the measurement range. With an incident power of 1.3 mW, the power meter signals vary 2.0 µW and 2.3 µW peak-to-peak for measurement ranges set to 6.941 mW and 69.41 mW, respectively. Because the measured drift amplitudes are nearly independent from the measurement range, we conclude that the measured drifts can be attributed to drifts in the optical power, rather than to drift of the power meter.

Normalization of the position signal

Because the output of the OPS depends on the incident power, the position signals are normalized with the sum of the four photodiodes. At zero incident power, however, a small offset of approximately 10 mV exists, that causes errors in the normalization. Figure 2.32.a shows how the normalized position signal changes with a change in incident power. The resulting estimated position clearly approaches a limit value, as the relative contributions of the offsets diminish. This error needs to be removed through calibration to reduce the error to approximately 1 %. The relative error is determined with respect to the limit value, and is depicted in Figure 2.32.b.

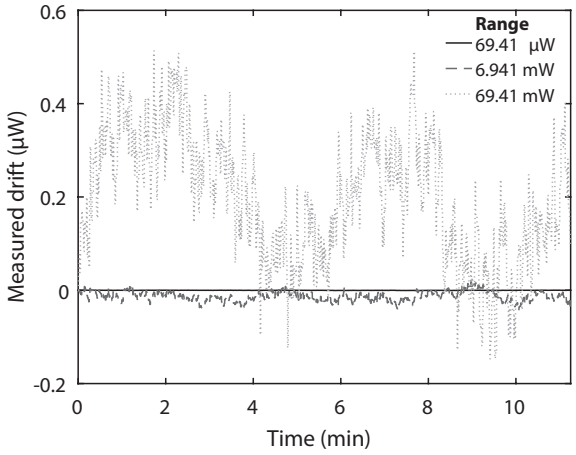

Figure 2.30: Measured drift in power meter signal without an incident beam for three settings of the measurement range. The peak-to-peak drift amplitudes depend on the measurement range and are 1.1 nW, 69 nW and 0.69 µW for the 69.41 µW, 6.941 mW and 69.41 mW measurement ranges, respectively. The corresponding mean power levels measured are 1.3 nW, 0.45 µW and 3.7 µW.

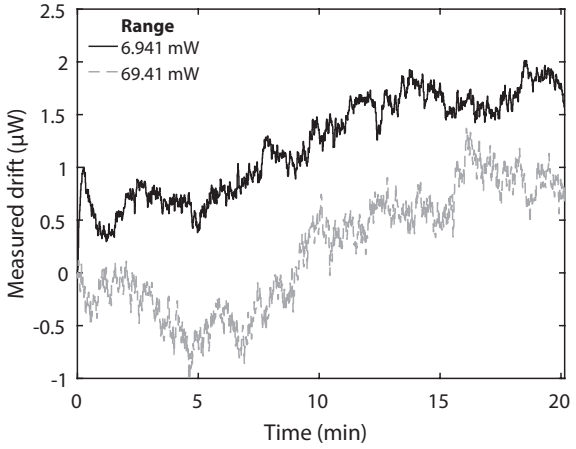

Figure 2.31: Measured drift in power meter signal with an incident beam of 1.3 mW average optical power for two settings of the measurement range. The peak-to-peak drifts are 2.0 µW and 2.3 µW for the 6.941 mW and 69.41 mW measurement ranges, respectively.

2.9.2 Data acquisition noise

The signal of the position sensitive detector is acquired and digitized using a National Instruments PCI-6251 system. To match the maximum output voltage of the detector the input range is set to ±10 V. Using the 16 bit discretization a resolution of $20/2^{16} = 3.1 \times 10^{-4}$ V is obtained. According to the specification of the data acquisition system [36], the system exhibits a

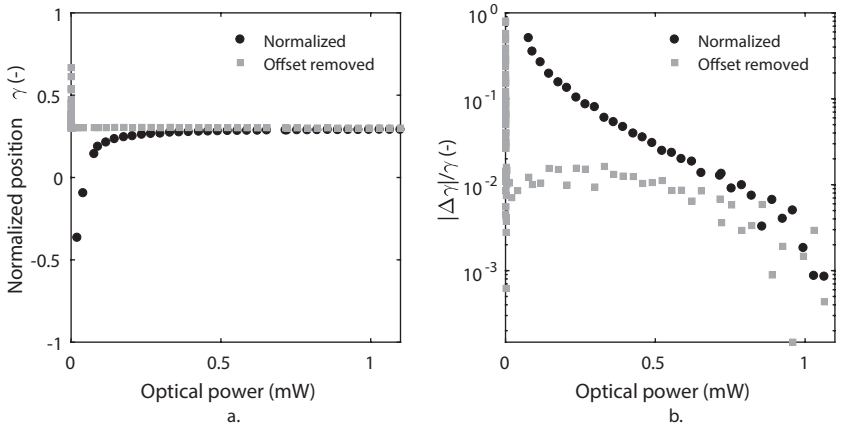

Figure 2.32: a. Normalized position as function of incident power. b. Relative error with respect to the limit value as function of incident power.

Table 2.3: Calculation of the data acquisition induced noise for a NI PCI 6251 system.

Component	**Value**	**Unit**
Random noise at full scale	2.8×10^{-4}	V, r.m.s., 1σ
Random noise at full scale	8.4×10^{-4}	V, r.m.s., 3σ
$\frac{\partial X_p}{\partial P}$	1.26×10^{7}	$\mathrm{V\,W^{-1}}$
Equivalent noise	6.64×10^{-11}	W
Resolution	3.1×10^{-4}	V
Equivalent resolution	2.41×10^{-11}	W

random noise of 280 µV (r.m.s., 1 standard deviation). Combined with the detection sensitivity of the detector (change in output voltage due to a supplied heat flux at the cantilever), these can be translated into equivalent uncertainties for the flux uncertainty. This calculation is worked out in Table 2.3.

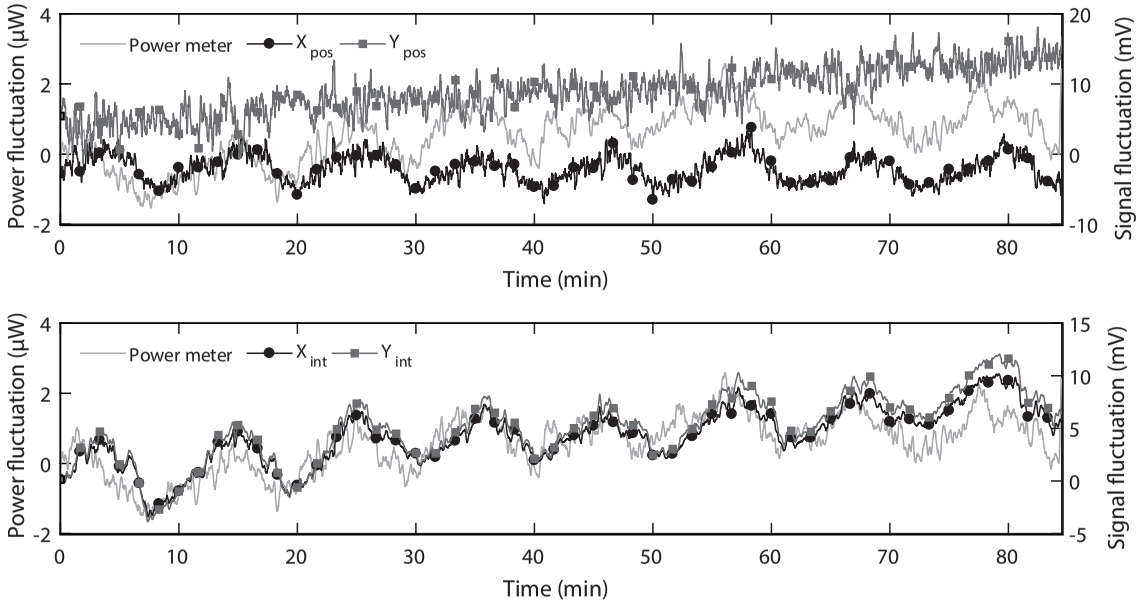

Figure 2.33: Drift of the measured laser power and the separate PSD signals (expressed in equivalent power fluctuations) for position (top) and intensity (bottom).

Acknowledgments

The author thanks Jeroen Hoogland of TNO and Roland Horsten of Delft University of Technology for lending the necessary equipment.

Bibliography

[1] G. Meyer and N. M. Amer. Novel optical approach to atomic force microscopy. *Applied Physics Letters*, 53(12):1045, 1988.

[2] E. Rousseau, A. Siria, G. Jourdan, S. Volz, F. Comin, J. Chevrier, and J.-J. Greffet. Radiative heat transfer at the nanoscale. *Nature Photonics*, 3(9):514–517, 2009.

[3] G. Binnig, C. F. Quate, and C. Gerber. Atomic Force Microscope. *Physical Review Letters*, 56(9):930–933, 1986.

[4] J. Brugger, R. A. Buser, and N. F. de Rooij. Micromachined atomic force microprobe with integrated capacitive read-out. *Journal of Micromechanics and Microengineering*, 2(3):218–220, 1992.

[5] A. Narayanaswamy, S. Shen, and G. Chen. Near-field radiative heat transfer between a sphere and a substrate. *Physical Review B*, 78(11):115303, 2008.

[6] S. Shen, A. Narayanaswamy, and G. Chen. Surface phonon polaritons mediated energy transfer between nanoscale gaps. *Nano letters*, 9(8):2909–13, 2009.

[7] P. J. van Zwol, L. Ranno, and J. Chevrier. Tuning Near Field Radiative Heat Flux through Surface Excitations with a Metal Insulator Transition. *Physical Review Letters*, 108(23):234301, 2012.

[8] P. L. Sambegoro. *Experimental Investigations on the Influence of Curvature and Materials on Near-field Thermal Radiation.* Doctoral dissertation, Massachusetts Institute of Technology, 2016.

[9] H. Rothuizen, M. Despont, U. Drechsler, C. Hagleitner, A. Sebastian, and D. Wiesmann. Design of Power-Optimized Thermal Cantilevers for Scanning Probe Topography Sensing. In *2009 IEEE 22nd International Conference on Micro Electro Mechanical Systems*, p. 603–606, Sorrento, Italy, 2009. IEEE.

[10] J.-B. Xu, K. Läuger, R. Möller, K. Dransfeld, and I. H. Wilson. Heat transfer between two metallic surfaces at small distances. *Journal of Applied Physics*, 76(11):7209, 1994.

[11] W. Müller-Hirsch, A. Kraft, M. T. Hirsch, J. Parisi, and A. Kittel. Heat transfer in ultrahigh vacuum scanning thermal microscopy. *Journal of Vacuum Science & Technology A: Vacuum, Surfaces, and Films*, 17(4):1205, 1999.

[12] A. Narayanaswamy and G. Chen. Thermal near-field radiative transfer between two spheres. *Physical Review B*, 77(7):075125, 2008.

[13] L. Helden, E. Eremina, N. Riefler, C. Hertlein, C. Bechinger, Y. Eremin, and T. Wriedt. Single-particle evanescent light scattering simulations for total internal reflection microscopy. *Applied Optics*, 45(28):7299, 2006.

[14] R. Bijster, J. de Vreugd, and H. Sadeghian. Dynamic Characterization of Bi-material Cantilevers. In S. Yurish and F. Pacull, editors, *SENSORDEVICES 2013: The Fourth International Conference on Sensor Device Technologies and Applications*, p. 1–8, Barcelona, Spain, 2013. IARIA.

[15] R. Bijster, J. de Vreugd, and H. Sadeghian. Automatic Alignment of Optical Beam Deflection Systems. In *Proceedings of 2013 Nanomechanical Sensing Workshop*, Stanford, California,USA, 2013.

[16] W. Young, R. G. Budynas, and A. Sadegh. *Roark's Formulas for Stress and Strain.* McGraw-Hill, New York, eigth edition, 2011.

[17] G. Janssen, M. Abdalla, F. van Keulen, B. Pujada, and B. van Venrooy. Celebrating the 100th anniversary of the Stoney equation for film stress: Developments from polycrystalline steel strips to single crystal silicon wafers. *Thin Solid Films*, 517(6):1858–1867, 2009.

[18] S. S. Injeti and R. K. Annabattula. Extending Stoney's equation to thin, elastically anisotropic substrates and bilayer films. *Thin Solid Films*, 598:252–259, 2016.

[19] H. J. Butt and M. Jaschke. Calculation of thermal noise in atomic force microscopy. *Nanotechnology*, 6(1):1–7, 1995.
[20] R. Herfst, W. Klop, M. Eschen, T. van den Dool, N. Koster, and H. Sadeghian. Systematic characterization of optical beam deflection measurement system for micro and nanomechanical systems. *Measurement*, 56:104–116, 2014.
[21] Edmund Optics. Simplifying Laser Alignment.
[22] P. E. Rutten. High speed two-dimensional optical beam position detector. *Review of Scientific Instruments*, 82(7):073705, 2011.
[23] J. A. Arnaud, W. M. Hubbard, G. D. Mandeville, B. de la Clavière, E. A. Franke, and J. M. Franke. Technique for Fast Measurement of Gaussian Laser Beam Parameters. *Applied Optics*, 10(12):2775, 1971.
[24] M. Mauck. Knife-edge profiling of Q-switched Nd:YAG laser beam and waist. *Applied Optics*, 18(5):599, 1979.
[25] S. A. Self. Focusing of spherical Gaussian beams. *Applied Optics*, 22(5):658, 1983.
[26] CVI Melles Griot. Gaussian Beam Propagation, 2017.
[27] N. D. Masters, W. Ye, and W. P. King. The impact of subcontinuum gas conduction on topography measurement sensitivity using heated atomic force microscope cantilevers. *Physics of Fluids*, 17(10):100615, 2005.
[28] A. F. Ismail, K. Chandra Khulbe, and T. Matsuura. *Gas Separation Membranes*. Springer International Publishing, Cham, 2015.
[29] G. Arya, H.-C. Chang, and E. J. Maginn. Molecular Simulations of Knudsen Wall-slip: Effect of Wall Morphology. *Molecular Simulation*, 29(10-11):697–709, 2003.
[30] Y. V. Polezhaev and N. V. Pavlyukevich. ACCOMMODATION COEFFICIENT. In *A-to-Z Guide to Thermodynamics, Heat and Mass Transfer, and Fluids Engineering*. Begellhouse, 2011.
[31] S. Rozhok, P. Sun, R. Piner, M. Lieberman, and C. A. Mirkin. AFM study of water meniscus formation between an AFM tip and NaCl substrate. *Journal of Physical Chemistry B*, 108(23):7814–7819, 2004.
[32] Thorlabs. Operation Manual Current Module LDC80xx, 2010.
[33] Thorlabs Tech Support. Private inquiry, 2015.
[34] H. Shi, D. Cohen, J. Barton, M. Majewski, L. A. Coldren, M. C. Larson, and G. A. Fish. Relative intensity noise measurements of a widely tunable sampled-grating DBR laser. *IEEE Photonics Technology Letters*, 14(6):759–761, 2002.
[35] Agilent Technologies. Digital Communication Analyzer (DCA), Measure Relative Intensity Noise (RIN) - Product Note 86100-7. Technical report, Agilent Technologies, Inc., 2008.
[36] National Instruments. NI 6251 Device Specifications, 2015.

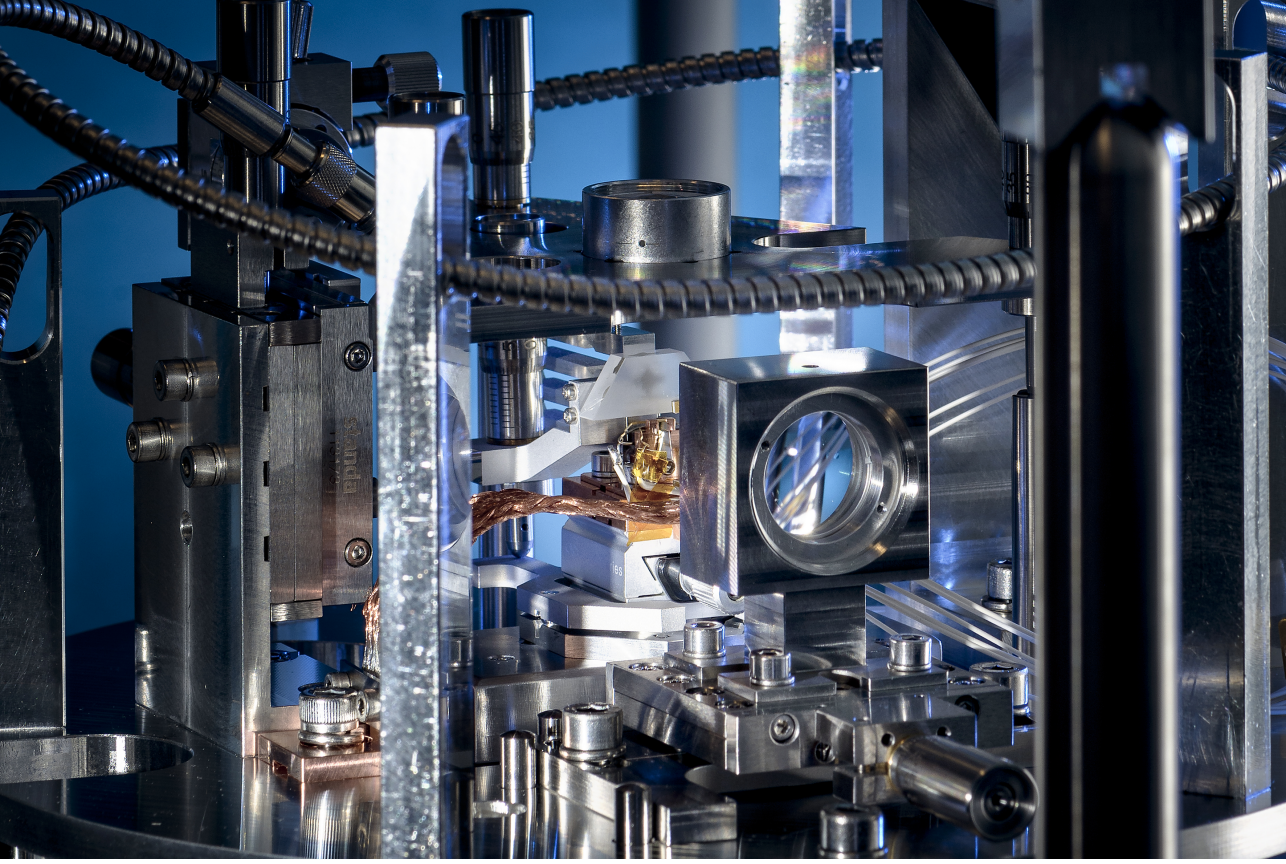

3. Total Internal Reflection Microscopy for Distance Measurement

The intent of the experiments is to measure near-field heat flux as a function of distance and eventually use heat flux to measure the separation between the probe and the sample. For both applications it is important that the separation between the probe and the sample is measured independently from the heat flux. In the first instance, it allows for a direct comparison with theorical models that describe near-field radiative heat transfer. In the second instance, it serves as a calibrated reference that the new separation sensor can be compared to.

For sub-micrometer separations, the distance between the probe and the sample can be determined using Total Internal Reflection Microscopy (TIRM). This method has been used since 1987 [1] to measure the separation

Title photo: overview photo of the internals of the instrument with the TIRM laser on the left, the prism in the center and the beam block in the top right corner. Photo by Rogier Bos, courtesy of TNO.

between a microsphere and a flat surface in particular. The implementation of this method is, however, not without its challenges as is demonstrated in this chapter. We were unsuccesful in realizing a working TIRM setup in the available time. Therefore, this chapter focuses on the advantages and disadvantages of four potential architectures and the challenges of their implementation.

3.1 Determining separation using scattered near-field radiation

In TIRM, the prism is illuminated from the backside at an angle greater than the critical angle such that the incident light is totally reflected from the glass-to-vacuum interface as depicted in Figure 3.1. This causes an evanescent field to exist on the opposite side of this interface. When a scatterer is brought into the field, the evanescent field is scattered into the far-field and can be detected there. The intensity of the scattered light I scales with the separation z as [2]

$$I(z) = I_0 \exp\left(-\frac{z}{\delta}\right), \tag{3.1}$$

where I_0 is the intensity at zero separation and δ is the characteristic penetration depth,

$$\delta = \frac{\lambda}{4\pi n_1 \sqrt{\left(\frac{n_0}{n_1}\sin\theta\right)^2 - 1}}. \tag{3.2}$$

The penetration depth and the critical angle depend on the refractive indices of the materials at both sides of the interface n_0 and n_1. On the side of the incident beam, the material is silicon dioxide for which $n_0 = 1.4563$ at a wavelength of $\lambda = 658\,\text{nm}$ and a mean temperature of $20\,^\circ\text{C}$ [3]. On the other side there is a vacuum for which $n_1 = 1$. For this combination of materials, $\theta_{\text{cr}} = \arcsin(n_1/n_0) = 43.37^\circ$. Figure 3.2 shows the penetration depth as a function of the incident angle. For a wavelength of 658 nm, δ reaches a minimum value of 50 nm at grazing incidence, whereas values of several micrometers are possible when the angle of incidence is very close to the critical angle.

In the instrument the angle of incidence can be tuned manually using a Standa 7R128V rotation stage, which has a readability of 1° and a listed sensitivity of $0.5'$ (assuming that the knob can be turned in steps of 3° accurate). In practice, this implies that characteristic penetration depths between 260 nm and 900 nm can reasonably be achieved.

3.1.1 Attainable resolution and range of the TIRM system

The light that is scattered in the interaction of the microsphere and the evanescent field is measured using a photodetector. If the output potential of the photodetector is linear with the intensity of the collected light (and has

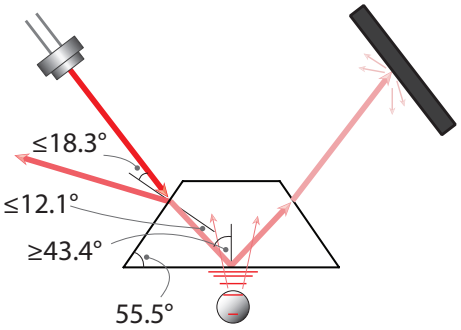

Figure 3.1: Geometry of the incident and reflected beams in the total internal reflection microscope. The incident beam is reflected off the first interface. The refracted light is incident on the glass-to-vacuum interface under total internal reflection and leaves the prism and lands on a beam block.

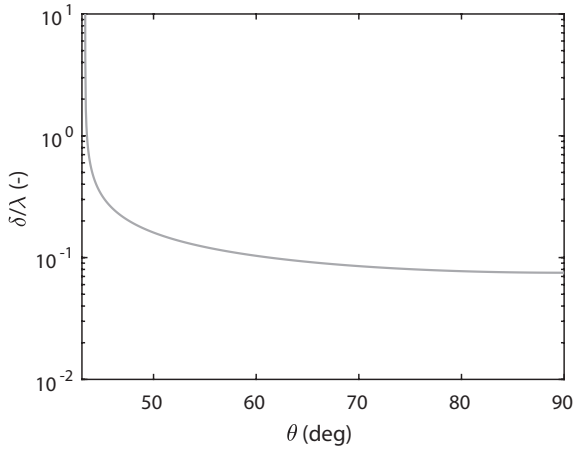

Figure 3.2: Normalized characteristic penetration depth of the evanescent field that is caused by total internal reflection of light on a silica-to-vacuum interface.

no offset at zero incident light), the output potential of the photodetector U_{PD} can be written as

$$U_{\mathrm{PD}} = U_{\mathrm{contact}} \exp\left(-\frac{z}{\delta}\right), \tag{3.3}$$

where U_{contact} is the maximum output signal that is associated with contact between the sphere and the prism.

In the absence of noise, the resolution in the distance measured with the TIRM system reads

$$\Delta z = \Delta U \left(\frac{\partial U_{\mathrm{PD}}}{\partial z}\right)^{-1} = -\delta \frac{\Delta U}{U_{\mathrm{contact}}} \exp\left(\frac{z}{\delta}\right), \tag{3.4}$$

where $\Delta U = U_{\text{range}}/2^{n_{\text{bits}}}$ using an analog-to-digital converter (ADC). The ultimate resolution is attained at contact (zero distance) and reads

$$\Delta z_{\text{ult}} = \delta \frac{\Delta U}{U_{\text{contact}}}. \tag{3.5}$$

The maximum distance at which the sphere can be detected is defined for $U_{\text{PD}} \leq \Delta U$. It is easily worked out that this happens at

$$z_{\text{ult}} = -\delta \ln\left(\frac{\Delta U}{U_{\text{contact}}}\right). \tag{3.6}$$

At this distance, however, the resolution $\Delta z = \delta$, which is not useful for the design of the system. Instead, a more useful measure of full-range is the distance at which the resolution exceeds $l\Delta z_{\text{ult}}$, where l is an arbitrary value larger than 0,

$$z_{\text{max}} = \delta \ln(l). \tag{3.7}$$

We have chosen a doubling of the resolution as a measure of the range, so that $l = 2$ and $z_{\text{max}} \approx 0.69\delta$.

To put these relations into perspective, four examples have been plotted in Figure 3.3 for the combinations of two typical ADCs with 12 bit and 16 bit resolution, respectively, with penetration depths of 50 nm at grazing incidence and 900 nm at angles of incidence close to the critical angle. Assuming an output voltage of 1.45 V at contact, a 16 bit ADC at a total range of 10 V and a decay length of 900 nm, an ultimate resolution of 0.1 nm is expected at a maximum sensitivity of $1.6\,\text{mV}\,\text{nm}^{-1}$.

To achieve this level of performance, the intensity of the scattered field has to be tuned and the means of detection have to be chosen. In the following section four architectures for the TIRM are compared.

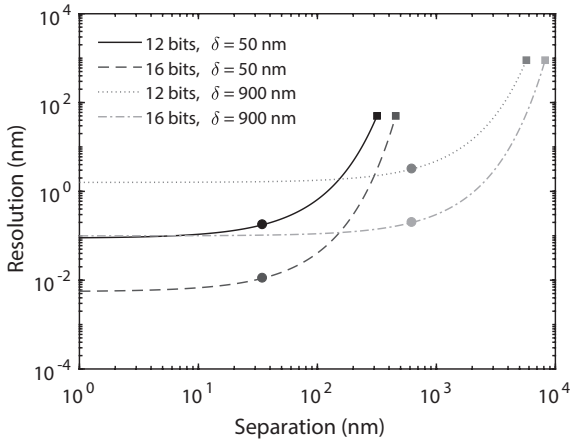

Figure 3.3: Resolution as function of separation distance and characteristic penetration depth. The circles indicate the range for which $\Delta z \leq 2\Delta z_{\mathrm{ult}}$. The squares mark the largest distance that can be detected. The shown limits are valid for a wavelength of 658 nm and an ADC range of ±5 V with a 5 % overrange.

3.2 Four architectures for capturing the scattered light

In the interaction of the sphere with the evanescent field, light is scattered in multiple directions. It is important to note here, that the scattering pattern differs from the scattering pattern caused by far-field radiation. The exact scattering behavior is determined by the size of the scatterer a relative to the wavelength λ of the light. In this case, the radius of the microsphere is used to characterize the size of the scatterer. This behavior can be categorized into roughly three domains that are separated by the values for the dimensionless parameter $x = 2\pi a/\lambda$. For $x \ll 1$ or $x \approx 1$ the scattering is called Rayleigh and Mie scattering, respectively, and depends strongly on the wavelength and the particle size. For $x \gg 1$ the scattering is called geometric and is governed by the projected area of the scatterer. The microspheres used in this setup are of size $a \approx 10\,\mu\mathrm{m}$. With a wavelength of $\lambda = 658\,\mathrm{nm}$, parameter x is approximately 95, placing the scattering well in the geometric scattering regime.

It is important to note that in the geometric scattering regime, multiple reflections between the scatterer and the prism can lead to a deviation from the assumed intensity profile of Equation (3.1). This was noticed in both the forward scattering architectures [4–6] and back-scattering architectures [2]. McKee *et al.* [2] showed that in the back-scattered direction, the collected intensity as a function of separation $I_{\mathrm{bsc}}(z)$ can be approximated well by the sum of two exponentials

$$I_{\mathrm{bsc}}(z) = I_0 \exp\left(-\frac{z}{\delta_0}\right) - I_1 \exp\left(-\frac{z}{\delta_1}\right), \tag{3.8}$$

where I_0 and I_1 are two fitting parameters that represent the contributions at contact and δ_0 and δ_1 are the decay lengths.

Bekshaev *et al.* [7] calculated the scattering pattern for the scattering of evanescent fields for all three domains and showed that for $x \gg 1$, the scattered field is strongly asymmetric in shape. In the far-field irradiance, a strong peak of scattered intensity exists in the forward scattering direction (along the cantilever length). The presence of the cantilever and its clamp, however, make this poorly accessible for detection. An architecture to measure the forward scattered radiation is presented in Section 3.2.4. Unlike the well-known scattering of propagating waves, a strong back-scattering component is also present. This direction can be accessed via the top side of the prism, as is discussed in Section 3.2.2. Light is also scattered to the sides. Detection of the scattered field perpendicular to the incident beam is possible by reusing the optics of the OBD system. This is described in Section 3.2.3. In the last of the four architectures, the scattered radiation is detected along the direction of the specularly reflected light. Section 3.2.5 discusses how scattered intensity can be measured from this direction.

3.2.1 The light source and the prism

All the system layouts below require a light source and a sample that is illuminated at total internal reflection. All layouts have the same illumination method with a wavelength of 658 nm and all use the same prism. Moreover, all layouts use a bandpass filter with a center wavelength of 660 nm and a bandwidth of 20 nm to isolate the TIRM light from the OBD, that operates at a wavelength of 635 nm.

The light emitted by a diode laser operating at a wavelength of 658 nm is coupled into a fiber and brought into the vacuum system via a vacuum-compatible optical fiber. The light is then collimated to a 2 mm beam and reflected off the glass-to-vacuum interface of the prism. The reflected light is blocked by a beam block, which is covered with a low-outgassing, space-qualified Acktar Vacuum-Black sheet, which has a hemispherical reflectance of approximately 1 % at 658 nm. This minimizes the amount of stray light that is scattered into the vacuum vessel.

The photodetector is a photo-multiplier tube (PMT) with integrated high voltage-electronics circuits. For this the Hamamatsu H11902-20 was selected with an adjustable gain, that reaches a maximum at approximately $300\,\mathrm{V\,nW^{-1}}$ at a wavelength of 658 nm.

3.2.2 Detection from the back-scattering direction

The back-scattered light can be detected from the top side of the prism. A collecting lens is placed right above the prism and the microsphere. A second lens focuses the collected light onto a photomultiplier module as depicted schematically in Figure 3.4. It allows for a large collection angle, which is mainly limited by the diameter of the optics and the space occupied by the

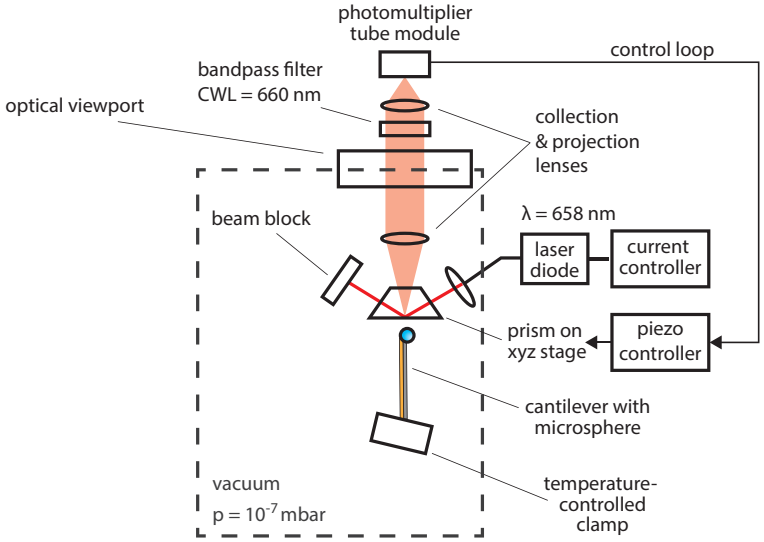

Figure 3.4: The scattered field can be collected from the same side as the incident beam.

prism. This architecture was succesfully used by McKee *et al.* [2]. It was used in favor of the more conventional detection of forward scattered radiation, because the presence of an atomic force microscopy probe prohibited detection from this direction.

This scheme was initially adopted in the instrument for its simplicity. Unfortunately, its proper functioning is impeded by the light that is scattered from the "rough" surface of the prism (see Section 6.4 for details on the roughness). Experiments show that without mitigation the scattering from the prism itself is strong enough to saturate the photodetector and effectively drown out the TIRM signal.

Reducing the surface scattering through polishing

The scattering from the rough surface can be minimized by further polishing the prism surface. As shown in Chapter 6, the roughness of the prism is $\leq 2\,\text{nm}$ r.m.s. with peaks at $0.8\,\text{nm}$ and $1.2\,\text{nm}$. The effect of polishing can be estimated using the simple relations presented by Bennet and Porteus [8], that allow the reflectivity of a surface R to be expressed as

$$R \approx R_0 \exp\left(-\frac{4\pi\sigma^2}{\lambda^2}\right), \tag{3.9}$$

as a function of the ideal reflectivity R_0, the r.m.s. roughness σ and wavelength λ. Under the assumption that the difference between R and R_0 can solely be attributed to the scattering due to the roughness, the fraction of

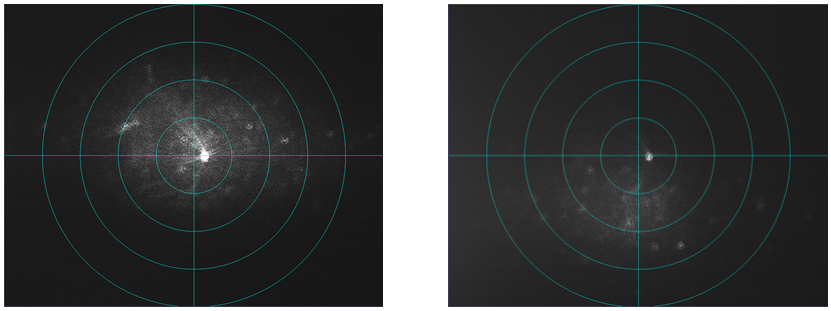

(a) (b)

Figure 3.5: Preliminary tests of scattering from the prism surface in (a) unpolarized light and (b) p-polarized light show that the scattering from the prism surface can be significantly reduced by switching from unpolarized light to p-polarization.

light that is scattered S can be written as

$$S = R_0 \left(1 - \exp\left(-\frac{4\pi\sigma^2}{\lambda^2}\right)\right). \tag{3.10}$$

At $\lambda = 658\,\text{nm}$, a reduction of σ from 2 nm r.m.s. to a realistic 0.7 nm r.m.s yields a decrease in the scattering due to roughness by a factor of ≈ 8.2. When polished to a roughness of 0.2 nm r.m.s., this reduction increases to a factor ≈ 100, at which $S \approx 1.16 \times 10^{-6}$. The latter option comes at great expense and effort and is considered unrealistic for practical application in this setup.

Reducing the surface scattering through polarization

The scattering of the surface prism is reduced by polarizing the illumination to p-polarization. Because the scattering of micron-sized spherical particles is mainly polarization-conserving - in contrast to the scattering of the scratches in the prism surface - a second polarizer can be placed in front of the photodetector to act as an analyzer. In this way the system can be biased to detect only the polarization-conserving part of the scattering [9].

Preliminary tests, in which the illuminated area of the prism was imaged onto a camera, show that the scattering of the prism surface is significantly reduced by switching to p-polarization, but is not completely eliminated. The images obtained for both unpolarized and p-polarized light are shown in Figure 3.5. The extent of the achieved reduction was not quantified, because project limitations prevented further implementation of this solution.

3.2.3 Detection perpendicular to the incident beam

As depicted in Figure 3.6, the objective lens used for the OBD system can double as a collection optic for the TIRM. By using a dichroic mirror with

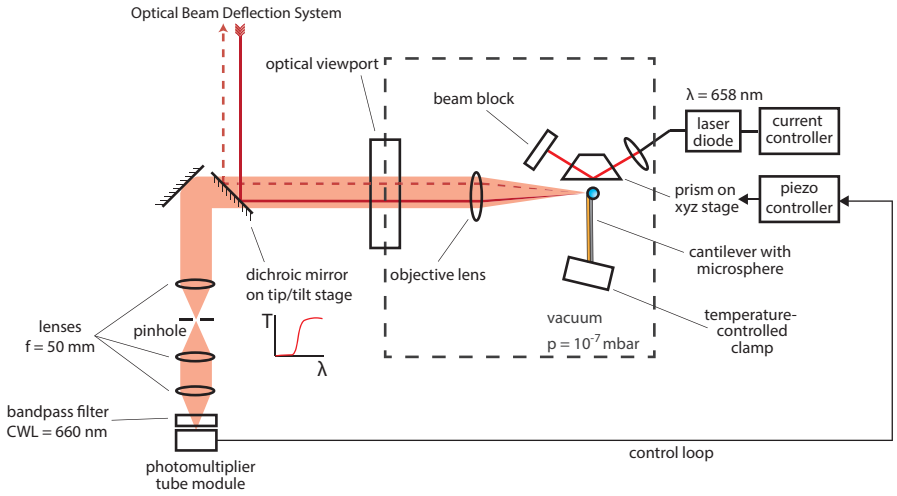

Figure 3.6: The scattered field can be collected using the objective lens used in the optical beam deflection system.

a steep separation between the reflection and the transmission bands, the TIRM and OBD signals can be separated. An additional bandpass filter is installed in front of the photodetector, to further suppress unwanted light sources. The field of view of the TIRM system is limited by placing a pinhole in the detection path and using relay optics to image the pinhole onto the detector. In this way, the steering mirrors of the OBD system can be used to position the OBD beams onto the cantilever, while the pinhole can be used to select the field-of-view of the TIRM system independently.

This geometry does not require additional optics inside the vacuum system and reduces the amount of light captured from spurious scattering of the prism surfaces. However, as shown by Bekshaev *et al.* [7], a collection half-angle larger than 30° (NA ≥ 0.5) is required to capture any light scattered by the microsphere. The numerical aperture NA can be approximated using the the diameter of the optics D, the focal length f of the objective lens and the refractive index n as

$$\mathrm{NA} \approx \frac{nD}{2f}. \tag{3.11}$$

Using the standard 1 in. diameter optics used for the OBD system and a focal length of 50 mm, the numerical aperture is limited to approximately 0.25. To increase it to the required level of ≥ 0.5, either the focal lengths needs to be reduced to half, or the diameter of the objective lens needs to be increased to double its value. Because the sensitivity of the OBD system is directly proportional to the focal length of the objective lens (see Equation (2.33)), a reduction of the focal length is highly undesirable. An increase of the diameter of the optics is achievable and can be attained with standard commercial off-the-shelf components. However, the mechanical design of the system has to

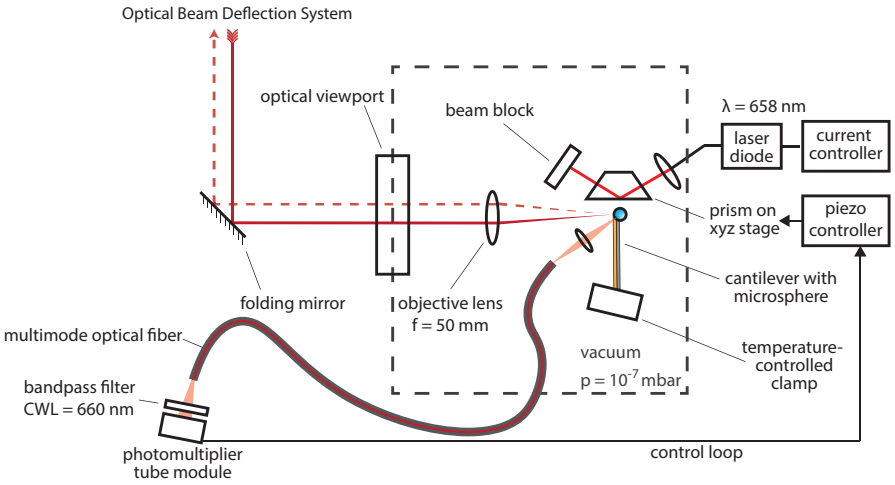

Figure 3.7: The scattered field is measured in the same plane as the incident beam on the vacuum side of the interface.

be changed to accomodate the larger diameter of the optics, which was not possible within the contraints of the project.

3.2.4 Detection in the forward scattering direction

The scattering is strongest in the forward scattering direction and is mainly confined to the plane of the illumination. A small collecting lens can be placed in this plane underneath the prism. This brings the detection into the plane of highest scattering intensity. Because the photomultiplier module is not vacuum-compatible, a lens is required to couple the light into a multimode fiber, that transports the light to the PMT, which resides outside of the vacuum system. Using a bandpass filter (Chroma MV660/20), spurious light of the OBD system ($\lambda = 635\,\mathrm{nm}$) can be separated from the light of the TIRM ($\lambda = 658\,\mathrm{nm}$). This architecture is schematically depicted in Figure 3.7. Because of volume constraints around the cantilever, its clamp and the prism, the collecting optics have to be small and positioned relatively far away from the sphere. This severely limits the attainable collection angle and thus the collected intensity.

3.2.5 Detection in line with the specular reflection

In 2010, Eremina *et al.* [10, 11] proposed to measure the scattered along the direction of the specularly reflected light. The specular reflection is blocked from reaching the photodetector by applying a central mask in the aperture of the collection optics. This layout is shown in Figure 3.8. The specular reflection is several orders of magnitude stronger than the scattered light and needs to be suppressed. The central cut required in the aperture to achieve

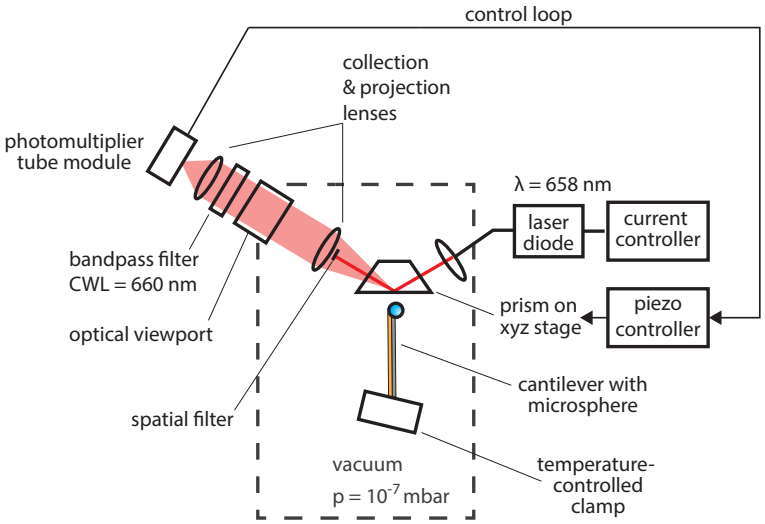

Figure 3.8: The power of the reflected illumination light is measured to determine the separation between the prism and the microsphere.

this also blocks the scattered light and thus needs to be kept as small as possible. This requires the beam width to be as small as possible, while remaining large enough to create a flat wavefront near the sphere. Eremina *et al.* show numerically that detection from this direction removes the oscillations in the scattered intensity, that are sometimes observed in TIRM measurements that rely on detection from the forward scattering direction. The resulting signal decreases monotonically with increasing separation so that a one-to-one relation is established.

In the available literature, no practical implementation of this technique was found. It is also sensitive to the scattering from the prism itself (see Section 3.2.2) and requires measures to suppress the scattering of the prism surface. It offers no additional advantages in addition to removing the oscillations in intensity that can be seen in other layouts.

3.3 Conclusions

TIRM is a tried method for measuring the separation between microspheres and a flat surface. However, its implementation next to the OBD system in this instrument is not straightforward and we have been unable to realize a working TIRM system in the available time. Because of volume restrictions, detection in the forward-scattering direction is difficult and requires the use of optics with a small numerical aperture and thus a reduces collected intensity. Detection from the scattered intensity perpendicular requires optics with a large numerical aperture that cannot be realized in the available volume without penalizing the OBD detection system. Detection from the back-scattered

direction suffers from the high intensity scattering caused by the roughness of the prism itself. This can be reduced by polishing the prism to a lower roughness, and adding additional polarizing optics. These changes can be made in locations that are further removed from the actual probe (where the available volume is limited). It therefore remains the most suitable solution for this instrument.

Acknowledgments

The author thanks Dr. Laurent Helden of the University of Stuttgart and Dr. Stefan Bäumer of TNO for fruitful discussions on the implementation of Total Internal Reflection Microscopy and the associated scattering from the prism surface.

Bibliography

[1] D. C. Prieve, F. Luo, and F. Lanni. Brownian motion of a hydrosol particle in a colloidal force field. *Faraday Discussions of the Chemical Society*, 83:297, 1987.

[2] C. T. McKee, S. C. Clark, J. Y. Walz, and W. A. Ducker. Relationship between Scattered Intensity and Separation for Particles in an Evanescent Field. *Langmuir*, 21(13):5783–5789, 2005.

[3] I. H. Malitson. Interspecimen Comparison of the Refractive Index of Fused Silica. *Journal of the Optical Society of America*, 55(10):1205, 1965.

[4] D. C. Prieve and J. Y. Walz. Scattering of an evanescent surface wave by a microscopic dielectric sphere. *Applied Optics*, 32(9):1629, 1993.

[5] L. Helden, E. Eremina, N. Riefler, C. Hertlein, C. Bechinger, Y. Eremin, and T. Wriedt. Single-particle evanescent light scattering simulations for total internal reflection microscopy. *Applied Optics*, 45(28):7299, 2006.

[6] C. Hertlein, N. Riefler, E. Eremina, T. Wriedt, Y. Eremin, L. Helden, and C. Bechinger. Experimental verification of an exact evanescent light scattering model for TIRM, 2008.

[7] A. Y. Bekshaev, K. Y. Bliokh, and F. Nori. Mie scattering and optical forces from evanescent fields: A complex-angle approach. *Optics Express*, 21(6):7082, 2013.

[8] H. E. Bennett and J. O. Porteus. Relation Between Surface Roughness and Specular Reflectance at Normal Incidence. *Journal of the Optical Society of America*, 51(2):123, 1961.

[9] L. Helden. Private Communication, 2019.

[10] E. Eremina, Y. Eremin, N. Grishina, and T. Wriedt. Total internal reflection microscopy: examination of competitive schemes via discrete sources method. *Journal of Optics*, 12(9):095703, 2010.

[11] N. Grishina, E. Eremina, Y. Eremin, and T. Wriedt. Modelling of different TIRM setups by the Discrete Sources Method. *Journal of Quantitative Spectroscopy and Radiative Transfer*, 112(11):1825–1832, 2011.

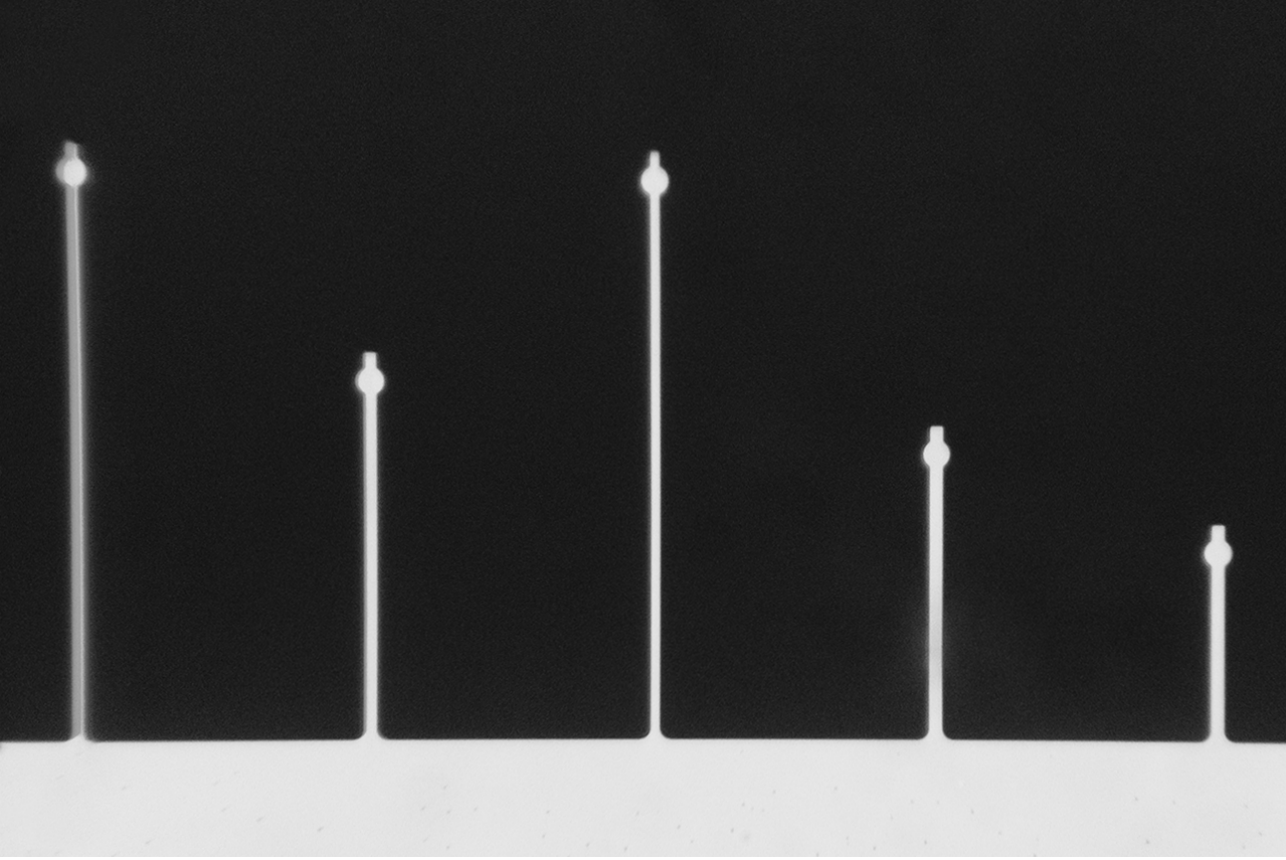

4. Design of a calorimeter for near-field heat transfer measurements and thermal scanning probe microscopy

4.1 Introduction

In 1969, Hargreaves [1] published a seminal paper on what he called "anomalous radiative transfer between closely spaced bodies". His measurements confirmed the predictions of Rytov's theory of fluctuational electrodynamics [2, 3], which were later further developed by Polder and Van Hove [4]. This effect, in which the heat flux increases rapidly with diminishing separations and exceeds the black-body limit due to near-field effects has since then been observed and quantified by several research groups. The measurement

Title picture: optical micrograph of the five cantilever designs. Micrograph by Roy Bijster. Parts of this chapter have been published in Review of Scientific Instruments **92**, 025008 (2021).

systems employed for this measurement can be roughly classified into three archetypes: (1) two closely spaced parallel plates in which one plate is kept at a constant temperature, while the temperature of the other is measured as a function of their separation [5–24]; (2) a miniature thermocouple scanning over a surface in which the temperature of the tip is measured as a function of separation [25–31] and (3) a thermo-mechanical probe scanning over a surface in which the deformation of the probe is used to determine the probe temperature or the heat flux [32–37].

Closely spaced parallel plates are ideal to mimic the conditions described in theoretical work and can be used to study applications such as thermophotovoltaics and photonic cooling [22]. They benefit from large interacting surfaces and the associated larger signals. In general, however, the required degree of parallelism is difficult to obtain at smaller separations. Miniature thermocouples and thermo-mechanical probes are generally easier to implement experimentally and can measure local variations in the thermal conductance. Moreover, probe-based techniques are less sensitive to alignment errors at smaller separations than parallel plates and offer shorter response times due to the smaller thermal capacitance of the probes. This allows their use for applications in scanning probe microscopy. The sensitive area of probes with integrated thermocouples is typically very small, making them suitable for thermal scanning probe microscopy applications with high spatial resolution. Heating elements are easily integrated in the probe during manufacturing. The thermo-mechanical probes, however, can be simple to manufacture and require no additional patterning steps. The size of the interacting area and its material can be tuned after manufacturing of the probe, by attaching different sizes of spheres. As no heating elements are typically integrated in the probe, the temperature needs to be controlled by external means and the achievable performance has a greater interaction with the supporting systems.

When using a thermo-mechanical probe, a glass microsphere is attached to the free end of a multilayer probe. The heat transfer occurs between the sphere and the sample, while the probe is used as a transducer. Because the layers expand at distinct rates, the thermal load results in a mechanical deformation, which can be measured using the optical beam deflection (OBD) method [38]. In this method, light is reflected off the reflective coating of the probe onto a position sensitive detector (PSD). The local rotation of the probe results in a shift of the spot on the PSD, as is shown schematically in Figure 4.1. In many instances, a probe with a triangular plan form, silicon nitride base and a gold reflective coating on one side is used. From the commercially available options, Wanders [39] identified the Bruker/Veeco MLCT-C probe as one of the most sensitive options for this specific measurement. Others have used very similar probes by other manufacturers, which are very comparable in terms of the dimensions and used materials [32–34].

When considering the entire measurement system, the sensitivity of the output signal of the PSD as the result of a flux P absorbed at the tip of the

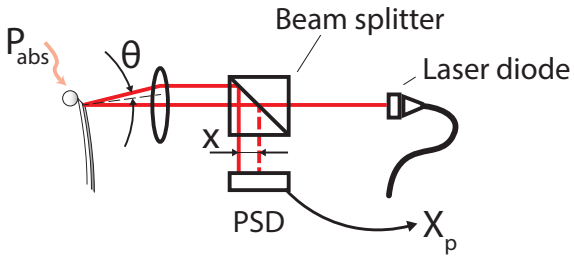

Figure 4.1: Schematic representation of a confocal optical beam deflection system. A laser beam is reflected off a rotated cantilever. Via a lens the rotation of the beam is translated into a shift on the position sensitive detector.

probe can be written as

$$\frac{\partial X_\mathrm{p}}{\partial P} = \frac{\partial X_\mathrm{p}}{\partial x}\frac{\partial x}{\partial \theta}\frac{\partial \theta}{\partial P}, \tag{4.1}$$

where X_p is the output of the PSD, x is the location of the spot on the PSD, and θ is the (local) rotation of the cantilever. While the first two terms, $\partial X_\mathrm{p}/\partial x$ and $\partial x/\partial \theta$, are specific to the design of the OBD system, the sensitivity $\partial \theta/\partial P$ can be designed separately by choosing the materials and dimensions of the cantilever.

Commercially available probes are not optimized for use as thermo-mechanical transducers. Probes that are designed specifically for this purpose can have a higher sensitivity and improved noise performance. Moreover, the performance of the measurement system can be improved further by considering the probe as an integral part of the system. For example, the sensitivity $\partial X_\mathrm{p}/\partial x$ is directly proportional to the intensity of the light incident on the PSD. This intensity is affected by the reflectance of the probe. Therefore, there is a need for cantilever probes that are designed for the particular purpose of measuring heat transfer at small separations and for which the interrelations with the measurement system are considered.

Bilayer cantilever probes have previously been designed and optimized for calorimetry applications with picowatt and femtojoule resolutions [40–42]. However, these designs consider only the cantilevers and the lock-in techniques used to measure their behavior. They do not consider the steady-state performance or the interrelations between the cantilever design and system performance. Moreover, they do not consider the presence of a microsphere at the free end of the cantilever either.

In this chapter, cantilever probe designs are presented that are dedicated to measuring near-field radiative heat transfer under vacuum conditions. In contrast to previous designs of thermo-mechanical probes, the optical contribution of the probe to the measurement system is taken into account, as well as thermal drift of the clamp. Moreover, the effects of the microsphere are considered. The designed probes have been manufactured and are benchmarked numerically and experimentally against the Bruker MLCT-C. The

resulting cantilever probes are shown numerically and experimentally to have significantly improved performance compared to the benchmark.

4.2 Designing the cantilever

The dimensions of the cantilever as used throughout this chapter are schematically indicated in Figure 4.2. The layer thicknesses t_i, the width w and the length L are chosen under multiple design contraints. A sphere is attached to the free end of the cantilever, which is perpendicular to the sample. The sphere and the sample are separated by a distance g.

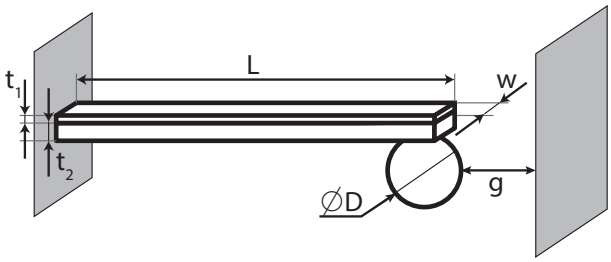

Figure 4.2: Schematic representation of calorimeter consisting of a bilayer cantilever that is clamped at one end and has a microsphere at its free end. The relevant dimensions of length, width and thicknesses are indicated. The subscripts 1 and 2 refer to the reflective coating and the substrate, respectively.

The sensitivity of the probe can be written as

$$\frac{\partial\theta}{\partial P} = \frac{L^2}{wt_2^2}\Gamma, \tag{4.2}$$

where Γ is an auxiliary term (unit of W^{-1}) that contains the relevant material properties and the ratio of layer thicknesses h:

$$\Gamma = \frac{3hm\Delta\alpha}{hk_1 + k_2}\left(\frac{1+h}{1+2hm\,(2+3h+2h^2)+h^4m^2}\right), \tag{4.3}$$

where $h = t_1/t_2$, $m = M_1/M_2$, $M_i = E_i/(1-\nu_i)$ and $\Delta\alpha = \alpha_1 - \alpha_2$ is the difference in the coefficients of thermal expansion. In this relation, E_i and ν_i are the Young's modulus and the corresponding Poisson ratio for layer i, and k_i is the associated thermal conductivity. The derivation of these equations is provided in Section 2.2.

From Equation (4.2) and Equation (4.3), it follows that the parameter L^2/w, the layer thickness t_2 (or t_1) and the thickness ratio h (through Γ) can be chosen independently to tune the sensitivity of the probe.

4.2.1 Choosing the layer thicknesses

The layer thicknesses tie into two parameters of the system sensitivity given by Equation (4.1): the sensitivity of the PSD signal to beam shift $\partial X_\mathrm{p}/\partial x$,

Table 4.1: Complex refractive indices at a wavelength λ of 635 nm for the studied thin films.

Material	Refractive index	Source
Gold, Au	$0.18016 + 3.4531\mathrm{i}$	Johnson and Christy [46, 47]
Aluminium, Al	$1.4622 + 7.5592\mathrm{i}$	Rakić [47, 48]
Silicon, Si	$3.8787 + 0.019221\mathrm{i}$	Aspnes and Studna [47, 49]
Silicon Nitride, Si_3N_4	2.022	Filmetrics [50]
Silicon Dioxide, SiO_2	1.457	Malitson [51]
Silicon Carbide, SiC	2.635	Filmetrics [52]

and the sensitivity of cantilever rotation to absorbed power $\partial\theta/\partial P$. The former is directly proportional to the amount of reflected light and benefits from a high reflectivity of the cantilever [43]. The reflectivity is predominantly determined by the thickness of the coating and is very sensitive to thickness variations at thin layers. The sensitivity $\partial\theta/\partial P$, on the other hand, can be tuned by other parameters. For these reasons, a two-step approach is chosen in which the minimum layer thickness is determined that maximizes the reflectance and that is robust against the small variations in thickness that arise from manufacturing tolerances. The thickness ratio h is chosen separately to maximize Γ. Combined, these yield the required substrate thickness.

Coating thickness for maximum reflectance

To determine the required coating thickness for maximum reflectance, the cantilever is modeled as a one-dimensional stratified medium consisting of a (thin) reflective coating on top of a (thick) substrate. Using the Fresnel equations and the Transfer Matrix Method (TMM) [44, 45], the reflectance and transmittance of this structure are calculated. The absorptance then follows from conservation of energy. The values for the complex refractive indices ($n = n' + \mathrm{i}\kappa$) of the considered materials are listed in Table 4.1 for a wavelength of $\lambda = 635\,\mathrm{nm}$.

The results of the TMM simulation for eight material combinations are shown in Figure 4.3 to Figure 4.5. The combinations consist of a gold or aluminium coating on top of a silicon, silicon dioxide, silicon nitride or silicon carbide substrate. Furthermore, the thickness ratios 0.1, 0.25 and 0.5 are considered for each combination.

In all cases, two clear branches can be distinguished as soon as bulk properties are attained. In that case, a gold coating outperforms an aluminium coating in terms of reflectance at equal thickness and equal thickness ratio. Moreover, as soon as bulk properties are attained, the substrate material becomes inconsequential for the reflectance.

For a gold coating, the reflectance is independent of layer thickness for $t_1 \geq 110\,\mathrm{nm}$ irrespective of the thickness ratio. Although almost similar reflectance can be obtained for lower thicknesses, the results are less robust

against manufacturing errors due to (strong) local dips in the reflectance at lower thickness ratios.

For aluminium coatings and thickness ratios of 0.25 and 0.5, a coating thickness of 35 nm on top of a silicon substrate suffices to attain a reflectance that is independent of coating thickness. For the lower thickness ratio of 0.1, a minimum coating thickness of 50 nm is required for the same effect.

Choosing the thickness ratio

A high sensitivity is attained by maximizing parameter Γ, which is plotted as a function of the thickness ratio h in Figure 4.6. It is important to note that, similar to Lai *et al.* [41], the thickness ratio h is found under the assumption that the material properties are independent of film thickness. The validity of this assumption is moot, as in practice these effective material properties can be strongly dependent on film thickness before reaching the bulk values (see, e.g., Abazari *et al.* [53] for the case of the elastic modulus). However, processing conditions seem to be equally, if not more, important contributors to the *effective* material parameters [54] and can vary with processing parameters from foundry to foundry. Because accurate data on the relation between material properties and the layer thickness is unavailable, the bulk values or the generally accepted values for thin films are used for this design. The used values are listed in Table 4.2 on page 76.

For all thickness ratios of practical interest ($h \leq 1$), combinations with an aluminium coating perform significantly better than the gold-coated counterparts. This is a direct consequence of the higher coefficient of thermal expansion of aluminium. The values of Γ are highest for combinations with a silicon dioxide substrate. However, the Young's modulus of SiO_2 is significantly lower than that of Si_3N_4 and SiC, making them comparatively compliant at equal h. To illustrate this, the spring constant C of the cantilevers is written as

$$C = \frac{3EI}{L^3} = \frac{wt^3}{4L^3}\Psi, \tag{4.4}$$

with $t_2 = \frac{t}{1+h}$, $t = t_1 + t_2$ and Ψ is

$$\Psi = \frac{hE_1E_2}{(1+h)^3(hE_1+E_2)}\left(4 + 6h + 4h^2 + \frac{E_1}{E_2}h^3 + \frac{E_2}{E_1}\frac{1}{h}\right). \tag{4.5}$$

This effective Young's modulus is shown as a function of the thickness ratio in Figure 4.7. At equal thickness ratio h, combinations with a Si_3N_4 substrate are up to 4.2 times stiffer than the SiO_2 alternatives. To achieve a practical bending stiffness, a silicon nitride substrate with an aluminium coating was selected as the next best alternative.

A coating thickness of $t_1 = 100$ nm was used to ensure a sufficiently stiff cantilever with an optical performance that is robust against small variations in the layer thicknesses. With Γ at its maximum value for this combination at $h \approx 0.32$ it follows that $t_2 = 310$ nm.

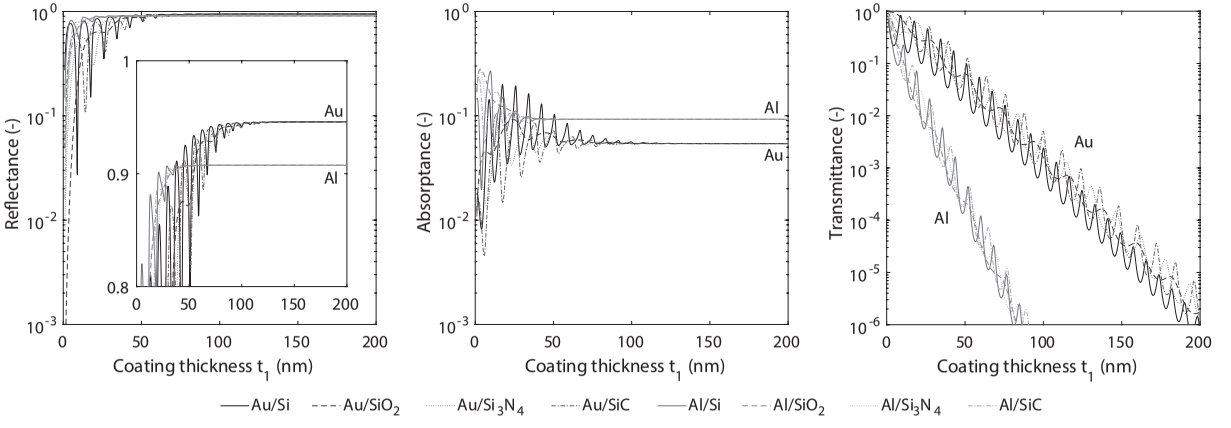

Figure 4.3: Absorptance, transmittance and reflectance for different coating and substrate combinations, thickness ratio $h = 0.1$.

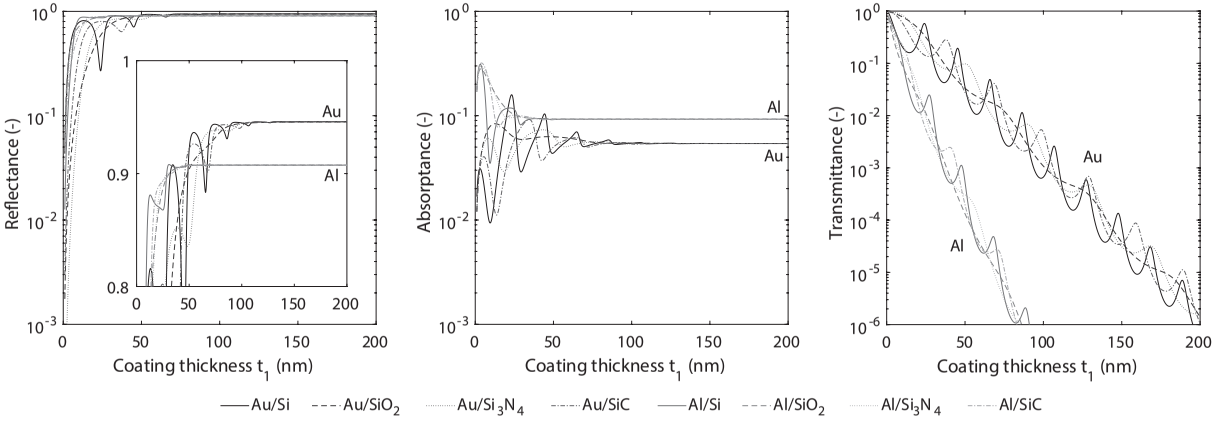

Figure 4.4: Absorptance, transmittance and reflectance for different coating and substrate combinations, thickness ratio $h = 0.25$.

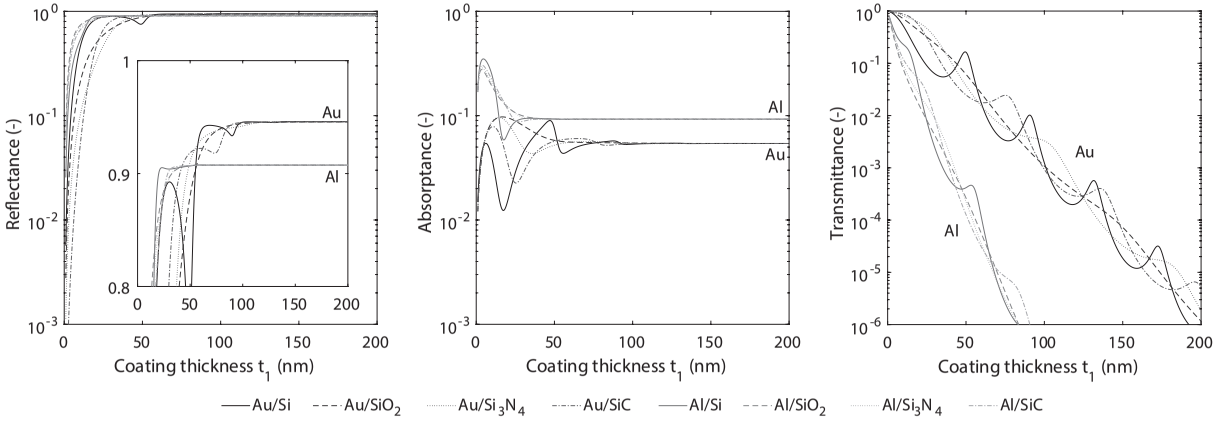

Figure 4.5: Absorptance, transmittance and reflectance for different coating and substrate combinations, thickness ratio $h = 0.5$.

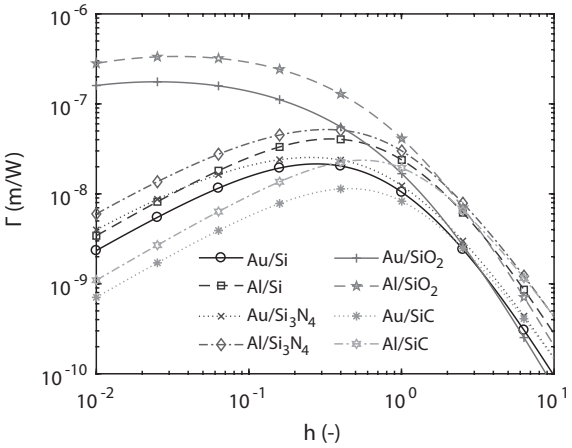

Figure 4.6: Auxiliary term Γ for the rotation of a cantilever beam at its tip as a function of $h = t_1/t_2$. Note: markers do not correspond to datums, but are used to identify the lines.

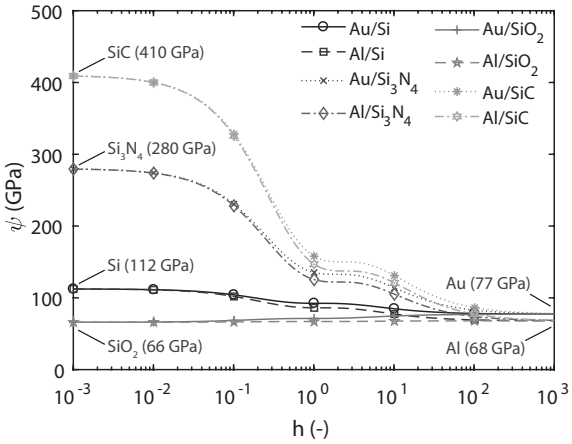

Figure 4.7: Effective Young's modulus Ψ as a function of the ratio of layer thicknesses $h = t_1/t_2$. In all cases, Ψ is dominated by the choice in substrate material. The choice for a coating material is of little influence in comparison. Note: markers do not correspond to datums, but are used to identify the lines.

4.2.2 Choosing the length and width

Following Equation (4.2), the sensitivity $\frac{\partial\theta}{\partial P}$ follows from appropriate values for the length and width of the cantilever, as well as the thickness of the substrate. The aspect ratio of the cantilever is constrained by the performance of the optical beam deflection system and the data-acquisition system (DAQ), and the requirements on resolution, noise contributions, and spring stiffness.

As per Equation (4.1), the sensitivity of the OBD is the product of the three sensitivities $\partial X_p/\partial x$, $\partial x/\partial\theta$ and $\partial\theta/\partial P\,(L)$. The first two are deter-

Table 4.2: Material properties used for optimization of the cantilever dimensions.

Property	Au [55]	Si [56]	Al [57]	Si_3N_4	SiO_2 [58]	SiC [59]
E (GPa)	77.2	112.4	68	280 [60, 61]	66	410
ν $(-)$	0.42	0.28	0.36	0.20 [60, 61]	0.17	0.14
k $\left(\mathrm{W\,m^{-1}\,K^{-1}}\right)$	301	124	210	30.1 [62]	1.1	120
α (ppm/K)	14.4	2.5	24	2.8	0.56	4
ρ $\left(\mathrm{kg\,m^{-3}}\right)$	19320	2329	2699	3187 [62]	2270	3100
c $\left(\mathrm{J\,kg^{-1}\,K^{-1}}\right)$	128	713	900 [62]	673 [63]	680	750

mined in the optical design and are limited by the practical limitations of the available hardware. The latter is set by the cantilever according to Equation (4.2). The smallest detectable change in the output potential of the PSD is

$$\Delta U_{\mathrm{DAQ}} = \frac{U_{\mathrm{range}}}{2^{n_{\mathrm{bits}}}}, \tag{4.6}$$

where U_{range} is the full range of the data-acquisition system and n_{bits} is the (effective) number of bits available in the analog-to-digital converter. From this the required value of $\partial X_p/\partial P$ is obtained as

$$\left.\frac{\partial X_p}{\partial P}\right|_{\mathrm{reqt}} = \frac{\Delta U_{\mathrm{DAQ}}}{\Delta P_{\mathrm{resolution}}}, \tag{4.7}$$

where $\Delta P_{\mathrm{resolution}}$ is the required static resolution of the calorimeter. The corresponding sensitivity of the cantilever is then obtained as

$$\left.\frac{\partial \theta}{\partial P}\right|_{\mathrm{reqt}} = \left.\frac{\partial X_p}{\partial P}\right|_{\mathrm{reqt}} \left(\frac{\partial X_p}{\partial x}\frac{\partial x}{\partial \theta}\right)^{-1}. \tag{4.8}$$

To create an envelope that is bounded by the design constraints, the constraints are written as functions of the form L^n/w. For the required sensitivity of Equation (4.2), this can be rewritten as

$$\frac{L^2}{w} = \frac{t_2^2}{\Gamma}\left.\frac{\partial \theta}{\partial P}\right|_{\mathrm{reqt}}, \tag{4.9}$$

and imposes a lower limit on L^2/w. Additional constraints are imposed by the thermal noise and the sensitivity to fluctuations in the base temperature.

The temperature of the cantilever clamp will in practice drift over time and will be known with limited accuracy. A change in temperature at the clamped end of the cantilever (the base) ΔT_{base}, affects the temperature distribution over the entire cantilever length, and thus the cantilever rotation and deflection. With the OBD method, this effect and the effect of a heat input at the free end of the cantilever cannot be distinguished. The corresponding uncertainty in the measured thermal input can be written as the

product of the uncertainty in the clamp temperature ΔT_{base} and the conductance G

$$\Delta \hat{P}\Big|_{\Delta T_{\text{base}}} = 2G\Delta T_{\text{base}}. \tag{4.10}$$

This can be rewritten to a corresponding constraint on the aspect ratio of the cantilever,

$$\frac{w}{L} = \frac{1}{t_1 k_1 + t_2 k_2} \frac{\Delta \hat{P}\Big|_{\Delta T_{\text{base}}}}{2\Delta T_{\text{base}}}, \tag{4.11}$$

where k_i is the thermal conductivity of the respective layers.

In a similar fashion, the uncertainty in the measured thermal input is limited by the Brownian motion of the cantilever and can be quantified as

$$\Delta \hat{P}_{\text{noise}} = \frac{2}{\Gamma}\sqrt{\frac{k_{\text{B}}}{EI}} \frac{wt_2^2}{L\sqrt{L}} \sqrt{T_{\text{avg}}}. \tag{4.12}$$

This can be rewritten for the constraint on length and width and their effects on the equivalent thermal noise. For this, either the tip temperature needs to be assumed constant for each cantilever (irrespective of the dimensions), or the incident laser power is assumed constant. Under the assumption that the incident laser spot is small enough to completely fit on the cantilever, a constant laser power is preferred as this makes the optical power reflected to the PSD independent of the cantilever.

Under vacuum conditions with heat added at the free end of the cantilever, a linear temperature distribution ($T_{\text{avg}} = P_{\text{abs}}/(2G) + T_{\text{base}}$) results. From Equation (2.4) and Equation (4.12) it then follows that

$$w = \frac{c_1 L^3 - P_{\text{abs}} L}{c_2}, \tag{4.13}$$

where P_{abs} is the absorbed laser power, and

$$c_1 = \frac{\Delta \hat{P}\Big|_{\text{thermalnoise}}^2 \Gamma^2 h E_1 E_2 K_1 (hk_1 + k_2)}{24 k_{\text{B}} (hE_1 + E_2)}, \tag{4.14}$$

$$c_2 = T_{\text{base}} t_2 (hk_1 + k_2). \tag{4.15}$$

The equations above describe a set of cantilevers that meet all the thermomechanical requirements and constraints. For a high measurement sensitivity, the cantilevers in this set are typically long, slender and very thin. At the same time, these cantilevers tend to be very compliant and difficult to handle in practice, e.g. during installation into the measurements setup and while gluing spheres to their tips. Therefore, a minimal spring constant of $1\,\text{mN}\,\text{m}^{-1}$ is introduced to minimize handling issues. Although significantly more compliant cantilevers [64] are available for scanning probe microscopy, these are typically intended for axial mechanical loading rather than bending.

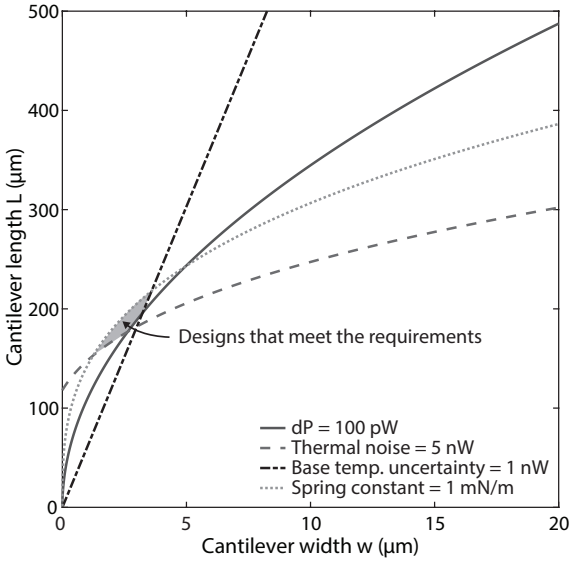

Figure 4.8: Required cantilever aspect ratio to meet the design requirements and constraints. The region of feasible designs is constrained from above by the minimum spring constant and from below by the minimum flux resolution, the thermal noise constraint and the base temperature uncertainty. Results for Al coating on Si_3N_4, 2 mW incident laser power, 9.3% absorptance, $T_{\mathrm{base}} = 298.15\,\mathrm{K}$ and $\Gamma = 5.2 \times 10^{-8}\,\mathrm{m\,W^{-1}}$.

In bending, a spring constant of $1\,\mathrm{mN\,m^{-1}}$ is considered a realistic minimum based on practical experience. This introduces a constraint of the form w/L^3 of

$$\frac{w}{L^3} = \frac{4C\,(t_1E_1 + t_2E_2)}{t_2^3 t_1 E_2 E_1 K_1}. \tag{4.16}$$

These requirements and constraints are combined in Figure 4.8 to form a set of feasible designs. The region of feasible cantilevers is constrained from above by the minimum spring constant ($1\,\mathrm{mN\,m^{-1}}$) and from below by the minimum measurement resolution (100 pW), the thermal noise constraint (5 nW equiv.) and the base temperature uncertainty (1 nW equiv.).

4.2.3 Selected cantilever dimensions

The cantilever dimensions that follow from the design procedure are listed in Table 4.3 on page 80 under column A. Three additional designs are included with increasing spring constants, while performance gets incrementally worse. Figure 4.9 shows an optical micrograph of the realized cantilevers. The designs are from hereon referred to as Cantilevers A to D.

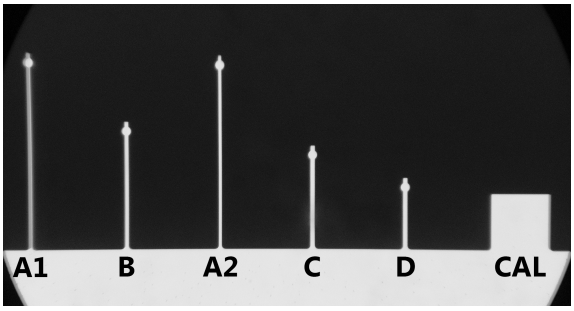

Figure 4.9: Optical micrograph of the manufactured cantilevers, labeled according to Table 4.3. The square on the right labeled CAL is used for measuring the optical properties of the cantilevers and has the same layer thicknesses as the probes.

Table 4.3: Nominal dimensions and calculated performance parameters for optimized cantilevers. All cantilevers have a silicon nitride substrate of 309 nm thick and an aluminium reflective coating of 100 nm thick on one side. The resonance frequency f_{L} is calculated assuming a 20 µm diameter silica sphere is attached at the free end.

Parameter	**A**	**B**	**C**	**D**
Length L (µm)	208	137	112	77
Width w (µm)	3.4	4.5	5.0	4.8
Spring constant C $\left(\mathrm{mN\,m^{-1}}\right)$	1.1	5.2	11	31
Conductance G $\left(\mathrm{W\,K^{-1}}\right)$	5.3×10^{-7}	1.1×10^{-6}	1.4×10^{-6}	2.0×10^{-6}
Rotation sensitivity $\frac{\partial \theta}{\partial P}$ $\left(\mathrm{W^{-1}}\right)$	6.9×10^{3}	2.3×10^{3}	1.4×10^{3}	6.7×10^{2}
Deflection sensititivy $\frac{\partial z}{\partial P}$ $\left(\mathrm{m\,W^{-1}}\right)$	4.8×10^{-1}	1.0×10^{-1}	5.1×10^{-2}	1.7×10^{-2}
Equivalent thermal noise (equal average temperature) $\left(\mathrm{nW\,K^{-1/2}}\right)$	0.27	0.57	0.82	1.4
Equivalent thermal noise (equal absorbed power) $\left(\mathrm{W^{1/2}}\right)$	3.7×10^{-7}	5.4×10^{-7}	6.9×10^{-7}	9.9×10^{-7}
Thermal time constant (cantilever only) τ (ms)	0.41	0.18	0.12	0.057
Thermal bandwidth $1/(5\tau)$ (kHz)	0.48	1.1	1.7	3.5
First resonance frequency (no sphere) f_1 (kHz)	11.4	26.3	39.3	83.0
First resonance frequency (with sphere) f_{L} (kHz)	1.58	3.41	4.87	8.40

4.3 Benchmarking against Bruker MLCT-C

To compare the designed cantilevers to the commercially available alternatives, the results are benchmarked against the Bruker MLCT-C. As explained before, this cantilever and very similar alternatives from other manufacturers were used by other groups for measuring the near-field heat transfer [32–34, 39], making it a relevant benchmark. A micrograph of this probe including its dimensions is shown in Figure 4.10.

The thermo-mechanical model presented in the previous sections is valid only for a rectangular cantilever with a rectangular cross-section and cannot be used directly for the triangular MLCT-C probe. In contrast to Wanders' effective-width method used to evaluate the MLCT-C, the probe is here modelled using a finite element model in COMSOL Multiphysics. This model is used to calculate the temperature gradients and the resulting mechanical deformation. The geometry of the MLCT-C probe, with its two separated legs that are joined in a triangular section at the free end, causes a non-linear temperature profile along the cantilever length as depicted in Figure 4.11. In the effective-width method of Wanders, a linear temperature profile is assumed that results in an overestimation of the deflection and rotation sensitivities.

For both the Bruker MLCT-C and the designed cantilevers, the tip temperature, the tip rotation and the tip deflection were calculated as a function of the heat flux absorbed at the probe tip. The results of these simulations are shown in Figure 4.12 and are used to calculate the effective conductances, as well as the sensitivities of rotation and deflection to heat input. Table 4.4 on page 84 presents a direct comparison between the MLCT-C and the designed Cantilever A, the latter of which is 41× more sensitive.

To compare the thermal noise levels of the designs, Equation (4.12) is used to calculate the temperature-normalized equivalent thermal noise

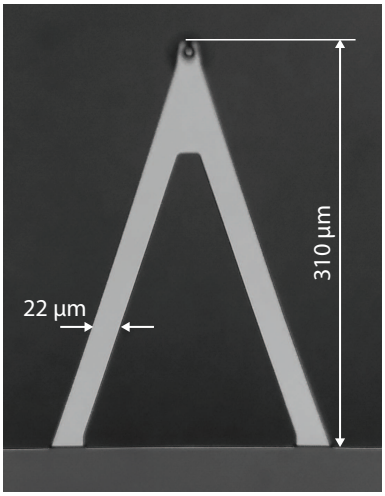

Figure 4.10: Micrograph of the Bruker MLCT-C probes with specified dimensions. The probe consists of a 0.55 µm thick silicon nitride substrate, a 40 nm thick gold reflective coating and a 5 nm thick titanium adhesion layer. All dimensions used in the finite element model were measured relative to the dimensions indicated in the micrograph.

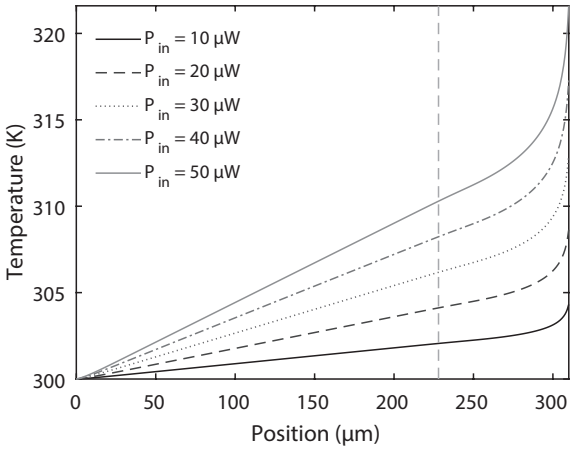

Figure 4.11: Calculated temperature profiles for the Bruker MLCT-C probes. The temperature at the clamped end is modeled to be constant at 300 K. The mentioned power values represent the heating power absorbed by the cantilever, not the incident power. The vertical line indicates the location where the two legs are joined and form a triangle from thereon to the free end. The 5 nm Ti adhesion layer is ignored.

$(\Delta\hat{P}_{\mathrm{noise}}/\sqrt{T_{\mathrm{avg}}})$ (integrated over all frequencies). This probe parameter can be used to estimate the equivalent thermal noise at infinite bandwidth (expressed in the measured flux), for equal average temperatures. It is estimated at $2.3\,\mathrm{nW\,K^{-1/2}}$ and $0.27\,\mathrm{nW\,K^{-1/2}}$ for the MLCT-C and the designed Cantilever A, respectively. However, at equal levels of absorbed heat from the OBD laser, the average temperature varies between the designs. Because the average temperature is inversely proportional to the conductance G, the previous metric can be multiplied by $\sqrt{1/G}$ for a metric that allows comparison at equal levels of absorbed power. The values of this metric are $1.5 \times 10^{-6}\,\mathrm{W^{1/2}}$ and $3.7 \times 10^{-7}\,\mathrm{W^{1/2}}$ for the MLCT-C and Cantilever A, respectively. Cantilever A performs 4.1× better than the MLCT-C in terms of equivalent thermal noise at equal levels of absorbed power. The signal-to-noise ratio can thus be improved by a factor of 168 compared to the benchmark.

To verify the theoretical model, the optimized cantilever is also modeled using the same multiphysics finite element method (FEM). The sensitivities derived using the analytical model and the sensitivities derived using the FEM are in very good agreement with each other, with a maximum difference of less than 1 %. The differences in conductance and spring constant are 6 % and 3 %, respectively, and are considered in adequate agreement for this discussion. The difference in the conductance values calculated using the analytical model and using the FEM can be attributed to the assumption of one-dimensional heat flow in the theoretical model, and thus the lack of interaction between the layers. Similarly, the difference for the spring constant values using both models can be attributed to the lack of the Poisson effect in the theoretical

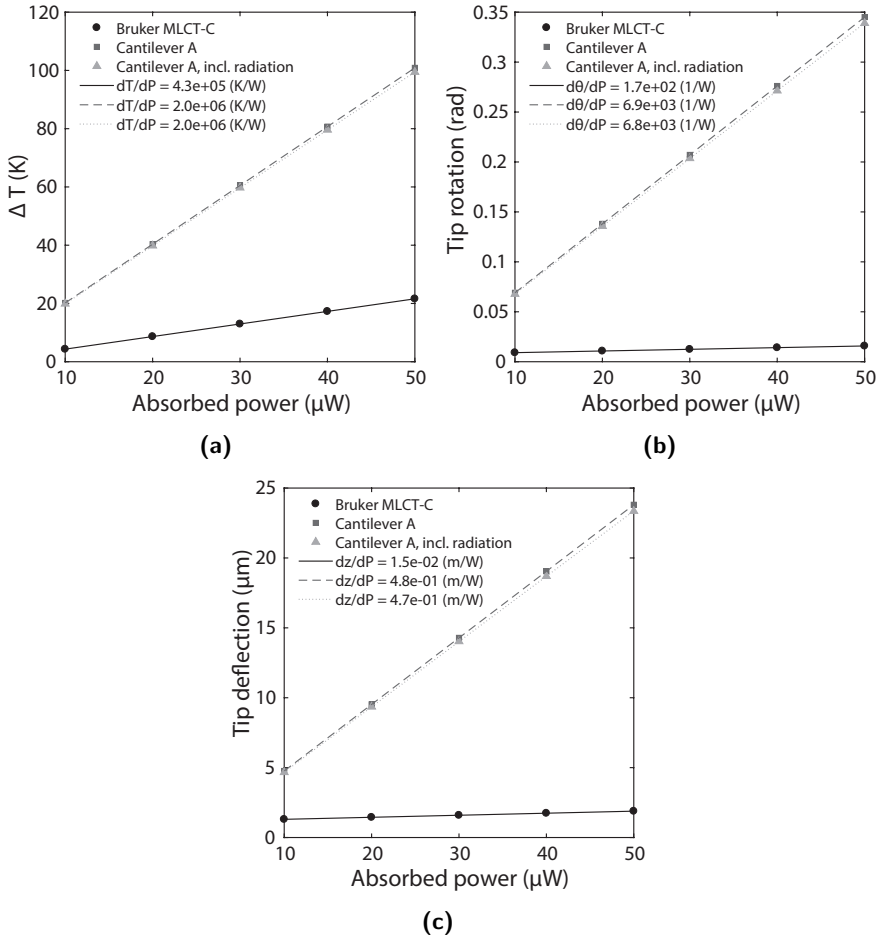

Figure 4.12: Temperature gradients (a), tip rotation (b) and tip deflection (c) for various levels of absorbed heat flux at the cantilever tip.

model.

Table 4.4: The table includes a comparison between the results obtained from the theoretical model, a FEM model that only includes conduction, and a FEM model taking into account both conduction via the probe and radiative heat losses to the environment. The relative performance is calculated as that of the optimized probe (FEM) relative to that of the Bruker MLCT-C. *Nota bene:* the spring constant calculated for the MLCT-C probe is higher than the nominal spring constant of $10\,\mathrm{mN\,m^{-1}}$ specified by Bruker, but is within the specified range of $5\,\mathrm{mN\,m^{-1}}$ to $20\,\mathrm{mN\,m^{-1}}$.

Parameter	**Bruker MLCT-C**	**Optimized (FEM)**	**Optimized (Theory)**	**Optimized (FEM + losses)**	**Relative performance**
Conductance G ($\mathrm{W\,K^{-1}}$)	2.3×10^{-6}	5.0×10^{-7}	5.3×10^{-7}	5.0×10^{-7}	2.1×10^{-1}
Rotation sensitivity $\partial\theta/\partial P$ ($\mathrm{rad\,W^{-1}}$)	1.7×10^{2}	6.9×10^{3}	6.9×10^{3}	6.8×10^{3}	4.1×10^{1}
Deflection sensitivity $\partial z/\partial P$ ($\mathrm{m\,W^{-1}}$)	1.5×10^{-2}	4.8×10^{-1}	4.8×10^{-1}	4.7×10^{-1}	3.3×10^{1}
Spring constant C ($\mathrm{N\,m^{-1}}$)	1.6×10^{-2}	1.1×10^{-3}	1.1×10^{-3}	1.1×10^{-3}	-
Equivalent thermal noise at equal average temperature ($\mathrm{nW\,K^{-1/2}}$)	2.3	0.27	0.27	0.27	8.5
Equivalent thermal noise at equal absorbed power ($\mathrm{W^{1/2}}$)	1.5×10^{-6}	3.7×10^{-7}	3.7×10^{-7}	3.7×10^{-7}	4.1

4.4 Experimental validation

To validate the design, the cantilevers are manufactured and the sensitivities are measured indirectly.

4.4.1 Cantilever manufacturing

The manufacturing of the cantilevers starts on a standard 380 µm thick (100) silicon wafer. A 315 nm thick silicon-rich nitride (SiRN) layer is deposited by Low Pressure Chemical Vapor Deposition (LPCVD). The deposited SiRN layer is then patterned using Reactive Ion Etching (RIE) to define the cantilevers. A second patterning step is employed to etch through the silicon wafer by Deep Reactive Ion Etching (DRIE). After the DRIE process the cantilevers are released by wet chemical etching of silicon in tetramethylammonium hydroxide (TMAH). After release, a 100 nm thick aluminum layer is sputtered on one side to form the reflective coating. These steps are illustrated in Figure 4.13.

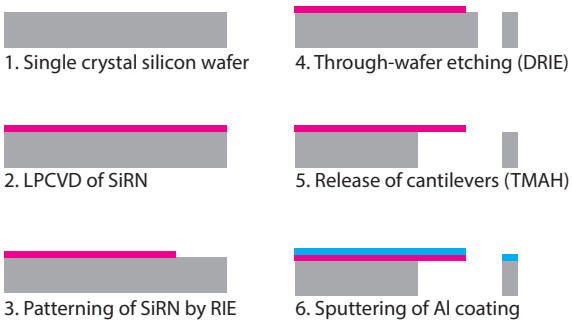

Figure 4.13: The cantilevers are manufactured in a six step process starting from a standard (100) silicon wafer. Silicon-rich nitride is deposited on top and the cantilevers are defined using (deep) reactive ion etching (RIE). After release using TMAH, an aluminium coating is sputtered on top.

In the design, the reflective coating is assumed to be perfectly flat. The scattering of light caused by the surface roughness, however, affects the reflectance of the probe. This effect is modeled using the simple model presented by Bennet and Porteus [65]. The specular reflectance R is calculated from the ideal reflectance R_0 under normal incidence as

$$R = R_0 \left(\exp\left(-\frac{4\pi\sigma^2}{\lambda^2} \right) + \frac{2^5\pi^4}{m^2} \left(\frac{\sigma}{\lambda} \right)^4 \Delta\theta^2 \right), \tag{4.17}$$

where σ is the root mean square surface roughness, λ is the wavelength of the light, m is the root mean square slope of the surface, and $\Delta\theta$ is the acceptance angle of the optics. The right-hand term vanishes quickly with larger λ, and

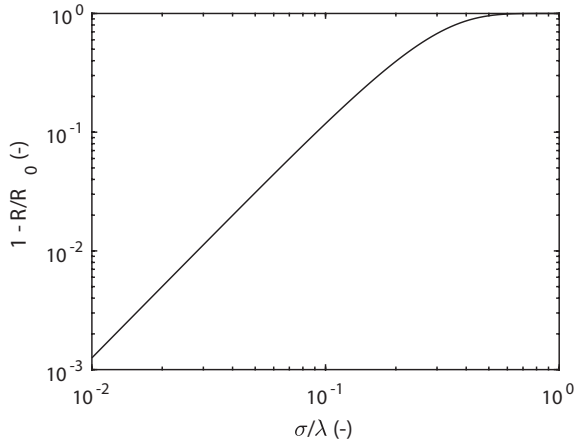

Figure 4.14: Relative error in specular reflectance $(1 - R/R_0)$ under normal incidence and as a function of the root mean square surface roughness σ relative to the wavelength λ.

the reflectance is approximated as

$$R \approx R_0 \exp\left(-\frac{4\pi\sigma^2}{\lambda^2}\right). \tag{4.18}$$

Figure 4.14 shows this relation in dimensionless form. A root mean square roughness of 3% or less of the wavelength limits the difference between ideal and non-ideal specular reflections to 1%. For a wavelength of 635 nm the relative roughness translates to a root mean square roughness of 19 nm.

The surface roughness of three chips (each with 5 cantilevers) was measured using a Park XE7 atomic force microscope and BudgetSensors SHR300 probes (1 nm tip radius) over a 1 µm × 1 µm area to be 3.4 nm ± 0.4 nm root mean square. The realized probes are thus smooth enough for scattering to be considered a minor contributor to the optical absorptance and reflectance values.

4.4.2 Measuring the cantilever sensitivity

To validate the design procedure, the sensitivity of the realized probes is measured under high vacuum conditions. The sensitivity of the probe cannot be measured directly and needs to be derived from measurable quantities using

$$\frac{\partial\theta}{\partial P_{\mathrm{abs}}} = \frac{\partial X_{\mathrm{p}}}{\partial P_{\mathrm{abs}}}\left(\frac{\partial X_{\mathrm{p}}}{\partial x}\frac{\partial x}{\partial\theta}\right)^{-1}. \tag{4.19}$$

The absorbed power is calculated from the incident power and the absorptance, which is measured separately (see Appendix B for details). The sensitivity $\partial X_{\mathrm{p}}/\partial x$ is measured by displacing the PSD by controlled amounts with respect to the reflected beam and the rest of the system in steady-state.

Unfortunately, the sensitivity $\frac{\partial x}{\partial \theta}$ cannot be measured directly in the available system, but it is estimated at $(99.6 \pm 3.0)\,\mathrm{mm\,rad^{-1}}$ (see Appendix A for details of this estimation).

The measured sensitivities are summarized in Table 4.5. For Cantilevers B, C and D the measured sensitivities are close to their designed values. The differences can be explained by the measurement uncertainty and the loss of sensitivity due to measuring not at the very tip of the probes, but slightly behind them. As is shown in Chapter 5, the actual sensitivity of the probe depends on the position of the laser spot along the length of the probe and the spot size. This causes the realized sensitivity to drop to a level between 55 % and 90 % of the theoretical sensitivity. If these effects are incorporated into the theoretical relations, however, the advantage of using theoretical relations for design purposes is lost due to the complexity and length of the equations.

Cantilever A is the most sensitive of the four designs, but the measured sensitivity differs significantly from the designed value. Optical micrographs and scanning electron micrographs (see Appendix C) showed significant damage to the cantilever coating after calibration which is probably caused by excessive heating. This unforeseen effect was not observed in the other designs, due to their higher thermal conductance and lower maximum temperatures. It is hypothesized that the deviation from the design value in this case can be traced to the sensitivity changing over time due the sustained damage.

Attempts to measure the sensitivity of the Bruker MLCT-C cantilever were unreliable due to large variations in the measured absorptance. For the MLCT-C, h is smaller than 0.10 with a coating thickness of 40 nm and a total thickness of 0.55 µm. As is clear from Figure 4.3, large fluctuations in absorptance are expected with small variations in thickness for this combination of coating thickness and thickness ratio. The absorptance ranges from 4.5 % to 8.5 % in a ± 5 nm interval around the nominal coating thickness. Using this range for the absorptance, the sensitivity is estimated between $337\,\mathrm{rad\,W^{-1}}$ to $562\,\mathrm{rad\,W^{-1}}$, which is significantly higher than is estimated from the finite element model. Because the processing conditions are unknown, it is likely that the effective material properties and layer thicknesses vary from those assumed in the theoretical model. This is also reflected in the stiffness range specified by the manufacturer which ranges from $5\,\mathrm{mN\,m^{-1}}$ to $20\,\mathrm{mN\,m^{-1}}$.

Table 4.5: Measured sensitivities and derived probe sensitivity.

Parameter	Cantilever A	Cantilever B	Cantilever C	Cantilever D
$\partial \bar{X}_p / \partial I \left(\mathrm{mA}^{-1}\right)$	1.58 ± 0.0706	1.12 ± 0.0738	0.217 ± 0.0418	0.143 ± 0.00872
$\partial P_{\mathrm{abs}} / \partial I \left(\mu\mathrm{W\,mA}^{-1}\right)$	3.43 ± 0.148	3.42 ± 0.212	3.29 ± 0.553	2.64 ± 0.155
$\partial \bar{X}_p / \partial x \left(\mathrm{m}^{-1}\right)$	906 ± 64	1220 ± 39	594 ± 106	815 ± 48
$\partial x / \partial \theta \left(\mathrm{mm\,rad}^{-1}\right)$ [a]	99.6 ± 3.0	99.6 ± 3.0	99.6 ± 3.0	99.6 ± 3.0
$\partial \theta / \partial P_{\mathrm{abs}} \left(\mathrm{rad\,W}^{-1}\right)$ [b]	$5.08 \times 10^3 \pm 503$ [c]	$2.70 \times 10^3 \pm 272$	$1.12 \times 10^3 \pm 355$	669 ± 101
$\partial \theta / \partial P_{\mathrm{abs}} \left(\mathrm{rad\,W}^{-1}\right)$, theory	6.9×10^3	2.3×10^3	1.4×10^3	6.7×10^2

[a] By design, theoretical value. See Appendix A for details.
[b] Calculated from the other sensitivities.
[c] Micrographs show local damage to the cantilever that is likely caused by excessive heating. Some samples had broken, while others were discolored locally which indicates changes in the optical properties.

4.5 Discussion

4.5.1 Limited speed of measurement

It is important to note that the cantilever dimensions and materials also influence the dynamics of the probe, which are directly linked to the speed of measurement that can be attained on a system level. When speed of measurement becomes a driving parameter, for example for microscopy applications, these influences on the cantilever dynamics will have to be considered in the design of the probe. To study the influence of the design parameters on the speed of measurement, the first mechanical resonance frequency and the characteristic thermal time constant are determined. These are used as first order estimates of the response time to a thermal load at the free end of the cantilever.

The majority of near-field heat transfer measurements are conducted under vacuum conditions. Therefore, contributions from mechanical or aerodynamic damping and heat transfer to the environment are neglected here. For a cantilever with a sphere attached to its free end, the first mechanical resonance frequency can then be estimated as [66]

$$f_L \approx \frac{1}{2\pi}\sqrt{\frac{3EI}{(0.24m + M)\,L^3}}, \tag{4.20}$$

where m is the mass of the cantilever and M is the mass of the sphere. According to Barnes *et al.* [40], the thermal response time for a heat load at the free end of the cantilever can be estimated as

$$\tau = \frac{1}{D}\frac{L^3}{3}, \tag{4.21}$$

where the thermal diffusivity D for the bilayer structure is equal to [67]

$$D = \frac{k_1 t_1 + k_2 t_2}{c_{p_1}\rho_1 t_1 + c_{p_2}\rho_2 t_2}. \tag{4.22}$$

Because 99.4 % of the total temperature change is achieved after 5τ has passed, the thermal bandwidth of the cantilever is defined as

$$f_{\mathrm{T,\,cant.}} = \frac{1}{5\tau}. \tag{4.23}$$

However, the microsphere plays a significant role in the thermal bandwidth. Using a lumped parameter model of the sphere that approximates the sphere as a cylindrical conductor of thermal conductance G and radius R, its thermal time constant can be estimated to first order as

$$\tau_{\mathrm{sphere}} \approx \frac{mc}{G} \approx \frac{8\rho c R^2}{3k}. \tag{4.24}$$

For a glass sphere, $\log_{10}(f_{\mathrm{T}}) \approx -7 - 2\log_{10}(R)$, which yields a wide range of $f_{\mathrm{R}} \approx 1 \times 10^{11}\,\mathrm{Hz}$ to $f_{\mathrm{T}} \approx 10\,\mathrm{Hz}$ for $R = 1\,\mathrm{nm}$ and $R = 100\,\mu\mathrm{m}$, respectively.

Table 4.3 on page 80 lists the first resonance frequency for a probe with no sphere attached, the resonance frequency with a sphere attached, the thermal time constant and the thermal bandwidth. The glass microsphere has a diameter of 20 µm. Although the addition of the sphere reduces the mechanical resonance frequency by $7-10\times$, the thermal response time remains the limiting factor for the achievable measurement speed. In the case of Cantilever A, the thermal measurement bandwidth of the cantilever itself is 483 Hz, while that of the sphere is 534 Hz.

The thermal response time of the probe (consisting of a cantilever with an attached sphere) can only be improved by using a smaller sphere and a smaller cantilever and at the cost of measurement sensitivity.

4.5.2 The effect of ignoring radiative losses

In the analysis above and in the analytical model, the contribution of radiative heat transfer between the cantilever and its surroundings is considered to be negligible. To confirm the validity of this assumption, the thermal and thermo-mechanical response of the designed cantilever probe are modeled using a finite element method in which heat transfer to the environment via black-body radiation is included. The clamped end of the probe is kept at a constant temperature of 300 K, while a constant flux of 10 µW to 50 µW is absorbed at its free end. The environment is set at a constant temperature of 293.15 K and at a perfect vacuum. The emissivity of all radiating surfaces is set at an unrealistically high, worst-case value of 1. At the highest power setting of the laser diode, the tip temperature of the probe does not exceed 400 K. The magnitude of the temperature gradients, the tip rotation and the tip deflection are shown in Figure 4.12. The corresponding sensitivities are summarized in Table 4.4 on page 84. Ignoring radiative heat losses introduces an error of less than 1.5 % in the conductance and less than 1.8 % in the sensitivities. At these temperatures, radiative losses are thus negligible for design purposes.

For a worst-case estimation of the radiative heat losses, the cantilever is assumed to take a uniform temperature distribution equal to the maximum tip-temperature. The corresponding loss is

$$q_{\text{rad.loss}} = \sigma A_{\text{rad}} \epsilon \left(T_{\text{tip}}^4 - T_{\text{env}}^4 \right), \tag{4.25}$$

where $\sigma = 5.67 \times 10^{-8}\,\text{W}\,\text{m}^{-2}\,\text{K}^{-1}$ is the Stefan-Boltzmann constant, $A_{\text{rad}} \approx 1.6 \times 10^{-9}\,\text{m}^2$ is the total radiating area, $\epsilon = 1$ the (assumed worst-case) effective emissivity, $T_{\text{tip}} = 400\,\text{K}$ is the tip temperature and $T_{\text{env}} = 293.15\,\text{K}$ is the temperature of the environment. From this, it follows that the thermal flux $\leq 1.6\,\mu\text{W}$, which is small in comparison to the power absorbed from the incident laser. The change in radiative losses due to a change in the temperature of the environment is estimated as

$$\frac{\partial q_{\text{rad.loss}}}{\partial T_{\text{env}}} = -4\sigma A_{\text{rad}} \epsilon T_{\text{env}}^3, \tag{4.26}$$

and amounts to approximately $9.1\,\mathrm{nW\,K^{-1}}$. In practice, the temperature variation inside the vacuum chamber is between 50 mK to 100 mK over the course of a day, which reduces the effect of radiative losses to less than 1 nW. This is a small contributor to the drift at system level, which is dominated by the drift of the laser power in the order of 50 nW in absorbed power.

4.5.3 The effect of ambient pressure

In the theoretical discussion, vacuum conditions were assumed and the effects of convective and conductive heat losses to the environment were ignored. Additional loss of heat to the environment via heat transfer to the ambient air results in a reduced temperature gradient along the length of the cantilever [68]. This results in a reduced mismatch strain between the layers for an equal thermal input at the cantilever tip, and thus a reduction of the sensitivity. Convective heat transfer at micrometer length scales is currently not well understood and experimental evidence suggests convective heat transfer coefficients ranging from $30\,\mathrm{W\,m^{-2}\,K^{-1}}$ to $10\,\mathrm{kW\,m^{-2}\,K^{-1}}$ at ambient pressure (see Bijster *et al.* [67] and the references therein). This makes it difficult to quantify the reduction in sensitivity with any reasonable degree of certainty.

However, experimental evidence provided by Lee *et al.* [69] suggests that convective losses can be ignored for Knudsen numbers larger than 10. The Knudsen number is the ratio between the mean-free path length in the gas and the physical length scale of the object. For the dimensions of the cantilevers that are presented here, no appreciable pressure effects on the sensitivity are expected for pressures below 0.1 mbar. The experiments are conducted at pressures between 1×10^{-7} mbar and 1×10^{-6} mbar (see Section 2.7 for details) to eliminate the effects of gas conduction between the sphere and the substrate. Pressure effects on the probe sensitivity can therefore safely be ignored.

4.5.4 The effect of Casimir and Van der Waals forces

When the probe approaches the sample, Casimir and Van der Waals forces will be exerted on the sphere. These forces increase with diminishing separation. At very small distances ($\leq 10\,\mathrm{nm}$) the sum of these forces can be estimated [70] using

$$F \approx \frac{A_{\mathrm{H}} R}{6 d^2}, \tag{4.27}$$

where A_{H} is Hamaker's constant (6.35×10^{-20} J for silica particles in vacuum [71]), R is the radius of the sphere and d is the separation. Because the sphere is not fixed in line with the cantilever, a torque is applied to the cantilever with an effective arm of length R. The equivalent thermal input can be expressed as

$$\hat{P}_{\mathrm{vdW}} = \frac{\partial P}{\partial \theta} \Delta\theta = \frac{\partial P}{\partial \theta} \frac{1}{2} \frac{A_{\mathrm{H}} R^2}{C d^2 L^2}, \tag{4.28}$$

where C is the spring constant in bending of the cantilever. At a separation of 10 nm, this equates to 97 nW for Cantilever A with a sphere 20 µm diameter sphere attached to its tip. It quickly diminishes to less than 1 nW for a separation of 100 nm. Although these forces are fairly small, they easily exceed other contributions at small separations. They can, however, be compensated for by measuring the spurious forces separately when the tip temperature and substrate temperature are equal. For this, the substrate temperature needs to be raised.

4.6 Conclusions

Near-field radiative heat transfer measurements benefit from probes that are designed for that specific purpose. Using a relatively simple analytical model, a family of feasibile cantilever designs which are constrained in terms of resolution, thermal noise, temperature drift and bending stiffness was derived. The model considers the cantilever as an integral part of the measurement system, and the effects of design decisions are evaluated considering system level performance.

The theoretical model used for this design matches well with the finite element model. The analytical model can be improved by incorporating the exchange of heat between the layers and the effects of finite spot size for the incident light. This will, however, result in theoretical relations that are no longer tangible for design purposes, because of their complexity and their length.

The chapter showed theoretically and experimentally that, under realistic design constraints, the designed probes are up to 41 times more sensitive than the benchmark. This was achieved by limiting the thermal conductance, while maintaining a large difference in thermal expansion coefficients between the two layers. In practice, the performance of the cantilever probes was limited by damage that was possibly sustained from carbon contamination. Future work will have to consider these practical effects if performance is to be further improved. Furthermore, for practical applications in scanning probe microscopy, measurement speed is an important parameter that was omitted from the design in this chapter. The microsphere plays an important role in the attainable measurement bandwidth and will have to be incorporated in the design process if dynamic system performance is to be further improved.

Acknowledgments

The authors thank Edin Sarajlic of Smart Tip for his efforts on manufacturing the cantilevers and his advice on material properties and processing conditions.

Bibliography

[1] C. Hargreaves. Anomalous radiative transfer between closely-spaced bodies. *Physics Letters A*, 30(9):491–492, 1969.

[2] S. Rytov. *Theory of Electrical Fluctuations and Thermal Radiation*. Izd-vo Akademii Nauk S.S.S.R., Moscow, 1953.

[3] S. Rytov. *Theory of Electric Fluctuations and Thermal Radiation, ser. AFCRC-TR-59-162*. Electronics Research Directorate, Air Force Cambridge Research Center, Air Research and Development Command, U.S. Air Force, Moscow (Originally), 1st englis edition, 1959.

[4] D. Polder and M. Van Hove. Theory of Radiative Heat Transfer between Closely Spaced Bodies. *Physical Review B*, 4(10):3303–3314, 1971.

[5] E. G. Cravalho, C. L. Tien, and R. P. Caren. Effect of Small Spacings on Radiative Transfer Between Two Dielectrics. *Journal of Heat Transfer*, 89(4):351, 1967.

[6] E. Cravalho, G. Domoto, and C. Tien. Measurements of thermal radiation of solids at liquid-helium temperatures. In *3rd Thermophysics Conference*, p. 531–542, Reston, Virigina, 1968. American Institute of Aeronautics and Astronautics.

[7] R. S. DiMatteo, P. Greiff, S. L. Finberg, K. A. Young-Waithe, H. K. H. Choy, M. M. Masaki, and C. G. Fonstad. Enhanced photogeneration of carriers in a semiconductor via coupling across a nonisothermal nanoscale vacuum gap. *Applied Physics Letters*, 79(12):1894–1896, 2001.

[8] X. J. Hu, A. Jain, and K. E. Goodson. Investigation of the natural convection boundary condition in microfabricated structures. *International Journal of Thermal Sciences*, 47(7):820–824, 2008.

[9] R. S. Ottens, V. Quetschke, S. Wise, A. A. Alemi, R. Lundock, G. Mueller, D. H. Reitze, D. B. Tanner, and B. F. Whiting. Near-Field Radiative Heat Transfer between Macroscopic Planar Surfaces. *Physical Review Letters*, 107(1):014301, 2011.

[10] T. Kralik, P. Hanzelka, M. Zobac, V. Musilova, T. Fort, and M. Horak. Strong Near-Field Enhancement of Radiative Heat Transfer between Metallic Surfaces. *Physical Review Letters*, 109(22):224302, 2012.

[11] S. Sadat, E. Meyhofer, and P. Reddy. Resistance thermometry-based picowatt-resolution heat-flow calorimeter. *Applied Physics Letters*, 102(16):163110, 2013.

[12] R. St-Gelais, B. Guha, L. Zhu, S. Fan, and M. Lipson. Demonstration of Strong Near-Field Radiative Heat Transfer between Integrated Nanostructures. *Nano letters*, 14(12):6971–6975, 2014.

[13] T. Ijiro and N. Yamada. Near-field radiative heat transfer between two parallel SiO 2 plates with and without microcavities. *Applied Physics Letters*, 106(2):023103, 2015.

[14] K. Ito, A. Miura, H. Iizuka, and H. Toshiyoshi. Parallel-plate submicron gap formed by micromachined low-density pillars for near-field radiative heat transfer. *Applied Physics Letters*, 106(8):083504, 2015.

[15] B. Song, Y. Ganjeh, S. Sadat, D. Thompson, A. Fiorino, V. Fernández-Hurtado, J. Feist, F. J. Garcia-Vidal, J. C. Cuevas, P. Reddy, and E. Meyhofer. Enhancement of near-field radiative heat transfer using polar dielectric thin films. *Nature Nanotechnology*, 10(3):253–258, 2015.

[16] B. Song, D. Thompson, A. Fiorino, Y. Ganjeh, P. Reddy, and E. Meyhofer. Radiative heat conductances between dielectric and metallic parallel plates with nanoscale gaps. *Nature Nanotechnology*, 11(6):509–514, 2016.

[17] R. St-Gelais, L. Zhu, S. Fan, and M. Lipson. Near-field radiative heat transfer between parallel structures in the deep subwavelength regime. *Nature Nanotechnology*, 11(6):515–519, 2016.

[18] K. Ito, K. Nishikawa, A. Miura, H. Toshiyoshi, and H. Iizuka. Dynamic Modulation of Radiative Heat Transfer beyond the Blackbody Limit. *Nano Letters*, 17(7):4347–4353, 2017.

[19] D. Thompson, L. Zhu, R. Mittapally, S. Sadat, Z. Xing, P. McArdle, M. M. Qazilbash, P. Reddy, and E. Meyhofer. Hundred-fold enhancement in far-field radiative heat transfer over the blackbody limit. *Nature*, 561(7722):216–221, 2018.

[20] A. Fiorino, D. Thompson, L. Zhu, B. Song, P. Reddy, and E. Meyhofer. Giant Enhancement in Radiative Heat Transfer in Sub-30 nm Gaps of Plane Parallel Surfaces. *Nano Letters*, 18(6):3711–3715, 2018.

[21] J. DeSutter, L. Tang, and M. Francoeur. A near-field radiative heat transfer device. *Nature Nanotechnology*, 14(8):751–755, 2019.

[22] L. Zhu, A. Fiorino, D. Thompson, R. Mittapally, E. Meyhofer, and P. Reddy. Near-field photonic cooling through control of the chemical potential of photons. *Nature*, 566(7743):239–244, 2019.

[23] H. Salihoglu, W. Nam, L. Traverso, M. Segovia, P. K. Venuthurumilli, W. Liu, Y. Wei, W. Li, and X. Xu. Near-Field Thermal Radiation between Two Plates with Sub-10 nm Vacuum Separation. *Nano Letters*, 20(8):6091–6096, 2020.

[24] X. Ying, P. Sabbaghi, N. Sluder, and L. Wang. Super-Planckian Radiative Heat Transfer between Macroscale Surfaces with Vacuum Gaps Down to 190 nm Directly Created by SU-8 Posts and Characterized by Capacitance Method. *ACS Photonics*, 7(1):190–196, 2020.

[25] C. C. Williams and H. K. Wickramasinghe. Scanning thermal profiler. *Applied Physics Letters*, 49(23):1587, 1986.

[26] J.-B. Xu, K. Läuger, R. Möller, K. Dransfeld, and I. H. Wilson. Heat transfer between two metallic surfaces at small distances. *Journal of Applied Physics*, 76(11):7209, 1994.

[27] W. Müller-Hirsch, A. Kraft, M. T. Hirsch, J. Parisi, and A. Kittel. Heat transfer in ultrahigh vacuum scanning thermal microscopy. *Journal of Vacuum Science & Technology A: Vacuum, Surfaces, and Films*, 17(4):1205, 1999.

[28] A. Kittel, W. Müller-Hirsch, J. Parisi, S.-A. Biehs, D. Reddig, and M. Holthaus. Near-Field Heat Transfer in a Scanning Thermal Microscope. *Physical Review Letters*, 95(22):224301, 2005.

[29] U. F. Wischnath, J. Welker, M. Munzel, and A. Kittel. The near-field scanning thermal microscope. *Review of Scientific Instruments*, 79(7):073708, 2008.

[30] K. Kloppstech, N. Könne, S.-A. Biehs, A. W. Rodriguez, L. Worbes, D. Hellmann, and A. Kittel. Giant heat transfer in the crossover regime between conduction and radiation. *Nature Communications*, 8(1):14475, 2017.

[31] L. Cui, W. Jeong, V. Fernández-Hurtado, J. Feist, F. J. García-Vidal, J. C. Cuevas, E. Meyhofer, and P. Reddy. Study of radiative heat transfer in Ångström- and nanometre-sized gaps. *Nature Communications*, 8(1):14479, 2017.

[32] A. Narayanaswamy, S. Shen, and G. Chen. Near-field radiative heat transfer between a sphere and a substrate. *Physical Review B*, 78(11):115303, 2008.

[33] E. Rousseau, A. Siria, G. Jourdan, S. Volz, F. Comin, J. Chevrier, and J.-J. Greffet. Radiative heat transfer at the nanoscale. *Nature Photonics*, 3(9):514–517, 2009.

[34] S. Shen, A. Narayanaswamy, and G. Chen. Surface phonon polaritons mediated energy transfer between nanoscale gaps. *Nano letters*, 9(8):2909–13, 2009.

[35] P. J. van Zwol, L. Ranno, and J. Chevrier. Tuning Near Field Radiative Heat Flux through Surface Excitations with a Metal Insulator Transition. *Physical Review Letters*, 108(23):234301, 2012.

[36] F. Menges, M. Dittberner, L. Novotny, D. Passarello, S. S. P. Parkin, M. Spieser, H. Riel, and B. Gotsmann. Thermal radiative near field transport between vanadium dioxide and silicon oxide across the metal insulator transition. *Applied Physics Letters*, 108(17):171904, 2016.

[37] P. L. Sambegoro. *Experimental Investigations on the Influence of Curvature and Materials on Near-field Thermal Radiation*. Doctoral dissertation, Massachusetts Institute of Technology, 2016.

[38] G. Meyer and N. M. Amer. Novel optical approach to atomic force microscopy. *Applied Physics Letters*, 53(12):1045, 1988.

[39] R. Wanders. *Near-field thermal radiation distance sensing*. Master thesis, TNO/TU Delft, Delft, 2014.

[40] J. R. Barnes, R. J. Stephenson, C. N. Woodburn, S. J. O'Shea, M. E. Welland, T. Rayment, J. K. Gimzewski, and C. Gerber. A femtojoule calorimeter using micromechanical sensors. *Review of Scientific Instruments*, 65(12):3793, 1994.

[41] J. Lai, T. Perazzo, Z. Shi, and A. Majumdar. Optimization and performance of high-resolution micro-optomechanical thermal sensors. *Sensors and Actuators A: Physical*, 58(2):113–119, 1997.

[42] C. Canetta and A. Narayanaswamy. Sub-picowatt resolution calorimetry with a bimaterial microcantilever sensor. *Applied Physics Letters*, 102(10):103112, 2013.

[43] P. E. Rutten. High speed two-dimensional optical beam position detector. *Review of Scientific Instruments*, 82(7):073705, 2011.

[44] B. Harbecke. Coherent and incoherent reflection and transmission of multilayer structures. *Applied Physics B Photophysics and Laser Chemistry*, 39(3):165–170, 1986.

[45] S. J. Byrnes. Multilayer optical calculations. 2016.

[46] P. B. Johnson and R. W. Christy. Optical Constants of the Noble Metals. *Physical Review B*, 6(12):4370–4379, 1972.

[47] M. N. Polyanskiy. Refractive index database.

[48] A. D. Rakić. Algorithm for the determination of intrinsic optical constants of metal films: application to aluminum. *Applied Optics*, 34(22):4755, 1995.

[49] D. E. Aspnes and A. A. Studna. Dielectric functions and optical parameters of Si, Ge, GaP, GaAs, GaSb, InP, InAs, and InSb from 1.5 to 6.0 eV. *Physical Review B*, 27(2):985–1009, 1983.

[50] Filmetrics. Refractive Index of Si3N4, Silicon Nitride, SiN, SiON.

[51] I. H. Malitson. Interspecimen Comparison of the Refractive Index of Fused Silica. *Journal of the Optical Society of America*, 55(10):1205, 1965.

[52] Filmetrics. Refractive Index of SiC, Silicon Carbide, 2018.

[53] A. Abazari, S. Safavi, G. Rezazadeh, and L. Villanueva. Modelling the Size Effects on the Mechanical Properties of Micro/Nano Structures. *Sensors*, 15(11):28543–28562, 2015.

[54] H. S. Marnani. *Mechanics of Ultra-sensitive Nanoelectromechanical Silicon Cantilevers: A Combined Experimental-Theoretical Approach*. Doctoral dissertation, Delft University of Technology, 2010.

[55] MatWeb. Gold, Au.

[56] MatWeb. Silicon, Si.

[57] MatWeb. Aluminium, Al.

[58] B. El-Kareh. *Fundamentals of Semiconductor Processing Technology*. Springer US, Boston, MA, 1995.

[59] Accuratus. Silicon Carbide, SiC Ceramic Properties, 2013.

[60] A. Khan, J. Philip, and P. Hess. Young's modulus of silicon nitride used in scanning force microscope cantilevers. *Journal of Applied Physics*, 95(4):1667–1672, 2004.

[61] K. Babaei Gavan, H. J. R. Westra, E. W. J. M. van der Drift, W. J. Venstra, and H. S. J. van der Zant. Size-dependent effective Young's modulus of silicon nitride cantilevers. *Applied Physics Letters*, 94(23):233108, 2009.

[62] MEMSnet. Material: Silicon Nitride (Si3N4).

[63] AZO Materials. Silicon Nitride (Si3N4) Properties and Applications.

[64] J. Vicary, A. Ulcinas, J. Hörber, and M. Antognozzi. Micro-fabricated mechanical sensors for lateral molecular-force microscopy. *Ultramicroscopy*, 111(11):1547–1552, 2011.

[65] H. E. Bennett and J. O. Porteus. Relation Between Surface Roughness and Specular Reflectance at Normal Incidence. *Journal of the Optical Society of America*, 51(2):123, 1961.

[66] E. Macho-Stadler, M. J. Elejalde-García, and R. Llanos-Vázquez. Oscillations of end loaded cantilever beams. *European Journal of Physics*, 36(5):055007, 2015.

[67] R. Bijster, J. de Vreugd, and H. Sadeghian. Dynamic Characterization of Bi-material Cantilevers. In S. Yurish and F. Pacull, editors, *SENSORDEVICES 2013: The Fourth International Conference on Sensor Device Technologies and Applications*, p. 1–8, Barcelona, Spain, 2013. IARIA.

[68] M. Toda, T. Ono, F. Liu, and I. Voiculescu. Evaluation of bimaterial cantilever beam for heat sensing at atmospheric pressure. *Review of Scientific Instruments*, 81(5):055104, 2010.

[69] J. Lee, T. L. Wright, M. R. Abel, E. O. Sunden, A. Marchenkov, S. Graham, and W. P. King. Thermal conduction from microcantilever heaters in partial vacuum. *Journal of Applied Physics*, 101(1):014906, 2007.

[70] G. Palasantzas, P. J. van Zwol, and J. T. M. De Hosson. Transition from Casimir to van der Waals force between macroscopic bodies. *Applied Physics Letters*, 93(12):121912, 2008.

[71] L. Bergström. Hamaker constants of inorganic materials. *Advances in Colloid and Interface Science*, 70:125–169, 1997.

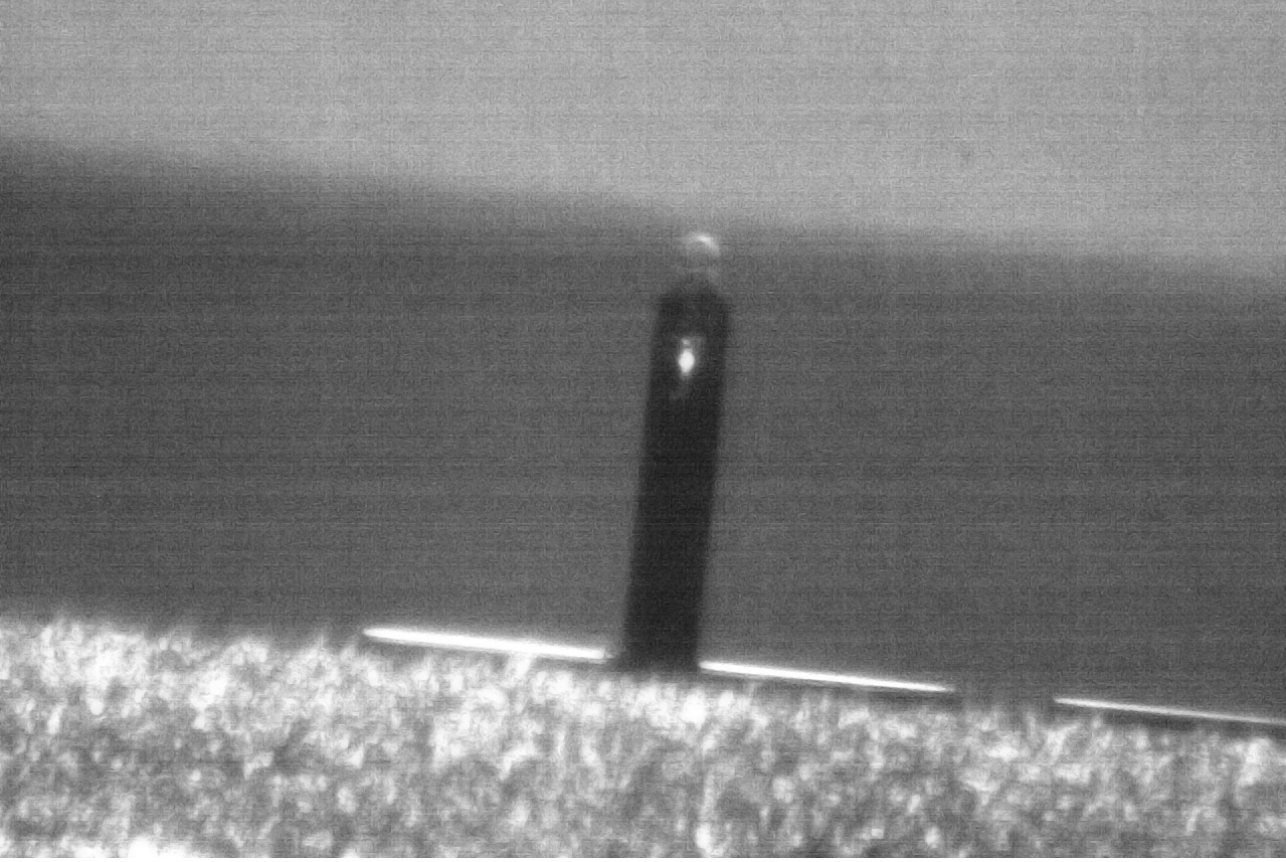

5. Reduction of cantilever sensitivity due to finite spot size and spot location

In the previous chapters, the incident illumination from the OBD system is assumed to be concentrated in an infinitely small spot that is situated at the very end of the cantilever. In this chapter, the effects of a finite spot size and of a realistic location along the cantilever length are calculated. The probe sensitivity is derived in Section 5.1, after which the influence of the spot position is discussed in Section 5.2. The influence of the spot size is further studied in Section 5.3.

Title picture: optical micrograph of a cantilever with an attached sphere in proximity to the prism. A small laser spot is visible near the tip of the probe. Micrograph by Roy Bijster. Parts of this chapter have been published in Review of Scientific Instruments **92**, 025008 (2021).

5.1 Sensitivity for a finite spot size

The sensitivity of the probe to heat input is derived in a manner that is similar to that of Section 2.2. The temperature profile along the cantilever length is found under the assumption that the temperature gradients across the thickness and across the width of the cantilever are negligible. Instead of a linear temperature distribution along the length of the cantilever, the temperature distribution $T(x,t)$ is found through solving the one-dimensional heat equation [1],

$$\frac{\partial T(x,t)}{\partial t} = D\frac{\partial^2 T(x,t)}{\partial x^2} + f(x,t). \tag{5.1}$$

In this equation, D is the effective thermal diffusivity of the beam, x is the position along the cantilever length ($x = 0$ at the clamped end, $x = L$ at the free end), t is the instance in time and $f(x,t)$ is the heat input function

$$f(x,t) = a(t)\exp\left(-\frac{(x-b)^2}{2\sigma^2}\right). \tag{5.2}$$

In this relation, the amplitude $a(t)$ is the power absorbed by the cantilever normalized by the specific heat capacity per unit of length

$$a(t) = \frac{1}{\sigma\sqrt{2\pi}}\frac{P}{w\left(t_1\rho_1 c_{p,1} + t_2\rho_2 c_{p,2}\right)}, \tag{5.3}$$

and b is the center location of the spot and σ is the standard deviation of the Gaussian power distribution that determines the effective spot size. The cantilever has a width w, two layers of thicknesses t_1 and t_2 and the layers have the associated densities ρ_i and specific heat capacities $c_{p,i}$.

When conduction through the cantilever is the main mode of heat transport and the heat transport is stationary, Equation (5.1) has the following solution:

$$\begin{aligned} T(x) = {} & \frac{a\sigma}{D}\sqrt{\frac{\pi}{2}}\left((x-b)\operatorname{erf}\left(\frac{b-x}{\sqrt{2}\sigma}\right) + b\operatorname{erf}\left(\frac{b}{\sqrt{2}\sigma}\right) - x\operatorname{erf}\left(\frac{b-L}{\sqrt{2}\sigma}\right)\right) \\ & + \frac{a\sigma^2}{D}\left(\exp\left(-\frac{b^2}{2\sigma^2}\right) - \exp\left(-\frac{(b-x)^2}{2\sigma^2}\right)\right) + T_{\text{base}}, \end{aligned} \tag{5.4}$$

where T_{base} is the constant temperature at the clamped end of the cantilever.

Following the same procedure as in Section 2.2, the rotation of the cantilever $\theta(x)$ as a result of this temperature distribution can be derived to read

$$\begin{aligned}\theta(x) = \beta\Delta\alpha\Bigg(&\frac{a\sigma}{D}\sqrt{\frac{\pi}{2}}\Bigg[\frac{1}{2}\left(b^2-2bx-\sigma^2+x^2\right)\operatorname{erf}\left(\frac{b-x}{\sqrt{2}\sigma}\right)\\&+\frac{\sigma}{\sqrt{2\pi}}(b-x)\exp\left(-\frac{(b-x)^2}{2\sigma^2}\right)-\frac{1}{2}\left(b^2-\sigma^2\right)\operatorname{erf}\left(\frac{b}{\sqrt{2}\sigma}\right)\\&-\frac{\sigma b}{\sqrt{2\pi}}\exp\left(-\frac{b^2}{2\sigma^2}\right)\Bigg]-\frac{a\sigma^3}{D}\sqrt{\frac{\pi}{2}}\left(\operatorname{erf}\left(\frac{b}{\sqrt{2}\sigma}\right)-\operatorname{erf}\left(\frac{b-x}{\sqrt{2}\sigma}\right)\right)\\&-\frac{a\sigma}{D}\sqrt{\frac{\pi}{2}}\left(\frac{x^2}{2}\operatorname{erf}\left(\frac{b-L}{\sqrt{2}\sigma}\right)-xb\operatorname{erf}\left(\frac{b}{\sqrt{2}\sigma}\right)\right)\\&+\frac{a\sigma}{D}x\sigma\exp\left(-\frac{b^2}{2\sigma^2}\right)+T_{\text{base}}x\Bigg)-\beta\Delta\alpha T_{\text{SFT}}x,\end{aligned} \tag{5.5}$$

where T_{SFT} is the stress-free temperature, β is a parameter defined in Section 2.2 and $\Delta\alpha$ is the difference in the thermal expansion coefficients of the reflective coating and the substrate. The sensitivity $\partial\theta(x)/\partial P = \partial\theta/\partial a\ \partial a/\partial P$ yields:

$$\begin{aligned}\frac{\partial\theta(x)}{\partial P} = \Bigg(&\frac{\sigma}{D}\sqrt{\frac{\pi}{2}}\Bigg[\frac{1}{2}\left(b^2-2bx-\sigma^2+x^2\right)\operatorname{erf}\left(\frac{b-x}{\sqrt{2}\sigma}\right)\\&+\frac{\sigma}{\sqrt{2\pi}}(b-x)\exp\left(-\frac{(b-x)^2}{2\sigma^2}\right)\\&-\frac{1}{2}\left(b^2-\sigma^2\right)\operatorname{erf}\left(\frac{b}{\sqrt{2}\sigma}\right)-\frac{\sigma b}{\sqrt{2\pi}}\exp\left(-\frac{b^2}{2\sigma^2}\right)\Bigg]\\&-\frac{\sigma^3}{D}\sqrt{\frac{\pi}{2}}\left(\operatorname{erf}\left(\frac{b}{\sqrt{2}\sigma}\right)-\operatorname{erf}\left(\frac{b-x}{\sqrt{2}\sigma}\right)\right)\\&-\frac{\sigma}{D}\sqrt{\frac{\pi}{2}}\frac{x^2}{2}\operatorname{erf}\left(\frac{b-L}{\sqrt{2}\sigma}\right)+\frac{\sigma^2}{D}x\exp\left(-\frac{b^2}{2\sigma^2}\right)\\&+\frac{b\sigma}{D}\sqrt{\frac{\pi}{2}}x\operatorname{erf}\left(\frac{b}{\sqrt{2}\sigma}\right)\Bigg)\frac{\beta\Delta\alpha}{\sigma\sqrt{2\pi}w\left(t_1\rho_1c_{p,1}+t_2\rho_2c_{p,2}\right)}\end{aligned} \tag{5.6}$$

5.2 Influence of the spot position

The sensitivity $\partial\theta(x=b)/\partial P$ is shown in Figure 5.1 as a function of the spot position. The shown sensitivities are normalized with the ideal sensitivity (for which the power is absorbed completely at the very end of the cantilever).

When the spot has a finite size, the power distribution $f(x,t)$ extends beyond the free end of the cantilever. When $\sigma \geq \frac{1}{4}(L-b)$, a noticeable amount of power passes beyond the free end of the cantilever. This causes

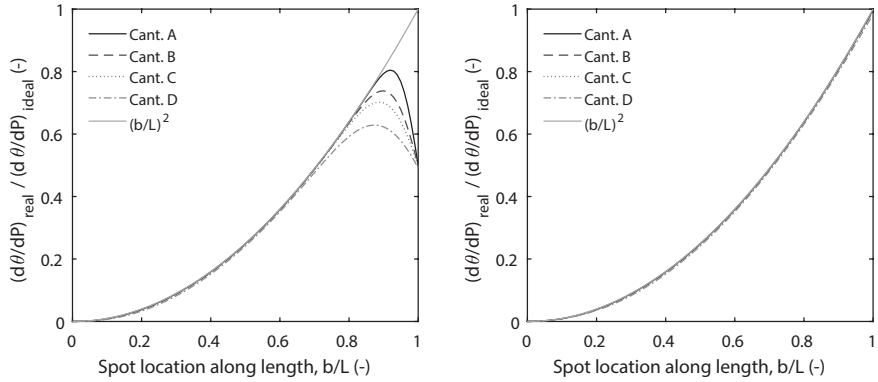

Figure 5.1: Rotation sensitivity of the optimized probe designs A to D (see main text) to variation in laser power as a function of spot location. The spot size $\sigma = 10\,\mu\text{m}$. In the left figure, the sensitivity $\frac{\partial\theta}{\partial P}$ is plotted. In the right figure, the sensitivity is corrected for power losses and $\frac{1}{F}\frac{\partial\theta}{\partial P}$ is displayed. Both have been normalized with the idealized sensitivity for which the power is absorbed completely at the free end.

the calculated sensitivity to drop when the spot is closer to the free end. The fraction of the power incident on the cantilever to the total power in $f(x,t)$ is equal to

$$F = \frac{\int_0^L f(x,t)\,\mathrm{d}x}{\int_{-\infty}^{+\infty} f(x,t)\,\mathrm{d}x} = \frac{1}{2}\left(\operatorname{erf}\left(\frac{b}{\sqrt{2}\sigma}\right) - \operatorname{erf}\left(\frac{b-L}{\sqrt{2}\sigma}\right)\right). \tag{5.7}$$

Figure 5.2 shows this fraction as a function of spot position for the four optimized cantilever designs. In experiments aimed at determining the cantilever sensitivity, this loss of incident power can be corrected for by measuring the power that passes by the cantilever using a power meter. The sensitivity measured after correction is shown in the right-hand figure of Figure 5.1.

For the limit case, where the spot is infinitely small, the rotation of the cantilever at the spot location can be calculated using Equation (2.9) (repeated here):

$$\theta(x) = \beta\Delta\alpha\left[\frac{P}{GL}\frac{x^2}{2} + (T_{\text{base}} - T_{\text{SFT}})\,x\right] + \theta(0),$$

with $x = b$ to represent the actual spot location instead of $x = L$ for the ideal case. The ratio between the sensitivity for an infinitely small spot located at $x = b$ and the ideal sensitivity for the same spot at $x = L$ is

$$\left(\frac{\partial\theta}{\partial P}\right) / \left(\left.\frac{\partial\theta}{\partial P}\right|_{\text{ideal}}\right) = (b/L)^2. \tag{5.8}$$

This relation is plotted in Figure 5.1 together with the results for a realistic, finite spot size of $\sigma = 10\,\mu\text{m}$. As can be seen in the figure, the influence of a realistic but finite spot size is small in comparison to the effect of the spot position along the cantilever length.

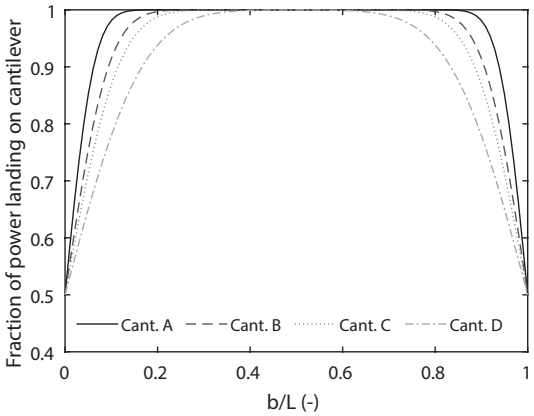

Figure 5.2: The fraction of the power incident on the cantilever to the total power present in the distribution $f(x,t)$ for the four optimized cantilever designs (see main text), and spot size $\sigma = 10\,\mu\text{m}$.

5.3 Influence of the spot size

The effect of the spot size on the cantilever sensitivity for a fixed position along the cantilever length is displayed in Figure 5.3. In this case, the spot is located at a distance of 10 µm from the free end of the cantilever. The cantilever designs of Chapter 4 have a wider section in that location to capture most of the incident illumination.

As can be seen from the Figure, the sensitivity is nearly independent from the spot size below $\sigma = 10\,\mu\text{m}$. The reduction in sensitivity is dominated by the effect of the spot position. For larger spot sizes, the cantilever sensitivity is reduced significantly, because the spot illuminates an increasingly larger section of the cantilever. For the given configurations, the spot size effect becomes noticeable when $\sigma/L \approx 0.1$. As the spot grows, it starts to approximate the situation of uniform heating of the cantilever. It is important to note, that even for a realistic spot size of $\sigma = 10\,\mu\text{m}$ located close to the free end of the cantilever, the sensitivity is reduced to 91 % and 74 % of the ideal values for cantilever Designs A and D, respectively, due to the spot location effect.

As $\sigma \to \infty$, the power distribution loses the spatial variation and becomes uniform. In a fashion very similar to the one shown above, the cantilever sensitivity can be derived for different power distributions. In this case, the power distribution $f(x,t)$ is

$$f(x,t) = \frac{P_0}{Lw\left(t_1\rho_1 c_{p,1} + t_2\rho_2 c_{p,2}\right)}. \tag{5.9}$$

Following the derivation above, the sensitivity can then be written as

$$\frac{\partial\theta(x)}{\partial P} = c\frac{\beta\Delta\alpha L^2}{w\left(k_1 t_1 + k_2 t_2\right)}, \tag{5.10}$$

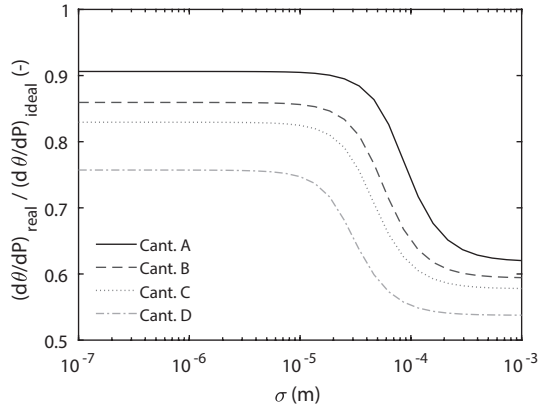

Figure 5.3: The sensitivity of four optimized probes as function of spot size σ normalized with the ideal sensitivity. The spot is located 10 µm from the free end and the sensitivity is corrected for the power losses.

where c depends on the position along the cantilever length. When an illuminating beam this large is used, the entire cantilever length contributes to the reflected beam and the effective beam displacement on the PSD. At the very end of the cantilever, the rotation is greatest and $c = 1/3$ ($x = L$). When considering the rotation at the center of the beam, the c takes the value $5/48$. When considering the average rotation of the cantilever, $c = 1/8$.

For comparison, $c = 1/2$ in the case of concentrated heating at the free end of the cantilever. At equal levels of incident power, the cantilever sensitivity at uniform power distribution is

$$\left.\frac{\partial\theta}{\partial P}\right|_{\text{uniform}} \leq 2/3 \left.\frac{\partial\theta}{\partial P}\right|_{\text{ideal}}. \tag{5.11}$$

Focused heating near the free end, therefore, always results in a higher cantilever sensitivity.

5.4 Conclusions

An illumination spot of finite dimensions can, in contrast to infinitely small spots, not be positioned at the very end of the cantilever. This results in a reduction of the effective length of the cantilever. Moreover, the deviation from a linear temperature distribution along the length of the cantilever grows with the size of the spot. This effect also results in the reduction of the cantilever sensitivity. However, this effect is only of significance when the spot covers a large section of the cantilever length. The sensitivity of the probe is highest for tightly focused spots that are located as close as possible to the free end of the cantilever.

Bibliography

[1] R. J. F. Bijster, J. de Vreugd, and H. Sadeghian. Phase lag deduced information in photo-thermal actuation for nano-mechanical systems characterization. *Applied Physics Letters*, 105(7):073109, 2014.

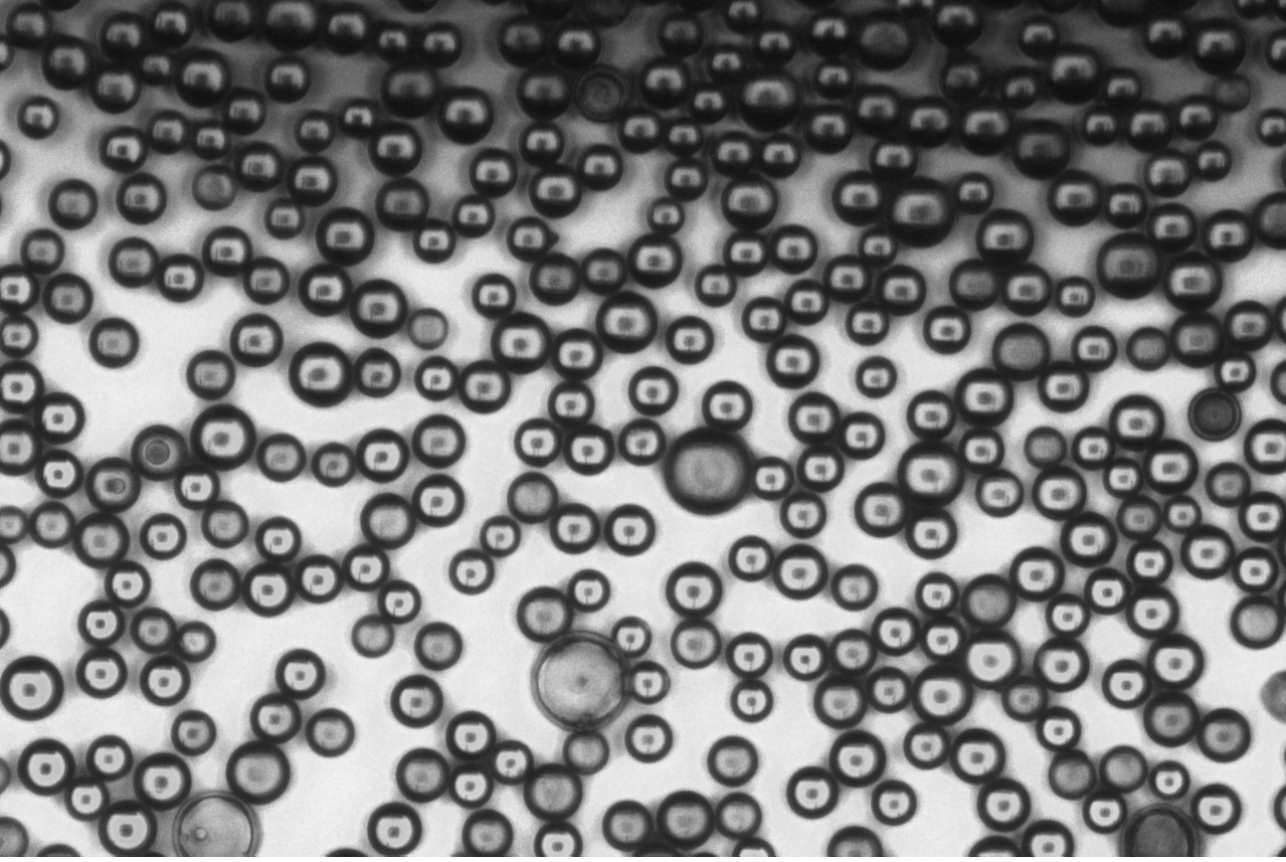

6. Characterizing the surface qualities of probe and sample

The probe consists of a bilayer cantilever and an idealized microsphere at its free end. The latter is positioned above a perfectly flat silica prism. Both the microsphere and prism, however, have non-ideal shapes and non-smooth surfaces. Their shape and surface roughness set limits to the minimum separation required at which comparison of experimental heat transfer data with theory is possible. Moreover, the presence of local features such as scratches or chips may cause premature contact between otherwise ideal surfaces [1]. Therefore, it is important to know how frequently these non-ideal features occur and what their sizes are. This information is typically not known to the manufacturer or not provided to the user, and thus needs to be determined experimentally.

Title picture: micrograph of microspheres embedded in a poly(methyl methacrylate) (PMMA) photoresist layer. Micrograph by Roy Bijster.

This chapter presents measurements of the overall shape and the surface quality of both the prism and the microspheres. Although well established techniques, such as whitelight interferometry and optical profilometry, exist to measure the surface roughness and shape of optical elements, the strongly curved surfaces of the microspheres pose non-trivial challenges. The aforementioned techniques are hampered by the strong internal reflections and large angles of reflection. The first part of this chapter, therefore, focusses on measurements of the topography of the microspheres taken with an atomic force microscope (AFM). The second part of this chapter covers both white light interferometry measurements and AFM measurements taken of the surface of the prism.

6.1 Characterizing the shape and roughness of the microspheres

The microspheres selected for the experiments are silica C-SIO-20.0 monodisperse spheres that are manufactured by Corpuscular (Cold Spring, NY, USA) [2] and are supplied on request as a dry powder. These spheres are made of pure silica and are ideal for direct comparison to theory, because of the well-known optical characteristics of the material. The surface of each sphere is imaged using a Park XE7 atomic force microscope supplied with Bruker FESPA V2 probes ($k = 2.8\,\mathrm{N\,m^{-1}}$, $f = 75\,\mathrm{kHz}$, $R_{\mathrm{tip}} = 8\,\mathrm{nm}$) and Budget Sensors SHR300 probes ($k = 40\,\mathrm{N\,m^{-1}}$, $f = 300\,\mathrm{kHz}$, $R_{\mathrm{tip}} \leq 1\,\mathrm{nm}$).

6.2 Immobilizing the spheres

To prevent the spheres from moving during imaging, they are fixed in position on a piece of silicon wafer using a thin layer of hardened (photo)resist. To this end, two samples were prepared by spin coating an approximately 10 nm thick layer of hydrogen silsesquioxane (HSQ) photoresist (also known as Flowable Oxide or FOx) [3] on top of a piece of silicon wafer, and by spin coating an approximately 500 nm thick layer of poly(methyl methacrylate) (PMMA) on another [4]. Both resists were tried and selected, because they were readily available and it was unknown *a priori* which one would be the most effective in this application. The spheres were then carefully dropped on top of the resist directly from their container, and the samples were baked to harden the resist. The deposition density of the spheres was not controlled, but appeared similar for both samples from visual inspection.

The spheres adhere better to the PMMA layer than to the HSQ layer, as illustrated in Figure 6.1. However, the PMMA sample had to be abandoned initially, because the spheres remained mobile during scanning. Meanwhile, the spheres that stuck to the HSQ remained completely immobile. Surprisingly, the situation reversed after a couple of weeks of aging, as spheres came loose from the HSQ sample and were firmly fixed in the PMMA. We hypothesize that thermo-mechanical wear due to a mismatch in coefficient of thermal expansion ($\alpha_{\mathrm{HSQ}} \approx 20 \times 10^{-6}$ [5], $\alpha_{\mathrm{SiO_2}} \approx 5 \times 10^{-7}$) causes cracks to form

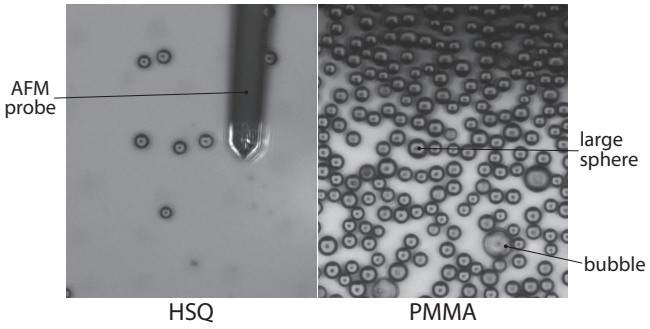

Figure 6.1: A typical (cropped) view from the Park XE7 optical microscope at similar enlargement. The microspheres are roughly 20 µm in diameter for scale. In the HSQ sample, the cantilever probe is visible. In the PMMA sample also larger spheres and bubbles in the resist are visible.

between the HSQ and the glass spheres. Over time, this will cause previously fixed spheres to break loose from the very thin adhesion layer. At the same time, exposure to daylight may have caused the PMMA to further cross-link and harden [6]. This was not further investigated. Roughness measurements were taken on spheres from both samples, without any discernible difference in the results. It is, therefore, unlikely that any contamination from the photoresist was present on top of the spheres.

6.3 Sphere shape and roughness measurement

Using the optical microscope in the Park XE7 AFM, the probe tip was visually aligned with the center of the spheres. Because the tip is hidden from view and its position on the probe is only known to within a few micrometers, the scan area is fine-tuned once the probe is successfully engaged to the surface of the sphere. The center of the scan area is placed to within 250 nm from the apparent top of the sphere. This is achieved by adjusting the center location such that line scans taken in both orthogonal scanning directions result in nearly equal changes in height from center-to-edge.

The effective radius of the sphere is extracted from the measured topography $z\,(x, y)$ by fitting a spherical surface of the form

$$z\,(x, y) = \sqrt{r^2 - (x - x_c)^2 - (y - y_c)^2} + z_0, \tag{6.1}$$

where r is the effective radius, x and y are coordinates along the perpendicular scanning directions, x_c and y_c are the coordinates of the center of the sphere and z_0 is the apparent center height of the sphere. Each scan of the roughly 20 µm diameter spheres measured 5 µm × 5 µm and 128 × 128 pixels. This causes a center-to-edge height difference of approximately 250 nm, which proved to be sufficient to reliably fit Equation (6.1) to the data. It also

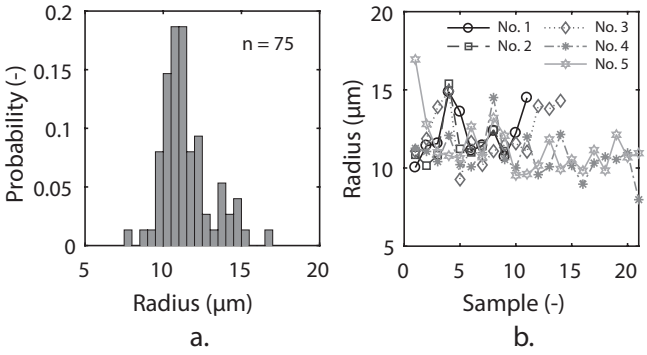

Figure 6.2: a. Probability distribution of effective sphere radii for the grand total of 75 samples; b. Estimated sphere radii for consecutively measured spheres for five different sets of varying number of samples. Within each set no clear trend is visible.

limited the vertical and sideways force of the AFM probe on the sphere, so that the sphere remained immobile.

Equation (6.1) was fitted to the data using the Least Absolute Residuals (LAR) method available in Mathworks Matlab. This method was selected over a least-squares method for its improved robustness against outliers due to local surface features. The fitting function approximates the global surface shape well, and results in an average R^2 coefficient of 0.98 ± 0.01 (1 standard deviation). For the purposes of the heat transfer measurements, the microspheres can thus be approximated well as ideal spheres with the addition of roughness for smaller separations between sphere and prism.

Figure 6.2a depicts the probability distribution of the radii of 75 samples. Close to the mean radius of 11.4 µm, a clear peak is visible for radii between 11 µm and 12 µm. The second peak at 14 µm to 15 µm is consistent with spheres of (approximately) double the volume of those at the main peak. We hypothesize that during manufacturing spheres can coalesce before they solidify. This results in larger spheres of which the volume is an integer multiple of the nominal size. Unfortunately, Corpuscular did not respond to our inquiries regarding the manufacturing process. In this sample, we did not encounter spheres that are larger than twice the nominal volume. The likelihood of their formation is either very low, or they are filtered out after manufacturing when the spheres are sorted for size.

As the AFM probe tip wears down and blunts or becomes contaminated, the derived effective sphere radius is expected to increase monotonically with time. Figure 6.2b shows the extracted radii of five measurement series, with each series representing consecutive measurements. There is no obvious trend present in the data and all sets span a similar range of sphere radii. Tip blunting is therefore not considered an important contributor to the measured sphere radii.

The surface roughness was measured on smaller areas using the same equipment and alignment procedure. The scan size was limited to an area

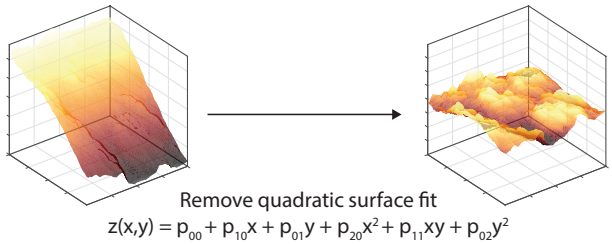

Figure 6.3: Flattening procedure to remove the surface curvature from the surface topography.

of 1 µm × 1 µm and 1000 × 1000 pixels to achieve 1 nm lateral resolution. Because of the small scan area, the height variation from center to edge at a nominal radius of 10 µm is 12.5 nm. In practice, this proves insufficient for fitting the spherical surface to the obtained topography in the presence of roughness. Therefore, the measured topography is flattened by subtracting a fitted second-order polynomial surface instead. By using the second-order polynomial, only the average height, the tilt and the mean curvature are removed, while height variation at shorter length scales, e.g. local features and roughness, remain unaltered.

The measured height distribution for each sphere fits a normal distribution reasonably well, but is sometimes highly skewed. This is caused by the presence of large defects that we found on 5 out of the 40 samples.

The tip radius of the FESPA-V2 probes is too large for roughness estimation. Therefore, roughness measurements were obtained using the SHR300 probes with a maximum tip radius of less than 1 nm. In an attempt to confirm that the tip is not a major contributor to the measured roughness values, the spheres were imaged using (white light) interferometry and 3D optical microscopy. Unfortunately, in both cases, internal reflections caused by the highly curved surfaces resulted in distorted micrographs that could not be interpreted successfully.

Figure 6.4 shows the extracted root mean square surface roughness, R_{q}, and the corresponding maximum peak-to-peak heights. The extracted values show no trend between consecutive samples, which indicates that tip wear does not significantly contribute to measured roughness. The measured root mean square roughness R_q varies between 7.2 nm and 29 nm, while the peak-to-peak values range from 55 nm to 198 nm. The high correlation between R_q and the peak-to-peak values indicates that the roughness is mostly uniform and not the result of tall isolated features. The measured probability distributions of R_q and the peak-to-peak roughness are depicted in Figure 6.5.

As Figure 6.6 shows, the surface roughness does not correlate with the sphere radius. Because the roughness - and thus the probability of premature contact between probe and sample - is independent of sphere size, there is no advantage in picking either smaller or larger spheres for conducting heat transfer measurements at small separations (≤ 100 nm).

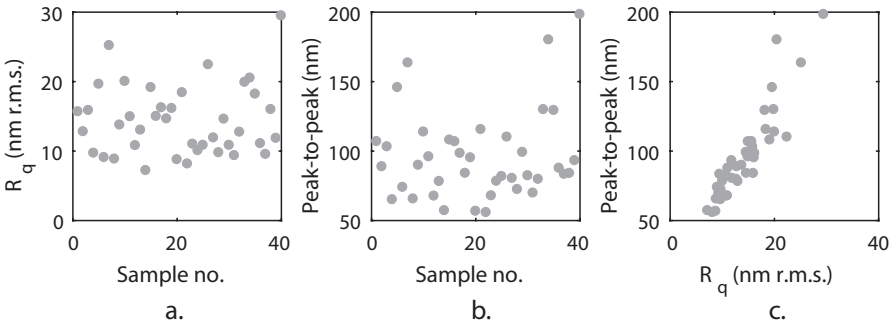

Figure 6.4: (a) Root-mean-square roughness and (b) maximum peak-to-peak height difference for a 1 µm × 1 µm scan area on top of the microspheres as function of sample number. The data was flattened before analysis. Data was obtained using the Park XE7 atomic force microscope and BudgetSensors SHR300 probes. (c) R_q and peak-to-peak values are highly correlated with a Pearson correlation coefficient and Spearman correlation coefficient of 0.91 and 0.93, respectively.

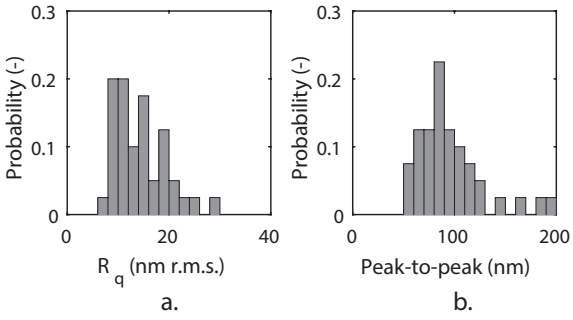

Figure 6.5: Probability distributions of (a) measured root mean square roughness R_q and (b) of measured peak-to-peak roughness of silica microspheres. Sample size of $n = 40$.

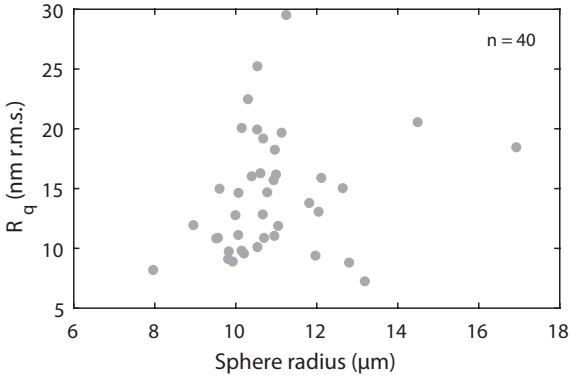

Figure 6.6: The size of the sphere and the root mean square roughness R_q are not correlated. The Pearson and Spearman correlation coeffients are 0.22 and 0.28, respectively.

6.4 Characterizing the roughness of the prism

The prism used in the heat transfer measurements is a modified version of the Newport 10SB10 fused silica prism. One of its corners was removed and all of its optically active surfaces were polished manually. Afterwards, the prism was split into two to create two copies. The first copy was installed in the setup, while the other one was kept as a back-up. To minimize the risk of damage to the original, we have characterized the surface of the second one as a proxy. The surface shape of its edge was measured using a Zygo Verifire 1000 interferometer. To minimize the effect of secondary reflections from the other sides of the prism, these sides are coated with a thin film of Vaseline. This is common practice for surfaces of which the reflections cannot be mitigated in another way [7, 8].

The roughness (short-scale variations in height) is studied separately by removing the waviness (the long-scale height variations) from the measured topography. The waviness can be removed, because in the heat transfer measurements the sphere and prism are separated by no more than 6 µm. To achieve this, a description of the long-scale height variations of the prism surface is required or an algorithm that removes the long-scale height variation. Unfortunately, simple two-dimensional polynomial surfaces or sinusoids do not accurately describe the surface, which makes it difficult to remove the waviness in a single step. Therefore, n sections of 1 mm × 1 mm are randomly selected from the surface data and studied individually. Each section is flattened by removing a second-order polynomial surface from the height data. The best result is obtained using a least-squares method as depicted in Fig-

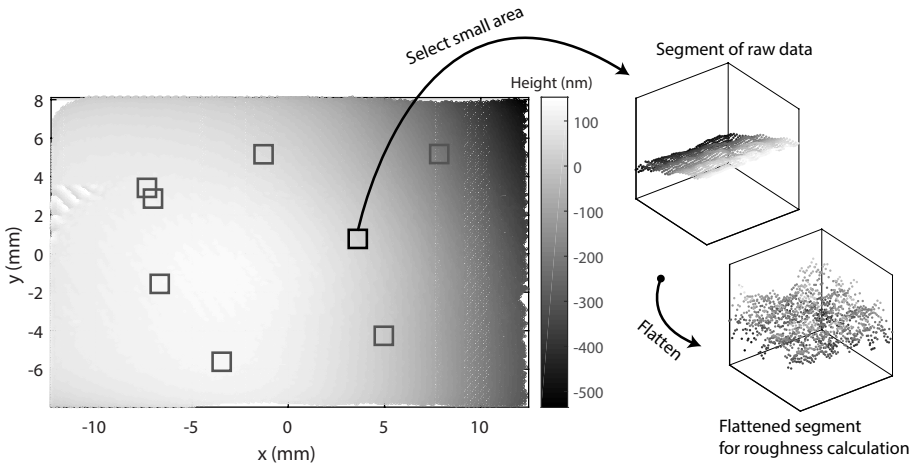

Figure 6.7: The raw data obtained from the Zygo Verifire 1000 interferometer is sampled at 1000 randomly chosen 1 mm × 1 mm areas (left). Each raw sample (top right) is flattened by subtracting a best-fit second-order polynomial surface to be left with the roughness (bottom right).

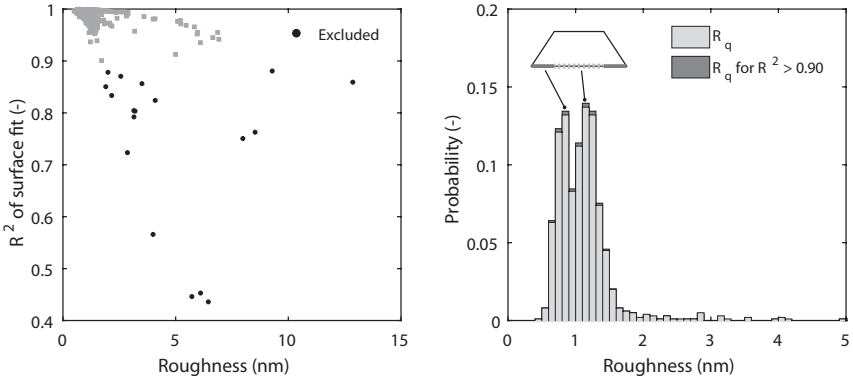

Figure 6.8: The quality of each surface fit is judged based on the R^2 value of the polynomial fit. Fits with values $R^2 \leq 0.9$ are excluded in estimating the surface roughness (left). The mean surface roughness is 1.2 nm r.m.s. (right). The secondary peak is hypothesized to be a spurious effect caused by secondary reflections from the back surface of the prism. The roughness axis has been limited to 5 nm. The inset shows a side view of the prism with the areas associated with the separate peaks highlighted. The statistical distributions of all data points and of all data points for which $R^2 \geq 0.9$ are laid on top of each other.

ure 6.7. The size of each section is significantly bigger than the microspheres, but small enough for a second order polynomial surface to be used for the flattening procedure. The centroid for each section is chosen at random using uniform probability distribution functions for both coordinates. This ensures that the results are not biased by oversampling or undersampling certain spatial frequencies that may be present in the surface topography.

The quality of each polynomial fit is judged by its R^2 value. All sections that resulted in a $R^2 \leq 0.9$ are excluded from the analysis, to prevent the waviness from factoring into the surface roughness estimate. In this manner, the root mean square roughness is estimated at 1.2 nm, with peaks of high probability at 0.8 nm and 1.2 nm. The probability distribution of the roughness of the sections is shown in Figure 6.8. The statistical distribution does not change significantly when the worser fits are excluded, as is apparent from plotting the distributions on top of each other.

The studied surface of the prism is in the center parallel to the back surface, as shown in the inset of Figure 6.8. The white light interferometer picks up spurious reflections from this surface, causing an increased apparent roughness. This was confirmed with local roughness measurements taken with a Bruker NPFlex optical profiler, that does not pick up these spurious reflections because of its limited field of view. The roughness values obtained from the center of the prism using the optical profiler were locally less than 0.6 nm r.m.s. (using a Gaussian filter to separate the waviness and roughness instead of a polynomial fit).

6.5 Roughness & shape limitations on heat transfer measurements

The microspheres can be described well by ideal spheres of an effective radius of approximately 11.4 µm and a root mean square roughness of 29 nm. The roughness of the prism is by comparison to the microspheres of no concern. For sphere-prism separations below 100 nm, the likelihood of point contacts increases due to the roughness of the microspheres and the presence of local features that can reach a height of 100 nm. This agrees well with results presented by Rousseau *et al.* [1], that show that their results had to be shifted by 31.8 nm to compensate for a local feature that caused premature contact between the sphere and their sample. Point contacts are troublesome, because the measured heat transfer is no longer solely determined by radiation, but can also contain some conduction.

We expect that the sphere roughness will also cause drastic deviations from the predicted heat transfer for distances smaller than 100 nm if point contact is not present. As predicted by Biehs and Greffet [9] and Krüger *et al.* [10], the roughness will severely limit the increase in heat transfer below 100 nm and diffuse reflections will cause the transfer to level off.

Considerably smoother glass microspheres are available. For example, Van Zwol [11] shows that Duke Borosilicate Glass 9020 spheres are very smooth at a roughness of 0.7 nm±0.1 nm r.m.s. However, we did not select these, because of the unknown composition of the borosilicate glass which may contain parts boric acid and alumina amongst others. This makes it difficult to estimate the dielectric function, that is necessary for comparison with theoretical models.

6.6 Conclusions

The minimum distance at which heat transfer experiments can be conducted is limited by the roughness of the microsphere and the occurance of tall features on its surface. The selected microspheres have a fairly consistent average radius of 11.4 µm and a root mean square roughness of 29 nm. However, higher local features exist on the surface that can reach up to 198 nm tall (peak-to-peak). These features can cause premature contact between the sphere and the sample. The roughness of the prism (the sample) is significantly lower with a mean value of 1.2 nm r.m.s. and is negligible in comparison to the spheres. The roughness of the sphere limits the minimum distance for heat transfer experiments in practice to approximately 100 nm. For smaller distances the premature contact is likely and deviations from the ideal smooth spheres assumed in theoretical models will be noticeable. Smoother microspheres have to be acquired to achieve smaller separations in future experiments.

Acknowledgments

The author would like to thank dr. Sasan Keyvani of Delft University of Technology for preparing the HSQ and PMMA coated samples in the cleanroom and Chester Schlagwein and dr. Guido Gubbels of TNO Optical Manufacturing for imaging the prism under the white light interferometer and optical profiler.

Bibliography

[1] E. Rousseau, A. Siria, G. Jourdan, S. Volz, F. Comin, J. Chevrier, and J.-J. Greffet. Radiative heat transfer at the nanoscale. *Nature Photonics*, 3(9):514–517, 2009.

[2] Microspheres-Nanospheres. Monodisperse plain SiO2 silica nanospheres and microspheres, 2011.

[3] Kavli Nanolab Delft. XR-1541.006 (FOx-12) Recipe.

[4] Kavli Nanolab Delft. PMMA for EBPG Recipe.

[5] J.-H. Zhao, I. Malik, T. Ryan, E. T. Ogawa, P. S. Ho, W.-Y. Shih, A. J. McKerrow, and K. J. Taylor. Thermomechanical properties and moisture uptake characteristics of hydrogen silsesquioxane submicron films. *Applied Physics Letters*, 74(7):944–946, 1999.

[6] D. J. Carbaugh, J. T. Wright, R. Parthiban, and F. Rahman. Photolithography with polymethyl methacrylate (PMMA). *Semiconductor Science and Technology*, 31(2):025010, 2016.

[7] C. Salsbury and A. G. Olszak. Spectrally controlled interferometry. *Applied Optics*, 56(28):7781, 2017.

[8] T. Sun, W. Zheng, Y. Yu, K. Yan, A. Asundi, and S. Valukh. Algorithm for Surfaces Profiles and Thickness Variation Measurement of a Transparent Plate Using a Fizeau Interferometer with Wavelength Tuning. *Applied Sciences*, 9(11):2349, 2019.

[9] S.-A. Biehs and J.-J. Greffet. Influence of roughness on near-field heat transfer between two plates. *Physical Review B*, 82(24):245410, 2010.

[10] M. Krüger, V. A. Golyk, G. Bimonte, and M. Kardar. Interplay of roughness/modulation and curvature for surface interactions at proximity. *EPL (Europhysics Letters)*, 104(4):41001, 2013.

[11] P. J. van Zwol. Roughness and microspheres. In *Contact mode Casimir and capillary force measurements*, chapter 3, p. 23–27. University of Groningen, Groningen, 2011.

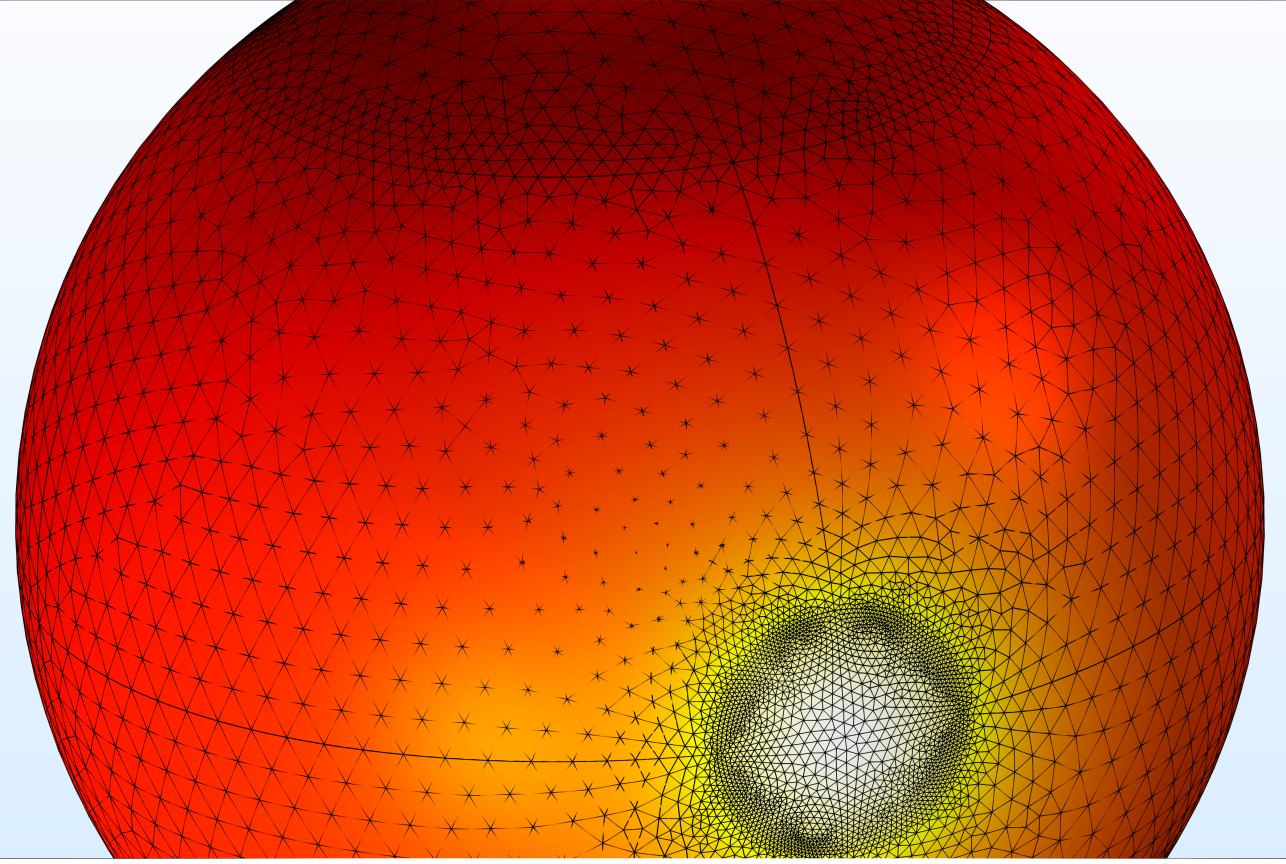

7. Lumped-parameter model for heat conduction across a solid sphere

Thermal network modeling or lumped parameter modeling [1, 2] is a method for evaluating heat fluxes and temperature gradients in complex geometries that is well suited for early stages of analysis and development. In this method, the geometry is simplified to one-dimensional conductors of simple shapes, such as cuboids, (hollow) spheres, and cylinders [3, 4]. For these shapes closed-form analytical solutions exist that are compact enough for evaluation by hand. These solutions use Fourier's law to express the thermal conductance (or its reciprocal, the thermal resistance) between two surfaces on a body. Typically, such a solution contains a measure of the cross-sectional area A of the conductor, the conductivity of the material k and the distance between the two ends L (see Figure 7.1). The simplification of the geometry

Title picture: rendering of the temperature distribution on the surface of a sphere as calculated using COMSOL Multiphysics for two unequal contact areas. Rendering by Roy Bijster.

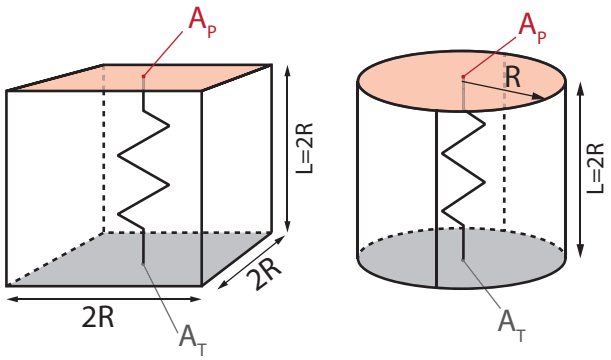

Figure 7.1: One-dimensional heat conduction through a sphere can be approximated by replacing the sphere using a cube or a cylinder. The one-dimensional representation in the form of a thermal resistance is sketched inside the cube and the cylinder.

leads to a reduction in accuracy, but provides the benefits of relating the design parameters directly to the temperatures and fluxes of interest while remaining tractable for hand calculation. For a cuboid - a shape that is often used to approximate one-dimensional conduction - the conductance can be written as

$$G \equiv \frac{P}{\Delta T} = \frac{kA}{L}. \tag{7.1}$$

in which P is the heat flow through the body and ΔT is the temperature difference over that body. While this is a simple and often useful relation for first-order estimations, it is inadequate for geometries in which this reduction to one dimension is not obvious, such as for the conduction of heat *across* a sphere. In contrast to the well-known problem for heat conduction *through* a sphere - between its center and its boundary - *across* is used here to name the problem of heat conduction from one area on its surface to another area on its surface. This is, for example, encountered in the calculation of the effective conductance of a packed bed of spheres [5–7], the calculation of conduction through granular media [8, 9], in thermal insulation [10] and in estimating the effective heat transfer through spherical probes in scanning probe microscopy [11, 12]. Although Kaganer [13] and Chan and Tien [5] presented theoretical descriptions of heat conduction across a sphere, their solutions use infinite series. This renders them unsuitable for calculation by hand.

In this chapter, the conduction across a sphere is studied numerically and simple relations suitable for hand calculations and lumped parameter modeling are presented. The presented results are particularly useful for the practicing engineer and for first-order estimation.

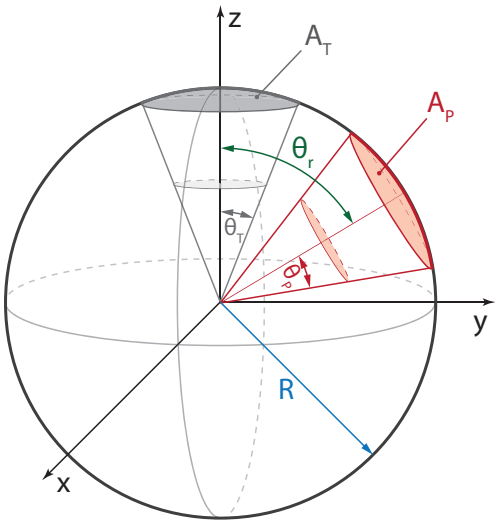

Figure 7.2: Sphere with one spherical cap at a constant temperature, and the other with a constant heat input.

7.1 Geometry

The studied geometry is depicted in Figure 7.2 and consists of a sphere of radius R with non-overlapping circular caps A_T and A_P that participate in the heat transfer across the sphere. The remaining boundary is considered to be isolated. The two boundaries are separated by an angle θ_r and the central axis of each boundary is contained within the yz-plane without the loss of generality. The areas of the two caps are given as fractions H_T and H_P of the total area of the sphere as

$$A_i = 4\pi H_i R^2, \tag{7.2}$$

and the related opening half-angles equal to

$$\theta_i = \arccos\left(1 - 2H_i\right), \tag{7.3}$$

with $i = \{T, P\}$.

7.2 One-dimensional approximation

Several issues arise when trying to approximate the heat conduction across a sphere as a one-dimensional problem using a relation similar to Equation (7.1). First, for a sphere the effective distance L between the source and the sink cannot easily be captured in a single parameter. Second, the cross-sectional area A of the conductor is not constant and scales with the radius. If the heat conduction across a sphere is approximated using Equation (7.1), the geometry can be adapted to reflect these issues. For example,

the sphere can be replaced by either a cube of sides $2R$ or a cylinder of radius R and height $2R$ as depicted in Figure 7.1. Note that these simplified geometries only approximate the related sphere for $\theta_r = \pi$ and $H_T = H_P = 1/2$.

Using a cube for the approximation, the conductance of the sphere is estimated as

$$G_{\text{cube}} = k\frac{(2R)^2}{2R} = 2kR, \tag{7.4}$$

while using the cylinder results in

$$G_{\text{cyl.}} = k\frac{(\pi R^2)}{2R} = \frac{\pi}{2}kR. \tag{7.5}$$

These approximations are special cases of the general form

$$G_s = kRf\left(H_T, H_P, \theta_r\right), \tag{7.6}$$

where the function $f\left(H_T, H_P, \theta_r\right)$ is a shape factor that accounts for the relative sizes and positions of the boundaries. These cube and cylinder approximations provide the correct order of magnitude ($f\left(1/2, 1/2, \pi\right) = \{2, \pi/2\}$, respectively), but underestimate the actual value of the shape factor of ≈ 4.82. In the remainder of this paper, the shape factors for different configurations of heat transfer across the sphere are determined. These shape factors provide a better estimate of the conductance and are applicable to a much broader set of configurations.

7.3 Analytical solution

In 1966, Kaganer [13] solved the problem of heat conduction across a sphere analytically for the case with small, flattened contact areas with $H_T = H_P = H$ and $\theta_r = \pi$. Kaganer's expression for the thermal resistance $R_{\text{kag.}}$ can be written as

$$\begin{aligned} R_{\text{kag.}} = {} & \frac{1}{kR}\frac{1}{4\pi H\left(1-H\right)}\times \\ & \times\sum_{n=0}^{\infty}\left(\frac{1}{2n+1}\left[P_{2n}\left(1-2H\right)-P_{2n+2}\left(1-2H\right)\right]\times\right. \\ & \left.\times\left[1+P_{2n+1}\left(1-2H\right)\right]\right) \end{aligned} \tag{7.7}$$

with P_k the Legendre polynomial of the first kind of k^{th} order. The thermal conductance $G_{\text{kag.}}$ is obtained as its reciprocal: $G_{\text{kag.}} = 1/R_{\text{kag.}}$.

Kaganer's series solution requires an infinite summation that in practice needs to be truncated. The truncation error of Equation (7.7) is calculated as a function of H and the number of terms n with respect to the case of $n = 1000$. For $n \geq 6$ the relative error is $\leq 10\,\%$, and for $n \geq 36$ the relative error is $\leq 1\,\%$, irrespective of the value of H. A solution very similar

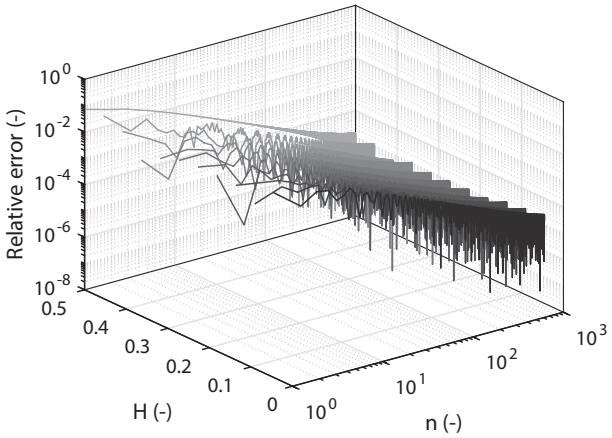

Figure 7.3: Convergence of Kaganer's series solution for the conduction of heat through a sphere as a function of the relative size of the caps H and the number of terms n in the summation of Equation (7.7). The relative error is calculated with respect to the solution for $n = 1000$.

to Kaganer's was derived by Chan and Tien [5] for both solid and hollow spheres. For an alternative model to find application in practice, it must require fewer terms for equal accuracy or it must be applicable to a broader range of configurations and parameters.

Kaganer simplified the solution by projecting the contact area onto a plane and effectively ignoring the curvature in the contact areas. Moreover, Kaganer calculates the effective temperature of the cap as the arithmethic mean of the maximum temperature of each cap and the temperature at its perimeter. These effective temperatures are used to calculate the thermal resistance. These approximations are valid for small values of H, but underestimate the contact area and temperature gradients across each cap. The comparison of Kaganer's solution with finite-element simulations that is presented in Figure 7.5, shows that the Kaganer approximation starts to underestimate the conductance for $H \geq 0.1$.

7.4 Numerical results and discussion

The conduction of heat across a sphere is described by the three-dimensional heat equation. Because the boundary conditions are not straightforward, this problem does not lend itself well for closed-form analytical solutions. Therefore, an empirical shape factor $f\left(H_T, H_P, \theta_r\right)$ is fitted to the solution to the heat equation that is obtained using finite-element software (COMSOL Multiphysics). This results in relations that are considerably more compact than Kaganer's solution and that can be used for lumped parameter modeling at equal or better accuracy.

Two sets of boundary conditions are of practical interest. In the first set,

a constant uniform heat flux is applied to area A_P (a Neumann boundary), while area A_T is kept at a constant temperature (a Dirichlet boundary). In the second set, a constant uniform heat flux is applied to area A_P and the same uniform heat flux is subtracted at area A_T (similar to Kaganer's solution). Although these boundary conditions clearly differ from each other, the temperature difference is the same for both cases in the one-dimensional heat equation. In the three-dimensional case for the sphere, however, a temperature gradient exists on the Neumann boundary. The magnitude of this gradient depends on the size of the cap and its vicinity to the other cap. For this reason, both cases are studied numerically and put side-by-side in the results.

A unit sphere with a conductivity of 1 is meshed using 2×10^5 to 4×10^5 tetrahedral elements (auto-meshed with mesh-adaptation results in a mesh size that is smaller at the source and the sink when H_i is smaller to capture the larger thermal gradients). The effective conductance of the sphere is calculated from the numerical results as

$$G_e \equiv \frac{P}{\Delta T} = \frac{P}{\text{mean}\,(T_{A_T}) - \text{mean}\,(T_{A_P})}, \tag{7.8}$$

where $\text{mean}\,(T_i) = 1/A_i \int_{A_i} T(R,\theta)\,\mathrm{d}A_i$ and A_i is the area of the cap. To extract the shape factor according to Equation (7.6), a function of the form

$$\begin{aligned} f\,(H_P, H_T) = {} & a_1\,(H_P^{e_1} + H_T^{e_1}) \\ & + a_2\,(H_P^{e_2} + H_T^{e_2}) \\ & + a_3 H_P^{e_1} H_T^{e_1} + a_4 H_P^{e_1} H_T^{e_2} \\ & + a_5 H_P^{e_2} H_T^{e_1} + a_6 H_P^{e_2} H_T^{e_2}, \end{aligned} \tag{7.9}$$

is fitted to the numerical results for $H \in [0.001, 0.5]$ using the Least Absolute Residuals (LAR) method available in Mathworks Matlab and the Levenberg-Marquardt algorithm. It is important to note that this function is only valid on the provided domain and cannot be used for extrapolation, as it yields a finite conductance for $H_i = 0$. In the special cases where $H_T = H_P = H$, the shape factor is simplified to

$$f\,(H) = c_1 H^{c_2} + c_3 H^{c_4}. \tag{7.10}$$

7.4.1 Opposing boundaries of equal size

For $H_T = H_P = H$, $H \in [0.001, 0.5]$, $\theta_r = \pi$, heat has to traverse through the entire diameter of the sphere. The shape factor $f\,(H_T, H_P, \theta_r) = f\,(H)$ can be written as

$$f\,(H) = 3.584 H^{0.516} + 28.272 H^{3.610}, \tag{7.11}$$

for the case of A_T at constant temperature (Standard Sum of Errors (SSE) of 6.7×10^{-3}, $R^2 = 0.999$), and can be written as

$$f\,(H) = 3.176 H^{0.495} + 11.499 H^{2.907}, \tag{7.12}$$

for the case at which A_T is a constant sink of $-P$ (SSE $= 1.3 \times 10^{-3}$, $R^2 = 1.000$). It is interesting to note that in both cases exponents close to $1/2$ and 3 are found. The square root like behavior given by the first term, gives a good approximation for values up to $H_i = 0.1$. In fact,

$$f\left(H, \theta_r = \pi\right) \approx \frac{10}{3}\sqrt{H}, \tag{7.13}$$

is an excellent fit for $H \in [0.001, 0.1]$ with maximum errors of 7.9 % and 4.8 % for A_T at constant temperature and A_T at constant power, respectively. The conductance for this domain can thus be written as

$$G \approx \frac{10}{3}\sqrt{H}kR. \tag{7.14}$$

The fitting coefficient has been approximated by the fraction $10/3$ for its simplicity in use.

To understand this behavior, consider an approximation of the sphere as a stack of three cylindrical conductors as depicted in Figure 7.4. The top and bottom cylinder are of identical dimensions (radius r and height L) and represent the boundaries A_P and A_T. The center cylinder is similar to that of Equation (7.5), but its height is adjusted to accomodate for the height of the other two cylinders ($2R - 2L$ instead of $2L$). The areas A_P and A_T are set as a fraction H of the total available area on the cylinder for heat transfer

$$A_i = 2\pi H R^2, \tag{7.15}$$

so that

$$r = \sqrt{2H}R. \tag{7.16}$$

The total conductance of the stack is equal to

$$G = k\frac{\pi}{2}\frac{2HR^2}{L + 2H\left(R - L\right)}. \tag{7.17}$$

If L is constant, the conductance G is proportional to H. However, for a sphere L is a function of r. Consider, for example, $L = ar$, for which case the conductance equals

$$G = kR\frac{\pi\sqrt{2H}}{2\left(a + \sqrt{2H} - 2aH\right)}. \tag{7.18}$$

This result provides a conductance that is proportional to $\sqrt{H}$ for small H and can be well approximated by Equation (7.10) on the domain $H \in [0, 0.5]$.

The simulated and fitted results are plotted in Figure 7.5. The difference between the two boundary conditions at larger values for H is caused by the temperature gradient in the boundary A_T. This effect gets more pronounced as the edges of the boundaries A_T and A_P are closer together (larger values of H). Figure 7.5 also shows the underestimations present in Kaganer's solution for H exceeding 0.1. The relative error of the fitting function is less than 3 % with respect to the finite-element method calculations for $H \geq 0.01$ as shown in Figure 7.6.

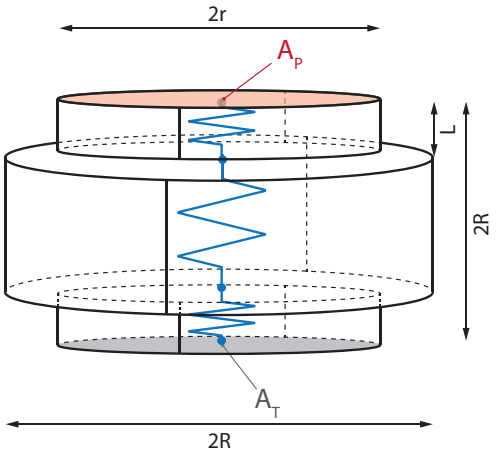

Figure 7.4: Approximation of a sphere as a stack of three cylinders with a total height of $2R$ and a maximum diameter of $2R$. The source and the sink of variable size are represented by two cylinders of radius r and height L.

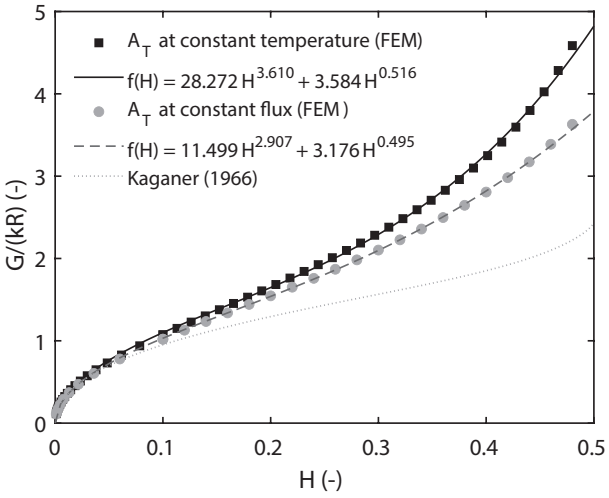

Figure 7.5: Shape factor for the conductance across a sphere for $H_T = H_P = H$ and $\theta_r = \pi$.

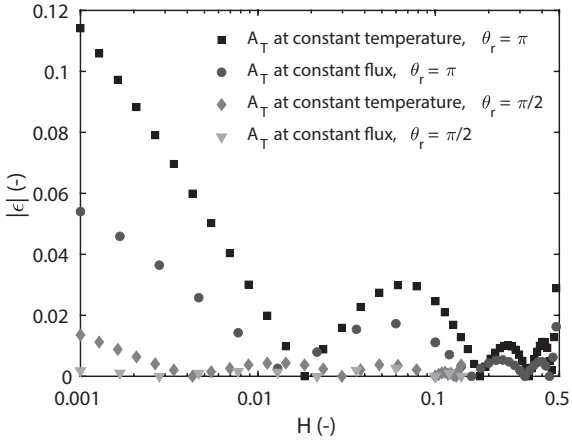

Figure 7.6: Relative error between the fitting functions and the finite-element method simulations for $H_T = H_P = H$ and $\theta_r = \{\pi/2, \pi\}$.

7.4.2 Orthogonal boundaries of equal size

For $H_T = H_P = H$, $H \in \left[0.001, \frac{1}{2}\left(1 - \frac{1}{\sqrt{2}}\right)\right]$, $\theta_r = \pi/2$, heat only has to traverse part of the sphere to reach the sink. The domain is chosen so that the two boundaries do not overlap. In this case, the shape factor $f\left(H_T, H_P, \theta_r\right) = f\left(H\right)$ can be written as

$$f\left(H\right) = 3.536H^{0.496} + 35.508H^{2.290}, \tag{7.19}$$

for the case of A_T at constant temperature ($\mathrm{SSE} = 1.1 \times 10^{-4}$, $R^2 = 1.000$), and can be written as

$$f\left(H\right) = 3.253H^{0.488} + 13.769H^{1.948}, \tag{7.20}$$

for the case at which A_T is a constant sink of $-P$ ($\mathrm{SSE} = 3.1 \times 10^{-6}$, $R^2 = 1.000$). The results of the simulations and the corresponding fitting functions are shown in Figure 7.7. The fitted shape factors give an excellent match with the FEM results, with a relative error less than 1.4 % for all calculated values of H as shown in Figure 7.6.

In both fitting functions, the first terms are close to multiples of $\sqrt{H}$. This result is very similar to that of $H_T = H_P$, $\theta_r = \pi$ for small values of H. However, the approximation using only the square-root term deteriorates at comparatively smaller values of H due to the proximity between the source and the sink in this configuration and the non-linearities that this introduces. On the domain $H \in [0.001, 0.1]$, the shape factor can be approximated as

$$f\left(H, \theta_r = \pi/2\right) \approx 3.6\sqrt{H}, \tag{7.21}$$

and yields maximum errors of 13 % and 5.9 % for A_T at constant temperature and A_T at constant power, respectively.

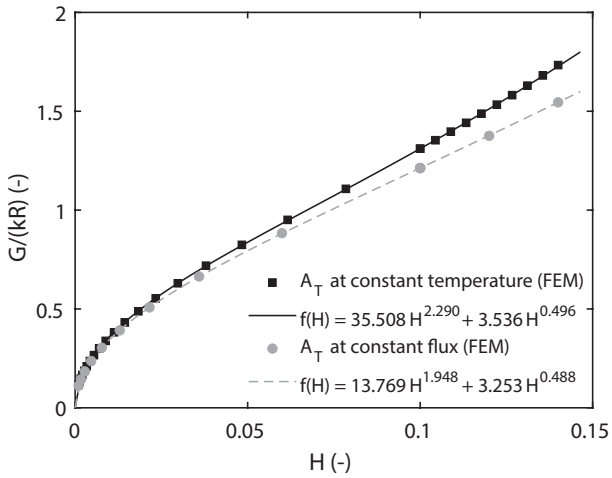

Figure 7.7: Shape factor for the conductance of a sphere for $H_T = H_P = H$ and $\theta_r = \frac{\pi}{2}$.

7.4.3 Opposing boundaries of unequal size

The two boundaries H_T and H_P do not have to be of equal size. Figure 7.8 and Figure 7.9 present the shape factors for easy lookup for the boundary conditions of A_T at a constant temperature or as a constant sink, respectively.

For the case $H_T, H_P \in [0.001, 0.5]$ and $\theta_r = \pi$, the calculated shape factors $f\left(H_T, H_P, \theta_r\right) = f\left(H_T, H_P\right)$ are fitted to Equation (7.6). The parameters are listed in Table 7.1. To achieve accurate fits to the numerical data, the domain is split into two sub-domains. The first sub-domain covers the cases where H_T and H_P are both in $[0.001, 0.1]$. The second sub-domain covers all the other cases where either one or both parameters are larger than 0.1. The fitting errors are plotted for A_T as an area of constant temperature (factors f_{11} and f_{12}) and A_T as a heat sink of uniform power $-P$ (factors f_{21} and f_{22}) in Figure 7.10 and Figure 7.11, respectively. The average error with respect to the simulation data is better than 2 % in both cases. While the maximum fitting error is 33 %, it only exceeds 10 % when the values of H_T and H_P are at opposing extremes (for example, $H_T = 0.001$ and $H_P = 0.48$).

7.4.4 Orthogonal boundaries of unequal size

The shape factors for unequally sized, orthogonal boundaries can be calculated in a similar fashion when $H_T, H_P \in [0.001, 0.5]$ and $\theta_r = \pi/2$. The combinations of H_T and H_P are constrained by $\theta_T + \theta_P \leq \pi/2$ to prevent the areas from overlapping. The shape factors are shown in Figure 7.12 and Figure 7.13 for easy look-up for the cases of A_T at a constant temperature or as a constant sink, respectively.

This particular configuration is of interest in estimations of heat conduction through spherical probes in scanning probe microscopy and measure-

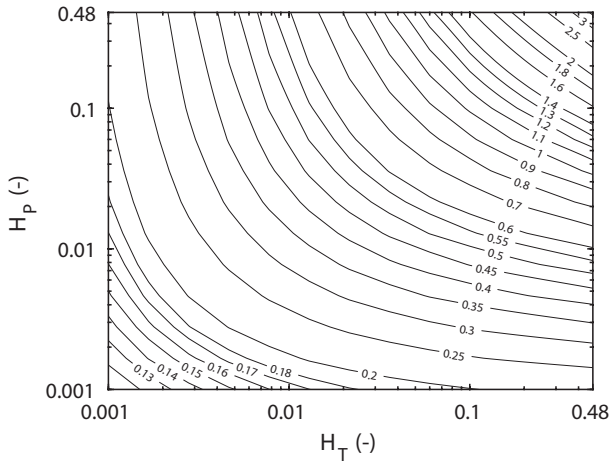

Figure 7.8: Values of the shape factor for heat conduction across a sphere with boundary A_T at constant temperature and for $\theta_r = \pi$.

ments of near-field radiative heat transfer [11, 12], where a small area of the sphere is heated, while the other is glued to a sink with a larger contact area.

The shape factors $f\left(H_T, H_P, \theta_r\right) = f\left(H_T, H_P\right)$ are obtained by fitting the simulation data to Equation (7.6). The parameters are listed in Table 7.1, with f_{31} and f_{32} for the cases where A_T is an area of constant temperature and f_{41} and f_{42} for the cases where A_T is a heat sink of constant uniform power $-P$. The fitting errors for these cases are plotted in Figure 7.14 and Figure 7.15. On average, the fitting error is 1.5 %. Similar to the cases $\theta_r = \pi$, the error only exceeds 10 % when the values of H_T and H_P are at opposing extremes.

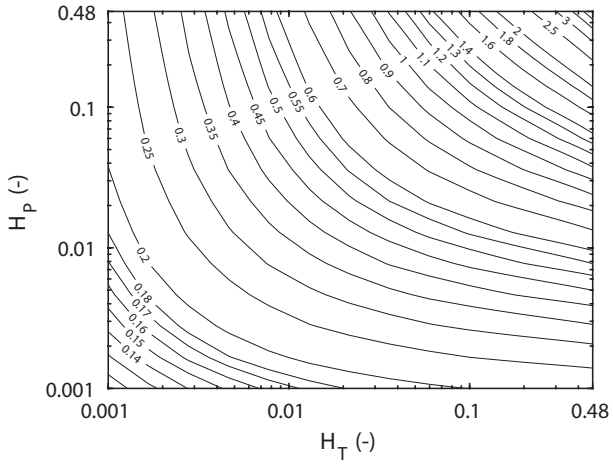

Figure 7.9: Values of the shape factor for heat conduction across a sphere with boundary A_T as a constant sink and for $\theta_r = \pi$.

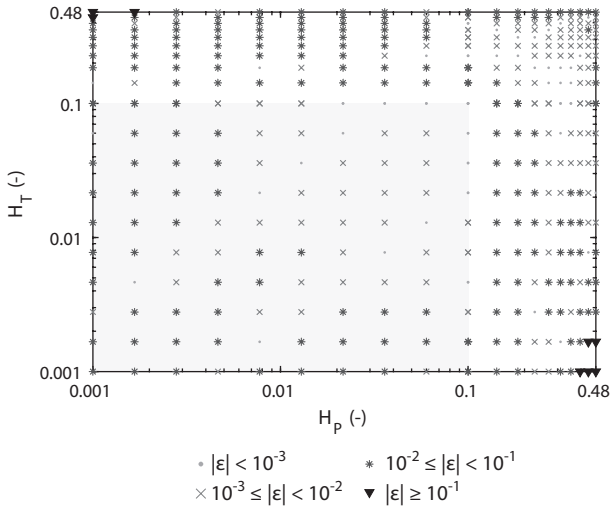

Figure 7.10: Relative error for the fitting function of Eqn. 7.6 with respect to the simulated data for the conductance of a sphere for $H_T \neq H_P$ and $\theta_r = \pi$. The maximum fitting error is 27 % and the mean fitting error is 2.0 %. The domain is split into two. The gray area is covered using the parameters of f_{11} in Table 7.1, while the white area is covered using the parameters of f_{12}.

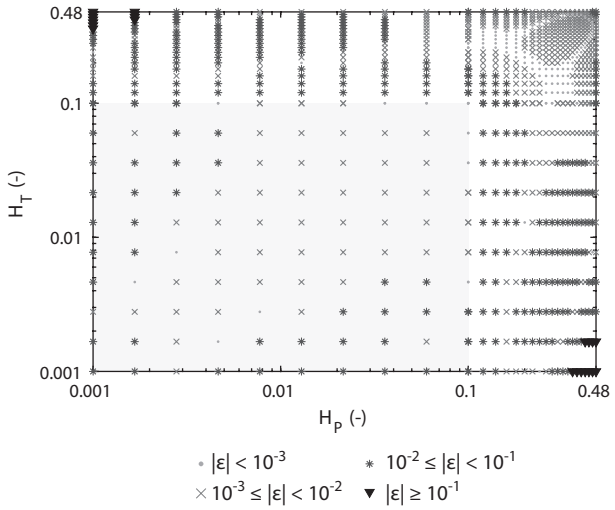

Figure 7.11: Relative error for the fitting function of Eqn. 7.6 with respect to the simulated data for the conductance of a sphere for $H_T \neq H_P$ and $\theta_r = \pi$. The maximum fitting error is 33 % and the mean fitting error is 1.6 %. The domain is split into two. The gray area is covered using the parameters of f_{21} in Table 7.1, while the white area is covered using the parameters of f_{22}.

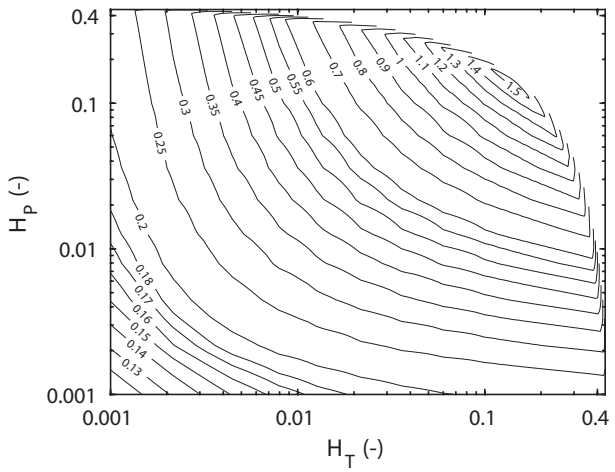

Figure 7.12: Values of the shape factor for heat conduction across a sphere with boundary A_T at constant temperature and for $\theta_r = \pi/2$.

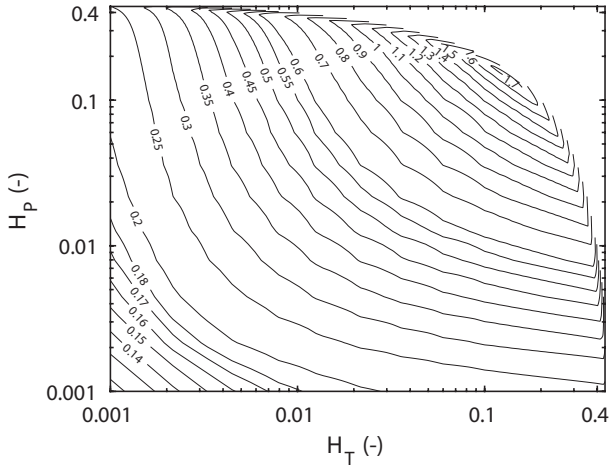

Figure 7.13: Values of the shape factor for heat conduction across a sphere with boundary A_T as a constant sink and for $\theta_r = \pi/2$.

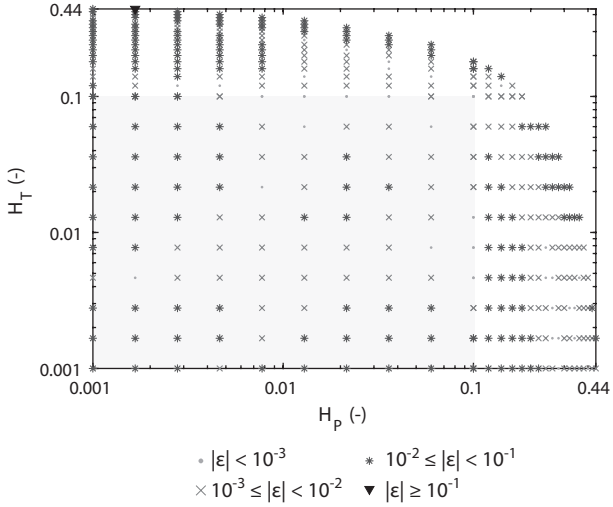

Figure 7.14: Relative error for the fitting function of Eqn. 7.6 with respect to the simulated data for the conductance of a sphere for $H_T \neq H_P$ and $\theta_r = \pi/2$. The maximum fitting error is 11 % and the mean fitting error is 1.5 %. The gray area is covered using the parameters of f_{31} in Table 7.1, while the white area is covered using the parameters of f_{32}.

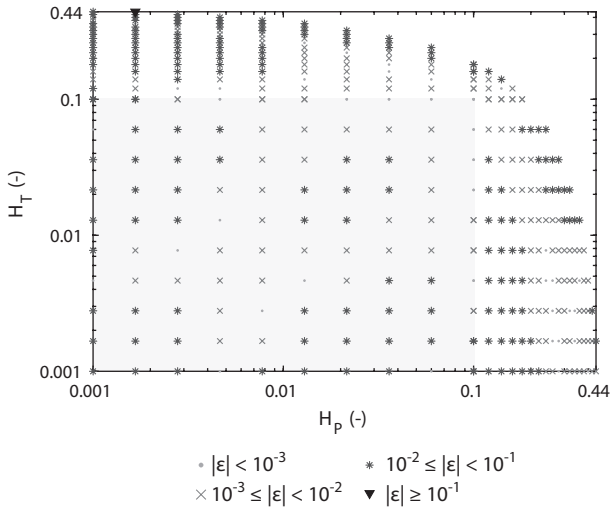

Figure 7.15: Relative error for the fitting function of Eqn. 7.6 with respect to the simulated data for the conductance of a sphere for $H_T \neq H_P$ and $\theta_r = \pi/2$. The maximum fitting error is 11 % and the mean fitting error is 1.5 %. The gray area is covered using the parameters of f_{41} in Table 7.1, while the white area is covered using the parameters of f_{42}.

Table 7.1: Parameters for the shape factors of form $f(H_P, H_T) = a_1\left(H_P^{e1} + H_T^{e1}\right) + a_2\left(H_P^{e2} + H_T^{e2}\right) + a_3 H_P^{e1} H_T^{e1} + a_4 H_P^{e1} H_T^{e2} + a_5 H_P^{e2} H_T^{e1} + a_6 H_P^{e2} H_T^{e2}$. For each situation, the domain is split into two areas where f_{x1} is the subdomain where both H_T and H_P are in the domain from $H_i = 0.001 - 0.1$ and f_{x2} covers the rest of the domain. For each fitting function, the Standard Sum of Errors (SSE) and the R^2 value are listed.

	$\theta_\mathbf{r} = \pi$				$\theta_\mathbf{r} = \pi/\mathbf{2}$			
	Constant T		**Constant -P**		**Constant T**		**Constant -P**	
	f_{11}	f_{12}	f_{21}	f_{22}	f_{31}	f_{32}	f_{41}	f_{42}
a_1	1.82	−0.826	−1.778	−0.149	2.03	1.61	−1.51	1.77
a_2	−2.33	−0.0985	1.243	−0.713	−2.17	−1.17	1.21	−1.48
a_3	719	37.1	688	4.50	753	22.1	1512	50.5
a_4	−723	0.630	−682	0.469	−708	−9.93	−1551	−37.4
a_5	−719	0.424	−682	0.470	−711	−9.97	−1551	−37.4
a_6	729	5.06	682	14.1	676	8.75	1598	33.4
e_1	0.356	2.13	0.349	0.297	0.353	0.504	0.335	0.467
e_2	0.379	0.333	0.328	1.75	0.324	0.187	0.353	0.300
SSE	2.4×10^{-3}	2.5×10^{-2}	6.4×10^{-4}	1.0×10^{-2}	2.8×10^{-3}	9.2×10^{-3}	2.5×10^{-3}	3.2×10^{-3}
R^2	0.9996	0.9999	0.9999	1.0000	0.9997	0.9998	0.9997	0.9999

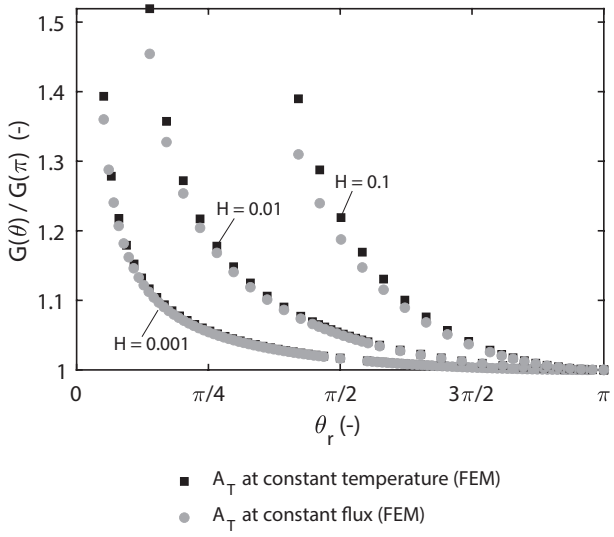

Figure 7.16: Change of conductance with angle θ_r for $H = 0.001$, $H = 0.01$ and $H = 0.1$. The angles are constrained such that the caps do not overlap.

7.4.5 Dependence on θ_r

The effective distance between the two areas A_P and A_T is set by the sizes of the areas and the angle θ_r between them. The conductance relative to the conduction of the case $\theta_t = \pi$ is plotted in Figure 7.16 for three values of H. The conductance drops quickly as the relative distance between A_T and A_P increases.

It is interesting to note that the difference in conductance between two adjacent spheres packed in a face-centered cubic (FCC, $\theta_r = \pi/2$) [14] or in a hexagonal close-packed (HCP, $\theta_r = \pi/3$) configuration is small at approximately 2 % for $H = 0.001$ and approximately 7 % for $H = 0.01$ and that the results presented here for $\theta_r = \pi/2$ can be used with reasonable accuracy in studying the conductance through a packed bed of spheres for either configuration. It should be noted though that in this chapter each sphere only has one source and one sink, while in a packed bed of spheres in FCC or HCP configuration the number of touching neighbors (the so called *coordination number*) is 12. Based on the results above an HCP-packed bed is expected to have a (slightly) higher conductance than an FCC-packed bed, even though they have the same configuration number.

7.5 Implications for conductance of the microsphere

The radiative heat transfer between a sphere and a flat surface depends on the distance, and scales in the near-field regime with the separation distance d

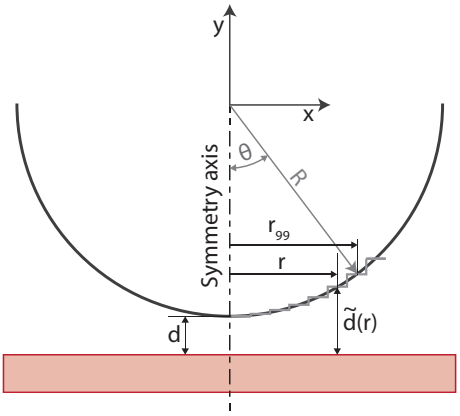

Figure 7.17: With the Derjaguin approximation for heat transfer, a sphere is approximated as concentric rings that each represent a plate that is parallel to the sample.

as $1/d^2$ according to the Derjaguin approximation [12]. This method reduces the spherical surface to a series of concentric rings. The heat transfer between each ring and the sample is approximated as that between two parallel plates. This approximation is valid, when the separation d is much smaller than the radius of the spheres as depicted in Figure 7.17.

Using the Derjaguin approximation, the conductance of the vacuum gap separating the sphere and the flat surface is written as

$$G_{\text{Derjaguin}}\left(d,T\right)=\int_0^R h\left[\tilde{d}\left(r\right),T\right]2\pi r\,\mathrm{d}r, \tag{7.22}$$

where the local separation $\tilde{d}$ is equal to $\tilde{d}\left(r\right)=d+R-\sqrt{R^2-r^2}$ and $h\left(d,T\right)$ is the heat transfer coefficient of the gap. From Mulet *et al.* [15], it is known that in that case $h\left(d,T\right)\propto 1/d^2$.

Without calculating the conductance of the vacuum gap, Equation (7.22) can be used to study the fraction H of the microsphere surface area that is involved in the interaction. For this purpose, the function is rewritten as

$$G_{\text{Derjaguin}}\left(d,T\right)=\tilde{h}\left(T\right)\int_0^R \frac{2\pi r}{d+R-\sqrt{R^2-r^2}}\,\mathrm{d}r. \tag{7.23}$$

The radius that contains 99 % of the integral on the right-hand side, r_{99} is calculated as a measure for the affected area. The temperature-dependent part of the heat transfer coefficient is captured in $\tilde{h}$ and is not further considered here. From geometry follows then that

$$H=\frac{1}{2}-\frac{1}{2}\sqrt{1-\left(\frac{r_{99}}{R}\right)^2}. \tag{7.24}$$

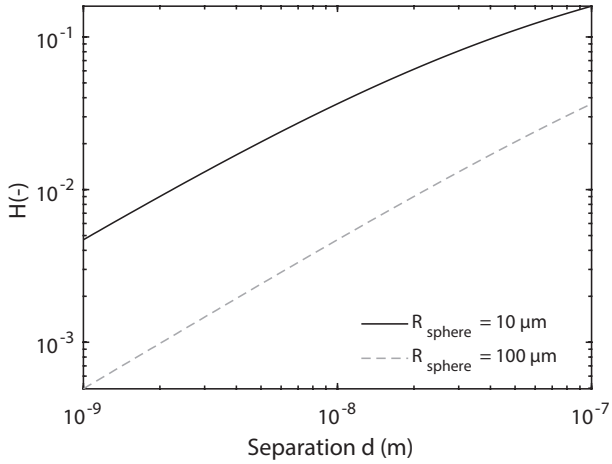

Figure 7.18: Fraction of the sphere surface that is involved in the near-field heat transfer for distances that are much smaller than the radius of the sphere.

The estimated fraction H is plotted in Figure 7.18 for spheres with radii of 10 µm and 100 µm. These sizes are typical for heat transfer measurements between a sphere and a sample. In both cases, the fraction changes more than an order of magnitude between separations of 10 nm and 100 nm. In theoretical models of the conductance of the gap, this change in affected surface area is automatically taken into account. However, in these models the resulting change in temperature gradient across the sphere is disregarded and instead the sphere is assumed to attain a constant temperature. This change of the temperature gradient is approximately proportional to the change in the conductance of the sphere, which can easily exceed a factor of two according to the conductance relations discussed earlier.

7.6 Conclusions

The conduction of heat across a sphere can be modeled with an accuracy of a few percent using a closed-form, parameterized, empirical shape factor that is combined with the thermal conductivity of the material and the radius of the sphere. The resulting relations are especially useful for lumped parameter modeling and outperform Kaganer's analytical solution at an equal number of terms. Moreover, the presented solutions are also applicable for non-opposing sources and sinks that cover up to half of the surface of the sphere and find application in a broader range of problems.

Bibliography

[1] V. Paschkis and H. Baker. A method for determining unsteady-state heat transfer by means of an electrical analogy. *Transactions of ASME*, 64(2):105–112, 1942.

[2] D. Lawson and J. McGuire. The Solution of Transient Heat-flow Problems by Analogous Electrical Networks. *Proceedings of the Institution of Mechanical Engineers*, 167(1):275–290, 1953.

[3] R. R. McMurchy, R. G. Payne, and R. L. Dotts. Thermal Network Modelling Handbook. Technical report, NASA, 1972.

[4] Y. A. Cengel. *Heat Transfer - A practical approach*. McGraw-Hill, New York, USA, 2nd edition, 2003.

[5] C. K. Chan and C. L. Tien. Conductance of Packed Spheres in Vacuum. *Journal of Heat Transfer*, 95(3):302–308, 1973.

[6] A. G. Dixon. Thermal resistance models of packed-bed effective heat transfer parameters. *AIChE Journal*, 31(5):826–834, 1985.

[7] E. Chang and A. Acrivos. Rate of heat conduction from a heated sphere to a matrix containing passive spheres of a different conductivity. *Journal of Applied Physics*, 59(10):3375–3382, 1986.

[8] G. Batchelor and R. O'Brien. Thermal or Electrical Conduction Through a Granular Material. *Proceedings of the Royal Society of London. Series A, Mathematical and Physical Sciences*, 355(1682):313–333, 1977.

[9] W. L. Vargas and J. J. McCarthy. Heat conduction in granular materials. *AIChE Journal*, 47(5):1052–1059, 2001.

[10] Y. Liao, X. Wu, H. Liu, and Y. Chen. Thermal conductivity of powder silica hollow spheres. *Thermochimica Acta*, 526(1-2):178–184, 2011.

[11] A. Narayanaswamy, S. Shen, and G. Chen. Near-field radiative heat transfer between a sphere and a substrate. *Physical Review B*, 78(11):115303, 2008.

[12] E. Rousseau, A. Siria, G. Jourdan, S. Volz, F. Comin, J. Chevrier, and J.-J. Greffet. Radiative heat transfer at the nanoscale. *Nature Photonics*, 3(9):514–517, 2009.

[13] M. G. Kaganer. Contact heat transfer in granular material under vacuum. *Journal of Engineering Physics*, 11(1):19–22, 1966.

[14] W. D. Callister Jr. Metallic Crystal Structures. In *Materials Science and Engineering - An Introduction*, chapter 3.4, p. 41–48. John Wiley and Sons, Inc., New York City, USA, 7th edition, 2007.

[15] J.-P. Mulet, K. Joulain, R. Carminati, and J.-J. Greffet. ENHANCED RADIATIVE HEAT TRANSFER AT NANOMETRIC DISTANCES. *Microscale Thermophysical Engineering*, 6(3):209–222, 2002.

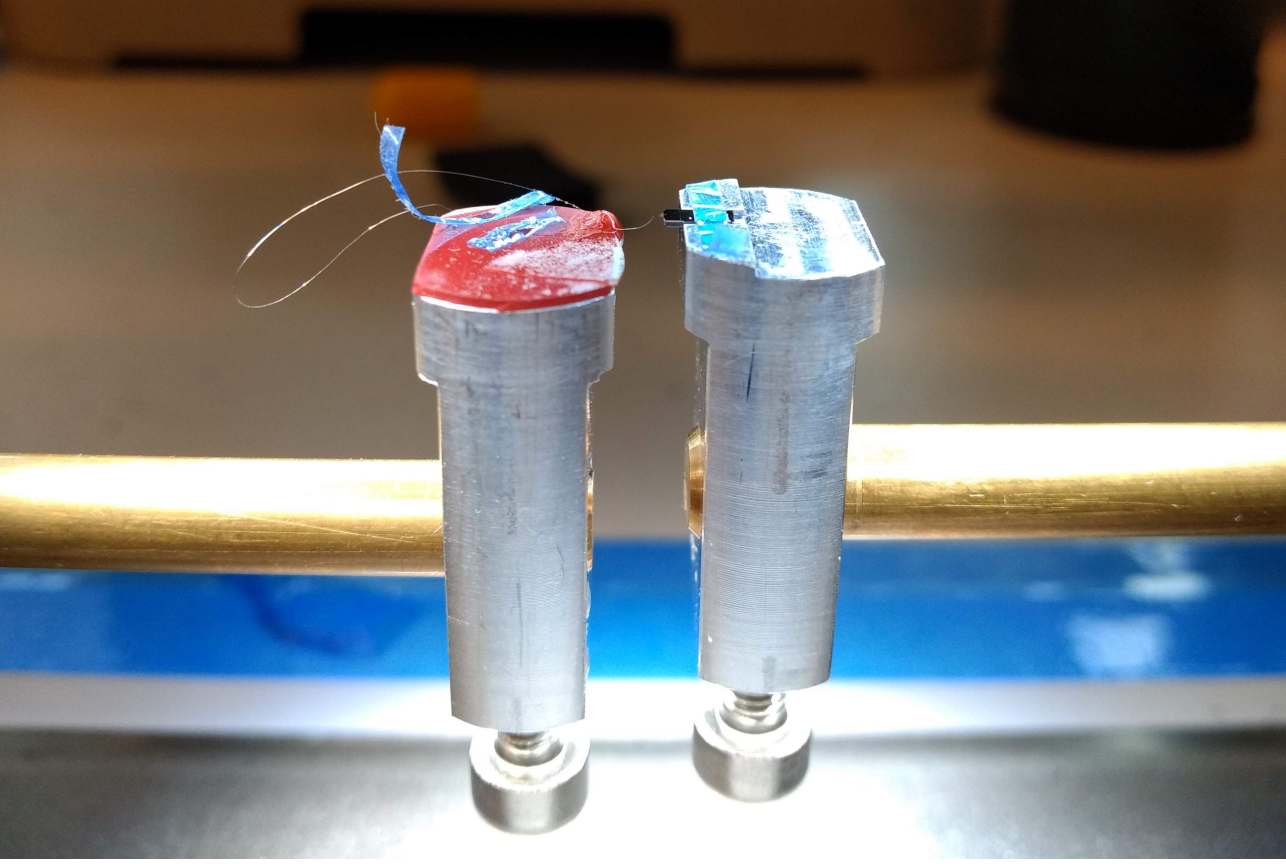

8. Adhering the microsphere to the cantilever

The probe consists of a microsphere that is glued to the free-end of a cantilever. To reach this result a bead of a suitable adhesive needs to be applied to the cantilever tip before it is brought into contact with the sphere.

In the optical beam deflection system used to measure the motion of the cantilever, the cantilever is heated by the illumination. The adhesive needs to remain stable at the resulting elevated temperatures. In this chapter, a suitable adhesive that can withstand these conditions is selected in Section 8.1. The methods employed to attach the microsphere to the cantilever are discussed in Section 8.2. Experiments showed that the adhesive withstands the elevated temperatures, but that the joint with the sphere breaks. This is briefly discussed in Section 8.3.

Title photo: a close-up view of the tooling used to hold the spheres, glue bead and microfiber on the left side and the cantilever chip on the right side. Photo by Roy Bijster.

8.1 Selection of the adhesive

An ideal adhesive for this application can withstand temperatures of 671 K (expected maximum tip temperature) continuously without degradation and has a high thermal conductivity to minimize the temperature gradient between the sphere and cantilever probe. Because of the small adhesion area, colloidal adhesives may not contain particles that are larger than or of comparable size as the microsphere (20 µm diameter). Moreover, the viscosity needs to be in the right ballpark so that it can be applied in small beads without the adhesive spreading over a large section of the cantilever. A viscocity close to 5000 cP (5 Pa s) works well in practice. In addition to this, the working time needs to be at least several minutes to allow manipulation of the probe near the microsphere after the adhesive has been applied.

Most adhesives are rendered unsuitable by their maximum service temperature, that in most cases is well below 500 K [1]. This limits the selection to inorganic adhesives (cements) such as the soluble silicates and Sauereisen's adhesives. The latter are composed of high-purity, inert particles, such as silica, alumina or other ceramics that are mixed with an appropriate binder. These particles, however, are typically tens of micrometers in diameter, and therefore unsuitable for this particular application. For this high-temperature application only the soluble silicates remain. The most common types, sodium silicate and potassium silicate, are supplied as colorless, viscous water solutions that, once fully cured, can withstand temperatures up to 1370 K. The viscosity can be controlled by the initial water content.

In the Netherlands, sodium silicate is readily available in small containers from pharmacies and art supply stores. Unfortunately, the available viscosity is too low for direct use in this application. Slowly heating the solution in a glass beaker to increase the viscosity by evaporating some of the water proved difficult to control and often led to a thin film forming on top of the solution.

In industrial settings, the soluble silicates are mainly used for industrial applications, such as paper bonding and the manufacture of cardboard boxes. The adhesives are available in several compositions and viscosities to meet these industrial needs. Upon consultation with PQ Corporation, their Kasil 6 (potassium silicate solution), Crystal 0079 (silicic acid sodium salt solution) and Crystal 0012 (sodium silicate solution) adhesives were tested. Of the tested adhesives, only Crystal 0012 had a working time (roughly 2 minutes) that was long enough for this application.

8.2 Gluing procedure

The spheres are glued to the cantilever using two three-axis translation stages that can move independently, as shown in Figure 8.1. The cantilever chip is seated in a small pocket to restrict its lateral motion and kept in place temporarily by a small piece of kapton tape. The cantilever hangs freely over the edge of the support structure. On the opposing side, microspheres are deposited on a silicone support. Shortly before gluing, a bead of adhesive

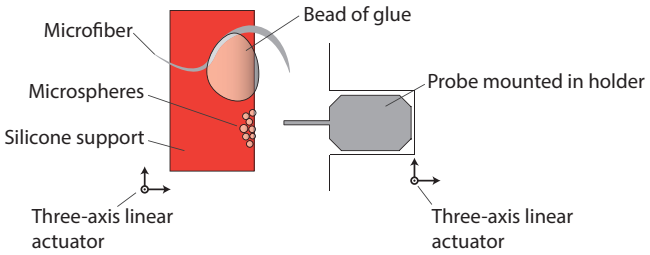

Figure 8.1: Schematic of the gluing procedure. The spheres, microfiber and bead of glue are deposited on a silicone support that is fixed on a three-axis positioner (not shown). Opposite to it is the probe, that is seated in a pocket on another three-axis positioner. Once the sphere is in the right location, the glue is hardened using an ultraviolet flood light.

is dispensed close to the edge of the support. The silicone layer prevents the microspheres from sticking to the surface and allows the dried glue bead to be easily removed afterwards. A torn microfiber has been glued next to the spheres, and has been bent such that its tip points upwards. By tearing it, a sharp tip is formed that can be used to manipulate the sphere. This glue tool is placed under a Olympus SZ-X12 stereoscope. The stereo vision allows a degree of depth perception which is indispensable when positioning the cantilever right above a microsphere during gluing.

Step 1: removing unwanted cantilevers from the chip

The chip holds cantilevers of four different lengths. If one of the shorter designs is used, the longer cantilevers need to be removed from the chip. To this end, the microfiber can be placed near the root of the cantilever. When the chip is then pushed forward, the microfiber slides vertically along the cantilever and shears against it, effectively 'sawing' it off at its base. This method is illustrated in Figure 8.2 and proved to be effective and quick. Other methods in which the cantilever is loaded axially or is loaded in bending to break it off are significantly slower and more difficult to align with the applicator.

Step 2: applying adhesive to the cantilever free-end

A bead of adhesive is dispensed shortly before gluing. The cantilever is partially dipped tip-first into the bead from the side. The cantilever is then quickly retracted and a small bead of adhesive forms at the free-end of the cantilever.

Step 3: adhering a microsphere

The cantilever is then moved to the vicinity of a suitably located microsphere that is situated near the edge of the sample holder. Once located, the can-

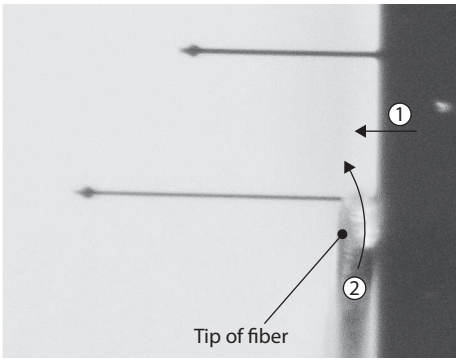

Figure 8.2: Unwanted cantilevers are broken off the chip by shearing a fiber against the cantilever and the chip. By pushing the chip against the fiber (1), the fiber starts to slide vertically (2) and shears off the cantilever.

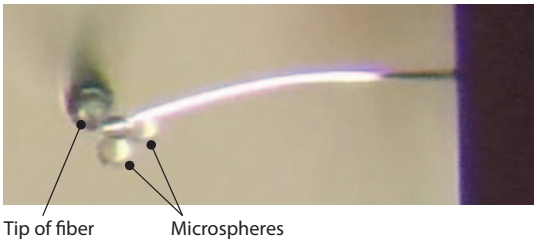

Figure 8.3: Micrograph of a cantilever with two microspheres attached to its tip. A fiber tip is used to exert a lateral force on the spheres, causing the cantilever to rotate about its axis.

tilever is moved up, positioned above the microsphere and then moved down slightly beyond the point of contact to apply positive pressure. After approximately 10 s of contact, the cantilever is retracted and the sphere is pulled along with it.

Step 4: checking the bond strength

To check that the sphere is firmly bonded to the cantilever tip, the cantilever is moved towards the tip of the microfiber. The sphere is pushed sideways against the microfiber tip. If this causes the cantilever to twist about its length (as shown in Figure 8.3) without the sphere moving or coming loose, the sphere is correctly bonded to the cantilever.

8.3 Issues at high temperatures

Although the bond is mechanically stable at room temperature, the bond fails at higher temperatures. During experiments where the cantilever was heated near its free-end using a laser, the spheres came loose. Using opti-

cal microscopy, it was confirmed that in most cases the glue bead was still present after the event. Given the high temperature stability of the adhesive, we hypothesize that (rapid) heating in combination with thermal expansion mismatch caused failure of the bond with the microsphere. We have been unable to confirm this experimentally. The failure of the bond at higher temperatures impedes heat transfer measurements using the instrument and will require further investigation.

8.4 Conclusions

At temperatures above 500 K, soluble silicate adhesives offer the required bond stability without the need for mixed-in particulates. Three soluble silicates were tested of which only Crystal 0012 had the right viscosity. The working time of this adhesive was two minutes and was sufficiently long to perform the gluing procedure. Although the adhesive appears stable at elevated temperatures, the bond failed at operational conditions. Although the glue bead was still present after failure, the microspheres had come loose. This impeded further measurement of heat transfer using the instrument and requires further investigation.

Acknowledgments

The author thanks Wim Peterse and Tjeerd Russchenberg of TNO for preparing the necessary tooling and Gere Kattenbeld of PQCorp for making small volume samples of their soluble silicate adhesives available.

Bibliography

[1] S. Ebnesajjad, editor. *Adhesive Technology Handbook*. Willam Andrew Inc., 2009.

9. Discussion

The initial outset of this thesis was to realize a proof-of-principle instrument that can be used for measuring the separation between a probe and a sample using heat transfer. In this chapter, the current state of affairs is discussed including future work that is required to finish the proof-of-principle setup. In addition to this, an outlook to the future is provided in which the concept of a one-dimensional distance sensor is taken to a multi-dimensional scanning probe microscopy technique.

Title photo: realized positioning and tracking platform for near-field imaging microscopes developed by TNO [1]. Shown is a three-stage positioning platform with a long-stroke linear stepper motor, a pre-stressed piezo stage and a micro electro-mechanical system (MEMS). A separation sensor based on heat transfer can be integrated in the MEMS device to measure the distance to the sample. Photo by Rogier Bos, courtesy of TNO/NOMI.

9.1 Opportunities

In this thesis, a direct relation is established between the heat flux between the microsphere and the sample on one hand and the output signal of the measuring system on the other hand. The discrepancies from the ideal or theoretical case are highlighted and are taken into account in evaluating the measured heat flux. This provides a new opportunity to (re)consider the discrepancies between the modeled heat flux and the measurements that were found by others. Previous research [2, 3] overlooked, e.g., the effects of the change in the temperature gradient over the microsphere (see Section 2.1.2 and Section 7.5) and the reduction of the effective cantilever length (see Section 5.2).

9.2 Limitations

The research and the designs presented in this thesis are limited in several ways. A separation sensor that relies on heat transfer is limited by the following factors. The first limitation is the attainable bandwidth that has to be traded against the signal-to-noise ratio and the sensitivity (see Section 4.5.1). Although this is true for most sensor technologies, the realizable bandwidths are comparatively low at several hundred hertz for the designed probes. The bandwidth can be extended to several kilohertz for smaller probes with relatively small sacrifices in terms of sensitivity. This will be a limiting factor for pairing this technology with high speed motion platforms [4] that run at bandwidths of several hundred kilohertz.

Second, the increase in heat transfer rate in the near-field regime depends strongly on the materials of the probe and the sample. If both support phonons or polaritons at the same wavelengths, the radiative heat transfer can be enhanced. If this is not the case, the effect is strongly limited. A separation sensor based on conductive heat transfer would therefore find a broader use for cases in which the application does not require vacuum.

Third, the theoretical model that describes the system performance (see Chapter 2 and Chapter 4) does not include the non-linear effects of film thickness and of temperature on the material properties. It is known that the mechanical properties can vary strongly with film thickness (see, e.g., Abazari *et al.* [5]) for films up to several hundred nanometers thick. When these effects are taken into account, the design of the corresponding probes will change and may be used to enhance the sensitivity of the system.

Last, the performance of the adhesives at micrometer length scales and at elevated temperatures nearing 1000 K is not well understood (see Chapter 8). The connection between the microsphere and the cantilever has to be modeled in more detail to understand why the bond breaks and how this issue can be resolved.

9.3 Future design improvements

In the previous chapters, recommendations were given to improve sub-system performance. On a system level, however, the existing design implementation can be changed in several ways to increase the overall performance and usability.

9.3.1 Redesign of the mechanical layout

In the current implementation, the vacuum chamber is raised above the optical table to accommodate the vacuum pumps and vacuum feed-throughs that are on the bottomside of the vessel. This requires the non-vacuum optics to be raised on a platform that needs to be aligned separately with the in-vacuum optics. A redesign of the system should place the in-vacuum optics and the non-vacuum optics on a shared platform that is ideally level with the tabletop of the optical table. This improves the mechanical stability and eases alignment. Moreover, the optical mounts should be redesigned so that they are aligned based on manufacturing tolerances and do not require manual adjustment. Furthermore, from a practical perspective the tabletop should be lowered to a level where the operator no longer needs to stand on top of the optical table to open the vacuum chamber. Usability is an often overlooked design aspect in research setups, but is paramount to the experience of the operator and thus ultimately to the accuracy of the measurements. A system that is hard to use, is prone to being used incorrectly.

9.3.2 Redesign of the cantilever geometry

The cantilevers designed in Chapter 4 have a widened section of 10 µm diameter near the free-end that serves as a target for the OBD laser. Together with the chosen beam widths for the OBD lasers in Section 2.4, this resulted in a significant fraction of the incident light passing by the cantilever probe. This necessitated that the power of the transmitted and the passing light is measured as part of the system calibration, which is cumbersome and introduces additional sources of uncertainty. The system can be improved by increasing the size of this target to double the radius. In that case, the amount of light that passes the cantilever is negligble and the calibration can be simplified significantly.

9.3.3 Smoother surfaces

In Chapter 6, the root mean square surface roughness of the microspheres was found to be 29 nm with peak-to-peak values up to 198 nm. To reduce the likelihood of point contacts at small separations, future experiments should investigate the use of smoother borosilicate spheres. The dielectric function of these spheres need to be measured or estimated for the comparison with theoretical models of near-field radiative heat transfer.

In addition to this, the scattering of light that is caused by the surface roughness of the prism (see Chapter 3) can be reduced by further polishing the prism. The associated investment can be minimized by using a smaller prism.

9.4 From a one-dimensional separation measurement to near-field thermal microscopy

The heat-transfer between a microsphere and a flat surface is essentially one-dimensional: the separation between the sphere and the surface can be set and does not change with relative lateral movement (parallel to the surface) between the two. Understanding the dependence between the heat flux and the separation is quintessential in constructing a practical separation-sensor and towards near-field thermal microscopy. This can be expanded to a (quasi-) one-dimensional system when the sample is replaced by, e.g., a staircase. It is evident that when the probe scans laterally across the sample that the change in separation with every step will result in a well-defined change in the measured flux. This does, however, conveniently ignore the three-dimensional effects that are encountered near the transitions between steps. For example, when a line scan is performed across the staircase, the sharp edges of the steps are expected to be smoother transitions in the measured flux. To take the (quasi-)one-dimensional separation sensor, that is described above, to the real three-dimensional world it is important to understand how the local geometry influences the measured heat flux. This will require further modeling and experimentation. From a theoretical and modeling perspective, this requires techniques that can calculate the flux for arbitrary geometries at various length scales. From an experimental perspective, this requires a platform that can move the sample relative to the probe. These topics are addressed separately below.

From the modeling perspective, significant progress has been made in the past 15 years in the development of tools that are suitable for calculation of near-field radiative heat transfer between arbitrary geometries. For a general review of the available techniques the reader is referred to the work of Didari and Mengüc [6]. It is, however, instructive to highlight two techniques that are applicable to the size and the length scales of interest here and that have been demonstrated using three-dimensional geometries. Rodriguez *et al.* proposed the Fluctuating Surface-Current (FSC) formalism for near-field heat transfer calculations [7, 8] and the Fluctuating Volume-Current (FVC) formalism [9]. Both techniques rely on a description of the scattering caused by electric and magnetic currents on the surface of the interacting bodies and in their volumes, respectively. The FSC formalism has been demonstrated in the design of a probe for measurement of near-field heat transfer in the extreme near-field [10, 11]. The second method of interest approximates a body of arbitrary shape by discretizing it as a large collection of dipoles. This so-called Thermal Discrete Dipole Approximation (T-DDA) of Edalatpour *et al.*

[12] discretizes the volume in cubic sub-volumes and combines these with theoretical relations to calculate the total heat flux. The accuracy of this technique depends strongly on the number of dipoles used and is mostly suitable for problems where surface polaritons dominate the heat transfer [13].

At the moment of writing, no studies were found that utilize either of these techniques to study the behavior of a probe scanning across features in the sample. All found studies were limited to calculating the one-dimensional dependency of the heat flux on the separation. Future studies will have to focus on determining the extent of smoothing effects in scanning near-field microscopy applications and the minimum feature sizes that can be detected. Examples of such features are deep and narrow trenches and sharp steps such as the ones that are used in the manufacturing of high-density digital memory chips [14].

From the experimental perspective, the probe needs to be scanned laterally relative to a sample that has height variations on its surface. The system architecture proposed in this thesis, uses a three-axis translation stage to move the sample with respect to the probe. In the current instance, the sample consists of a flat surface of a prism. The separation between the sample and the probe is measured independently using a total internal reflection microscope. This independent measurement is lost when the surface of the prism is structured, because the small features on its surface will increase the scattering intensity caused by the sample. The three-axis translation stage does, however, permit experiments in which the probe is scanned across a surface. Special care has to be taken though to mount the sample perpendicular to the probe. Moreover, the current instance uses a microsphere that is attached to the free-end of the cantilever. If the microsphere is to be replaced by another geometry, new production methods will have to be used to manufacture the tip or join it to the cantilever. For example, a microsphere can be attached to the free-end first and then be modified using micro-machining techniques such as focused ion beam (FIB) machining [15, 16].

Bibliography

[1] R. J. F. Bijster, R. W. Herfst, J. P. F. Spierdijk, A. Dekker, W. A. Klop, G. F. I. Kramer, L. K. Cheng, R. A. J. Hagen, and H. Sadeghian. A high speed positioning and tracking platform for near-field imaging microscopes. p. (submitted), 2016.

[2] A. Narayanaswamy and G. Chen. Thermal near-field radiative transfer between two spheres. *Physical Review B*, 77(7):075125, 2008.

[3] E. Rousseau, A. Siria, G. Jourdan, S. Volz, F. Comin, J. Chevrier, and J.-J. Greffet. Radiative heat transfer at the nanoscale. *Nature Photonics*, 3(9):514–517, 2009.

[4] R. Herfst, R. Bijster, A. Dekker, J. Wei, H. van Zeijl, R. Kruidhof, and H. Sadeghian. Nanopositioning MEMS stage for high speed positioning of metamaterials lenses for use in high resolution optical imaging. In *2017 IEEE International Conference on Advanced Intelligent Mechatronics (AIM)*, p. 1310–1315, Münich, Germany, 2017. IEEE.

[5] A. Abazari, S. Safavi, G. Rezazadeh, and L. Villanueva. Modelling the Size Effects on the Mechanical Properties of Micro/Nano Structures. *Sensors*, 15(11):28543–28562, 2015.

[6] A. Didari and M. Pinar Mengüç. A design tool for direct and non-stochastic calculations of near-field radiative transfer in complex structures: The NF-RT-FDTD algorithm. *Journal of Quantitative Spectroscopy and Radiative Transfer*, 197:95–105, 2017.

[7] A. W. Rodriguez, M. T. H. Reid, and S. G. Johnson. Fluctuating-surface-current formulation of radiative heat transfer for arbitrary geometries. *Physical Review B*, 86(22):220302, 2012.

[8] A. W. Rodriguez, M. T. H. Reid, and S. G. Johnson. Fluctuating-surface-current formulation of radiative heat transfer: Theory and applications. *Physical Review B*, 88(5):054305, 2013.

[9] A. G. Polimeridis, M. T. H. Reid, W. Jin, S. G. Johnson, J. K. White, and A. W. Rodriguez. Fluctuating volume-current formulation of electromagnetic fluctuations in inhomogeneous media: Incandescence and luminescence in arbitrary geometries. *Physical Review B*, 92(13):134202, 2015.

[10] K. Kim, B. Song, V. Fernández-Hurtado, W. Lee, W. Jeong, L. Cui, D. Thompson, J. Feist, M. T. H. Reid, F. J. García-Vidal, J. C. Cuevas, E. Meyhofer, and P. Reddy. Radiative heat transfer in the extreme near field. *Nature*, 528(7582):387–391, 2015.

[11] L. Cui, W. Jeong, V. Fernández-Hurtado, J. Feist, F. J. García-Vidal, J. C. Cuevas, E. Meyhofer, and P. Reddy. Study of radiative heat transfer in Ångström- and nanometre-sized gaps. *Nature Communications*, 8(1):14479, 2017.

[12] S. Edalatpour and M. Francoeur. The Thermal Discrete Dipole Approximation (T-DDA) for near-field radiative heat transfer simulations in three-dimensional arbitrary geometries. *Journal of Quantitative Spectroscopy and Radiative Transfer*, 133:364–373, 2014.

[13] S. Edalatpour, M. Čuma, T. Trueax, R. Backman, and M. Francoeur. Convergence analysis of the thermal discrete dipole approximation. *Physical Review E*, 91(6):063307, 2015.

[14] D. Hisamoto, W. C. Lee, J. Kedzierski, H. Takeuchi, K. Asano, C. Kuo, E. Anderson, T. J. King, F. Jeffrey Bokor, and C. Hu. FinFET-A self-aligned double-gate MOSFET scalable to 20 nm. *IEEE Transactions on Electron Devices*, 47(12):2320–2325, 2000.

[15] R. J. Young. Micro-machining using a focused ion beam. *Vacuum*, 44(3-4):353–356, 1993.

[16] D. Allen, P. Shore, R. Evans, C. Fanara, W. O'Brien, S. Marson, and W. O'Neill. Ion beam, focused ion beam, and plasma discharge machining. *CIRP Annals*, 58(2):647–662, 2009.

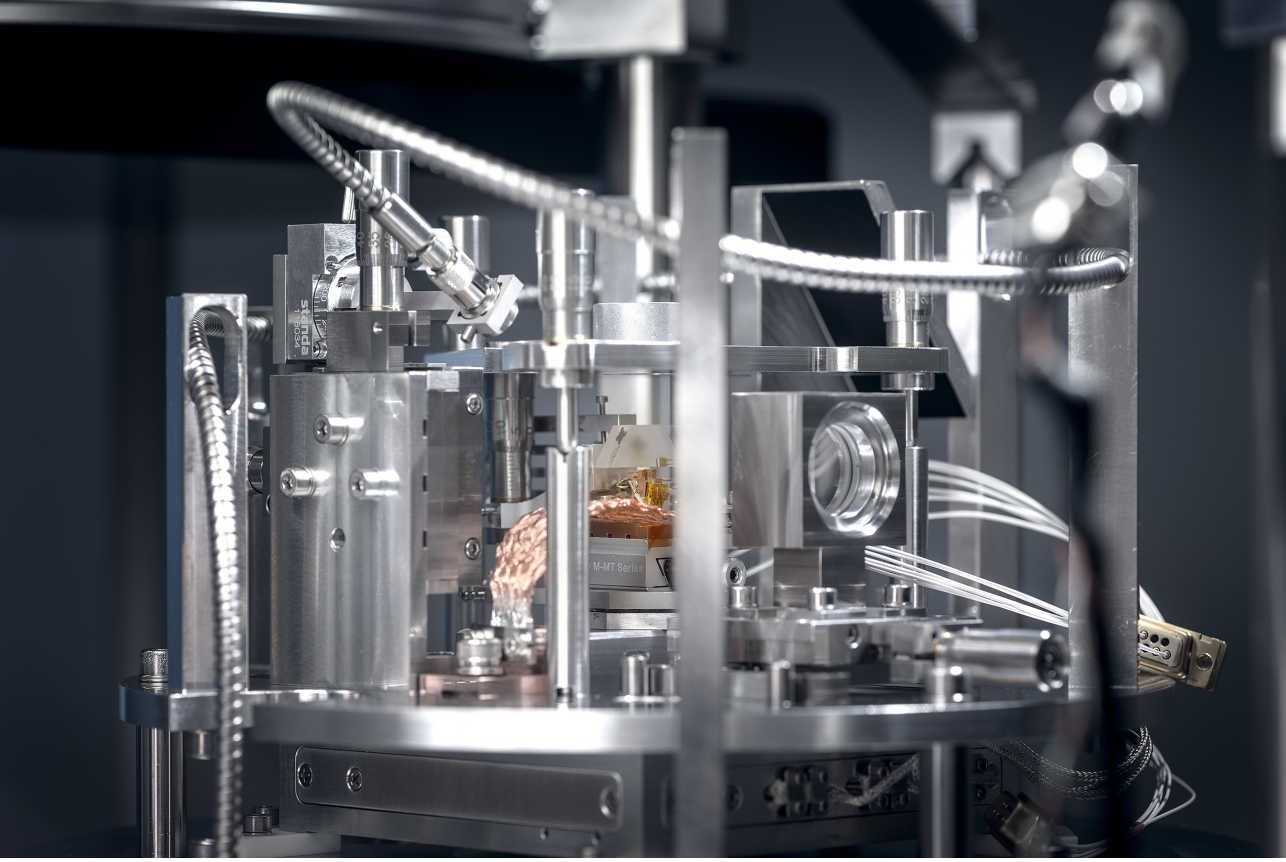

10. Conclusions

The aim of this thesis was to develop a proof-of-principle demonstration of using heat flux between two bodies for determining the distance between them. Towards realizing such an instrument, this thesis presented an instrument architecture that solves three problems that exist in comparable systems.

First, the distance between the probe and the sample is measured independently using a total internal reflection microscope (TIRM). In contrast to methods that rely on contact and accurate motion stages, the use of TIRM allows for a continuous measurement of the separation between the spherical probe and the sample. TIRM is a well-known technique for measuring the distance between a flat interface and microspheres. However, the implementation of this technique in combination with an optical beam deflection system is not straightforward. As is shown in Chapter 3, the presence of a microcantilever and its clamp limits the accessible volume. This makes it

Title photo: close-up photo of the internals of the instrument. Photo by Rogier Bos, courtesy of TNO.

impossible to capture the light scattered in the forwardscattering direction, in which the scattering intensity is highest. Moreover, the intensity of the light that is scattered by the roughness of the prism easily exceeds that of the TIRM signal. Although detection in the backscattering direction suffers strongly from this effect, it remains the most viable configuration. By further polishing the prism and using p-polarized light in the TIRM illumination, the scattering off the prism can be significantly reduced. This layout decouples the TIRM and OBD system and does not penalize the OBD performance.

Second, the thermal balance of the probe is kept constant using closed-loop control, such that the conditions are constant throughout the duration of the measurement. This allows the flux to be measured directly, rather than via an otherwise needed temperature change (Chapter 2). If the optical reflectivity, absorptivity and transmissivity of the cantilever probe are known, this has the added advantage that the measurement does not require calibration of the probe, but only of the actuator that is used in the control loop.

The work in this dissertation presented a system equation that relates the output signal of the instrument to the heat flux absorbed by the probe. This coupling of the top-level design parameters of the system to the output, allows the study and design of each separate contributor and its effect on the total system performance.

In addition to the design of the instrument, this research contributes a detailed study of the influences of the microsphere and of the microcantilever on the heat flux measurement. Regarding the microsphere it is shown in Chapter 2 and Chapter 7 that the thermal gradient across the microsphere cannot be ignored. Because the heat flux is determined at the tip of the cantilever and not at the point of the sphere that is closest to the sample, the thermal gradient needs to be taken into account in determining the effective conductance of the gap. However, the conductance of a spherical conductor depends on the size of the areas of the heat source and the heat sink. The area of the sphere that is involved in the heat transfer to the sample is distance-dependent. This causes the effective conductance across the sphere to change. Regarding the influence of the microcantilever, it has been shown in Chapter 4 and Chapter 5 that the size and the position of the illumination of the cantilever probe are large contributors to the sensitivity of the probe.

Appendices

A. Uncertainty due to defocus in the optical beam deflection system

In the confocal OBD method, a collimated laser beam is focused on the sample. On reflection, the optical beam is rotated by an angle 2θ (twice the rotation angle of the cantilever) and passes back through the focusing lens. This results in an effective beam displacement Δx. For an ideal lens, the sensitivity of the beam displacement to rotation can be estimated using Equation (2.31) as $\partial x/\partial\theta \approx 2f$. For a thick, non-ideal lens, however, a ray-trace model provides a more accurate estimation of the sensitivity. Moreover, a ray-trace simulation allows for quick estimation of the uncertainty of this parameter. This uncertainty is included in the uncertainty budget for determining the cantilever sensitivity.

The lens, a Thorlabs ACA254-050-A-VAC-SP, was modeled in Lambdares OSLO [1] using the nominal optical description provided by Thorlabs [2] (see Table A.1) at a test wavelength of 640 nm. A tilted mirror was placed in the focal plane of the lens. The vertical displacement of the chief ray was used as a measure for the beam displacement. The results of this are depicted in Figure A.1.

Table A.1: Optical description of the Thorlabs ACA254-050-A-VAC-SP.

#	**Radius** (mm)	**Thickness** (mm)	**Material**
1	32.53	6.82	Schott N-SSK2
2	−32.53	1.25	Air
3	−28.45	3.23	Schott N-SF57
4	−78.02	W.D.[a]	Air

[a] The nominal working distance (W.D.) is 42.75 mm.

To also account for slight defocus, the mirror was also placed 0.5 mm in front of and behind the nominal position. This results in an estimate for the sensitivity $\partial x/\partial\theta$ of 99.6 mm ± 3.0 mm.

Parts of this appendix have been published in Review of Scientific Instruments **92**, 025008 (2021).

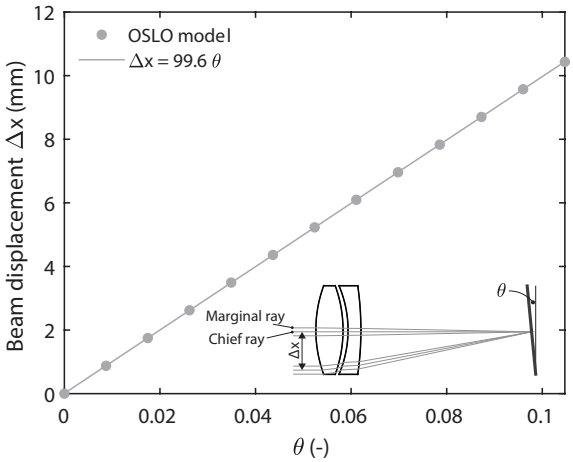

Figure A.1: Calculated beam displacement as a function of local tilt θ. These results are obtained using an Lambdares OSLO ray-tracing simulation of the Thorlabs ACA254-050-A-VAC-SP lens. The nominal working distance is 42.75 mm in the shown configuration. The beam displacement is equal to the vertical displacement of the chief ray.

Bibliography

[1] Lambda Research Corporation. OSLO (Optical Software for Layout and Optimization, 2019.

[2] Thorlabs. ACA254-050-A - Air-Spaced Achromatic Doublet, AR Coating: 350-700 nm, f=50 mm, 2012.

B. Measuring the optical absorptance of the cantilever

The heat transfer measurement relies on accurate knowledge of several thermal, optical and mechanical properties of the cantilever probe. Many of these cannot be measured directly, and need to be derived or calibrated using different measurements. To estimate the tip temperature, for example, it is paramount to know the conductance of the probe, measurement of which in turn relies on accurate knowledge on the power absorbed from the incident laser beam. A reliable and accurate method for measuring the optical absorptance is thus required.

B.1 Measurement of absorptance using the optical beam deflection system

The effective optical absorptance of the cantilever can be measured using the confocal OBD system and a calibrated optical power meter. This setup is shown in simplified form in Figure B.1. From conservation of energy, the absorptance α can be written as

$$\alpha = \frac{P_{\mathrm{ab}}}{P_{\mathrm{in}}} = 1 - \frac{P_{\mathrm{tr}}}{P_{\mathrm{in}}} - \frac{P_{\mathrm{sc}}}{P_{\mathrm{in}}} - \frac{P_{\mathrm{re}}}{P_{\mathrm{in}}}, \tag{B.1}$$

where P_{in}, P_{ab}, P_{tr}, P_{sc}, and P_{re} are the incident, absorbed, transmitted, scattered and specularly reflected power, respectively. The transmitted power also includes light that bypasses the cantilever.

The power incident on the cantilever can be directly measured at Location 3 (see Figure B.1), while the power transmitted (and bypassed) is measured at Location 4. The light which reflects off the cantilever surface passes back through the lens of the OBD system. Attenuation of the light in these optical elements is accounted for through calibration. Due to volume restrictions in the vacuum part of the OBD system, the efficiency of the lens and the efficiency of the OBD system need to be calibrated separately.

The losses incurred by the lens and by the window of the vacuum chamber are simply the ratios of the power incident on the windows and the power

Parts of this appendix have been published in Review of Scientific Instruments **92**, 025008 (2021).

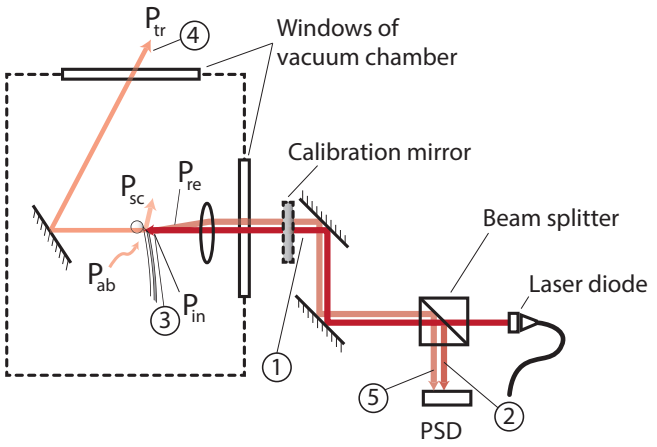

Figure B.1: Simplified representation of the OBD system with an included calibration mirror. By measuring the optical power at Locations 1 through 5 the absorbed power can be estimated.

transmitted by the lens,

$$\eta_{\text{lens}} = \frac{P_3}{P_1}. \tag{B.2}$$

The efficiency of the OBD system is measured using a calibrated mirror (efficiency η_{cal}) that is placed at Location 1. The optical power is then measured at Locations 1 and 2 to find

$$\eta_{\text{opt}} = \frac{1}{\eta_{\text{cal}}} \frac{P_2}{P_1}. \tag{B.3}$$

Light that is not specularly reflected, but is instead scattered in other directions, P_{sc}, cannot be measured using this method. As shown in the main text, the total scattered power is estimated to be less than 1 % of the specularly reflected light.

The light reflected off the cantilever is derived from the power measured in Location 5,

$$P_{\text{re}} = \eta_{\text{cal}} \frac{P_1^2 P_5}{P_2 P_3}, \tag{B.4}$$

from which the absorptance is approximated as

$$\alpha \approx 1 - \frac{P_4}{P_3} - \eta_{\text{cal}} \frac{P_1^2 P_5}{P_2 P_3^2}. \tag{B.5}$$

Each measured power level is nulled for any offset that is present in that measurement location due to other light sources that may reach the detector. The absorbed power causes the cantilever to deflect, and consequently the angle of incidence to change. To account for this effect, the optical power is modulated over the full range at each measurement location.

B.2 Calibration and uncertainty analysis

The calibration mirror is a Thorlabs BB05-E02 broadband dielectric mirror with a specified reflectivity of approximately $0.98 - 0.99$ at a wavelength of 635 nm. Its reflectivity is calibrated using the simple system schematically depicted in Figure B.2. The reflectivity of a dielectric mirror varies with wavelength and polarization state. Therefore, the laser diode is cycled through its full output range to compensate for any wavelength variations with output power, and the mirror is used close to normal incidence to minimize polarization-induced variation.

Figure B.2 shows the measurement geometry, where the reflected and incident powers are measured using an optical power meter at Locations 1 and 2, respectively. This configuration allows for a minimal angle of incidence of less than 0.9°. Data provided by Thorlabs shows that the reflectivity is only weakly dependent on the angle of incidence, as they measured reflectivities of 0.9909 and 0.9989 at 8° and 45° angles of incidences, respectively; a difference of 0.8 % over a 37° change in angle of incidence. Based on this data, we expect that at an angle of incidence of 0.9° an error of at most 0.02 % is introduced with respect to normal incidence. The effect is therefore not further quantified. Using this method, the reflectivity of the mirror was calibrated to be 0.9970 ± 0.0338, well within the cited range.

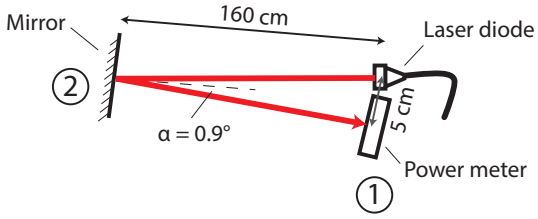

Figure B.2: The reflectivity of the calibration mirror is measured by illuminating it under a shallow angle and measuring the reflected power in Location 1 and the incident power in Location 2.

B.2.1 The effect of polarization

As explained in Chapter 2, the incident and reflected beams are separated in the optical beam deflection system using polarizing optics. This allows for maximum optical power to reach the PSD. However, the efficiency of the used multi-order half- and quarter-wave plates varies strongly with the incidence angle, introducing inaccuracies in the reflectivity measurement. Moreover, the deformation of the probe under heating causes changes in the polarization state that are not easily predicted. Therefore, a second OBD system that mimics the optical qualities of the original without the use of polarizing optics, is used to measure the absorptance and reflectance of the probe.

Table B.1: Uncertainty per power reading for a Newport 918D-UV-OD3R silicon detector and Newport 1936-R benchtop optical power meter at a full scale range of 6.941 mW.

Component	Value	Unit
Accuracy power meter	0.2 %	V, r.m.s., 1σ
Linearity silicon detector	0.5 %	V, r.m.s., 1σ
Uniformity silicon detector	2 %	V, r.m.s., 1σ

B.2.2 Variation introduced by the power meter

The power is measured using a Newport 918D-UV-OD3R silicon detector that is paired with a Newport 1936-R benchtop optical power meter. The detector sensitivity was measured to vary 2.4 % while moving ±2.5 mm from the center in any direction. It is therefore paramount that the beam is incident on the same location of the silicon detector across all measurement locations. This is achieved by temporarily placing a ⌀0.9 mm pinhole in front of the detector. After the power reading has been maximized by moving the detector, the pinhole is removed and a reading is taken. Using this method the beam is centered onto the detector.

B.2.3 Accuracy and uncertainty

The uncertainty in the estimated absorptance σ_α can be calculated as the sum of the uncertainties due to each contributor as

$$\sigma_\alpha^2 = \sum_{i=1}^{5} \left| \frac{\partial \alpha}{\partial P_i} \right|^2 \sigma_{P_i}^2. \tag{B.6}$$

The sensitivity to each contributor is found through partial differentiation of Equation (B.5) as:

$$\frac{\partial \alpha}{\partial P_2} = \eta_{\text{cal}} \frac{P_1^2}{P_2} \frac{P_5}{P_3^2}, \tag{B.7}$$

$$\frac{\partial \alpha}{\partial P_1} = -2\eta_{\text{cal}} \frac{P_1}{P_2} \frac{P_5}{P_3^2}, \tag{B.8}$$

$$\frac{\partial \alpha}{\partial P_3} = -\frac{P_4}{P_3^2} + 2\eta_{\text{cal}} \frac{P_1^2}{P_2} \frac{P_5}{P_3^3}, \tag{B.9}$$

$$\frac{\partial \alpha}{\partial P_4} = \frac{1}{P_3}, \tag{B.10}$$

$$\frac{\partial \alpha}{\partial P_5} = -\eta_{\text{cal}} \frac{P_1^2}{P_2} \frac{1}{P_3^2}. \tag{B.11}$$

C. Damaged cantilevers due to overheating

The A1 and A2 probes get damaged easily when illuminated with a laser, while the B, C and D cantilevers do not suffer from the same problem. In this Appendix, a possible failure mode for the A1 and A2 cantilevers is presented.

When observed under a conventional optical microscope (Leitz Laborlux K), it is clear that the cantilevers have undergone changes after illumination by the laser of the OBD system. As shown in Figure C.1.a, the cantilevers have discolored ('blackened') from the free end to approximately halfway the cantilever, and the spheres have moved. One of the cantilevers has even partially broken off. Imaging of the cantilevers using a scanning electron microscope (JEOL JSM-6010LA) in backscattered electron shadow mode (BES), reveals a clear difference between the discolored section and reflecting section of the cantilever. The scanning electron micrographs, shown in Figure C.1, are taken at 5 kV in backscattered electron shadow mode. This mode detects backscattered electrons with illumination from the side, and provides information on both the topography and the composition. In these micrographs, heavier elements appear brighter due to the larger amount of backscattered electrons. The transition areas marked in the figure, appear to contain the melt pools of the aluminium coating. This suggests that the aluminium has melted and possibly even evaporated from the cantilever.

The conductance of Cantilever A is approximately $5.3 \times 10^{-7}\,\mathrm{W\,K^{-1}}$. At an absorbed power level of approximately $200 \times 10^{-6}\,\mathrm{W}$ and a temperature at the clamped end of 294 K, the temperature at the free end reaches a maximum value of 671 K. This is not sufficient to melt the aluminium, which has a melting temperature of 933 K.

However, if hydrocarbons are present on the surface, these can decompose and cause carbon contamination of the surface. According to Miller and Haneman [1], this can occur at temperatures as low as 600 K. The carbon contamination of the surface will result in an increased absorption of the incident laser power, resulting in higher temperatures. This process can reinforce itself until the melting temperature, or possibly even the evaporation temperature (1073 K at 1×10^{-6} mbar [2]) is exceeded. The thermal gradient along the cantilever length can act as the driving force that moves the melt pool away from the tip. This scenario is depicted in Figure C.5, in which the temperature distributions for a clean and for a severely contaminated probe

Parts of this appendix have been published in Review of Scientific Instruments **92**, 025008 (2021).

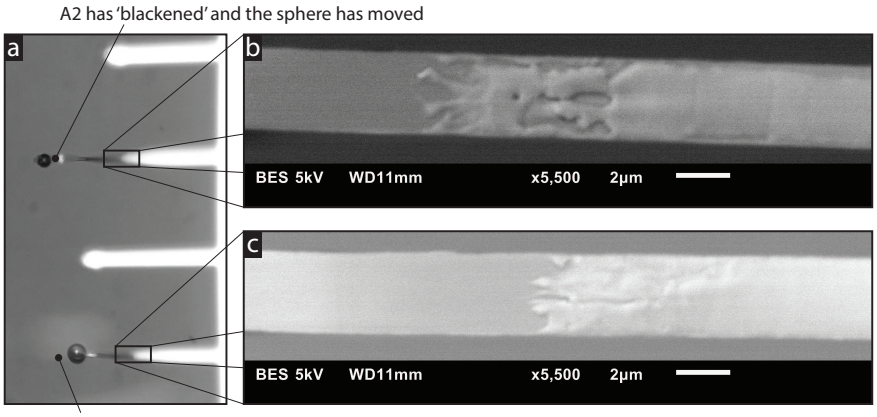

Figure C.1: The A1 and A2 cantilevers get damaged after heating with the laser of the optical beam deflection system. a) A micrograph taken using a conventional optical microscope shows discoloration/blackening at the free end of the cantilevers. A1 has partially snapped off, while in both cases the sphere has moved. b) and c) show scanning electron micrographs of the areas marked in a). Both are taken using a JEOL JSM-6010LA SEM and are the backscattered electron shadow images.

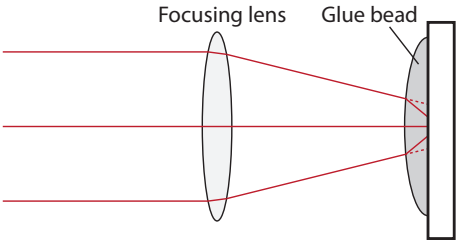

Figure C.2: The incident beam is focused by a focusing lens. The glue bead reduces the effective spot size by a factor n, the refractive index of the material.

are displayed. The evaporation temperature can be exceeded, if due to the contamination, the absorbed power is increased by a factor of 2.1.

Because the materials have a finite thermal conductivity, local hot spots can exist where the temperature is temporarily higher than in steady state. This effect is reinforced when the dried glue bead acts as a lens, and focuses the spot into a smaller area. The effect is illustrated in Figure C.2. According to Kim *et al.* [3], the spot can get smaller by a factor n, the refractive index of the bead material. If the bead material is glass-like, as is the case for sodium silicates, the refractive index is approximately $1.4 - 1.5$.

The transient temperature distribution of the probe can be simulated using finite-element software. The power input from a Gaussian spot of standard

deviation σ is simulated as

$$P(x,y) = \frac{P_0}{2\pi\sigma^2} \exp\left(-\frac{1}{2}\left(\frac{x}{\sigma}\right)^2\right) \exp\left(-\frac{1}{2}\left(\frac{y-y_0}{\sigma}\right)^2\right), \tag{C.1}$$

where the probe has a rectangular plan form of length L and width w, and the spot is located at a distance y_0 away from the clamped end of the cantilever. The input beam has a total power P_0. The total power incident on the cantilever P_t is

$$P_t = \int_0^L \int_{-w/2}^{w/2} P(x,y)\,\mathrm{d}x\,\mathrm{d}y = \frac{P_0}{2} \operatorname{erf}\left(\frac{w}{2\sqrt{2}\sigma}\right)\left(\operatorname{erf}\left(\frac{y_0}{\sqrt{2}\sigma}\right) - \operatorname{erf}\left(\frac{y_0-L}{\sqrt{2}\sigma}\right)\right). \tag{C.2}$$

In the limit case where $\sigma \ll w, L$, the total power $P_t \approx P_0$. In practice, however, $\sigma \approx w$, and a significant amount of power does not hit the probe. If the glue bead makes the spot on the cantilever surface smaller, only the power distribution changes, and the total incident power remains the same. The input power P_0 for the smaller spot, is normalized with P_t for the largest spot to compensate for this. Figure C.4 shows the maximum temperature in the volume of the cantilever as time progresses. The temperature profile is shown as a function of time in Figure C.3 for the original incident spot. The conductance of the cantilever is high enough for the heat to distribute quickly and prevent a significant hot spot from forming.

The lensing effect of the glue bead can therefore be disregarded and does not significantly contribute to the temperature of the cantilever.

This effects described above (melting and evaporation of the reflective coating) are not obserbed with the other cantilever designs (B to D), because the corresponding thermal conductances are so high that carbon contamination does not occur at equal levels of absorbed power.

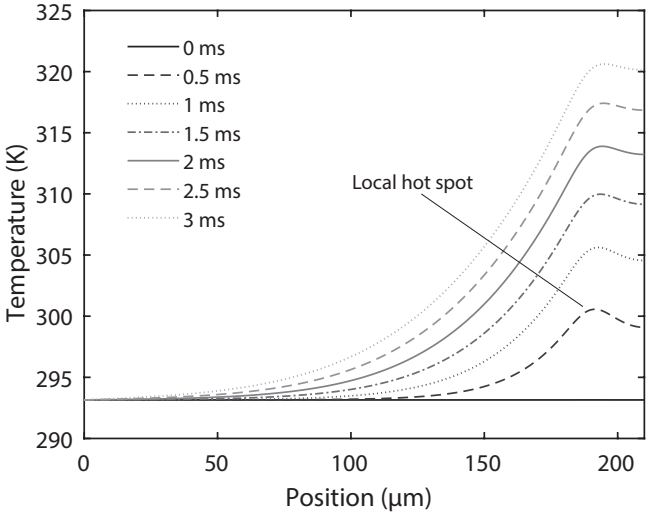

Figure C.3: Temperature profile along the length of a silicon nitride cantilever beam as a function of time. The cantilever has a rectangular plan form and is 210 µm long, 3.4 µm wide and 300 nm thick. The incident spot has a standard deviation of 5 µm. The beam is clamped at one end at which it is kept at a constant temperature of 293 K. The center of the spot is at 20 µm from the free end and contains an incident power $P_0 = 50\,\mu\text{W}$.

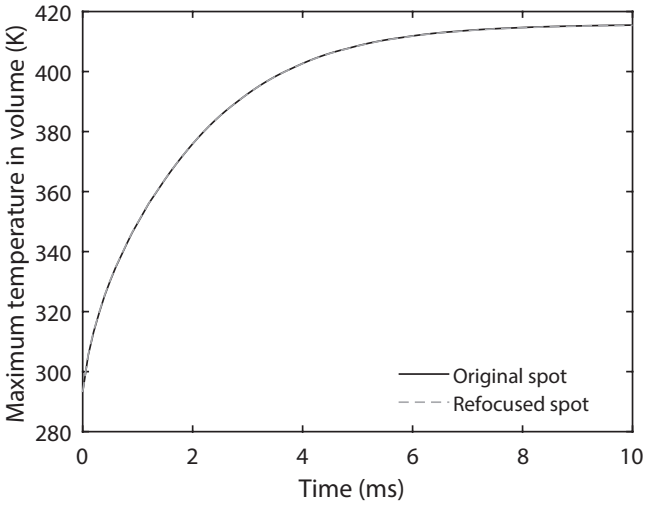

Figure C.4: Maximum temperature in the volume of a silicon nitride cantilever beam of 210 µm long, 3.4 µm wide and 300 nm thick. The original spot and refocussed spot have standard deviations of 5 µm and 3.3 µm, respectively. The beam is clamped at one end at which it is kept at a constant temperature of 293 K. The center of the spot is at 20 µm from the free end and contains an incident power $P_0 = 50\,\mu\text{W}$.

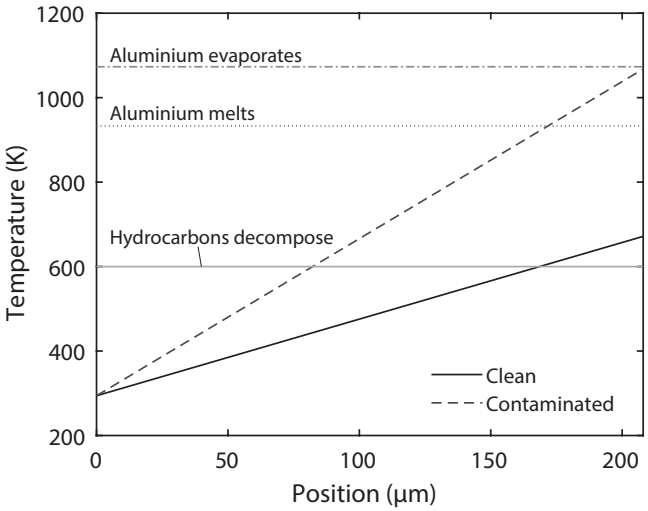

Figure C.5: Possible temperature distribution of probe A1/A2 due to carbon contamination. If the absorption increases by 210 %, the evaporation temperature can be reached.

Acknowledgments

The author thanks Saleh Aghajani of Delft University of Technology for his help with the SEM measurements, and Urs Staufer and Hans Goosen of Delft University of Technology for their insights in the failure mechanism based on their long experience with scanning probe microscopy and MEMS manufacturing.

Bibliography

[1] D. Miller and D. Haneman. Evidence for carbon contamination on vacuum heated surfaces by electron paramagnetic resonance. *Surface Science*, 19(1):45–52, 1970.

[2] A. Sarangan. Physical and Chemical Vapor Deposition. In *Nanofabrication, Principles to Laboratory Practice*, chapter 3, p. 53–98. CRC Press, Taylor & Francis Group, Boca Raton, FL, USA, 1st edition, 2016.

[3] M.-S. Kim, A. C. Assafrao, T. Scharf, A. J. H. Wachters, S. F. Pereira, H. P. Urbach, M. Brun, S. Olivier, S. Nicoletti, and H. P. Herzig. Submicron hollow spot generation by solid immersion lens and structured illumination. *New Journal of Physics*, 14(10):103024, 2012.

D. Implementing RF-injection for noise reduction

Laser diodes are ubiquitous in laboratory setups and are key components in broadband optical communication and the actuation and sensing of micro- and nanomechanical systems. Especially in the latter, intensity fluctuations in the illumination can limit the system bandwidth.

The optical beam deflection (OBD) system [1] is particularly sensitive to these intensity fluctuations. As an illustration of this, consider scanning probe microscopy. In such a microscope, a micro-cantilever is scanned over a sample surface while the interaction forces (van der Waals, Casimir, electromagnetic, thermo-mechanical, electrostatic, etc.) cause the motion of the cantilever to change. The cantilever is illuminated using a beam of light and the reflected beam is imaged onto a position sensitive detector (PSD). As the cantilever deflects and bends, the changing angles of incidence and reflection cause the spot of the reflected beam to move across the surface of the PSD. In practice the light source is typically a laser diode operating at a wavelength around 635 nm. The incident beam locally heats the cantilever, because a fraction of the incident light is absorbed. The hereby induced thermo-mechanical stresses cause the cantilever to deform. Fluctuations in the intensity of the illumination can thus introduce undesired motion of the cantilever. In addition to this, the intensity fluctuations can also introduce unwanted noise in the PSD when these cannot be fully compensated for. The attainable resolution and speed of such microscopes can thus be limited [2–4].

It has been suggested, that the intensity fluctuations of laser diodes can be reduced by injection of a high-frequency current into the laser diode [2, 3, 5, 6], a technique that is known as high-frequency injection (HFI). Injection of such a signal (typically in the radio frequency (RF) band of 300 MHz to 500 MHz) excites the laser in a multi-mode state [5]. This state makes the laser diode more robust against thermally induced variations in the cavity length and against optical feedback, which are considered the prime sources of the intensity fluctuations. The intensity fluctuations are reduced by the superimposition of modes, a phenomenon known as mode partition noise [7].

In practice, the laser diode is powered by a current source that supplies a stable DC current. An RF signal is generated by a signal generator and superimposed on the DC current by means of a bias-tee. To the best of our knowledge, a rigorous description of the implementation is lacking in

literature, which has led to contradictory conclusions about the effectiveness of this technique: some authors report a reduction in noise [2, 3, 5, 6], while others eventually abandoned the technique because of an apparent increase of noise rather than a decrease [8] or have reservations about its effectiveness on a system level [4].

Towards developing such a rigorous description, we provide a non-exhaustive overview of practical limitations that are encountered in implementation of HFI for OBD systems in this Appendix. In addition, we discuss system level considerations to realize intensity noise reduction in laser diodes for application in broadband nanomechanical systems.

D.1 Effect of Transverse Electromagnetic Modes

A multi-mode laser simultaneously emits several transverse electromagnetic (TEM) modes which have distinct spatial intensity distributions. The intensity distribution of the reflected beam can affect the output of the PSD.

To demonstrate this, we calculated the Hermite-Gaussian transverse electromagnetic modes (HG-TEM) that are typically encountered with laser diodes using the Matlab Laser Toolbox [9, 10]. Herein, the cavity is assumed to be square, and the total power equal to 1 W. A similar argument can be made for Hermite-Gaussian TEM modes, but these are less often encountered in practice. For illustration we assume a 2-cell PSD in which the position signal is proportional to the difference in the electric signal between the two cells, as shown in Figure D.1. The output of the PSD is given by

$$X_{\mathrm{p}} = X_{\mathrm{right}} - X_{\mathrm{left}}, \tag{D.1}$$

where X_{right} and X_{left} are the outputs of the right cell and the left cell, respectively. The combined response of the two cells is proportional to the total incidence power, therefore $X_{\mathrm{left}} = X_{\mathrm{total}} - X_{\mathrm{right}}$. The detector output that is normalized by the combined response of the cells reads:

$$\hat{X}_{\mathrm{p}} = \frac{2X_{\mathrm{left}} - X_{\mathrm{total}}}{X_{\mathrm{total}}}. \tag{D.2}$$

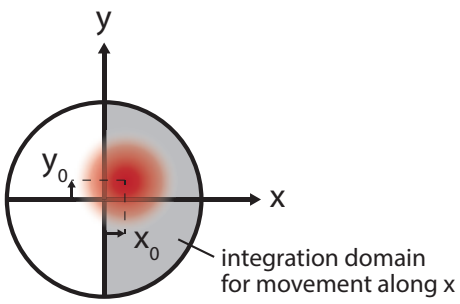

Figure D.1: The spot incident on an equivalent quad cell photo detector. The integration interval for motion along the x-axis is indicated.

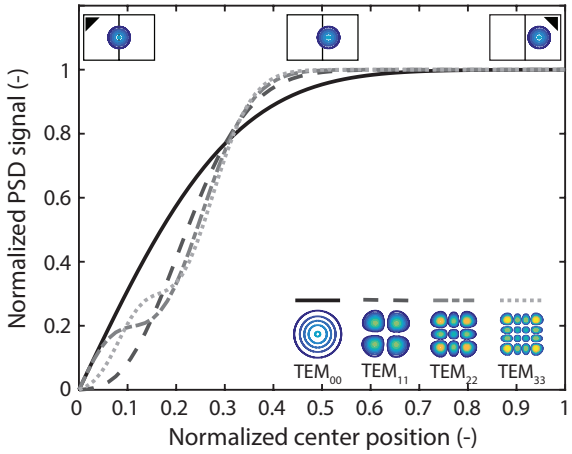

Figure D.2: Normalized output of a 2-cell PSD as a function of the center position of the laser spot. The center position is normalized with respect to the spot width. Its value is 0 when the spot is equally distributed over both cells and 1 when it is fully on one cell. In this example Hermite-Gaussian beam profiles are assumed.

This normalization yields a value of 0 when the spot is centered on the PSD, and goes to -1 or 1 when the spot is placed completely on the left cell or on the right cell of the PSD, respectively. The normalized detector output is plotted in Figure D.2 as function of the spot position. Because of symmetry in the results, only a shift onto the right cell is depicted. It is clear, that each TEM mode yields a different detector position response and that changes in the beam profile are therefore undesired. To ensure only the Gaussian TEM_{00} can propagate, laser diodes are coupled to a single-mode fiber. This fiber acts as a spatial low-pass filter and only allows the fundamental mode to propagate. This combination is ubiquitous in laboratory environments, because it offers an economical solution when space comes at a premium [11].

D.2 Measurement of intensity noise

The effectiveness of HFI on the intensity noise of laser diodes is studied via a naive implementation of the technique on laser diodes that we frequently use in table-top OBD systems [12, 13].

Previous studies of the technique relied on measurements of the total system noise at the PSD as a proxy for the optical intensity noise [2, 6]. To exclude spurious and coupled effects, we have removed the diode from the OBD system and measured the optical intensity noise directly.

The optical intensity is measured using a high-speed photo detector that is probed by a spectrum analyzer. This setup is similar in design to the one proposed by Shi *et al.* [14] and the one proposed by the Agilent corporation [15]. For the reader's reference, a schematic representation of the described setup is given in Figure D.3.

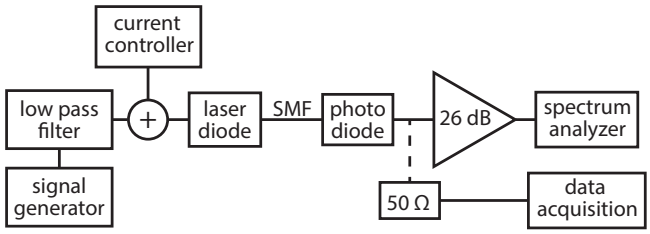

Figure D.3: Schematic of the experimental setup that is used to measure the relative intensity noise. The light is coupled from the diode into a single-mode fiber (SMF) and directly into the photo diode. The electrical output signal of the photo diode is then passed into a radio frequency (RF) amplifier and into the spectrum analyzer. The magnitude of the average signal is measured by terminating the output of the photo diode by 50 Ω and measuring the resulting voltage using a data acquisition system.

The used laser diode is coupled to a single-mode fiber (Thorlabs LP635-SF8) and is directly connected to a high speed photo detector (New Focus 1006, 60 GHz bandwidth) by means of said fiber. The output of the detector is amplified by a broadband amplifier (Miteq JS-3-01001800-29-5A) by 26 dB and is consecutively probed by a performance spectrum analyzer (PSA, Agilent E4446A). The relative intensity noise (RIN) is then determined as the ratio of the noise power spectral density $n(\omega)$ to the average power dissipated in the spectrum analyzer input P_{DC}. The measurements were performed at a measurement bandwidth of 4 GHz bandwidth. This bandwidth allows the detection of the relaxation peak in the intensity spectrum and a qualitative comparison of the measured spectra with the results obtained by Shi *et al.*

To obtain the noise power spectral density, the measured noise power $S(\omega)$ is corrected for the background noise $B(\omega)$ and the amplifier gain G and normalized by the corresponding resolution bandwidth $\Delta\omega$ of the PSA,

$$n(\omega) = \frac{S(\omega) - B(\omega)}{G\Delta\omega}. \tag{D.3}$$

The background noise is obtained when the system is fully connected, but the laser diode is switched off.

The average dissipated power cannot be measured using a PSA and is instead determined in a separate measurement via the voltage drop V_{out} over a 50 Ω resistor R. The resistor replaces the combination of the PSA and amplifier. By matching the impedance of these devices, it mimics the relevant electrical response and minimizes reflections of the RF signal. The average power dissipated in the resistor is easily determined via Ohm's law as $P_{\mathrm{DC}} = V_{\mathrm{out}}^2/R$. This leaves the RIN to be expressed as

$$\frac{\Delta I}{I} = \frac{n(\omega)\,R}{V_{\mathrm{out}}^2}. \tag{D.4}$$

The relative fluctuations given by this expression can be translated into absolute noise densities by scaling with the average optical power emitted by the

laser diode $\Delta P = (\Delta I/I)\, P_{\mathrm{av}}$. This average power is known through calibration of the laser diode with an optical power meter. The root mean square intensity noise for a given bandwidth is obtained via

$$\Delta P_{\mathrm{RMS}} = \int_0^{\tilde{\omega}} \frac{\Delta I}{I}(\omega)\, P_{\mathrm{av}} \mathrm{d}\omega. \tag{D.5}$$

To minimize signal drift of the laser diode, its temperature is stabilized to within a millikelvin from the set reference temperature by a thermo-electric heater in the diode mount (Thorlabs LM9LP) and a temperature controller (Thorlabs TED8020).

The injection of a high-frequency signal into the laser diode is realized using a radio frequency (RF) signal generator (HP 8663A, 2 GHz bandwidth). The DC drive current and the RF signal are combined using a bias-tee that is embedded in the laser diode mount. Using the setup described above, a signal was injected with an amplitude of 10 mA and a frequency of 100 MHz to 1000 MHz. In agreement with the results of Kassies *et al.* [6], the signal amplitude was chosen such that the total drive current drops slightly below the threshold current of the diode at which the laser starts to lase. Kassies *et al.* found this to be a necessary condition to excite the laser diode in a multi-mode state.

D.3 Results

The intensity noise integrated over a measurement bandwidth of 4 GHz as a function of modulation frequency is shown in Figure D.4. It is evident that modulation causes the intensity noise to increase significantly compared to an unmodulated signal (data point at 0 Hz corresponds to 6 µW).

It should be noted here that the output of the RF signal generator is not a pure single tune harmonic. This is clear from the measured output spectrum of the signal generator as shown in Figure D.5 as the higher harmonic components are also present in the spectrum. From the same figure, it is also evident from the corresponding spectrum of the laser diode that the higher harmonics are strong enough to excite the laser diode. This results in a noise floor that is lifted over a broad range of frequencies. In the latter measurement the generator is not coupled to the spectrum analyzer directly. The measured peaks are rather the output of the photo diode. Therefore these cannot be considered to be spurious electrical signals that are injected via the signal generator directly, but have to be the result of effects in the laser diode.

To minimize the effect of these higher harmonics on the intensity noise of the laser diode, the signal of the generator is cleaned up using a set of low-pass, high-rejection filters that provide 40 dB isolation up to 20 GHz (Mini-Circuits VLFX-80, -225, -500, -825, and -1100). As can be seen in Figure D.4, the 40 dB suppression of the higher harmonics is effective in reducing the intensity

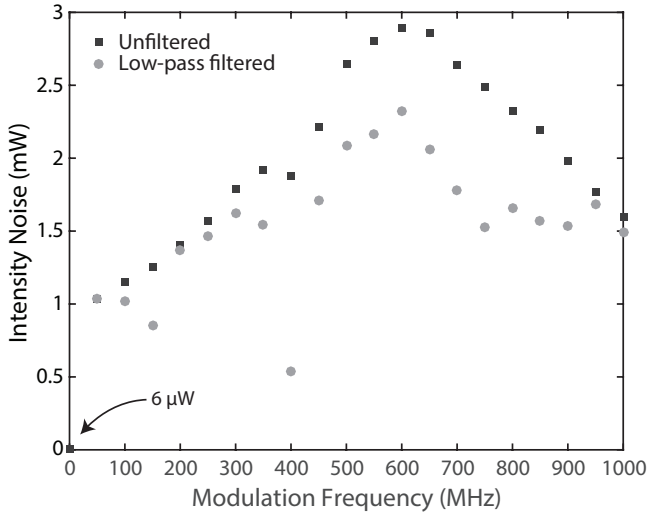

Figure D.4: Experimentally determined intensity noise (root mean squared) as a function of a modulation frequency between 100 MHz to 1000 MHz and a measurement bandwidth of 4 GHz. The low-pass filter evidently helps in reducing the intensity noise, but does not reduce it to a level below that of the unmodulated signal.

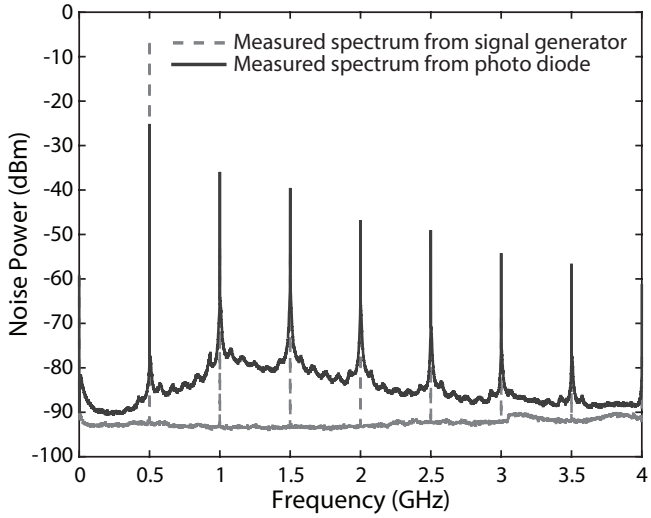

Figure D.5: Measured noise spectrum of the laser diode versus the measured output spectrum of the signal generator for a driving frequency of 500 MHz. It is evident that the spectrum of the laser diode is correlated with that of the generator.

noise, but not to the extent that the noise is lower than for an unmodulated signal. As higher harmonics can be introduced by non-linearities in the system, these results indicate that the purity of the source is of high importance.

D.4 Discussion

Using this naive implementation of the HFI technique, we were unable to lower the intensity noise to below that of an unmodulated laser in our system. A closer observation of the setup reveals there are several possible reasons for this.

Firstly, it is clear from the results that impurities in the injected signals can cause a strong response in the intensity noise spectrum. The frequency at which the intensity noise is minimal is diode-specific. Although the frequency can be calculated using rate-equations [5], the required design parameters are typically unknown, which leaves empirical determination as only option. This implies the use of a tunable source, which could later be replaced by a single tune oscillator.

Secondly, it should be noted that high frequency injection reduces the intensity noise by mode partition. Although the superposition of the modes results in lower intensity fluctuations, the individual modes may show larger fluctuations. The single-mode fiber allows only the TEM_{00} mode to propagate, causing us to only measure the fluctuations of this mode. This explains why the intensity fluctuations apparently increase in the measurements described earlier. Removing this spatial filtering from the setup may yield a lower intensity noise. In this specific case, this requires the single-mode fiber to be replaced by a multi-mode fiber or a separate laser diode in combination with a collimator lens to realize a collimated free-space beam.

However, in case multi-mode operation is effective in reducing the optical intensity noise, this may not be advantageous for overall system noise. As explained in Section D.1 and as highlighted by Enning [4], the superimposed laser modes result in a beam profile that is no longer Gaussian or point-symmetric, and may vary in time. This increases the system noise by introducing additional noise in the PSD. In such a scenario choosing a low-noise laser or an incoherent source, such as the collimated light from a light emitting diode (LED), may improve system performance more than reduction of intensity noise through HFI can. This, however, remains to be confirmed.

Thirdly, laser intensity noise is notoriously sensitive for optical feedback into the laser diode. When the diode is coupled to a fiber, optical feedback is caused by the reflection at the end of the fiber. The glass-to-air interface yields that $\approx 4\%$ of the light is reflected back into the laser cavity for both single-mode and multi-mode fibers. Although this is significant, Gray *et al.* [5] have predicted that by means of HFI a laser diode can be made nearly insensitive to optical feedback upwards to 10%. Using the setup described above, the effect of optical feedback could not be determined. However, an OBD system can be made more robust against optical feedback without the

use of HFI. This can be achieved by the use of an anti-reflection coated fiber or an optical isolator in the optical path for a confocal system. For non-confocal systems, the geometry of the system can be used to minimize the intensity of the light that is reflected back into the diode.

Lastly, it should also be noted here that not only the intensity of the feedback, but also the round-trip time of the beam influences the effectiveness of HFI, as Imran and Yamada [16] have demonstrated. Depending on the geometry, it may be necessary to stabilize the temperature of the full setup, rather than just the temperature of the laser diode to minimize the effects of thermally-induced changes in the length of the extended cavity.

D.5 Conclusion

Intensity fluctuations in laser diodes introduce noise in OBD systems, such as scanning probe microscopes, by disturbing the probe and introducing additional noise in the PSD. Contradictory reports on the efficacy of high frequency injection as a means for reducing the amplitude of the intensity fluctuations, can be traced to choices made in the system architecture and the corresponding parameters. For example, the use of a multi-cell PSD and single-mode fibers.

We have shown that the purity of the injected signal and its frequency affect the efficacy of HFI. In practice, the system parameters such as the driving frequency and the length of the extended cavity need to be determined experimentally, which can be costly and time consuming. The introduction of spatial filters, such as single-mode fibers, further constrains an effective implementation by limiting the effects to the cavity and by allowing only a single-mode to propagate. Due to mode partition the amplitude fluctuations of this propagating mode may be significantly higher once the laser is operated in a multi-mode state.

We conclude that system level considerations, such as the need for single-mode operation to limit the noise of the PSD, contradict the conditions required for effective implementation of HFI.

More research is required to arrive at a set of system requirements and conditions under which this technique is effective. Noise reduction in laser diodes knows no single solution, and can only be achieved by a priori consideration of the system architecture. Based on the reported experiences we recommend users to reconsider the system architecture and use low noise optical sources whenever possible, before considering the application of high frequency injection.

Acknowledgments

The author thanks Jeroen Hoogland of TNO and Roland Horsten of Delft University of Technology for lending the necessary equipment and Rodolf Herfst of TNO for useful discussions on mode-hopping in laser diodes.

Bibliography

[1] G. Meyer and N. M. Amer. Novel optical approach to atomic force microscopy. *Applied Physics Letters*, 53(12):1045, 1988.

[2] T. Fukuma, M. Kimura, K. Kobayashi, K. Matsushige, and H. Yamada. Development of low noise cantilever deflection sensor for multienvironment frequency-modulation atomic force microscopy. *Review of Scientific Instruments*, 76(5):053704, 2005.

[3] T. Fukuma and S. P. Jarvis. Development of liquid-environment frequency modulation atomic force microscope with low noise deflection sensor for cantilevers of various dimensions. *Review of Scientific Instruments*, 77(4):043701, 2006.

[4] R. Enning. *High frequency atomic force microscopy*. Doctoral and habilitation theses, ETH Zürich, 2011.

[5] G. R. Gray, A. T. Ryan, G. P. Agrawal, and E. C. Gage. Control of optical-feedback-induced laser intensity noise in optical data recording. *Optical Engineering*, 32(4):739, 1993.

[6] R. Kassies, K. O. Van Der Werf, M. L. Bennink, and C. Otto. Removing interference and optical feedback artifacts in atomic force microscopy measurements by application of high frequency laser current modulation. *Review of Scientific Instruments*, 75(3):689–693, 2004.

[7] K. Petermann. *Laser Diode Modulation and Noise*. Springer Netherlands, Dordrecht, first edition, 1988.

[8] I. Schlesinger, K. Kuchuk, and U. Sivan. An ultra-low noise optical head for liquid environment atomic force microscopy. *Review of Scientific Instruments*, 86(8):083705, 2015.

[9] G. Römer and A. Huis in 't Veld. Matlab Laser Toolbox. *Physics Procedia*, 5(B):413–419, 2010.

[10] G. Römer. Matlab Laser Toolbox User Manual, Version 0.1 beta, 2010.

[11] H. Sadeghian, B. Dekker, R. Herfst, J. Winters, A. Eigenraam, R. Rijnbeek, and N. Nulkes. Demonstration of parallel scanning probe microscope for high throughput metrology and inspection. In J. P. Cain and M. I. Sanchez, editors, *Proc. SPIE 9424, Metrology, Inspection, and Process Control for Microlithography XXIX*, p. 94240O, San Jose, CA, USA, 2015. SPIE Digital Library.

[12] R. Herfst, W. Klop, M. Eschen, T. van den Dool, N. Koster, and H. Sadeghian. Systematic characterization of optical beam deflection measurement system for micro and nanomechanical systems. *Measurement*, 56:104–116, 2014.

[13] R. Bijster, H. Sadeghian, and F. van Keulen. Non-contact distance measurement and profilometry using thermal near-field radiation towards a high resolution inspection and metrology solution. In M. I. Sanchez and V. A. Ukraintsev, editors, *SPIE Conference Proceedings Volume 9778: Metrology, Inspection, and Process Control for Microlithography XXX*, p. 97780H, San Jose, CA, United States of America, 2016. SPIE Digital Library.

[14] H. Shi, D. Cohen, J. Barton, M. Majewski, L. A. Coldren, M. C. Larson, and G. A. Fish. Relative intensity noise measurements of a widely tunable sampled-grating DBR laser. *IEEE Photonics Technology Letters*, 14(6):759–761, 2002.

[15] Agilent Technologies. Digital Communication Analyzer (DCA), Measure Relative Intensity Noise (RIN) - Product Note 86100-7. Technical report, Agilent Technologies, Inc., 2008.

[16] S. M. S. Imran and M. Yamada. Numerical Analysis of Suppression Effects on Optical Feedback Noise by Superposition of High Frequency Current in Semiconductor Lasers. *IEEE Journal of Quantum Electronics*, 49(2):196–204, 2013.

Acknowledgments

I would be lying, if I said this has been a smooth ride. To be frank, it rather was a road full of bumps and potholes. By the time I am writing this, I am glad it is over. I am therefore extra grateful to those that supported me during the 6.5 years that I spent on this research.

First and foremost, I would like to thank Fred and Giampiero, who, even though the topic drifted away from their respective areas of expertise, managed to offer out-of-the-box perspectives or insights that I needed at times. The same holds for Stefan who often provided a helpful hand. Also, I want to thank Hamed and Jan for enabling this research in the first place, by welcoming me to TNO and making the position available. Of course, the same holds for Wouter, Monique and Rolf, who opened doors and supported me to continue my research. I appreciate their patience and willingness to help keep treasure seekers at bay for as long as they did. Special thanks go to Nicole, who during the years that she managed the TNO ERP, juggled the finances of my project and offered a helping hand in all things project management related.

As a PhD candidate at TNO and TU Delft, I had the pleasure of not one but two desks and many colleagues who offered insights and plenty distractions. There are too many to name here all, but I would like to especially thank Kitty, Kim, Mehmet, Sasan, Hugo, Max, Floris, Jan, Doris, and Martin. Sharing an office or even adjoining desks with you has been completely my privilege.

There are plenty of people that challenged and encouraged me to do this PhD in the first place, and supported me along the way. I thank my parents, Johan and Francis, for laboring hard so that Mike and I had the opportunities to study. I also thank my parents-in-law, Frank and Anita, for welcoming me into their family and the endless discussions over dinner and their sincere interest in the progress of my research. On the other hand, I want to thank my brother Mike, and brothers-in-law Timo and Job for *not* discussing research with me.

Finally, I want to wholeheartedly thank my wife, Nina, for her support during this journey. Although plenty of people knew about the setbacks that I faced, she is the only one that really knew my doubts and troubles. Without her encouragement and kind words, I would probably have stopped at one point to regret it later.

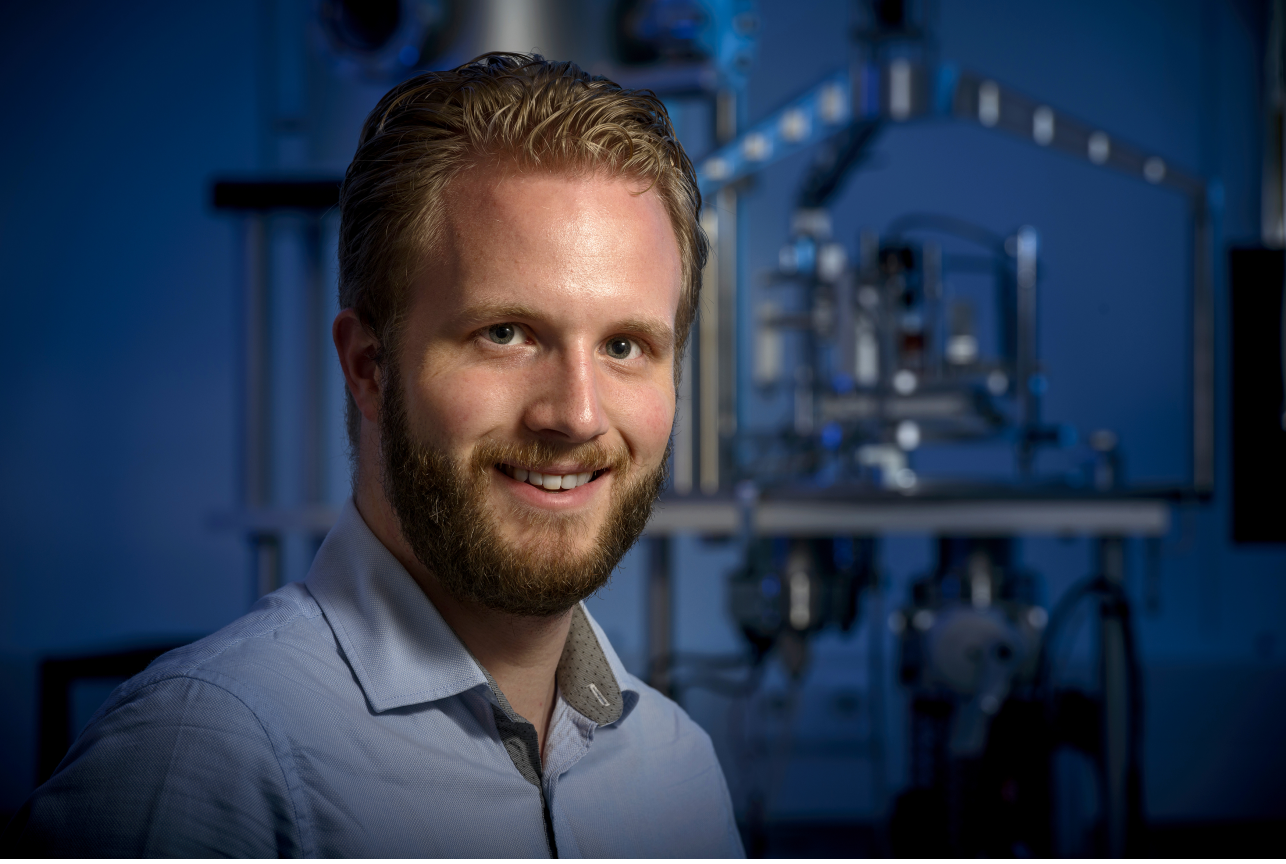

About the author

Roy Jacobus Franciscus Bijster (2 January 1990) was born and raised in Valkenswaard, the Netherlands where he attended the local Gymnasium of SG Were Di from 2001 to 2008. He obtained the degrees of Bachelor of Science and Master of Science in Aerospace Engineering from Delft University of Technology (Delft, the Netherlands) in 2011 and 2014, respectively. From 2014 to 2021, Roy was affiliated with the optomechatronics department of The Netherlands Organisation of Applied Scientific Research TNO and the department of Precision and Microsystems Engineering of Delft University of Technology, where he conducted the doctoral research that is described in this thesis. Since late 2018, Roy has been working as a Systems Engineer at Hittech Multin (The Hague, the Netherlands) working on projects for the instrumentation, healthcare and semiconductor manufacturing industries.

List of publications

Journal papers

R. J. F. Bijster and F. van Keulen, "Design of a calorimeter for near-field heat transfer measurements and thermal scanning probe microscopy", Review of Scientific Instruments, vol. 92, no. 2, p. 025008, Feb. 2021.

Conferences

R.J.F. Bijster, H. Sadeghian, F. van Keulen, "Towards contactless scanning thermal microscopy: measuring probe-sample separation", Proceedings of the 15th International Workshop on Nanomechanical Sensing NMC2018, Incheon, South-Korea, 2018

R.W. Herfst, **R.J.F. Bijster**, A. Dekker, J. Wei, H.W. van Zeijl, R. Kruidhof and H. Sadeghian, "Nanopositioning MEMS stage", AIM 2017 IEEE International Conference on Advanced Intelligent Mechatronics, 3 Jul 2017, Munich, Germany

R.J.F. Bijster, H. Sadeghian, F. van Keulen, "A new horizon: Using heat transfer to measure distance in high performance metrology solutions", Proceedings of the 13th International Workshop on Nanomechanical Sensing NMC2016, Delft, The Netherlands, 2016

R.J.F. Bijster, H. Sadeghian, F. van Keulen, "Towards an effective reduction of intensity noise in laser diodes", Proceedings of the 13th International Workshop on Nanomechanical Sensing NMC2016, Delft, The Netherlands, 2016

R.J.F. Bijster, H. Sadeghian, F. van Keulen, "Non-contact distance measurement and profilometry using thermal near-field radiation towards a high resolution inspection and metrology solution", Proc. SPIE 9778, Metrology, Inspection, and Process Control for Microlithography XXX, 97780H (21 April 2016); https://doi.org/10.1117/12.2218877

R.J.F. Bijster, "Accurate measurement of near-field thermal radiation", 3rd Thermal Probe Workshop, Zurich, Switserland, 21 Jan 2016

R.J.F. Bijster, H. Sadeghian, F. van Keulen, "How to measure near-field radiative heat transfer at submicron distances and at high fidelity?", Nano City 2015, Amsterfoort, The Netherlands, 5 October 2015

R.J.F. Bijster, H. Sadeghian, F. van Keulen, "High Fidelity Measurement of Near-Field Radiative Heat Transfer for Thermal Microscopy and Distance Sensing", 18th Engineering Mechanics Symposium, 2015

Patents

H. Sadeghian and **R.J.F. Bijster**, "Thermal probe for a near-field thermal microscope and method for generating a thermal map", WO2017010884A1, 2017

H. Sadeghian and **R.J.F. Bijster**, "Thermal probe", WO2016204611A1, 2016